Doctorado en Oceanografía y Cambio Global

Universidad de Las Palmas de Gran Canaria

Tesis Doctoral

Variability of the Meridional Overturning Circulation in the South Atlantic and Pacific Oceans

Cristina Arumí Planas

Las Palmas de Gran Canaria, 10 de febrero de 2025

Dª MAGDALENA SANTANA CASIANO, COORDINADORA DEL PROGRAMA DE DOCTORADO EN OCEANOGRAFÍA Y CAMBIO GLOBAL DE LA UNIVERSIDAD DE LAS PALMAS DE GRAN CANARIA

INFORMA,

De que la Comisión Académica del Programa de Doctorado, en su sesión de fecha de febrero de 2025 tomó el acuerdo de dar el consentimiento para su tramitación, a la tesis doctoral titulada "*Variability of the Meiridonal Overturning Circulation in the South Atlantic and Pacific Oceans"* presentada por la doctoranda Dª Cristina Arumí Planas y dirigida por el Profesor Doctor Alonso Hernández Guerra y la Doctora María Dolores Pérez Hernández.

Y para que así conste, y a efectos de lo previsto en el Artículo 11 del Reglamento de Estudio de Doctorado (BOULPGC 04/03/2019) de la Universidad de Las Palmas de Gran Canaria, firmo la presente en Las Palmas de Gran Canaria, a de febrero de dos mil veinticinco.

UNIVERSIDAD DE LAS PALMAS DE GRAN CANARIA

ESCUELA DE DOCTORADO

Programa de doctorado en Oceanografía y Cambio Global.

Título de la Tesis: Variability of the Meridional Overturning Circulation in the South Atlantic and Pacific Oceans

Tesis Doctoral presentada por Dª Cristina Arumí Planas.

Dirigida por el Dr. D Alonso Hernández Guerra.

Codirigida por la Dra. Dº María Dolores Pérez Hernández.

Las Palmas de Gran Canaria, a 10 de febrero de 2025.

El Director, La Codirectora, La Doctoranda,

A la meva família, amigues i amics

No es pot nedar cap a nous horitzons

fins no tenir el coratge de perdre de vista la costa.

— ***William Faulkner***

Acknowledgements

He soñado con este instante durante mucho tiempo, y ahora, mientras escribo estas líneas, no puedo evitar que se me escape alguna sonrisa entremezclada con un poco de nostalgia por los innumerables recuerdos que me vienen a la cabeza. Termina una etapa que me ha encantado vivir y ha sido así gracias a las personas con las que he compartido estos años de doctorado. Este viaje de investigación ha sido como un oleaje, y cada uno de vosotros ha sido una ola que me ha empujado hacia delante, permitiéndome llegar hasta aquí.

No podría empezar estos agradecimientos por otra persona que no fuese a mi director de tesis, Alonso. Gracias por confiar en mí siempre, incluso en aquellos momentos en los que yo misma dudaba. Gracias por darme la oportunidad de formarme a tu lado, saber llevar mis nervios y tu incansable dedicación. Has sido mi guía, y sin tu supervisión constante y exigente, no habría logrado llegar hasta aquí.

A mi codirectora de tesis, Lola. Gracias por tu dedicación y disposición por compartir tu conocimiento. Tu ayuda incondicional y tus valiosos consejos me han hecho crecer tanto a nivel profesional como personal durante todos estos años. Has sido un modelo que seguir para mí.

A Pedro Vélez, Josep Lluís Pelegrí, Ignasi Vallés, Riccardo Farneti, Luis Cana, Covadonga Orejas y a todos los demás coautores que han contribuido esencialmente en algunos capítulos de mi tesis. Gracias por compartir vuestra experiencia y hacer brillar mis estudios con valiosos comentarios. También agradecer al equipo de iAtlantic por el apoyo recibido a lo largo de este camino.

To Renellys Perez, Shenfu Dong, Matthew Mazloff, and Eleanor Frajka-Williams, I am immensely grateful for the opportunity to conduct my research stays with you. Thank you for generously dedicating your time, enabling me to learn from your acknowledge and experience. Your support has been invaluable, and I truly appreciate the guidance you have provided throughout this learning journey.

A la Irene i la Clara, us vull agrair la relació que tenim i per ser dues amigues tan extraordinàries i diferents. Sou la família que he escollit i m'heu demostrat que l'amistat no té límits en la distància. Tot i ser completament diferents, ens complementem d'una manera inexplicable. Gràcies per fer-me veure la vida més dolça i senzilla en qualsevol circumstància. Us estimo molt, estigueu a l'Amazones, Berlín, Mèxic o Barcelona.

Als meus estimats amics Helena, Berta, Maty, Pol Thomas, Dalmau i el tete Martí, sou una part molt especial d'aquest camí. Encara que la nostra comunicació sigui majoritàriament per missatges, és sempre un plaer retrobar-nos i comprovar que tot continua igual. Gràcies per escoltar-me, per compartir amb mi els moments de felicitat i per estimar-me incondicionalment.

A les meves grans amigues de la Costa Brava, Aliona, Sandra, Mire, Diana i Ainara, sou una part imprescindible de la meva vida. Sense que suposi cap mena d'esforç, sou el pilar en què puc recolzar-me en qualsevol moment i situació. Desitjo que aviat puguem estar més a prop i compartir molts més moments meravellosos juntes. Vull fer una menció especial per a la Sandra: gràcies pel teu suport incondicional, per haver fet realitat el nostre duo "*Zipi i Zape*" i per arrencar-me un somriure en qualsevol moment. T'estimo molt, germaneta!

No podia oblidar-me d'agrair a la Marta i en David per tots els dies i nits d'estiu sota un cel estrellat i la llum de la lluna, en què les nostres xerrades recarreguen les meves forces entre rialles i energia positiva.

A mis amigos del Erasmus, Clara, Sofia, Álvaro, Josep, Alberto, Sergio, Bea y María, gracias por convertiros en mi familia en Bergen. Me llenan de vida nuestros reencuentros que entre fotos, risas y cervezas se convierten en momentos inolvidables.

A mis amistades del máster, los *Oceanitos*, especialmente a Kevin, Neus, Leyre, Natalia, Marta, Dani, Diego, Nacho, David, Andrea, Javi y Pepelu. Gracias por el viaje a Almería, las comilonas de los domingos y las risas que hacen mejor mis días. La menció especial és per a tu, Marta. Valoro immensament haver-te tingut com amiga des del primer instant del màster. Gràcies per suportar-me durant trenta-nou dies a la llitera de dalt compartint menys d'un metre quadrat, per ser tal com ets i per la sort de comptar amb tu al meu costat. Ets una persona molt especial per a mi, i, encara que ara estiguem lluny, almenys per un temps, sàpigues que tens una casa allà on jo sigui!

A mis *Frutas,* Jordi, David, Sarai, Javi, Tania, Miguel, Celina, Marta, Yeyo, Baixulo y Begoña. Gracias por contagiarme de vuestra energía y alegría. Por ayudarme a relativizar nuestros dramas con un Karaoke tonto cualquier día de la semana o un domingo de asadero con las paellas de nuestro valenciano. La mención especial va para Tania, por ser uno de mis pilares durante estos años, por escucharme, cuidarme y hacerme sentir que juntas podemos con todo. Estoy segura de que he ganado una amiga para siempre.¡Quérote moito!

También quiero agradecer a personas muy especiales que he conocido en el paraíso de Canarias. A Rubén Castro, tu apoyo ha sido clave en muchos momentos de este camino, y tu amistad significa mucho para mí. A Carlitos Marrero, fuiste una de las primeras personas que conocí en canarias y convertiste mi primer año de resi en uno de los mejores de mi vida; y aunque ya no vivamos tan cerca, las risas nunca faltan cada vez que nos reencontramos. A Ari Aldrich, Juan Melian e Inés Sastre, aunque nos veamos de forma intermitente, vuestro apoyo y ánimo han sido constantes. A Paula (y Trufa), te convertiste en una persona muy especial para mí; gracias por tu manera de luchar por lo que quieres, eres una fuente de inspiración para todos los que te conocen. Y a mis *Orquídeas*, en especial a Raúl, Fran, Abraham, Alexis y Ana, gracias por recogerme en tierra y llevarme a otro mundo lleno de burbujas y risas, pero, sobre todo, gracias por cuidarme tanto.

To everyone I had the pleasure of meeting during my time in the United States: Daniel, and specially Mia, our shared love for sharks brought us together in 2018, and since then, you have always been there to make my time memorable, both in and out of the water. To Bryony, thank you for replying to my email and for becoming one of the best friends I've ever made in such a short time. A Rubén, Jorge, Edu y Leire, gracias por cuidarme tanto, por hacerme reír y por compartir conmigo muchos momentos felices en San Diego.

A todos mis queridos amigos de Hamburgo, y en especial a Lucía y a mis *Sirenas del Alster*: Alexandra, Nicole, Paloma, Natalia y Clara. Gracias por iluminar mis días en Hamburgo con vuestra energía, alegría y calidez. Me he ido con el corazón lleno, y sintiéndome enormemente afortunada por haber compartido mi tiempo con vosotras en Alemania. También quiero dar las gracias a David, no solo por recogerme en Kleken, sino también por haber demostrado ser un gran amigo. ¡Os espero con los brazos abiertos en las islas o en cualquier rincón del mundo en el que me encuentre!

Tampoco podía faltar el grupo de Tafira: Vero, Mel, Dani, Miguel, Patry, Mara, Alex, Ion, Tania, David, Marta, Chema, Adrián… Gracias por todo el ánimo recibido a lo largo de estos años, por ser un gran equipo y por las incontables horas compartidas en el campus de Tafira. No hay momento más valioso que las pausas para un café en Arquitectura o una cena al terminar de trabajar en Las Canteras. No solo por el café o la comida, sino por las conversaciones, las risas, la compañía y el apoyo constante. La mención especial es para mi gran amiga Maria. Quería agradecerte una vez más por todo lo que hiciste por mi para que pudiera llegar hasta aquí. Gracias por estar siempre a mi

lado y contagiarme de toda tu alegría. No puedes imaginar cuánto te echo de menos.

Todo lo que he vivido durante esta tesis nunca habría sido posible sin Dani, mi *Gemelier*. Muchas gracias por el soporte diario, tanto dentro como fuera del laboratorio, por compartir las alegrías y las penas de nuestro día a día. Recorrer juntos el camino, desde alfombrillas hasta doctores, pasando por funcionarios un martes cualquiera, nos ha hecho un gran equipo, ya sea en Las Palmas, en mitad del Atlántico (viendo Harry Potter), o en los congresos internacionales de Berlín, Hamburgo, New Orleans (con un paseíto por Dallas) ... Sin duda, espero tenerte como amigo siempre.

Com ja he dit, aquest és el final d'una etapa, i quan aquests dies miro enrere i faig memòria del camí recorregut, et veig a tu, Jordi, en cada revolt, cuidant-me i estimant-me. Has estat la meva fortalesa i suport constant, i no puc imaginar haver arribat aquí sense tu. Gràcies per estimar-me tal com sóc, per agafar tots els vols necessaris, per fer-me feliç i per recórrer aquest camí junts. Em sento molt afortunada de tenir-te al meu costat.

Gràcies infinites als meus pares, que amb només disset anys em vau permetre volar sola i gràcies a això he arribat fins aquí. En especial a la meva mare, segurament la persona més orgullosa d'aquestes pàgines; gràcies per encoratjar-me sempre amb tot allò que m'he proposat fer. Al meu pare, gràcies per ajudar-me a desconnectar cada cop que torno a casa i per ser una font inesgotable de força i alegria. A les meves germanes, Marta i Viscosin, gràcies per creure en mi en tot moment i per ser les millors companyes de vida. Finalment, vull agrair a la meva família Planas i Cal Mundu, tant als que hi sou com als que ja no hi sou: us estimo pel vostre suport i l'admiració constant per tot el que he anat aconseguint. És la prova que necessitàveu per confirmar que no em dedicava a nedar amb dofins...

Per tot això, aquesta tesi és també en part vostra.

13 de enero de 2025

Table of Contents

List of Figures

List of Tables

List of Abbreviations

AABW	Antarctic Bottom Water
AAIW	Antarctic Intermediate Water
ACC	Antarctic Circumpolar Current
ADCP	Acoustic Doppler Current Profiler
AMOC	Atlantic Meridional Overturning Circulation
CCHDO	CLIVAR and Carbon Hydrographic Data Office
CGCM	Coupled General Circulation Model
CMEMS	Copernicus Marine Environment Monitoring Service
CMIP6	Coupled Model Intercomparison Project 6
CTD	Conductivity-Temperature Depth
DEBC	Deep Eastern Boundary Current
DWBC	Deep Western Boundary Current
EAC	East Australian Current
ECCO	Estimating the Circulation and Climate of the Ocean
EPR	East Pacific Rise
ESPCW	Eastern South Pacific Central Water
ESSW	Equatorial Subsurface Water
GFDL	Geophysical Fluid Dynamics Laboratory
GLORYS	Global Ocean Physics Reanalysis

GO-SHIP	Global Ocean Ship-Based Hydrographic Investigations Program
GRACE	Gravity Recovery and Climate Experiment
GTSPP	Global Temperature and Salinity Profile Program
IDW	Indian Deep Water
ITF	Indonesian Throughflow
JAMSTEC	Japan Agency for Marine Earth Science and Technology
LADCP	Lowered Acoustic Doppler Current Profiler
LCDW	Lower Circumpolar Deep Water
L-PMOC	Lower Pacific Meridional Overturning Circulation
MAR	Mid-Atlantic Ridge
MHT	Meridional Heat Transport
MOC	Meridional Overturning Circulation
MOM	Modular Ocean Model
M_{ov}	Freshwater Transport by the AMOC
NADW	North Atlantic Deep Water
NCEP	National Centers for Environmental Prediction
NEMO	Nucleus for European Modeling of the Ocean
NZ	New Zealand
OFES	Ocean general circulation model For the Earth Simulator

OGCM	Ocean General Circulation Model
ORCHESTRA	Ocean Regulation of Climate by Heat and Carbon Sequestration and Transports
PCC	Peru-Chile Current
PCUC	Peru-Chile Undercurrent
PDW	Pacific Deep Water
PIES	Pressure-Equipped Inverted Echo Sounders
PMOC	Pacific Meridional Overturning Circulation
SACW	South Atlantic Central Water
SADCP	Shipboard Acoustic Doppler Current Profiler
SAGA	South Atlantic Gateway
SAMBA	South Atlantic MOC Basin-wide Array
SAMW	Subantarctic Mode Water
SPCW	South Pacific Central Water
SPSTMW	South Pacific Subtropical Mode Water
SSHA	Sea Surface Height Anomalies
TKR	Tonga-Kermadec Ridge
UCDW	Upper Circumpolar Deep Water
U-PMOC	Upper Pacific Meridional Overturning Circulation
WOA18	World Ocean Atlas 2018
WOCE	World Ocean Circulation Experiment

WSPCW	Western South Pacific Central Water
XBT	eXpendable BathyThermograph
ZVS	Zero Velocity Surface

Abstract

The ocean circulation dynamics in the Southern Hemisphere have an important role in the global climate system. The system of ocean currents knwon as Meridional Overturning Circulation (MOC) connects and redistributes salt, heat, and other biogeochemical tracers across the different ocean basins. Here, we detail the South Atlantic Ocean circulation patterns by analyzing hydrographic data from several cruises using an inverse box model to adjust the reference-level velocities. The upper layer currents, such as the northwestward-flowing Benguela Current and southward-flowing Brazil Current, describe the South Atlantic anticyclonic gyre. The deep layers feature the southward transports of the deep boundary currents and a west-to-east flow between the basins near 24°S (7.5 ± 4.4 Sv) above the Mid-Atlantic Ridge. Both upper and deep layers connect the eastern and western basins; however, the abyssal waters present northward mass transports through Argentina and Cape Basins without any interbasin exchange across the Mid-Atlantic Ridge. Furthermore, the cruise data allow us to compute the upper AMOC (Atlantic MOC) strength, as well as the transports of mass, heat, and freshwater, demonstrating the characteristic northward heat transport and the dominance of evaporation over precipitation across the subtropical South Atlantic.

Currently, the freshwater transport by the AMOC (M_{ov}) across 34.5ºS in the South Atlantic has been identified as a possible indicator of AMOC stability, with a negative (southward) freshwater transport indicating a possible bistable AMOC regime and positive (northward) transport indicating a monostable regime. This Ph.D. thesis computes the M_{ov} using observations from 49 eXpendable BathyThermograph (XBT)

transects, from South America to South Africa, over nearly two decades (2002-2019), resulting a negative M_{ov} mean of −0.15 ± 0.09 Sv which suggests a bistable AMOC regime. These results are complemented with two data sets derived from Argo float observations, four Ocean General Circulation Models (OGCMs: GLORYS, OFES, MOM6-JRA, and MOM6-MERRA), and thirty-two Coupled General Circulation Models (CGCMs: CMIP6). Both Argo and OGCMs data sets agree with the sign of the M_{ov} computed from the XBT data. Nevertheless, more than half of the examined CGCMs, 20 out of 32, present positive M_{ov} mean values. To investigate the causes of the differing signs of the M_{ov} across the models, we examine the salinity vertical structure in CGCMs with positive and negative M_{ov}. Importantly, our work highlights the different salinity structures in CMIP6 models with positive M_{ov} means (fresher upper and saltier deep waters compared to those estimating negative M_{ov} values), suggesting that salinity biases may be responsible for the opposite sign of M_{ov}. As a result, this thesis highlights the importance of improving CMIP6 model representations, especially the salinity bias. In addition, we compute the South Atlantic meridional fluxes (mass, heat, and salt) at 34.5ºS, which show linear relationships, with a negative slope (positively correlated in magnitude) between M_{ov}/MOC and M_{ov}/MHT (Meridional Heat Transport) and a positive slope (positively correlated) between MHT/MOC. Seasonally, the South Atlantic meridional fluxes across 34.5ºS from most of the data sets considered in this thesis show a more negative M_{ov} and a more positive MOC and MHT in the austral fall and winter, from April to August.

This research further extends to the South Pacific Ocean. In the same way as the South Atlantic, we use cruise data with an inverse box model to compute the meridional circulation and transports. We use hydrographic data to compare the circulation of three decades: 1992, 2003, 2009, and 2017. This comparative analysis reveals different horizontal circulation schemes, particularly the emergence of a "bowed gyre" in 2009, which is not replicated over the entire length of any of the four OGCMs (ECCO, GLORYS, SOSE, and MOM) used. In addition, our observational and numerical model data highlight discrepancies in the representation of the East Australian Current. However, the representation of the Peru-Chile Current is consistent across the data sets. Furthermore, this thesis computes the temperature and freshwater transports from the cruise data, estimating significantly different results during the “bowed gyre” in 2009. A linear Rossby wave model is adopted to clarify the causes of these different circulation schemes, which includes the wind stress curl variability as a remote forcing and the response to sea surface height changes along 30°S in the Pacific Ocean.

The present Ph.D. thesis significantly contributes to understanding ocean circulation variability in the South Atlantic and South Pacific Oceans. By combining data from observations with numerical model outputs, this research provides a comprehensive perspective on ocean dynamics and offers implications for future climate change projections.

Resumen

La circulación oceánica en el hemisferio sur desempeña un papel fundamental en el sistema climático global. En particular, la Circulación Meridional de Retorno (MOC, por sus siglas en inglés, *Meridional Overturning Circulation*) es un sistema de corrientes oceánicas que interconecta las distintas cuencas oceánicas, redistribuyendo salinidad, calor y otros trazadores biogeoquímicos.

En esta tesis se analizan los patrones de circulación en el Atlántico Sur mediante datos hidrográficos obtenidos en tres campañas oceanográficas, utilizando un modelo inverso de cajas para ajustar las velocidades en el nivel de referencia. Además, se describen las corrientes superficiales, tales como la Corriente de Benguela, que fluye hacia el noroeste, y la Corriente de Brasil, que se desplaza hacia el sur; ambas formando parte del giro anticiclónico del Atlántico Sur subtropical. En las capas profundas, las corrientes de frontera transportan masas de agua hacia el sur y se observa un flujo entre las cuencas, de oeste a este, por encima de la Dorsal Mesoatlántica a una latitud de alrededor de 24°S, con un transporte de 7,5 ± 4,4 Sv. Tanto las corrientes superficiales como las profundas conectan las cuencas del oeste y el este; sin embargo, las aguas abisales se mueven hacia el norte desde las cuencas de Argentina y del Cabo, sin presentar ningún intercambio por encima de la Dorsal Mesoatlántica. Asimismo, el análisis de datos hidrográficos nos ha permitido estimar la intensidad de la Circulación Meridional de Retorno Atlántica (AMOC, por sus siglas en inglés, *Atlantic Meridional Overturning Circulation*) así como los transportes de masa, calor y agua dulce. De esta forma, este estudio nos ha permitido corroborar la existencia del transporte característico de calor hacia el norte y la predominancia de

la evaporación sobre las precipitaciones en toda la zona subtropical del Atlántico Sur.

Actualmente, el transporte de agua dulce por la AMOC (M_{ov}) en la latitud de 34,5ºS en el Atlántico Sur se ha identificado como un posible indicador de la estabilidad de la AMOC. Un transporte de M_{ov} negativo (hacia el sur) sugiere un régimen biestable, mientras que un transporte positivo (hacia el norte) indica un régimen monoestable. Esta tesis estima el M_{ov} a partir de datos observacionales de 49 transectos entre Sudamérica y Sudáfrica, obtenidos mediante BatiTermógrafos eXpendibles (XBT) a lo largo de casi dos décadas (2002-2019). El valor medio estimado del M_{ov} es de -0,15 ± 0,09 Sv, lo que indica que la AMOC se encuentra en un régimen biestable. Este resultado se complementa con dos conjuntos de datos de boyas Argo, cuatro Modelos de Circulación General Oceánica (OGCMs: GLORYS, OFES, MOM6-JRA y MOM6-MERRA) y 32 Modelos de Circulación General Acoplados (CGCMs: CMIP6). Tanto los conjuntos de datos de boyas Argo como los OGCMs coinciden en estimar un M_{ov} negativo, similar al obtenido con los datos XBT. Sin embargo, más de la mitad de los CGCMs examinados, 20 de 32, presentan valores medios de M_{ov} positivos. Para investigar las causas de estas discrepancias, se examina la estructura vertical de la salinidad en los CGCMs con M_{ov} positivo y negativo. Los resultados sugieren que el sesgo en la salinidad podría explicar estas discrepancias, ya que los modelos con M_{ov} positivo presentan aguas superficiales más dulces y aguas profundas más salinas en comparación con los modelos con M_{ov} negativo. Por lo tanto, esta tesis enfatiza la necesidad de mejorar las representaciones de los modelos CMIP6, en particular el sesgo de salinidad. Además, se calculan los flujos meridionales de masa (MOC), calor (MHT, por sus siglas en inglés, *Meridional Heat Transport*) y sal (M_{ov}) del Atlántico Sur, revelando relaciones lineales entre ellos. Se observa una pendiente negativa (correlación positiva en magnitud) entre M_{ov}/MOC y M_{ov}/MHT, mientras que la relación entre MHT/MOC muestra una pendiente positiva (correlación positiva). Estacionalmente, estos flujos meridionales presentan un M_{ov} más negativo y un MOC y un MHT más positivos durante el otoño y el invierno austral (de abril a agosto), lo que se observa de forma consistente en la mayoría de los conjuntos de datos analizados en esta tesis.

Esta investigación se extiende también al Océano Pacífico Sur, utilizando datos de campañas oceanográficas y un modelo inverso de caja para calcular la circulación meridional y los transportes de masa, calor y agua dulce. El análisis se realiza comparando tres décadas (1992, 2003, 2009 y 2017) y se revelan diferencias en los patrones horizontales de circulación. Se destaca la aparición de un "giro arqueado" en 2009, que no es replicado por ninguno de los cuatro OGCMs utilizados (ECCO, GLORYS, SOSE y MOM). Adicionalmente, utilizando datos observacionales y OGCMs, se identifican discrepancias en la representación de la Corriente de Australia Oriental, mientras que la Corriente de Perú se muestra coherente. Las estimaciones de los transportes de calor y agua dulce también presentan valores significativamente diferentes en 2009, el año del "giro arqueado". Para comprender estas diferencias, se adopta un modelo lineal de ondas de Rossby, considerando la variabilidad del estrés del viento como forzamiento remoto y la respuesta de la altura del nivel del mar a lo largo de 30°S en el océano Pacífico.

En conjunto, la presente tesis doctoral contribuye significativamente a la comprensión de la variabilidad de la circulación oceánica en los océanos Atlántico Sur y Pacífico Sur. Mediante el uso de datos observacionales junto con datos de modelización numérica, esta investigación ofrece una perspectiva completa de la dinámica oceánica en estas regiones, lo que tiene importantes implicaciones para las proyecciones futuras sobre el cambio climático.

Chapter 1

General introduction

1.1 Meridional Overturning Circulation

The Meridional Overturning Circulation (MOC) is a large-scale system of ocean currents that links the Atlantic, Pacific, Indian, and Arctic Oceans through the Southern Ocean (Figure 1.1). Its main driving mechanisms include diapycnal mixing in the abyssal layers, wind-driven upwelling in the Southern Ocean, and deep convection in the North Atlantic's high-latitude regions and near Antarctica (Lee et al., 2023; Munk & Wunsch, 1998; Schmitz, 1995; Talley, 2013). The MOC is a cornerstone of the Earth's climate system, driving the redistribution of heat, salt, carbon, nutrients, and other biogeochemical tracers across hemispheres and ocean basins, with profound implications for global climate stability (e.g., Caínzos et al., 2022a; 2022b; Macdonald & Wunsch, 1996; Talley, 2008).

In the context of climate change, rising sea surface temperatures and melting polar ice sheets are intensifying near-surface stratification globally, particularly in the regions of the North Atlantic and Antarctic oceans, which are key areas for deep water formation. These changes could slow or even lead to a collapse of the AMOC (e.g., Li et al., 2020), which, in turn, would disrupt the distribution of the ocean properties, potentially causing significant impacts on marine ecosystems, the climate system, extreme weather events, and other related processes (e.g., Little et al., 2019; van Westen et al., 2024; Zhang et al., 2019).

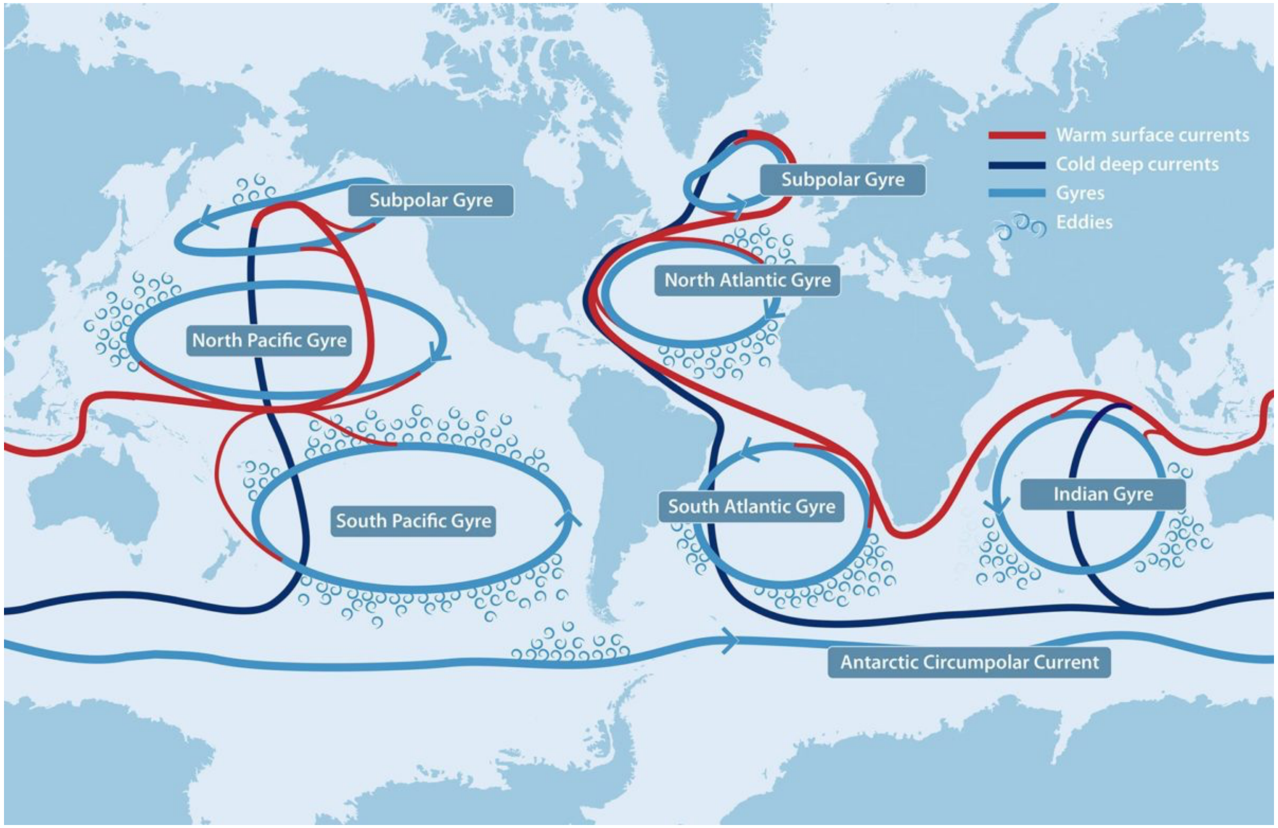

Figure 1.1. A schematic representation of the Meridional Overturning Circulation (MOC) (Illustration by Natalie Renier, © Woods Hole Oceanographic Institution).

1.2 The WOCE and GO-SHIP programs

In the 1990s, a major global international oceanographic research program, the World Ocean Circulation Experiment (WOCE), was conducted. This research program used closely spaced stations across transoceanic zonal and meridional sections to collect high-quality hydrographic data from all ocean basins. This has allowed the estimation of mass, heat, freshwater, and other property transports from the surface to the seafloor (Chapman, 1998; Ganachaud, 2003; Ganachaud & Wunsch, 2000; Macdonald & Wunsch, 1996).

Building on the key findings of WOCE, the Global Ocean Ship-Based Hydrographic Investigation Program (GO-SHIP) continues to advance this important research. GO-SHIP conducts repeated hydrographic transects and high-accuracy sampling of ocean properties. Although the general characteristics of the ocean's global overturning were established before WOCE (Gordon, 1986;Schmitz, 1995), the quantification of these global transports is greatly improved by the application of inverse modeling techniques (Roemmich & Wunsch, 1985; Wunsch, 1996).

Therefore, inverse methods are applied to repeated transoceanic hydrographic sections collected by the WOCE and GO-SHIP programs, along with current measurements, to provide a robust schematic view and estimation of the MOC, as well as the property transports in each ocean (Caínzos et al., 2023; Casanova-Masjoan et al., 2020; Lumpkin & Speer, 2007; Santana-Toscano et al., 2023).

1.3 Atlantic Meridional Overturning Circulation

In the context of the overturning circulation, the Atlantic Meridional Overturning Circulation (AMOC) is unique as it transports heat northward from all latitudes of the Atlantic basin, playing a significant role in the North Atlantic heat budget (Kelly et al., 2014), as well as regulating the European (e.g., Moffa-Sánchez & Hall, 2017) and global (e.g., Lynch-Stieglitz, 2017) climate through air-sea exchange.

The large-scale AMOC is formed by the upper and deep ocean current systems, together with the wind-driven transports in the surface Ekman layer. Therefore, the AMOC can be divided into the upper and lower limbs that flow in opposite directions. The upper limb starts in the South Atlantic at ~34.5ºS and is fed by waters from the Southern Ocean and two primary water pathways: the cold and warm routes (Rousselet et al., 2023). The upper limb of the AMOC transports warm and salty waters northward and accounts for ~90% of the subtropical North Atlantic's northward heat transport (e.g., Johns et al., 2011). As the AMOC flows into the highest latitudes of the subpolar North Atlantic, reaching the Nordic and Labrador Seas, the deep-water forms as North Atlantic Deep Water (NADW), primarily via heat loss and increased density (e.g., Smethie & Fine, 2001; Talley, 2003).

The lower or return limb of the AMOC begins with the formation of the cold and dense NADW in high-latitude regions, which flows southward towards the Southern Ocean mainly via the Deep Western Boundary Current (DWBC) in the deep layers. Thus, the lower limb of the AMOC compensates the northward flow of the warm upper ocean currents in the upper limb (Ganachaud & Wunsch, 2000; Garzoli et al., 2013;

Talley, 2003). In the Southern Ocean, the Ekman transport driven by strong westerly winds favors upwelling. The latter mechanism drives diapycnal mixing, which contributes to the transformation of water from lower to upper layers and mainly closes the upper cell of the AMOC (Johnson et al., 2019; Marshall & Speer, 2012; Sloyan & Rintoul, 2001).

Finally, the southward flow of the NADW in the lower cell is counterbalanced by the northward-flowing Antarctic Bottom Water (AABW). The AABW is the densest water mass and is formed by the sinking of cold waters that originate in the Southern Ocean. Its northward extent is limited by the presence of topographic features, such as the Walvis Ridge in the eastern basin, and therefore, the AABW is primarily confined to the western basin (G. D. McCarthy et al., 2020; Talley, 2013).

1.3.1 AMOC stability

One of the most important questions in climate studies is how the AMOC will respond under a changing climate (e.g., McCarthy et al., 2020). The coupled (atmosphere-ocean) climate numerical model scenarios of the Intergovernmental Panel on Climate Change (IPCC) reports have suggested a gradual weakening of the AMOC by 25% or more due to anthropogenic warming trends in the subpolar North Atlantic during the twenty-first century (Zhu et al., 2015). The collapse of the AMOC represents a critical tipping point in the climate system, not only because it reduces the heat supply to the subpolar North Atlantic region and thus to Europe, but also because it reduces the salt transport, which in turn reduces the formation of deep water and thus the intensity of the AMOC (Chidichimo et al., 2023; Weijer et al., 2019).

In contrast to the view of an AMOC decline, some numerical model simulations have suggested significant natural variability across different time scales (Wunsch & Heimbach, 2009). Furthermore, observations from AMOC monitoring arrays, such as the RAPID array, have revealed high variability (Frajka-Williams et al., 2019). Additionally, three decades of sparse transatlantic hydrographic sections collected through the GO-SHIP and WOCE projects have shown no significant long-term weakening of the AMOC (Caínzos et al., 2022a).

The AMOC is particularly vulnerable to the variability in ocean freshwater forcing from freshwater input (via river runoff, ice melt, precipitation, etc.). Several numerical modeling studies have demonstrated that an increase of freshwater forcing can slow down the AMOC (van Westen et al., 2024). In the southern border of the Atlantic Ocean, Rahmstorf (1996) identified that the freshwater transport by the AMOC at 34.5ºS, often referred to as M_{ov} or F_{ov}, is a key indicator for monitoring the stability of the AMOC. A positive or negative M_{ov} value indicates a monostable (one stable state, AMOC importing freshwater into the Atlantic) or bistable (two stable states, AMOC exporting freshwater from the Atlantic basin) AMOC, respectively. More recently, van Westen et al. (2024) showed that the M_{ov} minima at 34ºS in the Atlantic Ocean coincide with an AMOC tipping point.

1.4 Interbasin Exchange

The Antarctic Circumpolar Current (ACC) is the world's strongest and most extensive current (Talley, 2013). The ACC, located in the Southern Ocean, is primarily driven by strong westerly winds, buoyancy forcing, and large-scale changes in the thermohaline circulation (Karsten

& Marshall, 2002; Marshall & Radko, 2003). Its clockwise flow connects the three major ocean basins (Atlantic, Pacific, and Indian Oceans) as it encircles the Antarctic continent, thus allowing the interbasin exchange of ocean properties (e.g., Sloyan & Rintoul, 2001).

In the South Atlantic, the upper limb of the AMOC is fed by waters from the Southern Ocean, as well as two major water pathways originating from the Pacific and Indian Oceans (e.g., Rousselet et al., 2023). The cold water route is characterized by cold and fresh waters entering the South Atlantic from the Pacific Ocean via Drake Passage and the Malvinas Current (e.g., Rintoul, 1991). Meanwhile, the warm water route involves warmer and saltier waters from the Indian Ocean, which are transported by the Agulhas Current and the associated Agulhas leakage into the South Atlantic Ocean (e.g., Gordon, 1985). Due to the differing thermohaline properties of the water masses involved in the three sources, these water contributions impact the salt and heat balance of the Atlantic Ocean, thus influencing the variability and stability of the AMOC (Weijer et al., 1999).

1.5 Pacific Meridional Overturning Circulation

The Pacific Meridional Overturning Circulation (PMOC) is one of the main components of the MOC that redistributes ocean properties across the Pacific basin. Similar to the AMOC, the PMOC also consists of two main limbs: the upper limb (U-PMOC), found between 2,000 and 3,500 m depth, and the deep or lower limb (L-PMOC), which extends from approximately below 3,500 m depth (Kawabe et al., 2006, 2009).

The L-PMOC is essential for the northward transport of deep and abyssal water masses originating in Antarctica via the Pacific Deep

Western Boundary Current (DWBC) (Johnson et al., 2007). In particular, it is critical in influencing the distribution of the Lower Circumpolar Deep Water (LCDW), a remnant of the NADW characterized by high salinity and low silica content (Johnson & Toole, 1993). In contrast, the U-PMOC transports and redistributes Upper Circumpolar Deep Water (UCDW), which is a warmer and fresher water mass compared to the LCPW (Kawabe et al., 2006; Kawabe & Fujio, 2010).

Despite its critical importance, observational data on the PMOC, especially its lower limb, remain sparse compared to the extensive research conducted on the AMOC. This knowledge gap underscores the need to understand the PMOC pathways and their variability better, particularly as they relate not only to notable changes in circulation patterns but also to observed shifts in heat and freshwater transports, as previously noted in Hernández-Guerra & Talley (2016).

1.6 Motivation

In a warming climate, the MOC is likely to undergo significant changes that could disrupt the global distribution of ocean properties that sustain marine ecosystems, the carbon cycle, and other key processes (Lee et al., 2023; van Westen et al., 2024). For this reason, an accurate estimate of the MOC variability is crucial and can be computed using multiple sources. This research focuses on the large-scale ocean variability under a changing climate by understanding the ocean circulation dynamics of the South Atlantic and South Pacific Oceans in terms of mass, heat, and freshwater transports, which play a crucial role in global climate processes, employing in situ observations and numerical model outputs.

Specifically, the first focus of this thesis is to describe the South Atlantic circulation above the Mid-Atlantic Ridge (MAR), employing an inverse box model to analyze hydrographic section data in conjunction with velocity measurements. Our motivation is not only to determine the mass transport of the southward-flowing Brazil Current and the northwestward-flowing Benguela Current in the upper and intermediate layers but also to estimate the relatively unexplored return pathway of the lower limb of the AMOC carrying the cold deep waters that sink in the higher latitudes of the basin. Furthermore, this thesis aims to estimate the upper AMOC strength, including the characteristic heat and freshwater transport in the South Atlantic basin.

Another chapter of this thesis examines the freshwater transport by the AMOC at 34.5ºS, referred to as M_{ov}, which serves as a key indicator of the AMOC stability by analyzing multiple data sets (eXpandable BatiThermograph (XBT), Argo floats, Ocean General Circulation Models (OGCM), and Coupled General Circulation Models (CGCM)). Therefore, the second focus of this thesis is dedicated to describing the stability of the AMOC through the computation of M_{ov} using XBT observations to provide an updated analysis of the study carried out by Garzoli et al. (2013). In addition, we will compare these results with multiple data sets, aiming to highlight and explain the differences between them, specifically the salinity biases in the coupled models to improve AMOC projections and inform the Intergovernmental Panel on Climate Change (IPCC) risk analyses.

Addressing another significant question, this thesis seeks to describe the horizontal and overturning circulation of the South Pacific Ocean, employing a second inverse box model to hydrographic and velocity data in 1992 and 2017 to complement the previously published study by Hernández-Guerra & Talley (2016) for 2003 and 2009. We will also employ a linear Rossby wave model that incorporates wind stress curl variability and the ocean responses forced by changes in sea surface height anomalies (SSHA) along the South Pacific region. In this chapter, we attempt to describe the two circulation patterns in this region using hydrographic data from three different decades (1992, 2003, 2009, and 2017), as well as to estimate the PMOC strength in this basin, its associated heat and freshwater transports, and the dynamic forcing causing the change in the ocean circulation.

In summary, this thesis aims not only to make significant contributions to the field of physical oceanography by describing the South Atlantic and Pacific Oceans dynamics using both observations and numerical model outputs but also to provide actionable insights for predicting climate variability and evidence for improving global climate policy reports.

1.7 Thesis Outline

This thesis presents the results of three studies conducted in the Southern Hemisphere, focusing on the dynamical processes within the South Atlantic and Pacific Ocean regions. The studies include an analysis of the South Atlantic Ocean circulation using an inverse box model, a multi-data set analysis of freshwater transport by the AMOC, and a second inverse box model using three decades of in situ data combined with wind and altimeter data to analyze the South Pacific Ocean circulation. This thesis is organized into three main chapters, each of which includes an introduction, a detailed section on the data and methodology used, a presentation of the results, an in-depth discussion, and conclusions. The thesis ends with a chapter of general conclusions, which summarizes the main findings of this research.

Chapter 2 uses an inverse method to examine the schematic circulation of the South Atlantic Ocean between 34.5ºS, 24ºS, and above the Mid-Atlantic Ridge. Published in the *Journal of Geophysical Research: Oceans* (Arumí-Planas et al., 2023), this study describes the horizontal and overturning circulation of the South Atlantic using data from hydrographic sections and analyzes the transport of mass, heat, and freshwater within the region.

Chapter 3 focuses on examining the freshwater transport by the AMOC at 34.5ºS based on XBT observations and comparisons with Argo floats, OGCMs, and CGCMs data sets. Additionally, this chapter quantifies the meridional mass and heat transports, the correlation between them and their interannual and seasonal variability. This chapter has also been published in the *Journal of Geophysical Research: Oceans* (Arumí-Planas et al., 2024).

Chapter 4 studies the South Pacific circulation using an inverse method and has been published in *Progress in Oceanography* (Arumí-Planas et al., 2022). This chapter identifies two different circulation patterns based on hydrographic data collected over three decades and analyzes mass, heat, and freshwater transports. In addition, wind stress curl and sea surface height anomalies data are used to explain the observed differences in circulation patterns using a linear Rossby wave model.

Finally, Chapter 5 provides a comprehensive overview and highlights the main conclusions of the thesis.

Chapter 2

The South Atlantic Circulation Between 34.5ºS, 24ºS and Above the Mid-Atlantic Ridge From an Inverse Box Model

---

Chapter published at:

Arumí-Planas, C., Pérez-Hernández, M.D., Pelegrí, J. L., Vélez-Belchí, P., Emelianov, M., Caínzos, V., Cana, L., Firing, Y. L., García-Weil, L., Santana-Toscano, D. & Hernández-Guerra, A. (2023). The South Atlantic Circulation above the Mid-Atlantic Ridge between 34.5ºS and 24ºS from an Inverse Box Model. *Journal of Geophysical Research: Oceans*, 128(5), 1-21. https://doi.org/10.1029/2022JC019614

2.1 Introduction

The Earth's climate system is regulated by both ocean and atmosphere, which on average transfer heat from the equator to the subpolar regions. The South Atlantic Ocean plays an important and distinctive role in this heat exchange, as it hosts the returning flow of the Atlantic Meridional Overturning Circulation (AMOC), with its warm upper-ocean currents transporting heat northward from the subtropics to the tropics, hence compensating the southward flow of the cold and dense North Atlantic Deep Water (NADW) (Ganachaud & Wunsch, 2000; Garzoli et al., 2013; Talley, 2003). The Atlantic Ocean is different from all ocean basins because of the resulting net northward heat transport at all latitudes (Kelly et al., 2014), and it plays a major role in modulating European (e.g., Moffa-Sánchez & Hall, 2017; Palter, 2015) and global (e.g., Buckley & Marshall, 2016; Lynch-Stieglitz, 2017) climates.

The AMOC's upper limb is predominantly supplied by waters entering the South Atlantic via the Drake Passage and the Malvinas Current, the so-called "cold water route", or via the Agulhas Current and the Agulhas leakage, the "warm water route" (Gordon, 1986; Speich et al., 2001). Off the west coast of southern Africa is found the Benguela Current in the upper and intermediate layers, which forms the eastern boundary current of the anticyclonic South Atlantic subtropical gyre. The Benguela Current is supplied by both the South Atlantic Current, flowing along the southern margin of the South Atlantic subtropical gyre ($\approx$5 Sv), and by South Indian Ocean waters via the Agulhas Current ($\approx$10 Sv) in the upper $\sim$1,500 m of the South Atlantic Ocean (Gordon et al., 1992; Guo et al., 2023; Peterson & Stramma, 1991).

The Deep Western Boundary Current (DWBC) carries deep water from the Labrador Sea and the North Atlantic's Overflow Water layers to the southern latitudes (Talley & McCartney, 1982). The DWBC is the primary southward pathway for the cold and lower limb of the AMOC and has been extensively studied in the North Atlantic Ocean (e.g., Meinen et al., 2017; Toole et al., 2011). The deep pathways of the AMOC in the South Atlantic Ocean, however, are not as well documented (Garzoli et al., 2015). Arhan et al. (2003) confirmed two eastward pathways of NADW near the equator. Arhan et al. (2003) and Reid (1989) suggested similar circulation patterns in the South Atlantic at 2,500 m depth, indicating that most of the NADW enters the eastern basin between 20ºS and 25ºS, and then turns southeastward and flows above the Walvis Ridge through passages south of 28ºS, entering the Cape Basin.

The zonal transports at the Mid-Atlantic Ridge (MAR) are crucial for connecting the eastern and western South Atlantic basins. There is one single realization of a meridional hydrographic section in the South Atlantic Ocean close to the MAR, which was done along 9ºW (A14), from 4.3ºN to 45.5ºS during January and February 1995, as part of the World Ocean Circulation Experiment (WOCE) (Arhan et al., 2003; Mercier et al., 2003). To monitor flows across the MAR, the South Atlantic GAteway (SAGA) Array was deployed at the MAR at 10ºW, between 34ºS and 19ºS at about 4,000 m depth. The array configuration consists of four pressure-equipped inverted echo sounders (PIES) separated by about 5º of latitude, with deep instrumented moorings located in between.

Our main goal in this study is to use these hydrographic measurements at 10ºW along with an inverse box model in order to describe the circulation above the MAR between 34.5ºS and 24ºS in the

South Atlantic (Figure 2.1). To achieve this objective, we must determine the mass transport of the Brazil Current flowing southward and the northwestward flow of the Benguela Current, in both the thermocline and intermediate layers; the deep ocean currents that carry cold waters from the North Atlantic toward the southern latitudes in the western and eastern basins; as well as the northward flow of the abyssal layers. A significant result of the present study is that we will be able to determine the upper AMOC strength, including the heat and freshwater transports, at both latitudes.

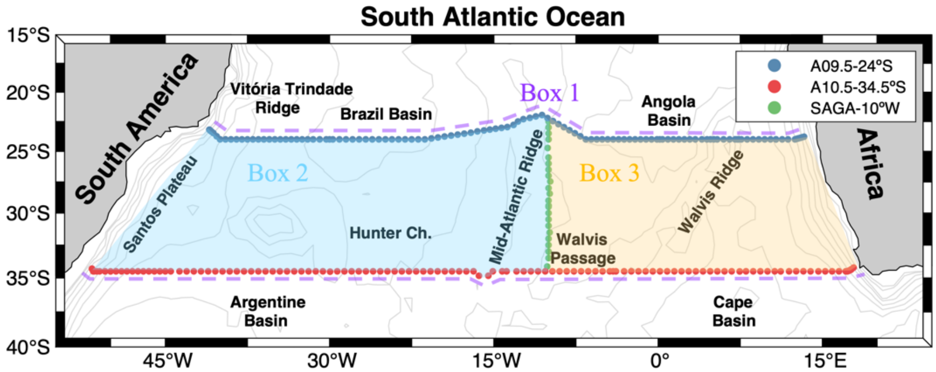

Figure 2.1. Positions of the hydrographic stations for the three South Atlantic cruises carried out at nominally 24ºS, 34.5ºS, and 10ºW. The different boxes used in this study are identified as Box 1 (purple dashed lines), Box 2 (light blue), and Box 3 (light orange).

The structure of this Chapter is outlined as follows. The hydrographic and Ocean General Circulation Model (OGCM) data are described in Section 2.2. Section 2.3 presents the vertical sections of different ocean properties to describe the water masses along 34.5ºS, 24ºS, and 10ºW in the South Atlantic Ocean. The initial geostrophic transport and the inverse model characteristics are presented in Section 2.4. This is followed by the final adjusted transports and the resulting AMOC estimate in Section 2.5. The resulting horizontal circulation for the upper, deep and bottom layers are described in Section 2.6, the heat and freshwater transport obtained for both latitudes are provided in Section 2.7, and a scheme of the upper, deep and bottom pathways is shown in Section 2.8. Finally, Section 2.9 provides a discussion and concluding remarks on this work.

2.2 Hydrographic and Ocean General Circulation Model (OGCM) Data

For our study we use three hydrographic cruises carried out in the South Atlantic Ocean: 34.5ºS in 2017, 24ºS in 2018, and 10ºW in 2021 (Figure 2.1). The hydrographic data at 34.5ºS were collected during the expedition of German Research Vessel *Maria S. Merian* conducted in summer 2017 (MSM60); the hydrographic data at 24ºS were collected in fall 2018 on the RRS *James Cook* (JC159) as part of the Ocean Regulation of Climate by Heat and Carbon Sequestration and Transports (ORCHESTRA) project and the international Global Ocean Ship-Based Hydrographic Investigations Program (GO-SHIP) (Talley et al., 2016); and the hydrographic data at 10ºW were collected in fall 2021 as part of the SAGA project onboard the R/V *Sarmiento de Gamboa.* The distance between stations was generally ≈50 km, with narrower spacing over boundary currents and steep topographic slopes. At each station, we use vertical profiles of potential temperature and salinity every two dbars as obtained from the conductivity-temperature depth (CTD) probes. For the three hydrographic cruises, a shipboard acoustic Doppler current profiler (SADCP, of 38 kHz for MSM60 and the SAGA cruise, and 75 kHz for JC159) was employed at each station pair to provide a velocity profile from the sea surface down to depths between 800 and 1,500 m. Also, for the 34.5ºS and 10ºW cruises, a velocity profile from the sea surface to the seafloor at each station was obtained from a paired (at 34.5ºS, 300 kHz upward-looking and 150 kHz downward-looking) or single (at 10ºW, 150 kHz downward-looking) lowered acoustic Doppler current profiler (LADCP). As in Hernández-Guerra and Talley (2016) and Hernández-Guerra et al. (2019), the ADCP data will prove to be useful in the inverse model to constrain the boundary currents.

Our hydrographic data are complemented by simulations from two different numerical ocean models. ECCOv4r4 (Estimating the Circulation and Climate of the Ocean Version 4 Release 4; ECCO, hereafter) is a data-assimilating model developed by the Jet Propulsion Laboratory. It incorporates oceanographic observations, such as altimetry-derived sea surface height, hydrography from Argo profilers, ocean bottom pressure from the Gravity Recovery and Climate Experiment (GRACE) and hydrographic and current data from moorings, among others (Fukumori et al., 2020). The adjoint method is applied to repeatedly minimize the squared sum of weighted model-data misfits and control adjustments, improving the fit of the numerical data to the observations (Wang et al., 2020). ECCO provides the state of the ocean's evolution over time on a monthly data basis, with 50 standard levels and a nominal 1/2º (≈48 km in our region) horizontal resolution configuration of the Massachusetts Institute of Technology general circulation model over the entire world, covering 26 years from 1992 to 2017 (ECCO Consortium et al., 2020, 2021; Forget et al., 2015).

The GLORYS12V1 (Global Ocean Physics Reanalysis; GLORYS, hereafter), an ocean model developed by Mercator and distributed by the European Copernicus Marine Environment Monitoring Service (CMEMS), is an eddy-resolving global ocean reanalysis that describes ocean circulation and includes sea-level forcing from satellite altimetry measurements covering the period of 1993-2019. GLORYS is developed using the current real-time global forecasting CMEMS system and the Nucleus for European Modeling of the Ocean (NEMO) model-based hydrodynamics. The CORA4 database and the ERA-Interim data are used for assimilating in situ observations and atmospheric forcing, respectively. Additionally, in situ temperature and salinity vertical profiles, altimeter data (sea level anomaly), sea ice concentration and satellite sea surface temperature are assimilated together. This numerical model provides monthly gridded data sets at 1/12º (≈8 km in our region) horizontal resolution and 50 vertical levels (Drévillon et al., 2018).

To summarize, the ocean models used (ECCO and GLORYS) are data-assimilating models varying from coarse to eddy-permitting horizontal resolution (1/2º and 1/12º, respectively). After applying the inverse model, mass transports from hydrographic data are compared with monthly data for the whole water column in the South Atlantic Ocean, along 24ºS and 34.5ºS for 2017-2019 (GLORYS) and 2017 (ECCO). No data from these models are yet available for 2021, the year of the 10ºW expedition.

2.3 Vertical Sections and Water Masses

The existing water masses are identified using the zonal (34.5ºS and 24ºS) and meridional (10ºW) vertical sections of potential temperature, salinity, and oxygen for the three hydrographic cruises following Katsumata & Fukasawa (2011) and Talley et al. (2011) (Figure 2.2). The meridional section at 10ºW, just east of and roughly parallel to the MAR, divides the transatlantic sections into western and eastern basins.

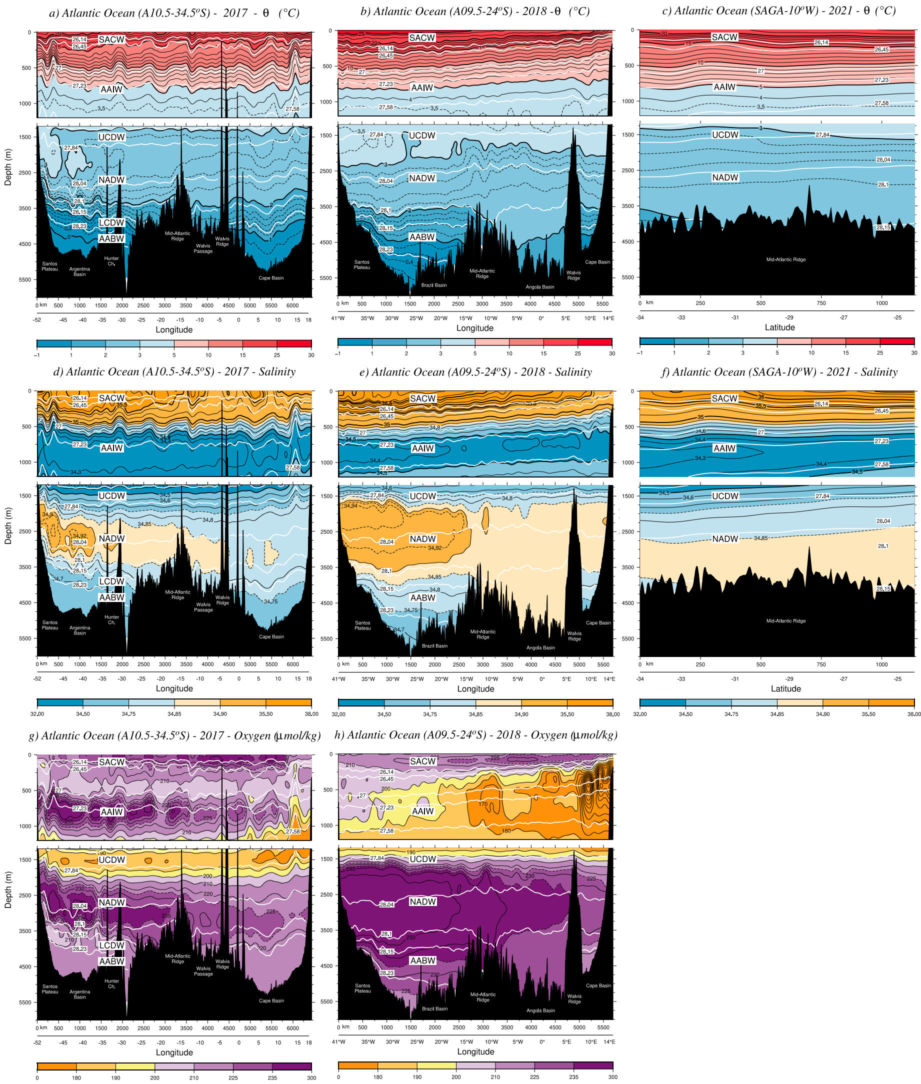

Figure 2.2. Vertical sections of (a−c) θ (ºC), (d−f) salinity, and (g, h) oxygen (µmol/kg) in the South Atlantic Ocean for data collected at 34.5ºS in 2017, at 24ºS in 2018 and at 10ºW in 2021, respectively. The water masses identified are: South Atlantic Central Water (SACW), Antarctic Intermediate Water (AAIW), Upper Circumpolar Deep Water (UCDW), North Atlantic Deep Water (NADW), Lower Circumpolar Deep Water (LCDW), and Antarctic Bottom Water (AABW). The location of stations is indicated with the tick-marks on the top axis indicate the location of stations. The γ^n layers identified by isoneutral labels (white lines) are those used to compute the geostrophic transport.

In the upper layers, the South Atlantic Central Water (SACW) is found between the sea surface and the neutral density γ^n = 27.23 kg/m^3 (above ≈ 730 m depth), with relatively high potential temperature (> 5ºC; Figs. 2.2a-c), relatively high salinity (> 34.7; Figure 2.2d-f), and high dissolved oxygen of about 210-235 µmol/kg (Figure 2.2g and h). This water mass is formed by the subduction of fluid via Ekman pumping out of the mixed layer in the Subtropical Convergence region (Gordon, 1981, 1989; Sprintall & Tomczak, 1993). The SACW is conveyed to the eastern basin by the South Atlantic Current and northwestward through the Benguela Current (Stramma & England, 1999), with a high contribution from the Indian Ocean through the Agulhas Current (warm water route) (Gordon, 1985; Poole & Tomczak, 1999; Sprintall & Tomczak, 1993), including the large and slow contribution of Agulhas rings transporting warm and salty waters into the Atlantic (Casanova-Masjoan et al., 2017).

The upper thermocline layers (γ^n < 27.23 kg/m^3) of the transoceanic vertical sections present titled isotherms and isopycnals that allow us to identify the signals of the Brazil and Benguela Currents in the western and eastern margins, respectively (Figure 2.2a, b, d, and e). The thermohaline isolines in the ocean interior indicate equatorward mass transport, as they descend to the west. Below this upper layer, we find the Antarctic Intermediate Water (AAIW) (27.23 kg/m^3 < γ^n < 27.58 kg/m^3, which corresponds to depths between 730 and 1,140 m). This water mass presents relatively cold waters of potential temperatures of 3-5ºC (Figure 2.2a-c), profile-minimum salinity values (34.3-34.5; Figure 2.2d-f). Its dissolved oxygen concentration is relatively low at 24ºS (< 200 µmol/kg; Figure 2.2g) and higher at 34.5ºS (> 220 µmol/kg at 34.5ºS; Figure 2.2h). The AAIW is formed in the Southern Ocean, near the Subantarctic Front of the Antarctic Circumpolar Current (ACC) (Talley, 1996). Its formation is driven by a combination of cooling and mixing processes, as well as interactions between ocean currents, such as the ACC, before spreading into the South Atlantic (Matano et al., 2010; Sloyan & Rintoul, 2001). The main AAIW sources to the Atlantic Ocean are from the Southeastern Pacific, entering through the northern Drake Passage, the narrowest gap connecting the South Atlantic and Pacific Oceans between the Antarctic Peninsula and South America, and the Malvinas Current loop, a large clockwise circulation feature in the South Atlantic that flows around the Falkland Islands (Suga & Talley, 1995). At 34.5ºS in the eastern basin of the South Atlantic Ocean, the high salinity of the AAIW density class is attributed to the mixing of older AAIW with the Red Sea Water coming from the Indian Ocean, which has a much higher salinity than that of the AAIW layers located in the southwestern Atlantic Ocean (Shannon & Hunter, 1988). The lower oxygen levels (<180 µmol/kg) in the eastern basin also point to an Indian Ocean source. This is supported by the fact that the Indian deep waters, which originate from upwelled bottom waters of greater age than those from the Atlantic Ocean sourced from surface waters (Gordon et al., 1992; Talley, 1996, 2013). Specifically, the Indian Ocean presents oxygen levels of 160-220 µmol/kg between 600 and 1,200 m depth (McDonagh et al., 2008). The low oxygen concentrations are more noticeable in the 24ºS section, further suggesting that these waters originate from the Indian Ocean and spread westward as they flow north in the Atlantic, before feeding the NADW overturn (Talley, 2013). Also, the minimum salinity patches (< 34.3) in the western basin at 34.5ºS suggest that the northward flow in the ocean interior transports more recently ventilated AAIW (Hernández-Guerra et al., 2019).

In the deep layer, with a neutral density range of 27.58 kg/m^3 < γ^n < 27.84 kg/m^3, extending from about 1,140 to 1,600 m, we find the core of the Upper Circumpolar Deep Water (UCDW). The UCDW originates from the mixture of deep waters from the Indian, Pacific and Southern Oceans. This is a relatively oxygen-poor (180-200 µmol/kg; Figure 2.2g, and h), fresh (34.5-34.7; Figure 2.2d, e, and f), and cold water mass (2.5-3ºC; Figure 2.2a-c).

NADW is also found in the deep layers, below the UCDW, at depths ranging from about 1,600 to 3,800 m (27.84 kg/m^3 < γ^n < 28.15 kg/m^3). This water mass is formed as a result of the mixing and aging of deep waters flowing latitudinally toward the Southern Ocean. NADW is identified in the vertical by relatively low potential temperature (1.5-2.5ºC; Figure 2.2a-c), high salinity (34.85-34.9; Figure 2.2d-f), and high dissolved oxygen concentration (200-250 µmol/kg; Figure 2.2g, and h). The properties of the NADW are best observed in the western region, due to the eastward decrease in salinity and oxygen, toward the MAR. Additionally, the presence of the Deep Western Boundary Current (DWBC) shows up as anomalous values of potential temperature (1.53ºC), salinity (34.7) and oxygen (206.7 µmol/kg) near the seafloor (≈ 2800 m depth) at about 50ºW, which contrasts with the respective values of 3.2ºC, 34.9 and 228.9 µmol/kg observed at 2,110 m depth (e.g., Reid et al., 1977; Zemba, 1991) (Figure 2.2).

The AABW is the densest water mass in the Atlantic, from ≈ 3800 m to the seafloor (γ^n > 28.15 kg/m^3). The AABW is colder (θ < 1.5ºC; Figure 2.2a and b), fresher (34.7-34.75; Figure 2.2d and e) and has lower dissolved oxygen concentrations (220-240 µmol/kg; Figure 2.2g and h) than the NADW. The main source of the AABW is the mixed Antarctic waters and the NADW (de Carvalho Ferreira & Kerr, 2017; Heywood & King, 2002; Mantyla & Reid, 1983; Peterson & Whitworth, 1989; Reid et al., 1977). The Walvis Ridge limits the northward flow of AABW in the eastern basin. The hydrographic section at 10ºW is on the MAR with shallower depths than the AABW and, therefore, is not present in this section (Figure 2.2c, f, and i). The AABW can be separated into two different components at 34.5ºS. The upper part of the AABW is formed in the Antarctic Circumpolar Current, which is a combination of AABW and NADW, resulting in a new water mass called Lower Circumpolar Deep Water (LCDW) (Mantyla & Reid, 1983; Stramma & England, 1999). The LCDW is the primary water mass in contact with the AABW within the Argentine Basin (Coles et al., 1996), between 28.15 kg/m^3 < γ^n < 28.23 kg/m^3, between about 3,800 and 4,700 m. These water masses differ only slightly in most of the properties so that they are not clearly separated in the water column (Vanicek & Siedler, 2002). However, at 34.5ºS the LCDW has slightly higher temperatures (≈ 1.0-1.5ºC; Figure 2.2a), higher salinity (34.75-34.8; Figure 2.2d) and lower dissolved oxygen concentrations (210-220 µmol/kg; Figure 2.2g) than the AABW (θ <1ºC, S ≈ 34.7, O_2 ≈ 220 µmol/kg; Figure 2.2a, d, and g).

2.4 Relative Geostrophic Transport and Inverse Model

At each station pair, the relative geostrophic velocity is computed using the thermal wind equation so the absolute velocity depends on the chosen reference layer. For section 34.5ºS we choose the NADW-LCDW interface at $\gamma^n = 28.15$ kg/m^3 (≈ 3,800 m depth) as reference layer (Figure 2.2). Similarly, for sections 24ºS and 10ºW we select the interface UCDW-NADW, located at the neutral density $\gamma^n = 27.84$ kg/m^3 (≈ 1,600 m depth) (Figure 2.2). If the reference layer is deeper than the deepest common depth of a pair of stations, the bottom is selected as the reference level of no motion.

Otherwise, the SADCP and LADCP data from the sections at 34.5ºS and 10ºW are used to estimate the velocities at the reference level, and only SADCP data from the section at 24ºS (Comas-Rodríguez et al., 2010; Joyce et al., 2001). Figure 2.3 presents the initial geostrophic velocity (dashed black lines), the average SADCP velocity along the station-station track segment (red line), the mean LADCP velocity from each hydrographic station pair LADCP velocities (blue line), and the geostrophic velocity adjusted to the ADCP velocity (black solid line). The velocity adjustments are performed under four different cases (a through d) for the sections at 34.5ºS, 10ºW, and 24ºS. First, if either both SADCP and LADCP (case a) or just SADCP (case b) match the geostrophic velocity profile, then SADCP data is used to adjust the initial geostrophic velocity. Next, if only the LADCP matches the profile of the geostrophic velocity but SADCP does not, then LADCP data is used to adjust the initial geostrophic velocity (case c). When neither the SADCP nor LADCP patterns match the geostrophic velocity profile, then the initial geostrophic velocity is not adjusted (case d). Notice that the LADCP velocities are located at each station rather than over the whole interval over which the geostrophic velocity is computed, while the underway SADCP continuously collects data, so SADCP can better match the location of the geostrophic calculation. Consequently, SADCP data is considered to be more appropriate for estimating the reference level velocities in most cases (Arumí-Planas et al., 2022). Then, the adjusted reference velocity is estimated as the average velocity of the selected depths in the range of the dashed horizontal lines.

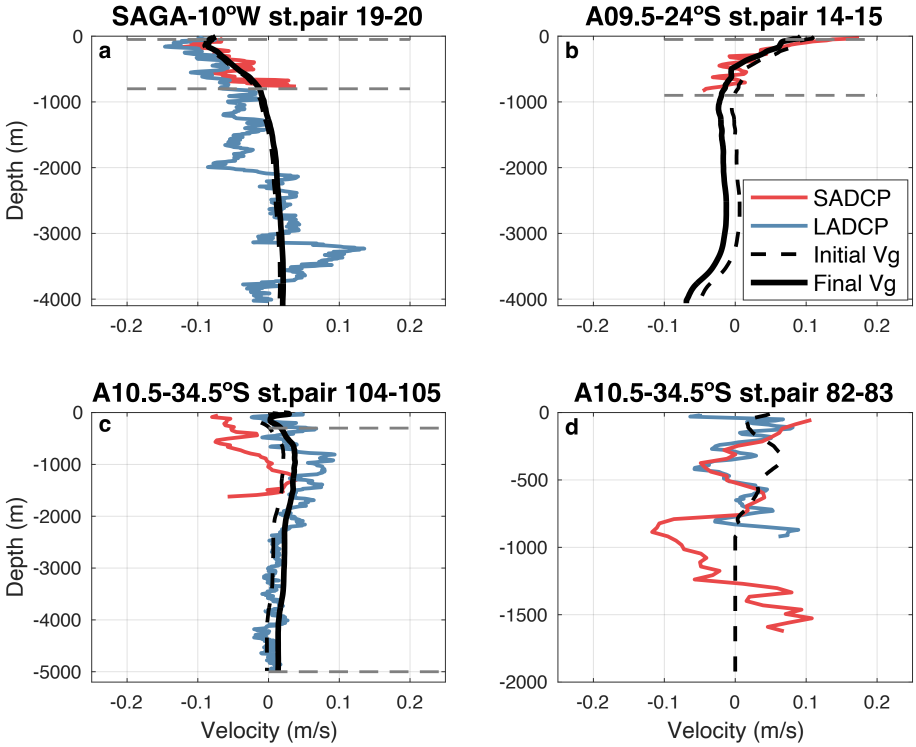

Figure 2.3. Comparison between the profiles of the initial geostrophic velocity (dashed black lines), the SADCP (red line) and LADCP (blue line) velocity normal to the station pairs, and the geostrophic velocity adjusted using the SADCP or LADCP data (black solid line) for four different cases of adjustment: (a) geostrophic velocities agree with both SADCP and LADCP data, (b) only SADCP data agree, (c) only LADCP data agree, and (d) neither SADCP nor LADCP data agree.

Mass transports are computed for 11 isoneutral layers following Arumí-Planas et al. (2022), Hernández-Guerra et al. (2019), Hernández-Guerra & Talley (2016), and Talley (2008) (Figure 2.2 and 2.4). The NCEP wind stress is used to calculate the Ekman transports (Kalnay et al., 1996) at the time of each hydrographic cruise (Arumí-Planas et al., 2022; Hernández-Guerra et al., 2019; Hernández-Guerra & Talley, 2016). The resulting Ekman transports, of -1.6±0.1 Sv at 24ºS, 0.1±0.2 Sv at 34.5ºS, and 0.1±0.1 Sv at 10ºW, are included in the uppermost layer of each section.

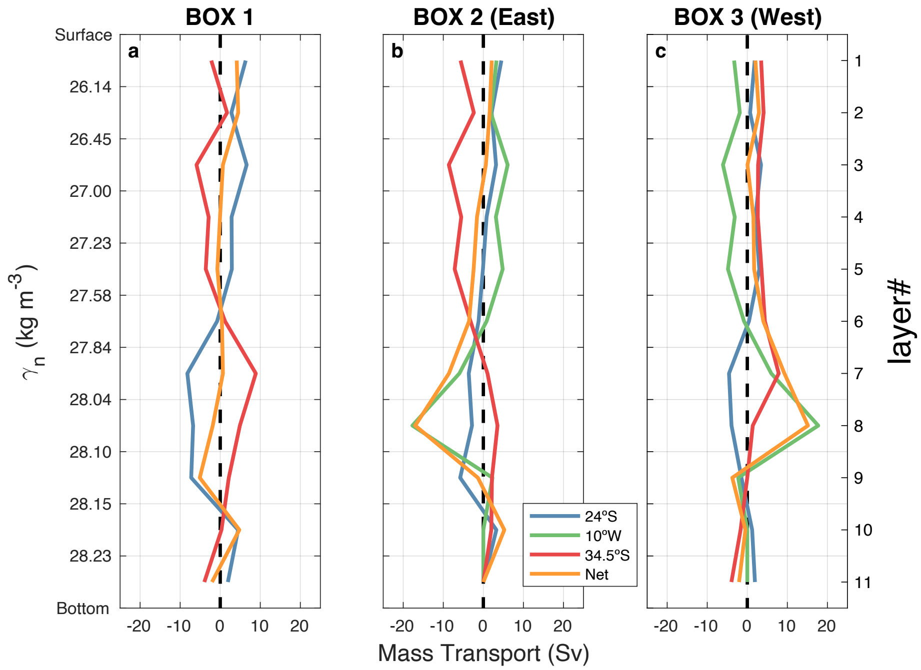

Figure 2.4. Initial integrated mass transports (Sv) per neutral density layer at 24ºS (blue line), 10ºW (green line) and 34.5ºS (red line), and the net (orange line) in the South Atlantic Ocean. The three panels correspond to the mass transport in (a) Box 1, (b) Box 2 and (c) Box 3. The sign of the transports is changed as to maintain the same sign convention in all boxes: positive mass transports flow out of the box and negative mass transports flow into the box.

In our study, there are three enclosed regions (Figure 2.1): Box 1 is formed by the combined transatlantic sections at 34.5ºS and 24ºS, and Boxes 2 and 3 are respectively formed by the eastern and western stations of sections 34.5ºS and 24ºS combined with section 10ºW. Figure 2.4 presents the initial integrated mass transports per layer for each enclosed region in the Atlantic Ocean; these initial estimates use the velocity at the reference layer as obtained from the ADCP data. There is an initial imbalance, integrated over all layers, of 5.3 Sv in Box 1, 30.4 Sv in Box 2, and -25.0 Sv in Box 3 (Table 2.1; positive and negative values represent divergence and convergence, respectively). The initial fields for the upper and bottom layers have a northward mass transport, while the deep layers present a southward mass transport across both the 34.5ºS and 24ºS transoceanic sections, and a westward and eastward mass transport for upper and deep layers through the 10ºW meridional section, respectively.

The inverse box model (Wunsch, 1978, 1996) uses constraints on transports to adjust the reference velocities and produce a consistent solution for each enclosed region, reducing the large initial imbalances. The following equation for mass transport is solved:

$$\iint \rho b dx dz = -\iint \rho v_r dx dz + E_k$$

where ρ is the seawater density, b designates the unknown reference velocity, v_r is the initial estimate for the geostrophic velocity derived from the thermal wind equation and after incorporating the reference velocities through an adjustment to the SADCP or LADCP data, E_k is the normal Ekman transport to the section, and the along-section and vertical coordinates are denoted by x and z, respectively. Appendix A provides the full matrix equation and its derivation, while the constraints used are given in Table 2.1.

Table 2.1. Constraints and Results of the Inverse Model for the South Atlantic Ocean as Obtained Using the 34.5ºS, 24ºS, and 10ºW Sections.

South Atlantic Ocean	Property	Longitude	Layers	Constraint (Sv)	Initial (Sv)	Final (Sv)
A10.5 – 34.5ºS	Bering imbalance[a]	All	All	-0.8 ± 0.6	-0.5	-0.7 ± 2.9
	Vema Channel[b]	50.8ºW to 34.9ºW	9:11	4.0 ± 0.4	6.5	4.0 ± 0.9
	Hunter Channel[c]	33.6ºW to 27.0ºW	9:11	2.9 ± 1.2	-0.7	2.8 ± 1.0
	Brazil Current[d]	Coast to 49.2ºW	1:5	-14.0 ± 8.8	-20.0	-16.5 ± 1.3
	Benguela Current[e]	10.9ºE to coast	1:5	24.0 ± 17.0	27.5	26.3 ± 2.0
	DEBC[e]	13.6ºE to coast	6:9	-12.0 ± 17.0	-8.3	-15.1 ± 3.5
	DWBC[f]	Coast to 47.3ºW	6:9	-15.0 ± 23.0	-18.7	-13.9 ± 3.0
	$DWBC_{rec}$	47.3ºW to 46.8ºW	6:9	NC	3.3	3.0 ± 1.3
A09.5 – 24ºS	Bering imbalance[a]	All	All	-0.8 ± 0.6	4.8	-0.7 ± 3.1
	Walvis R. North[g]	4.6ºE to coast	9:11	0.0 ± 1.0	5.0	-0.7 ± 0.7
	Brazil Current[h]	Coast to 40.5ºW	1:5	-8.4 ± 5.0	-8.4	-7.3 ± 0.9
	Benguela Current	27.6ºW to coast	1:5	NC	25.8	21.2 ± 1.8
	DEBC	2.6ºE to coast	6:9	NC	-3.5	-16.3 ± 4.7
	DWBC	Coast to 35.2ºW	6:9	NC	-9.2	-8.7 ± 3.8
	$DWBC_{rec}$	35.2ºW to 33.7ºW	6:9	NC	6.5	6.4 ± 2.7
34.5ºS (West) – 10ºW – 24ºS(East)	Bering imbalance[a]	Coast to 10.6ºW (34.5ºS) All (10ºW) 9.9ºW to coast (24ºS)	All	-0.8 ± 0.6	22.7	-0.9 ± 11.0

24ºS (West) – 10ºW – 34.5ºS(East)	Bering imbalance[a]	Coast to 10.4ºW (24ºS) All (10ºW) 10.0ºW to coast (34.5ºS)	All	-0.8 ± 0.6	29.9	-1.9 ± 9.4
34.5ºS – 24ºS	Total mass conserved in Box 1	All (34.5ºS) All (24ºS)	All	0.0 ± 1.0	5.3	0.0 ± 15.5
34.5ºS (West) – 10ºW – 24ºS (West)	Total mass conserved in Box 2	Coast to 10.4ºW (34.5ºS) All (10ºW) Coast to 10.6ºW (24ºS)	All	0.0 ± 1.0	30.4	1.2 ± 10.2
34.5ºS (East) – 10ºW – 24ºS (East)	Total mass conserved in Box 3	10.0ºW to coast (34.5ºS) All (10ºW) 9.9ºW to coast (24ºS)	All	0.0 ± 1.0	-25.0	-1.2 ± 12.6

Note. Positive transports are northward-eastward, and negative are southward-westward; while in the box imbalances, positive/negative values represent divergence/convergence. Initial and final transports relative to the reference layer (at γ^n=28.15 kg/m^3 for the 34.5ºS section and γ^n=27.84 kg/m^3 for the 24ºS and 10ºW sections) are listed. The constraints set in the inverse model for the regional transports are also shown; NC stands for non-constraint.

[a] Bering imbalance in Total Mass Conservation from Coachman & Aagaard (1988).[b] Bottom transport constraint in the Vema Channel from Hogg et al. (1982).[c] Bottom transport constraint in the Hunter Channel from Zenk et al. (1999).[d] Brazil Current constraint from Chidichimo et al. (2021).[e] Benguela Current and Deep Eastern Boundary Current (DEBC) constraints from Kersalé et al. (2019).[f] Deep Western Boundary Current (DWBC) constraint from Meinen et al. (2017). [g]Bathymetric constraint from Warren & Speer (1991). [h] Boundary current constraints from cruise-based ADCP profiles.

The approach used for the inverse model solution is the same approach as the one developed by Joyce et al. (2001) and later applied by Arumí-Planas et al. (2022), Casanova-Masjoan et al. (2020), and Hernández-Guerra et al. (2014). The unknown geostrophic reference velocity at each station pair, as well as the section adjustment to the Ekman velocity, along with their standard deviations, are estimated using a system of mass conservation equations, which requires an enclosed region. This procedure provides 48 equations for the vertically integrated mass constraints with 262 unknowns (the total number of station pairs of the three hydrographic sections combined). For each box, both total mass and mass in each neutral density layer are conserved, with the Ekman transport adjustment included in the first layer. The next four constraints are the mass balance (based on the Bering Strait transport) for sections 24ºS and 34.5ºS separately, as well as mass balance for two transatlantic sections composed of the western/eastern station pairs section 24ºS plus section 10ºW and the eastern/western station pairs of section 34.5ºS, respectively. In addition to the total mass constraints, eight regional constraints across several longitude and depth ranges were introduced to reduce this underdetermined system (Table 2.1). These constraints have been previously applied in earlier studies of the South Atlantic Ocean as in other inverse models (Table 2.1; Hogg et al., 1982; Warren & Speer, 1991; Zenk et al., 1999), although the recent study of Finucane & Hautala (2022) suggested that the bottom transport estimated in the Hunter Channel by Zenk et al. (1999) could be overestimated. We have also included new constraints for 34.5ºS from recent studies by Chidichimo et al. (2021), Kersalé et al. (2019), and Meinen et al. (2017) using data from the moored arrays deployed along this section as part of the South Atlantic MOC Basin-wide Array (SAMBA) (Ansorge et al., 2014; Garzoli & Matano, 2011; Meinen et al., 2013, 2017, 2018). Moreover, we use ADCP data from section 24ºS to constrain the Brazil Current (as previously done for the hydrographic section at 30ºS by Hernández-Guerra et al. (2019).

The Gauss-Markov method is used to solve the inverse problem (Wunsch, 1996), which requires a priori variances for each equation and solution. The a priori variances for each equation, corresponding to each regional constraint, are expressed as standard deviations (Table 2.1), except the Brazil Current at 24ºS where we have assigned 5 Sv to consider the uncertainty of the Brazil Current transport based on the differences between hydrographic sections at 24ºS in 2009 (Bryden et al., 2011) and 2018, as also considered in Hernández-Guerra et al. (2019) for a 30ºS section. Furthermore, we have assigned a priori variances for the layer mass conservation equations: 3.6 Sv in each of layers 1-4, 2.2 Sv for layers 5-7, and 1.1 Sv for layers 8-11. The a priori velocity variance for the ocean interior's solution is set to $(2\ \mathrm{cm/s})^2$, while it is raised to $(4\ \mathrm{cm/s})^2$ in regions with strong shear, which corresponds to both eastern and western boundaries. The a priori variances are large enough to adjust the mass transports for every oceanographic cruise condition with the inverse model (Table 2.1). The Gauss-Markov method solves the underdetermined system of equations by selecting the solution with the least variance, given the reference level velocities along with their corresponding uncertainties. Finally, we compute the adjusted mass transports and their uncertainties.

The initially adjusted velocities estimated at the reference level, those from the SADCP and LADCP data, and as produced by the inverse model are shown in Figure 2.5. The velocities adjusted using the ADCP data (Figure 2.5a) are greater than those obtained from the inverse model (Figure 2.5b). The inverse solution velocities are not significantly different from zero (i.e., -0.02±0.08 cm/s) in most ocean interior stations, as in earlier inverse models (Arumí-Planas et al., 2022; Hernández-Guerra et al., 2019; Hernández-Guerra & Talley, 2016), as well as on the eastern and western boundaries (i.e., -0.04±0.08 cm/s). The inverse model adjustment does not produce a significant change to initial Ekman transports on any section (inverse estimates of -1.6±0.2 Sv at 24ºS, 0.1±0.2 Sv at 34.5ºS, and 0.1±0.1 Sv at 10ºW).

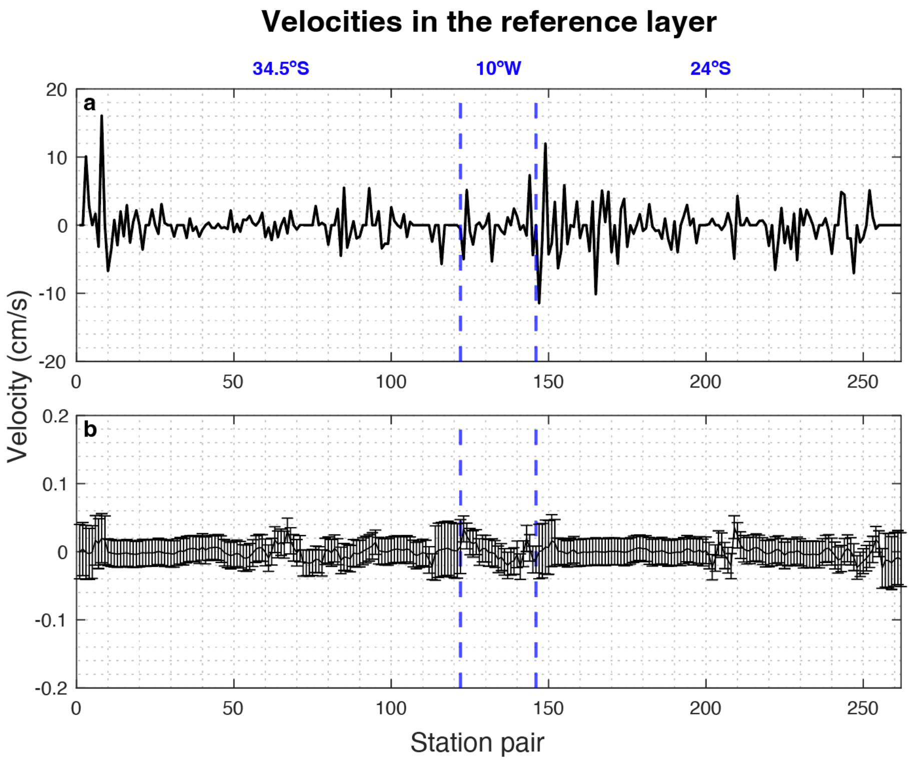

Figure 2.5. (a) Reference velocities (cm/s) as adjusted using ADCP data and (b) velocity adjustment from the inverse model with error bars as a function of station pair numbers for the three hydrographic sections: 34.5ºS (station pair from 1 to 122), 10ºW (stations pair from 123 to 146), and 24ºS (station pair from 147 to 262). The blue dotted lines separate the transect, as shown in the upper legend. Positive and negative velocities are north/east or south/west, respectively.

2.6 Adjusted Meridional and Zonal Transports

After applying the inverse model, the final adjusted mass transports per neutral density layer in each enclosed region model are presented in Figure 2.6. The total mass imbalance in each closed box is insignificantly different from zero, well within the corresponding uncertainties (0.0±15.5 Sv in Box 1, 1.2±10.2 Sv in Box 2, and -1.2±12.6 in Box 3). Therefore, we may say that mass transport is conserved in all three closed regions.

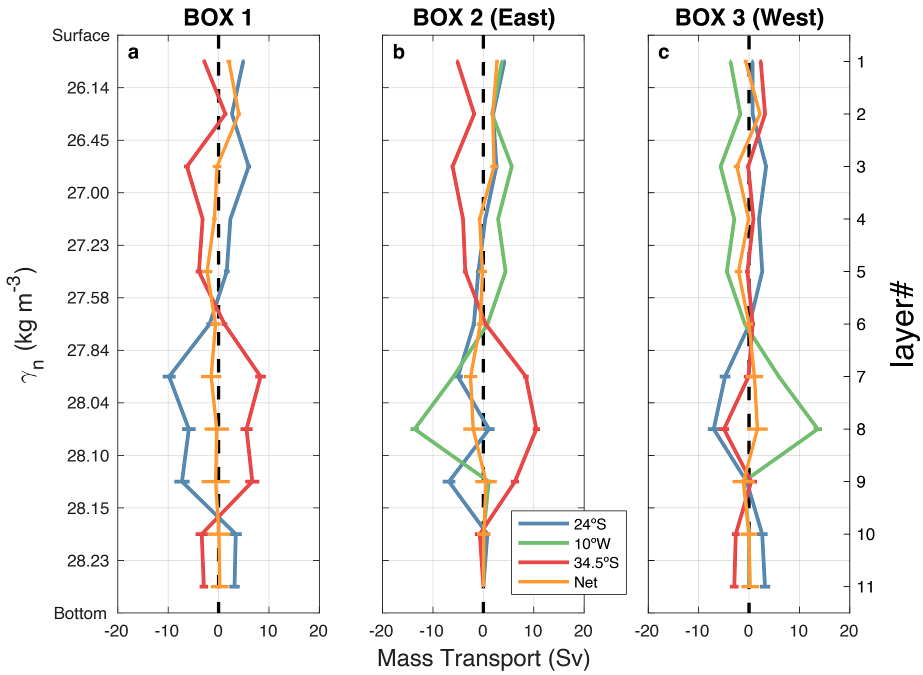

Figure 2.6. Final integrated mass transports (Sv) per neutral density layer at 24ºS (blue line), 10ºW (green line), 34.5ºS (red line) and the net (orange line) with the corresponding error bars, in the South Atlantic Ocean; the net imbalance per layer is also shown. The three panels correspond to the mass transport in (a) Box 1, (b) Box 2 and (c) Box 3. The sign of the transports is changed as to maintain the same sign convection in all boxes: positive mass transports flow out of the box and negative mass transports flow into the box.

The meridional overturning transports across the transatlantic sections at 34.5ºS and 24ºS are computed by zonally and vertically integrating the mass transport from the bottom to the sea surface (Figure 2.7). The strength of the AMOC at each latitude is defined as the vertical maximum of the stream function, which is always found in the upper cell (Buckley & Marshall, 2016). The AMOC intensity at 24ºS is 17.5 ± 0.9 Sv, which is stronger than the 14.8 ± 1.0 Sv estimated at 34.5ºS. Based on Figure 2.7, we may divide the Atlantic Ocean in a three-layer system at 24ºS and 34.5ºS, with mass transports flowing northward in the uppermost layers (1-5), southward in the deep layers (6-9), and northward in the

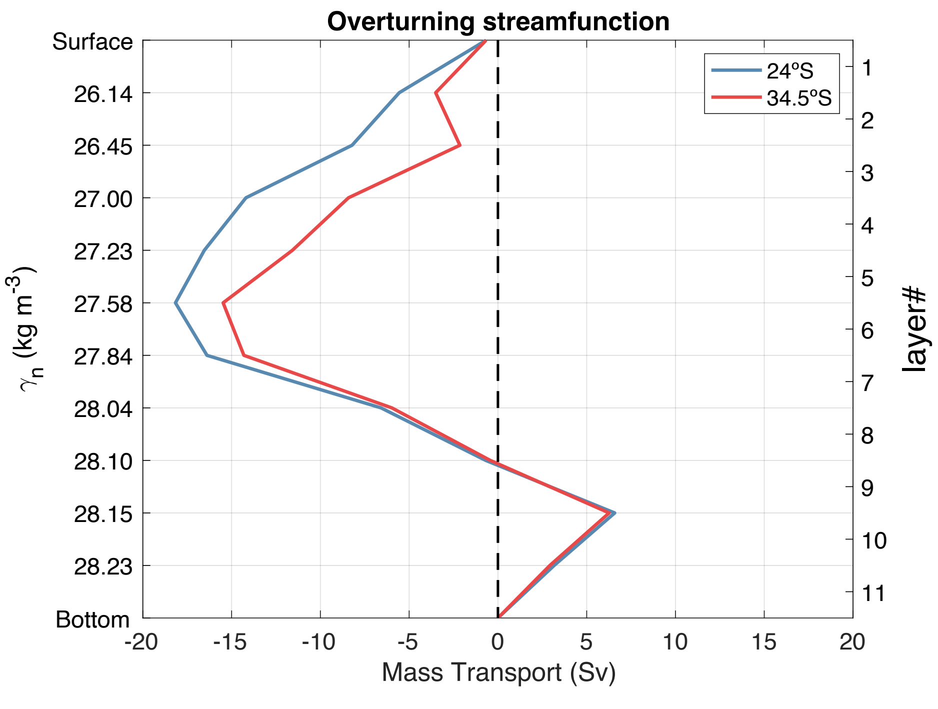

Figure 2.7. Overturning stream function of mass transport across 24ºS (red line) and 34.5ºS (blue line) in the Atlantic Ocean for 2018 and 2017, respectively. The function is computed by integrating the mass transport vertically and horizontally in isoneutral layers, from the seafloor to the sea surface across the entire section.

abyssal layers (10-11); it is the upper cell that differs most between 24ºS and 34.5ºS. In contrast, in the meridional 10ºW section (not shown) there is no mass transport in the abyssal layers (Figure 2.6b and c), hence it can be viewed as a two-layer system, with mass transports flowing westward in the uppermost layers (1-5) and eastward in the deep layers (6-9).

2.6 Horizontal Circulation from Adjusted Transport

Figure 2.8 presents the horizontally accumulated mass transport for different isoneutral layers along 24ºS (a, b, c), 34.5ºS (d, e, f), and 10ºW (g, h). The inverse model results are presented with positive northward/eastward transports and negative southward/westward transports. For sections 24ºS and 34.5ºS, the mass transport is accumulated integrating eastward, whilst for section 10ºW, it is accumulated integrating northward. As the inverse box solution finds a solution that satisfies mean constraints and uses hydrographic data from different years, they represent in some sense a time mean circulation. For this reason, we have included in Figure 2.8 the accumulated transports using ECCO (2017) and GLORYS (2017-2019) to examine averages over the time period from both models for 24ºS and 34.5ºS sections, and none for 10ºW because no models are available for 2021.

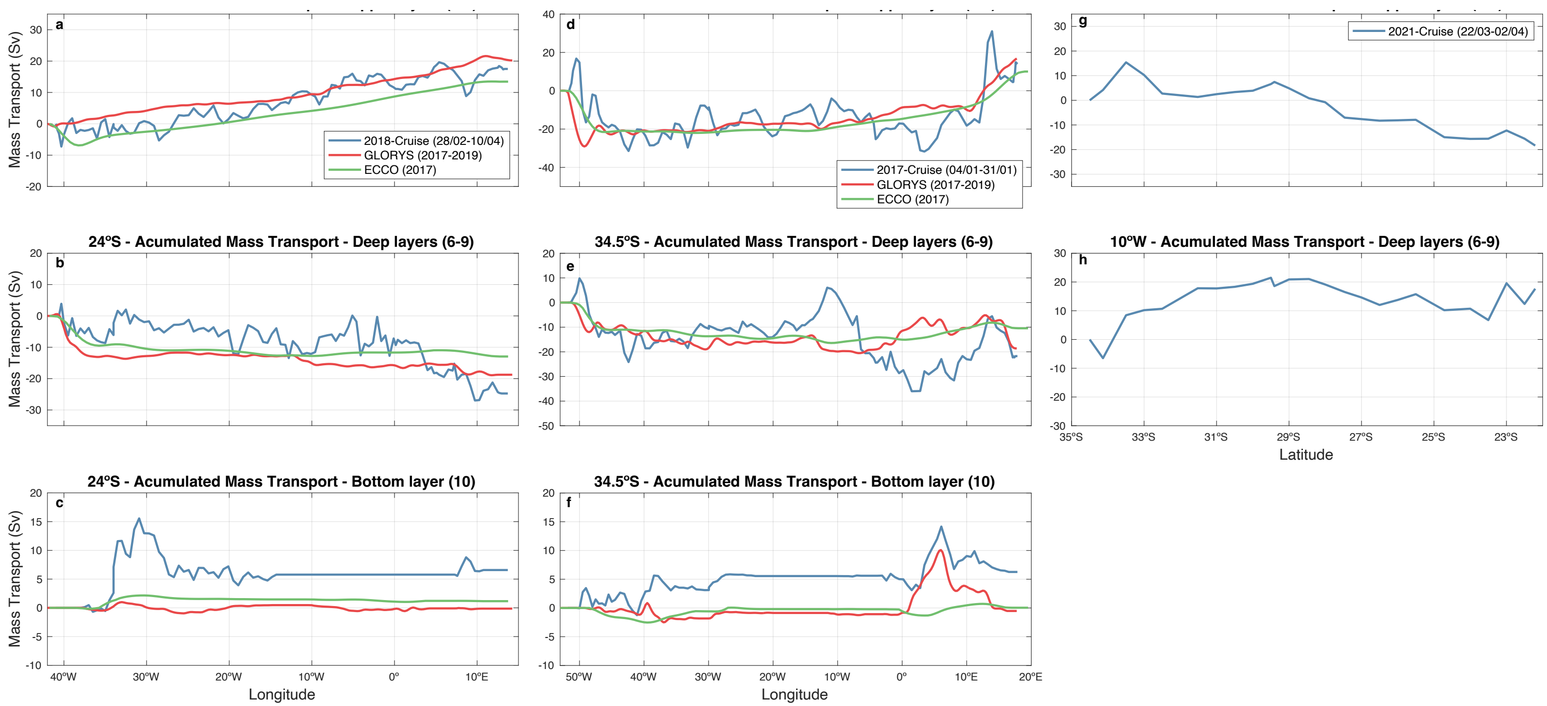

Figure 2.8. Eastward accumulated mass transports (Sv) at 24ºS (a,b,c) and 34.5ºS (d,e,f), and northward accumulated mass transport (Sv) at 10ºW (g,h) in the Atlantic Ocean for the upper (1:5), deep (6:9), and bottom (10:11) layers; the positive/negative mass transports are northward/southward at 24ºS and 34.5ºS, and eastward/westward at 10ºW. The mass transports obtained from the inverse model (blue curves) are compared with the available simulations from the ECCO (green curves) and GLORYS (red curves) circulation models averaged over time.

2.6.1 Upper Ocean

The SACW-AAIW stratum includes the thermocline and intermediate waters (from the sea surface down to $\gamma^n = 27.23$ kg/m^3, approximately down to 730 m; Figures 2.8a, d, and g). The mass transport in these upper layers presents a northward recirculation near the western boundary, a net northward mass transport through the ocean interior, and a wide and slow Benguela Current in the eastern boundary, rendering the typical pattern of the subtropical gyre (Figure 2.8a and d). The alternating mass transports in the entire subtropical gyre are caused by mesoscale eddies, bringing the saw-like streamfunction described in Hernández-Guerra et al. (2005).

In the western boundary, off the east coast of South America, a relatively strong Brazil Current flows poleward. The Brazil Current has been previously described by Garzoli et al. (2013) from XBTs at 35ºS, by Müller et al. (1998) from current moorings between 20ºS and 28ºS, and by McDonagh & King (2005) and Hernández-Guerra et al. (2019) from hydrographic data at 30ºS. In our study, the Brazil Current shows up clearly by the tilting isopycnals, at 24ºS as a narrow jet (≈ 37 km) from the coast to about 40.5ºW with a southward mass transport of -7.3 $\pm$ 0.9 Sv at 24ºS, and at 34.5ºS as a much wider jet that extends from the coast to about 49.2ºW (127 km) with a southward transport of -16.6$\pm$1.3 Sv (see also Manta et al., 2021) (Table 2.1). Thus, the Brazil Current increases its mass transport to the south. In these upper layers, the OGCM reproduces reasonably well the inverse model transports at 24ºS and 34.5ºS (Figure 2.8a and d, respectively), but with some significant differences in the extension and intensity of the boundary transports. Specifically, at 24ºS GLORYS does not show a western boundary current, while ECCO presents a similar Brazil Current transport of -6.8 $\pm$ 1.5 Sv from the coast to 38.3ºW. The OGCM transports at 34.5ºS are stronger (-28.7 $\pm$ 12.7 Sv from the coast to 49.3ºW in GLORYS and -21.5 $\pm$ 1.9 Sv from the coast to 46.5ºW) than the inverse model.

In the eastern margin, between the African coast to about 10.9ºE (Reid, 1989), the Benguela Current is observed as a relatively wide and strong northward eastern boundary current of the South Atlantic Subtropical Gyre. The Benguela Current flows northward becoming wider at 24ºS (from 27.6ºW to the coast). The strength of the Benguela Current, from above ~730 m depth (layers 1-5, between the surface and γ^n = 27.23 kg/m^3), is estimated to be 26.4 $\pm$ 2.0 Sv at 34.5ºS, which is slightly stronger than the much wider Benguela Current of 21.2 $\pm$ 1.8 Sv at 24ºS (Table 2.1). The mass transport at 10ºW, between 28.4º and 22.4ºS, is –19.2 $\pm$ 1.4 Sv, which corresponds to the branch of the Benguela Current that runs above the MAR (Figure 2.8g). At 24ºS, GLORYS and ECCO represent a weaker Benguela Current in the western boundary of 14.6 $\pm$ 2.7 and 15.3 $\pm$ 0.8 Sv, respectively, from 27ºW to the coast. Furthermore, at 34.5ºS OGCM presents a similar Benguela Current transport to the hydrographic data from 9.3ºE to the coast of 26.9 $\pm$ 14.1 Sv and from 8.5ºE to the coast of 28.1 $\pm$ 0.7 Sv in GLORYS and ECCO, respectively.

2.6.2 Deep Layers

The mass transport for the UCDW-NADW deep layers flows southward and eastward (layers 6-9, from 27.58 kg/m^3 to 28.1 kg/m^3) (Figure 2.8b, e, and h). The accumulated poleward mass transport in these layers presents no significant differences through 24ºS (-24.7 $\pm$ 2.5 Sv) and 34.5ºS (-21.7 ± 2.2 Sv). Moreover, the accumulated mass transport for these layers at 10ºW presents a net mass transport of 17.7 ± 1.1 Sv, which reflects that part of the deep waters flow eastward from 34.5ºS to 33.5ºS (10.2 ± 2.8 Sv) before recirculating in the south, an eastward flow close to 24ºS (7.5 ± 4.4 Sv), and other recirculation routes along the meridional section (Figure 2.8h).

According to multiple research studies (e.g., Ganachaud, 2003; Meinen et al., 2017; Meinen & Garzoli, 2014; Müller et al., 1998), NADW is principally transported southward in the Atlantic Ocean by the DWBC. Based on the hydrographic sections examined in the present study, the DWBC presents a southward mass transport of -8.7 ± 3.8 Sv from the coast to 35.2ºW at 24ºS and -13.9 ± 3.0 Sv from the coast to 47.3ºW at 34.5ºS (Table 2.1). The northward recirculation of the DWBC is found just east of these longitudes (to about 33.7ºW and 46.8ºW at 24ºS and 34.5ºS, respectively), presenting an equatorward mass transport of 6.4 ± 2.7 Sv at 24ºS and 3.0 ± 1.3 Sv at 34.5ºS (Table 2.1). In the deep layers, at 24ºS GLORYS presents a stronger DWBC poleward mass transport (-13.0 ± 3.8 Sv) than the inverse model (Figure 2.8b), while ECCO presents a similar DWBC of -9.4 ± 2.6 Sv both from the coast to 35.8ºW. At 34.5ºS, the OGCM replicates fairly well the intense DWBC (-11.7 ± 7.4 Sv from the coast to 48.5ºW in GLORYS, and -11.1 ± 1.6 Sv from the coast to 46ºW in ECCO). However, both numerical models have substantial differences from the inverse model in the ocean interior (Figure 2.8e). These differences could be explained by the fact that our inverse model results present higher resolution because they are based on observations. In contrast, OGCMs often use assumptions and parameterizations to simplify the complexity of ocean processes, introducing errors and biases into the model results, particularly in the ocean interior and deep layers where observational data are limited.

From our inverse model results, the DEBC presents a northward mass transport of -16.3 $\pm$ 4.7 Sv at 24ºS, which is similar to the -15.1 $\pm$ 3.5 Sv obtained at 34.5ºS. Therefore, the branch from the DWBC feeding the DEBC comes from latitudes north of 24ºS, which is corroborated with the westward flow above the MAR close to 24ºS at 10ºW. At 24ºS in the eastern boundary, GLORYS (-3.0 $\pm$ 3.3 Sv from 3.8ºE to the coast) and ECCO (-1.8 $\pm$ 1.8 Sv from 7.3ºE to the coast) present a weaker DEBC than the inverse model, and at 34.5ºS ECCO also displays a weaker DEBC of -2.3 $\pm$ 0.5 Sv from 14ºE to the coast, while GLORYS estimates a similar transport (-13.5 $\pm$ 12.7 Sv from 12.8ºE to the coast) if compared with the inverse model.

2.6.3 Bottom Layers

The LCDW-AABW water masses (layers 10-11, below γ^n=28.15 kg/m^3) present a low net equatorward mass transport of 6.6 $\pm$ 1.6 Sv at 24ºS and 6.3 $\pm$ 1.5 Sv at 34.5ºS (Figures 2.8c and f). In the western basin, the northward transport over the Argentine Basin at 34.5ºS (5.6 $\pm$ 1.1 Sv) passes through the Vema Chanel (3.5 $\pm$ 0.7 Sv) and Hunter Channel (2.3 $\pm$ 0.9 Sv) to reach 24ºS (5.8 $\pm$ 1.5 Sv). Whereas in the eastern basin, the equatorward flow over the Cape Basin at 34.5ºS (8.6 $\pm$ 3.5 Sv) barely reaches 24ºS (3.0 $\pm$ 0.8 Sv), as some flow recirculates (2.2 $\pm$ 0.7 Sv) and some flow turns back to 34.5ºS (-7.9 $\pm$ 3.6 Sv). Additionally, the MAR limits the east/westward flow of the abyssal waters at 10ºW, presenting no mass transport in these layers. At 24ºS, GLORYS shows no mass transport in the abyssal layers (Figure 2.8c) but does fairly well at 34.5ºS, reproducing the alternating mass transport between both basins, while the ECCO output differs greatly from the inverse results at both latitudes.

2.7 Heat and Freshwater Transports

The heat transport is computed by using the following expression:

$$HT = \sum_i \sum_j \rho_{ij} c_{p_{ij}} \theta_{ij} v_{ij} \Delta x \Delta z$$

where ρ_{ij} is the density, $c_{p_{ij}}$ is the heat capacity of the seawater, θ_{ij} is the potential temperature, and v_{ij} is the absolute cross-section velocity, and the i, j subindexes identify the station pair and layer, respectively. Positive values indicate a northward heat flux, while negative values imply a southward heat flux.

The positive values estimated from the meridional heat transports after the inverse model at 34.5ºS (0.30 $\pm$ 0.05 PW) and 24ºS (0.80$\pm$0.05 PW) indicate an increase in the equatorward flux in the subtropical South Atlantic. In addition, these results reflect the northward direction of the warm waters in the upper layers at both latitudes in the South Atlantic Ocean. The heat transport in GLORYS agrees with the inverse model results at these latitudes (0.43$\pm$0.26 PW and 0.71 $\pm$ 0.14 PW at 24ºS and 34.5ºS, respectively), while ECCO presents a similar heat transport at 34.5ºS (0.34 $\pm$ 0.15 PW) and weaker at 24ºS of 0.44 $\pm$ 0.10 PW than our inverse model results at this latitude but yet reproduces the increase in northward heat transport.

The freshwater flux (in FSv, Sverdrup for freshwater transport without mass balance) is estimated according to Joyce et al. (2001), taking into account the precipitation over evaporation:

$$\bar{F} = -\sum_{i}\sum_{j} T_{ij}S'_{ij}/S_0$$

where T_{ij} is the absolute mass transport, S'_{ij} is the anomaly of salinity (Salinity-S_0), both in layer i at station pair j, and S_0 is the global ocean mean salinity set to 34.9 as in Arumí-Planas et al. (2022), Hernández-Guerra & Talley (2016), and Talley (2008). At 24ºS there is a southward transport of freshwater (-0.07 $\pm$ 0.02 FSv), while at 34.5ºS there is a northward transport of freshwater (0.18 $\pm$ 0.02 FSv). Therefore, our results suggest that in the 24ºS-34.5ºS domain, evaporation predominates over precipitation (as in Caínzos et al. (2022a)). The freshwater transports from the OGCM and the inverse model are not significantly different. The GLORYS freshwater transports have the same direction as the inverse model at 24ºS (-0.05 $\pm$ 0.07 FSv) and 34.5ºS (0.25 $\pm$ 0.11 FSv), while ECCO presents a slightly higher value at 24ºS (0.01 $\pm$ 0.05 FSv) and weaker freshwater transport at 34.5ºS (0.07 $\pm$ 0.07 FSv) than the inverse model.

2.8 South Atlantic Schematic Circulation

Figure 2.9 sketches a circulation in the upper, deep and bottom layers in the South Atlantic between 24ºS and 34.5ºS and above the MAR that is coherent with the mass transports as inferred from our inverse box model. The net mass transport from the inverse model indicates that the predominant northward path of the upper layers is found in the easternmost region of the 34.5ºS section (26.3 ± 2.0 Sv), expanding to a wider area at 24ºS (8.1 ± 0.7 Sv east of the 10ºW). It also shows that a fraction of the northward flow turns west through the MAR in the northern stations of 10ºW, between 22.4ºS and 28.4ºS (-19.2 ± 1.4 Sv), which then splits into two branches, one flowing north to 24ºS (13.1 ± 1.6 Sv west of 10ºW, summing a total northward flow of 21.2 ± 1.8 Sv at 24ºS) and the second branch reaching the western boundary (6.1 ± 1.4 Sv). These mass transports together with the southward flow at the westernmost part of the 24ºS section to 34.5ºS describe the anticyclonic course of the South Atlantic subtropical gyre.

In the deep layers, the DWBC and DEBC flow southward from 24ºS (-8.7 ± 3.8 Sv and -16.3 ± 4.7 Sv, respectively) to 34.5ºS (-13.9 ± 3.3 Sv and -15.1 ± 3.5 Sv, respectively). The scheme turns more complicated as an eastward branch flows over the MAR (7.5 ± 4.4 Sv) near 24ºS and several recirculation routes appear to take place throughout the entire 10ºW section (Figure 2.8).

Finally, the abyssal waters present a northward mass transport from the Argentine Basin (5.6 ± 1.1 Sv at 34.5ºS) to the Brazil Basin (5.8 ± 1.5 Sv at 24ºS), as well as an equatorward flow from the Cape Basin (8.6 ± 3.5 Sv at 34.5ºS), which barely reaches the 24ºS (3.0 ± 0.8 Sv) section before returning southwards (-2.2 ± 0.7 Sv) until 34.5ºS (-7.9 ± 3.6 Sv).

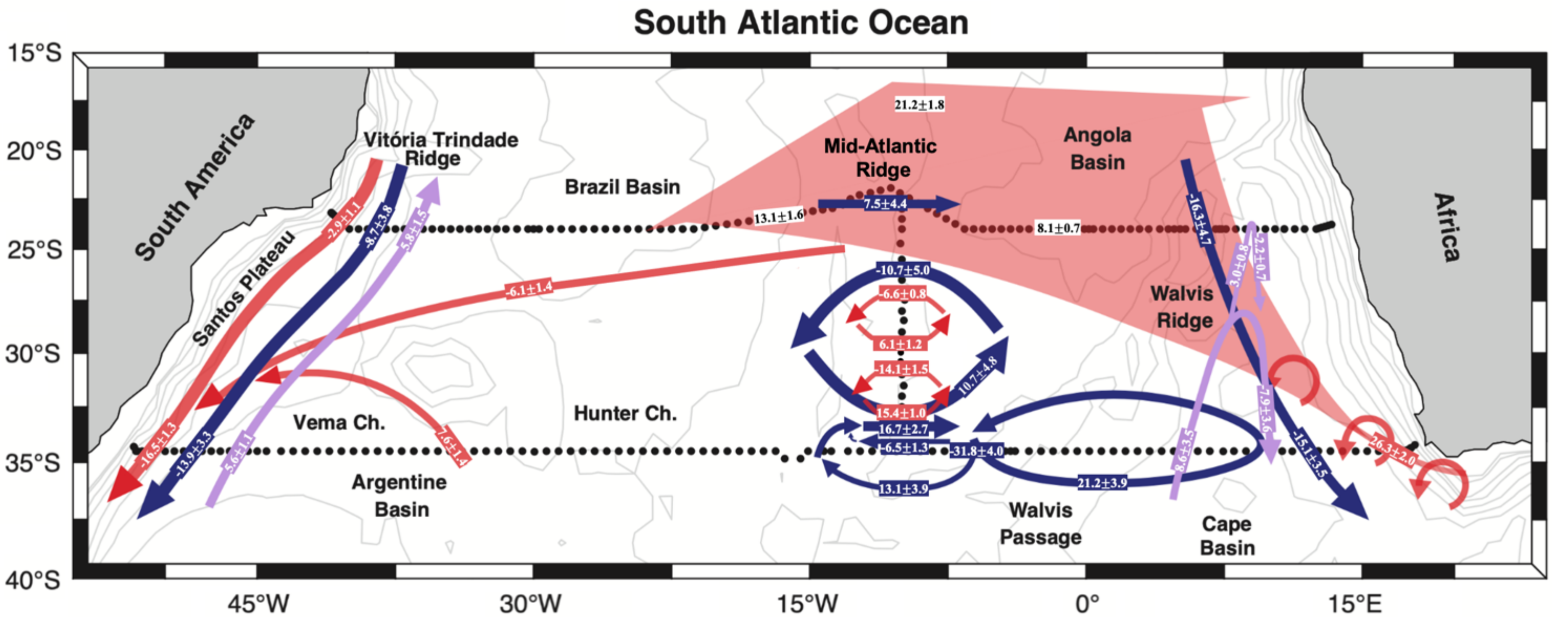

Figure 2.9. Schematic circulation in the upper (red), deep (blue) and bottom (purple) layers of the South Atlantic Ocean, consistent with the mass transports calculated across 24ºS, 10ºW and 34.5ºS. The net mass transports (in Sv) are indicated, with the positive transports northward and eastward and the negative transports southward and westward.

2.9 Discussion and Concluding Remarks

We have used hydrographic data sampling three enclosed regions for inverse modeling in the South Atlantic subtropical gyre. The initial geostrophic velocity is first adjusted to the velocities from ADCP data, and subsequently with the reference velocities as obtained from an inverse box model, such as to satisfy water mass balances in the three enclosed regions.

In the upper layers, the Brazil Current flows as a relatively intense western boundary current, increasing southward from -7.3 $\pm$ 0.9 Sv at 24ºS to -16.6 $\pm$ 1.3 Sv at 34.5ºS. The GLORYS and ECCO models do not properly represent the Brazil Current at 24ºS, but both represent a slightly weaker (GLORYS: -12.7 Sv in January; ECCO -9.8 Sv in 2017 mean) or stronger (GLORYS -29.1 Sv in 2017-2019 mean; ECCO -22.5 Sv in January) Brazil Current transport at 34.5ºS. Our result at 24ºS agrees with the 4.9-12.3 Sv estimated by Bryden et al. (2011) but is slightly higher than the 5.8 $\pm$ 0.1 Sv estimated by Evans et al. (2017). Further, our estimates for the Brazil Current are consistent with a recirculation cell south of 28ºS in the western South Atlantic, found both by Stramma (1989) (from -9.6 Sv at 24ºS to -17.5 Sv at 33ºS) and by Garzoli et al. (2013) (from -8.6 $\pm$ 4.1 Sv at 24ºS to -19.4 $\pm$ 4.3 Sv at 35ºS). Moreover, Schmid & Majumder (2018) combined Argo-float and sea surface height data to propose that the Brazil Current intensifies to the south, but with weaker mean mass transports (-2.3 $\pm$ 0.9 at 24ºS and -12.6 $\pm$ 2.6 Sv at 35ºS).

The Benguela Current flows in the upper layers as a broad and relatively strong equatorward eastern boundary current, which changes from 26.4 $\pm$ 2.0 Sv at 34.5ºS to 21.2 $\pm$ 1.8 Sv at 24ºS. The GLORYS and ECCO models present a similar transport at 34.5ºS, of 21.6 Sv and 20.3

Sv, respectively, and GLORYS shows a Benguela Current of 25.5 Sv at 24ºS. Our transports at 34.5ºS agree with the previously reported values by Kersalé et al. (2019) (24.0 $\pm$ 17.0), Garzoli et al. (2013) (22.5 $\pm$ 4.7 Sv), and Majumder & Schmid (2018) (19 $\pm$ 3 Sv). These results show that the Benguela Current is a relatively strong eastern boundary current, much stronger than the Canary Current in the North Atlantic (Casanova-Masjoan et al., 2018) and the Peru-Chile Current in the South Pacific (Arumí-Planas et al., 2022). The accumulated mass transport at 10ºW presents a westward mass transport in the upper layers (-18.4 $\pm$ 0.4 Sv), consistent with the westward branch of the Benguela Current over the MAR (Garzoli & Gordon, 1996; Richardson & Garzoli, 2003; Rodrigues et al., 2007; Stramma, 1991).

The accumulated mass transport in the deep layers presents a net northward mass transport of UCDW-NADW through 24ºS and 34.5ºS of -24.7$\pm$2.5 Sv and -21.7$\pm$2.2 Sv, respectively. In the western boundary, the deep waters are transported southwards by the DWBC, which presents a southward mass transport of -8.7 $\pm$ 3.8 Sv at 24ºS and -13.9 $\pm$ 3.0 Sv at 34.5ºS. At 24ºS, the GLORYS output presents a stronger DWBC poleward mass transport (-19.1 Sv) than the inverse model. While at 34.5ºS, neither of the two ocean models properly represents the interior circulation in the deep layers, but both display the intense poleward DWBC (-13.4 Sv in GLORYS and -13.2 Sv in ECCO). Adjacent to the DWBC, we find a northward transport of 6.4 $\pm$ 2.7 Sv at 24ºS and 3.0 $\pm$ 1.3 Sv at 34.5ºS. Further, the interior NADW pathway, which originates close to the Vitória-Trindade Ridge at about 20ºS, extends eastward crossing the MAR between 20º and 25ºS (Arhan et al., 2003; Garzoli et al., 2015; Speer et al., 1995; van Sebille et al., 2012), then it moves to the Cape Basin and flows southward across the African continental slope as a DEBC (Arhan et al., 2003; Palma & Matano, 2017; Stramma & England, 1999). In the eastern boundary, the deep waters are transported southward by the DEBC (-16.3 $\pm$ 4.7 Sv at 24ºS and -15.1 $\pm$ 3.5 Sv at 34.5ºS). For comparison, at 24ºS, GLORYS presents a weaker DEBC (-6.8 Sv) than the inverse model, while at 34.5ºS both GLORYS and ECCO have weaker transports than the inverse model (-6.0 Sv and 1.4 Sv, respectively). At 10ºW, the deep layers display a net eastward transport of 17.7 $\pm$ 1.1 Sv, with some 10 Sv recirculating between the eastern and western basins. An eastward transport is found close to 24ºS (7.5 $\pm$ 4.4 Sv), reflecting the NADW pathway into the eastern basin between 20ºS and 25ºS previously described by Arhan et al. (2003) and Reid (1989).

In this study, we find a northward heat transport in the subtropical South Atlantic, both at 34.5ºS (0.30 $\pm$ 0.05 PW) and 24ºS (0.80 $\pm$ 0.05 PW), which reflects the equatorward mass transport in the warm upper layers. The northward heat transport in GLORYS is similar to our estimate at both latitudes (0.43 $\pm$ 0.26 PW and 0.71 $\pm$ 0.14 PW at 24ºS and 34.5ºS, respectively), while the heat transport in ECCO is similar at 34.5ºS (0.34 $\pm$ 0.15 PW) but weaker at 24ºS (0.44 $\pm$ 0.10 PW) than our inverse model results. The heat transport estimated at 34.5ºS agrees with the 0.27 $\pm$ 0.10 PW estimated by Manta et al. (2021) using the same hydrographic section, the 0.49 $\pm$ 0.23 PW from altimetry data computed by Dong et al. (2015), the 0.5 $\pm$ 0.2 PW from acoustic inversion reported by Kersalé et al. (2021), as well as with the 0.42 $\pm$ 0.18 PW from numerical model data obtained by Perez et al. (2011). In the same way, our result at 24ºS presents no significant differences from previous estimations with hydrographic data − 0.64 $\pm$ 0.18 PW (Fu, 1981) and 0.7 $\pm$ 0.1 PW (Bryden et al., 2011) − but is higher values than the 0.4 $\pm$ 0.1 PW estimated by Evans et al. (2017) and slightly higher than the 0.66 $\pm$ 0.07

PW reported by Caínzos et al. (2022a). Some of these differences are likely the result of the differences in years and months when the cruises were carried out (Caínzos et al., 2022a).

The negative freshwater flux at 24ºS (-0.07 $\pm$ 0.02 FSv) and the positive freshwater transport at 34.5ºS (0.18 $\pm$ 0.02 FSv) indicate a convergence of freshwater in the 24ºS-34.5ºS domain, pointing out that this is a region where evaporation predominates over precipitation. The freshwater transports from GLORYS present no significantly different values from the inverse model at both latitudes (-0.05 $\pm$ 0.07 FSv and 0.25 $\pm$ 0.11 FSv at 24ºS and 34.5ºS, respectively), while ECCO presents slightly higher (0.01 $\pm$ 0.05 FSv at 24ºS) and weaker (0.07 $\pm$ 0.07 FSv at 34.5ºS) freshwater transports than the inverse model. Our result at 24ºS agrees with the weak northward freshwater transport (0.01 $\pm$ 0.09 FSv) obtained by Caínzos et al. (2022a) using WOCE and GO-SHIP data for the period 2010-2019. The freshwater flux obtained at 34.5ºS is moderately lower than the freshwater transport of 0.23 $\pm$ 0.02 Sv obtained by Manta et al. (2021) at this same latitude.

The comparison of the circulation patterns as deduced from the inverse model with two different OGCM (ECCO and GLORYS) suggests that these ocean models are useful to study these sections in the upper layers (γ^n < 27.58 kg/m^3, 1,140 m depth) with some differences in the estimated boundary currents. However, the ECCO and GLORYS patterns of circulation in the deep and, especially, bottom layers (γ^n > 27.58 kg/m^3) do not properly resemble the circulation pattern of the hydrographic data at 24ºS and 34.5ºS in the Atlantic Ocean. The comparison of the heat and freshwater transports from the inverse model with the OGCM suggests that ECCO presents noticeable differences from our results, but GLORYS can be useful for determining the direction and strength of these deep ocean fluxes.

Our inverse model results show an AMOC strength of 17.5 $\pm$ 0.9 Sv at 24ºS and 14.8 $\pm$ 1.0 Sv at 34.5ºS. The AMOC strength at 24ºS agrees fairly well with previous estimates at 24ºS by Evans et al. (2017) (20.2 $\pm$ 2.0 Sv), and Bryden et al. (2011) (21.5/16.5 Sv in 2009/1983). Furthermore, our estimate of the AMOC strength at 34.5ºS agrees well with earlier estimates at this latitude, 15.6 $\pm$ 1.4 Sv (Manta et al., 2021), 17.3 $\pm$ 5.0 Sv (Kersalé et al., 2021), 14.7 $\pm$ 8.3 Sv (Meinen et al., 2018), 15.6 $\pm$ 3.1 Sv (Perez et al., 2011), and 18.1 $\pm$ 2.3 Sv (Garzoli et al., 2013). However, it is weaker than transports obtained by Dong et al. (2015) and Majumder et al. (2016), 19.5 $\pm$ 3.5 Sv and 20.7 $\pm$ 4.1 Sv, respectively. The weaker upper AMOC strength and heat transport at 34.5ºS as compared with 24ºS could be partly explained by the intense southward transport of the Brazil Current (-16.6 $\pm$ 1.3 Sv at 34.5ºS and -7.3 $\pm$ 0.9 Sv at 24ºS) during the period of this hydrographic cruise (Kersalé et al., 2021; Manta et al., 2021). Furthermore, mesoscale eddies also probably play a role in upper limb transport, as the mesoscale activity at 34.5ºS is higher than at 24ºS (Laxenaire et al., 2018).

Our inverse box model has provided a detailed view of the South Atlantic circulation by estimating the different ocean current transports at each layer set through 24ºS and 34.5ºS, as well as over the MAR between these two latitudes. The transports in the upper layers are consistent with the course of the subtropical South Atlantic anticyclonic gyre and the northwest route of the Benguela Current. The deep waters show the southward flow of the DWBC and DEBC, together with an eastward interbasin flow at the northern stations (close to 24ºS) of the 10ºW section, and different recirculation routes linking both basins. The abyssal layers exhibit northward mass transports through the Argentina and Cape basins, before the latest returns southward in the ocean interior, with no flow crossing above the MAR. Our results have also confirmed the characteristic northward heat transport across the subtropical South Atlantic Ocean, as well as the dominance of evaporation over precipitation.

Chapter 3

A Multi-Data Set Analysis of the Freshwater Transport by the Atlantic Meridional Overturning Circulation at Nominally 34.5ºS

Chapter published at:

Arumí-Planas, C., Dong, S., Perez, R., Harrison, M. J., Farneti, R., & Hernández-Guerra, A. (2024). A multi-data set analysis of the freshwater transport by the Atlantic meridional overturning circulation at nominally 34.5°S. Journal of Geophysical Research: Oceans, 129, e2023JC020558. https://doi.org/10.1029/2023JC020558

3.1 Introduction

One of the key questions in climate studies is how the Atlantic Meridional Overturning Circulation (AMOC) will respond to the effects of global warming and subsequent alterations in the hydrological cycle (de Vries & Weber, 2005; Keller et al., 2000). The oceans play an essential role as a redistribution agent and global reservoir for several important constituents, such as heat, freshwater, and carbon, of the Earth's climate system. The AMOC is a crucial element of the Atlantic Ocean climate system, as it carries heat northward at all latitudes, thereby warming surface air temperatures in Western Europe (Ganachaud & Wunsch, 2000; Mecking et al., 2017; Talley, 2003). As a result, a weakening or even collapse of the AMOC could lead to a strong cooling of surface air temperatures in regions surrounding the North Atlantic (Jackson et al., 2015; Manabe & Stouffer, 1988; Vellinga & Wood, 2002), and a convergence of warm water in the tropical and subtropical North Atlantic, which could lead to weaker and less frequent Atlantic hurricanes (Yan et al., 2017). It is important to understand the interplay between AMOC-induced cooling and background global warming, as Liu et al. (2020) did in a numerical modeling study focused on the 21st century.

In the southernmost latitude of the Atlantic Ocean, nominally 34.5ºS, the freshwater transport by the AMOC, referred to as M_{ov} hereafter, is used as a possible indicator of the AMOC bistability with significant global climate effects (Cimatoribus et al., 2012; de Vries & Weber, 2005; Huisman et al., 2010; Matos et al., 2020; Mecking et al., 2016, 2017; Rahmstorf, 1996; Skliris et al., 2020). The South Atlantic Ocean has historically been less studied than the North Atlantic, as a result, model estimates of the M_{ov} have been poorly constrained in this basin (Garzoli et al., 2013; Weijer et al., 2019). Nevertheless, the repeated high-density eXpendable BathyThermograph (XBT) lines (trans-basin AX18 line from South America to Cape Town; AX22 and AX25 lines across the Drake Passage and the Agulhas retroflection, respectively), together with the Argo program collecting a large number of temperature and salinity profiles (Roemmich & Owens, 2000), and the quasi-decadal occupation of trans-basin hydrographic lines (Arhan et al., 2003; Arumí-Planas et al., 2023; Bryden et al., 2011; Hernández-Guerra et al., 2019; Manta et al., 2021; McDonagh & King, 2005; Saunders & King, 1995) have increased data coverage in the South Atlantic region. Consequently, observed and simulated estimates of mean AMOC and Meridional Heat Transport (MHT) in the South Atlantic have become more consistent over the last decade (Baringer & Garzoli, 2007; Chidichimo et al., 2023; Dong et al., 2009, 2011; Kersalé et al., 2021; Pita et al., 2024; Sitz et al., 2015; Weijer et al., 2020), with fairly good agreement in terms of AMOC and MHT variability between models and some observations in more recent studies (Baker et al., 2023; Biastoch et al., 2021; Dong et al., 2021). However, previous estimations of freshwater transport from observations are limited in the South Atlantic, and models and observations have shown disagreement about the freshwater transport direction in this region (e.g., Bryden et al., 2011; Caínzos et al., 2022a; Dijkstra, 2007; Drijfhout et al., 2011; Garzoli et al., 2013; Huisman et al., 2010; Liu et al., 2014, 2017; de Vries & Weber, 2005; Weijer & Dijkstra, 2003).

The main goal of this study is to present a multi-data set analysis of the M_{ov} at nominally 34.5ºS in the South Atlantic Ocean, using an updated AX18-XBT data set from April 2002 to October 2019 (following Garzoli et al. (2013) which only analyzed transects through 2011).

Furthermore, we have examined the consistency between observed and simulated multidecadal variability of the South Atlantic meridional fluxes using two data sets derived from Argo floats measurements, Ocean General Circulation Models (OGCMs), and Coupled General Circulation Models (CGCMs), and we have diagnosed the causes of the differences in the sign of M_{ov}. Finally, we have analyzed the seasonal variability of South Atlantic meridional fluxes and examined how the fluxes covary on longer timescales.

3.2 Data and Methods

3.2.1 Observational and numerical model data

In this study, our focus is on the variability of the M_{ov} nominally across 34.5ºS in the South Atlantic and how it covaries with meridional mass (or volume which is strongly linked to mass transport) and heat transports by the overturning circulation. As our primary data set, we have used 49 realizations of the AX18 repeat high-density XBT line from April 2002 to October 2019. The 49 transects of the AX18-XBT line used in this study are presented in Figure 3.1. These transects were conducted using Evergreen container ships that crossed the South Atlantic from South America to South Africa. AX18-XBT measures water temperature profiles from the sea surface to a nominal depth of 850 m. Salinity profiles were generated using a historical T-S relationship (Goes et al., 2018). To extend the T & S profiles down to the seafloor, we utilized the 1/4º horizontal resolution NCEI World Ocean Atlas 2018 (WOA18) T-S climatology. Specifically, we used monthly averages of WOA18 data between 800-1,500 m and seasonal averages below 1,500 m (Garcia et al., 2019;

Locarnini et al., 2018; Zweng et al., 2019). This data set comprises 57 vertical levels spanning from 0 to 1,500 m for the monthly averages, while it encompasses 112 vertical levels spanning from 0 to 5,500 m for seasonal averages. Then, each T-S profile is linearly interpolated from the surface to the seafloor with 140 predefined depths, using intervals of 5-10 m up to 750 m, 50 m intervals until 2,000 m, and finally, 100 m intervals reaching the seafloor. The T-S relationship method for estimating the mass transport from XBT data presents an uncertainty that might be similar to that estimated by Hernández-Guerra et al. (2002) for the region of the Canary Islands. The Ekman transport contribution is computed using NCEP annual mean winds and is included in the shallowest layer, employing the same methodology as outlined in both Baringer & Garzoli (2007) and Garzoli & Baringer (2007).

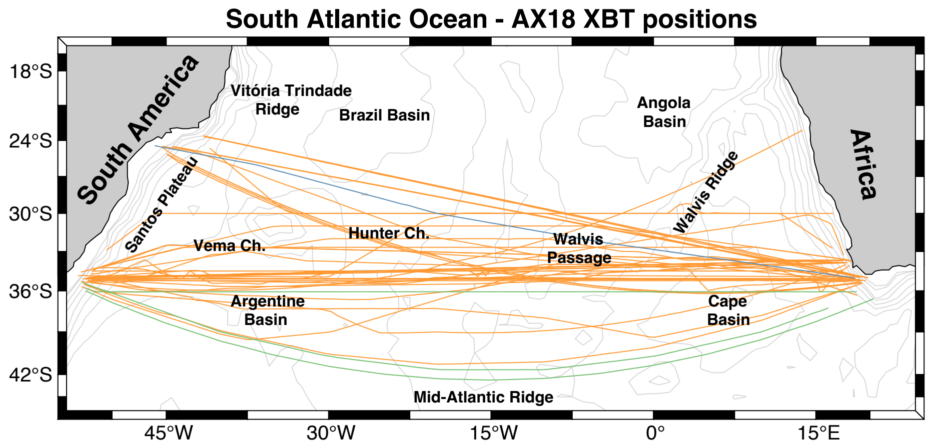

Figure 3.1. Locations of the high-density AX18-XBT lines conducted in the South Atlantic Ocean. The green color lines correspond to the individual AX18-XBT transects for which positive M_{ov} values were observed, whereas the blue line represents the transect exhibiting large negative M_{ov}.

The AX18-XBT data were complemented with data from Argo floats and different simulations of OGCMs and CGCMs across 34.5ºS in the Atlantic Ocean, as described below.

The first data set used to compare with the AX18-XBT results in this study is monthly data from the Argo Altimetry product (Argo Alt. hereafter). The Argo Alt. consists of the daily sea level anomaly (SLA) observations processed and distributed by the Copernicus Marine Environment Monitoring Service (CMEMS) (Pujol et al., 2016), as well as temperature and salinity (T-S) profiles from the Global Temperature and Salinity Profile Program (GTSPP) (Sun et al., 2010). The Argo Alt. data set has a 0.25º horizontal resolution and is available from January 1993 to August 2022, with 305 vertical levels from the surface to the bottom of the ocean (Dong et al., 2015; 2021).

The Roemmich-Gilson (RG) Argo Climatology, RG Argo hereafter, is the next data set used in this study. This data set provides monthly gridded hydrographic salinity-temperature profiles based on the Argo Buoy Observation Network (Roemmich & Gilson, 2009). The RG Argo has a 1º horizontal resolution and 58 vertical levels from 2.5 to 1,975 dbar. For this study, we used data in the South Atlantic Ocean across 34.5ºS, covering the period from January 2004 to August 2022. The gridded-field RG Argo was estimated based on a weighted least-squares fitting method that utilized the nearest 100 Argo profiles within a given month. Potential density, steric height, and relative geostrophic velocity with the reference layer at 1,000 m depth were calculated using the salinity and temperature fields from 223 months of data. In addition, the velocities at the parking depth (1,000 m) from the YoMaHa data set were summed to the RG Argo derived relative geostrophic velocity profiles to provide an absolute velocity (Lebedev et al., 2007).

The Ocean general circulation model For the Earth Simulator (OFES) run by the Japan Agency for Marine-Earth Science and

Technology (JAMSTEC) is the first OGCM examined in this study. This high-resolution eddy-resolving model has a horizontal resolution of 0.1º and 54 vertical levels from the surface to the ocean bottom. To simulate ocean circulation, the OFES model was spun up for 50 years using a monthly climatology derived from NCEP/NCAR reanalysis atmospheric fluxes (Masumoto et al., 2004), and then was forced with daily mean NCEP/NCAR reanalysis data from 1950 to 2017 (Sasaki et al., 2008). Model fields were provided by JAMSTEC at the full resolution (0.1º) for the region across 34.5ºS in the Atlantic Ocean, covering the period from January 1980 to December 2017.

The second OGCM, the GLORYS12V1 model (Global Ocean Physics Reanalysis; GLORYS, hereafter) developed by the CMEMS, examined in this study is an eddy-resolving global ocean reanalysis model. GLORYS is based on the current real-time global forecasting CMEMS system. The model hydrodynamics are based on NEMO (Nucleus for European Modeling of the Ocean) and assimilates in situ observations from the CORA4 database and atmospheric forcing from ERA-Interim data. Additionally, it assimilates altimeter data (sea level anomaly), sea ice concentration, satellite sea surface temperature, and in situ temperature and salinity vertical profiles. This results in monthly gridded data sets with a horizontal resolution of 1/12º and 50 vertical levels from the surface to the seafloor (Drévillon et al., 2018). GLORYS12V1 data from January 1993 to December 2019 are used in this study.

The Geophysical Fluid Dynamics Laboratory (GFDL) OM4 ocean/sea ice model (Adcroft et al., 2019) is the third OGCM used in this study. The ocean component of OM4 uses the Modular Ocean Model version 6, forced with the JRA55-do atmospheric reanalysis product

(Tsujino et al., 2020; MOM6-JRA, hereafter), and monthly averages were stored for the entire simulation period. MOM6-JRA has a nominal horizontal spacing of 0.25º, with no mesoscale eddy parameterization and 50 vertical levels spanning from the surface to the ocean bottom. MOM6-JRA data from January 1988 to December 2017 are used in this study. MOM6-JRA dynamical core is based on hydrostatic primitive equations formulated in their generalized vertical coordinate form.

A second MOM6 simulation using MERRA-2 forcing is the fourth OGCM included in this study (Rienecker et al., 2011; MOM6-MERRA2, hereafter). MOM6-MERRA2 has a nominal 0.25º horizontal spacing and 35 vertical levels spanning from the ocean surface to the bottom. Differences between the MOM6 simulations can be primarily attributed to the atmospheric forcing used. MERRA2 reanalysis includes an adjustment of precipitation and evaporation over both the ocean and the earth's surface (Harrison et al., 2022). Additionally, the MERRA2 atmospheric forcing covers a more recent period as it extends up to December 2020.

Finally, monthly outputs from 32 historical CGCM simulations from the Coupled Model Intercomparison Project 6 (CMIP6) for the period 1850-2014 have been used in this study. CMIP6 models were obtained from the Earth System Grid Data Portal, but not all the CMIP6 models have the "r1i1p1f1" ensemble member available. Therefore, we have used different ensemble members when the first is not available, as indicated in Table 3.1. The corresponding institution for each model, experiment ID ("Historical"), member ID, horizontal resolution (usually 1º), and citation are also included in Table 3.1. A multi-model mean is computed using the 32 CMIP6 models for comparison with other data sets.

Table 3.1. List of the 32 Coupled Global Climate Models (CGCMs) From the CMIP6 Project.

Source ID	Institute ID	Experiment ID	Member ID	Resolution	Citation
TaiESM1	AS-RCEC	Historical	r1i1p1f1	1.13º	Lee & Liang (2020)
BCC-CSM2-MR	BCC	Historical	r1i1p1f1	1.00º	Wu et al. (2018)
BCC-ESM1	BCC	Historical	r1i1p1f1	1.00º	Zhang et al. (2018)
FGOALS-g3	CAS	Historical	r1i1p1f1	1.00º	Li (2019)
CanESM5	CCCma	Historical	r10i1p2f1	1.00º	Swart et al. (2019)
CMCC-CM2-SR5	CMCC	Historical	r1i1p1f1	1.00º	Lovato & Peano (2020)
CMCC-ESM2	CMCC	Historical	r1i1p1f1	1.00º	Lovato et al. (2021)
CNRM-CM6-1	CNRM-CERFACS	Historical	r2i1p1f2	1.00º	Voldoire (2018)
CNRM-ESM2-1	CNRM-CERFACS	Historical	r1i1p1f2	1.00º	Seferian (2018)
ACCESS-ESM1-5	CSIRO	Historical	r1i1p1f1	1.00º	Ziehn et al. (2019)
ACCESS-CM2	CSIRO-ARCCSS	Historical	r1i1p1f1	1.00º	Dix et al. (2019)
E3SM-1-0	E3SM Project	Historical	r1i1p1f1	1.00º	Bader et al. (2019a)
E3SM-1-1	E3SM Project	Historical	r1i1p1f1	1.00º	Bader et al. (2019b)
EC-Earth3	EC-Earth Consortium	Historical	r10i1p1f1	1.00º	EC-Earth (2019)
EC-Earth3-AerChem	EC-Earth Consortium	Historical	r1i1p1f1	1.00º	EC-Earth (2020)
IPSL-CM6A-LR	IPSL	Historical	r22i1p1f1	1.00º	Boucher et al. (2018)

MIROC-ES2L	MIROC	Historical	r2i1p1f2	1.00º	Hajima et al. (2019)
MIROC6	MIROC	Historical	r2i1p1f1	1.00º	Tatebe & Watanabe (2018)
HadGEM3-GC31-LL	MOHC	Historical	r1i1p1f3	1.00º	Ridley et al. (2019)
UKESM1-0-LL	MOHC	Historical	r1i1p1f2	1.00º	Tang et al. (2019)
MPI-ESM1-2-HR	MPI-M	Historical	r1i1p1f1	0.45º	Jungclaus et al. (2019)
GISS-E2-1-G	NASA-GISS	Historical	r1i1p1f1	1.25º	NASA/GISS (2018)
GISS-E2-1-G-CC	NASA-GISS	Historical	r1i1p1f1	1.25º	NASA/GISS (2019)
CESM2	NCAR	Historical	r10i1p1f1	1.13º	Danabasoglu (2019b)
CESM2-WACCM	NCAR	Historical	r1i1p1f1	1.13º	Danabasoglu (2019a)
NorESM2-LM	NCC	Historical	r1i1p1f1	1.00º	Seland et al. (2019)
NorESM2-MM	NCC	Historical	r1i1p1f1	1.00º	Bentsen et al. (2019)
GFDL-CM4	NOAA-GFDL	Historical	r1i1p1f1	0.25º	Guo et al. (2018)
NESM3	NUIST	Historical	r1i1p1f1	1.00º	Cao & Wang (2019)
SAM0-UNICON	SNU	Historical	r1i1p1f1	1.13º	Park & Shin (2019)
CIESM	THU	Historical	r1i1p1f1	1.13º	(Huang, 2019)
MCM-UA-1-0	UA	Historical	r1i1p1f1	1.88º	(Stouffer, 2019)

Note. For each model, the corresponding modeling center, experiment ID, member ID, horizontal resolution, and citation are indicated. Ten out of the 32 models did not have the “r1i1p1f1” ensemble member available.

For all data sets considered in this study, we have examined statistics such as mean and trends over the full period of each data set, as well as over the years 2004-2014 which is the period of overlap among all the observations and models used.

To compare the vertical profiles from the CGCMs with observations, we have used salinity and temperature profiles from hydrographic data collected at nominally 34.5ºS in the Atlantic Ocean which will be referred to as MSM60 in the figures.

3.2.2 M_{ov}, MOC, and MHT calculations

The total freshwater and heat transports can be divided into components corresponding to different driving mechanisms of vertical and horizontal circulation in the ocean, allowing for the breakdown of these transports into barotropic (throughflow), baroclinic (overturning), and horizontal (gyre) components (Bryden & Imawaki, 2001; Caínzos et al., 2022a; Kersalé et al., 2021). In this study, we have only focused on the overturning component of freshwater transport (M_{ov}). The oceanic freshwater transport is the part of mass transport that is not saline. Its divergence can be understood as the balance of precipitation, river runoff, ice processes, and evaporation. To calculate it, the salt flux (or the non-freshwater portion of the mass transport) is constrained across the section, remaining unaffected by the strength of the freshwater divergence, given that this occurs at zero salinity. In this study, we have computed the M_{ov} as the zonally averaged vertical circulation of the salt at a specific zonal section at 34.5ºS in Sverdrup units (1 Sv = 10^9 kg/s), following McDonagh et al. (2015) and Caínzos et al. (2022a):

$$M_{ov} = -\frac{1}{S_0}\int_{-B}^{0} \rho\, \overline{v^*}(z)\langle S'(z)\rangle dz$$

where S_o is the area-weighted section average of salinity, z represents depth, $-B$ is the depth of the ocean bottom, ρ is the seawater density, $\overline{v^*}(z)$ is the meridional baroclinic ocean velocity and overbar denotes zonal integral, and $\langle S'(z)\rangle$ denotes the area-weighted zonally averaged deviations from the salinity average, S_o. Following this equation, we have also computed the Ekman contribution to the M_{ov} for the AX18-XBT sections, resulting in a mean transport of -0.03 $\pm$ 0.05 Sv within the Ekman layer. Unfortunately, due to the difficulty of consistently identifying the time-varying depth of the interface between the AABW and NADW cells across all observations and models, we have only integrated M_{ov} down to $z = -B$.

The M_{ov} is a diagnostic for basin-wide salt-advection feedback in the southern border of the Atlantic Ocean and it is widely considered an indicator for monitoring the stability of the AMOC (Bryden et al., 2011; de Vries & Weber, 2005; Dijkstra, 2007; Drijfhout et al., 2011; Gent, 2018; Liu et al., 2017; Matos et al., 2020; Rahmstorf, 1996; Weber & Drijfhout, 2007; Weijer et al., 2019). At approximately 34.5ºS, a positive value of the M_{ov} (freshwater convergence) indicates that the AMOC is importing freshwater into the Atlantic, while a negative M_{ov} value (freshwater divergence) indicates that the AMOC is exporting freshwater from the Atlantic Basin. If the AMOC shuts down or weakens dramatically, M_{ov} would weaken and be closer to zero. Then, a positive (negative) change in the M_{ov} would occasion an anomalous import of salt (freshwater) into the Atlantic Ocean and as a result, the AMOC will destabilize (establish) the AMOC off-state (Mecking et al., 2017). Therefore, a $M_{ov} > 0$ provides a monostable AMOC and, conversely, a $M_{ov} < 0$ provides a bistable AMOC (Bryden et al., 2011; Caínzos et al., 2022a; Garzoli et al., 2013; McDonagh & King, 2005; Mecking et al., 2017; Saunders & King, 1995; Stommel, 1961; Weijer et al., 1999). It is worth noting that the sign of the M_{ov} at 34.5ºS is not the only indicator for considering the multiple equilibrium regimes of the AMOC. One critical issue is that in climate models, the idealized hypothesis from Rahmstorf's (1996) box model may not be valid for the CGCM, as the collapsed AMOC has a minor strength of 3-4 Sv and induces a nonzero M_{ov} across the Atlantic basin (Liu et al., 2013). According to Dijkstra (2007), Huisman et al. (2010), and Yin & Stouffer (2007), another valuable parameter for assessing AMOC stability is the divergence of the M_{ov} between two latitudes in the North Atlantic Subtropical Gyre (i.e., 35ºS and 60ºN). Additionally, Liu & Liu (2013, 2014), suggest examining the difference between the M_{ov} across 34.5ºS and the overturning liquid freshwater transport from the Arctic to the North Atlantic Ocean as an improved divergence indicator of AMOC stability, although this is not always possible to estimate M_{ov} divergence from in situ observations. More recently, van Westen et al. (2024) demonstrated that the M_{ov} minima at 34ºS in the Atlantic coincides with the AMOC tipping point. Altogether, it's important to note that the M_{ov} at 34.5ºS consistently appears as an important term in all these studies.

The meridional mass transport by AMOC across 34.5ºS for the Atlantic Ocean is computed by zonally and vertically integrating the mass transport from the ocean's surface to its bottom, measured in Sv (e.g., Frajka-Williams et al., 2019). The intensity of the overturning, MOC, is typically defined as the maximum value in the overturning stream function in the upper cell. Thus, the strength of the MOC can be expressed as:

$$MOC = \int_{-M}^{0} \int_{x_{west}}^{x_{east}} \rho \, v \, (x, z) \, dx \, dz$$

which is integrated over depth (z) and across the section from west (x_{west}) to east (x_{east}), where ρ is the seawater density, v represents the absolute meridional velocities, and $-M$ is the depth of the maximum overturning stream function. A positive MOC indicates northward mass transport and a negative MOC suggests southward mass transport. Some estimates of the MOC from moored arrays compute the volume transport by the AMOC rather than mass transport (e.g., Chidichimo et al., 2023; Frajka-Williams et al., 2019), and these transports can be considered interchangeable.

The MHT is computed at a zonal section at latitude 34.5ºS, in Petawatts (1 PW = 10^{15} W), by using the following expression:

$$MHT = \int_{-B}^{0} \int_{x_{west}}^{x_{east}} \rho \, c_p \, \theta(x, z) \, v(x, z) \, dx \, dz$$

which is integrated over depth (z) and across the section from west (x_{west}) to east (x_{east}), where ρ is the seawater density, c_p is the heat capacity of the seawater, θ is the potential temperature, v is the absolute meridional velocities, and $-B$ is the depth of the ocean bottom. A positive value of MHT indicates northward heat transport, whereas a negative value suggests southward heat transport.

The mean and standard deviation of M_{ov}, MOC, and MHT for Argo Alt., RG Argo, OFES, GLORYS, MOM6-JRA, MOM6-MERRA, and CMIP6-mean are computed without considering seasonal variability. Therefore, we have first computed the annual mean for each year and, subsequently, the mean and standard deviation.

3.3 Results

3.3.1 XBT data analysis

The 49 AX18-XBT realizations from 2002 to 2019 have a negative mean of M_{ov} at 34.5ºS in the Atlantic Ocean of -0.15 $\pm$ 0.09 Sv (Table 3.2). Only three transects have positive M_{ov} values: September 2014, May 2016, and May 2017 (Figure 3.2a). Two of these transects, September 2014 and May 2017, followed a bowed southerly path between South America and South Africa (green lines in Figure 3.1), and as a result, sampled through different water masses and can be considered as outliers. The positive M_{ov} trends presented in Table 3.2, suggest a slightly decreasing negative M_{ov} during the full period of the AX18-XBT data at a rate of 0.0033 $\pm$ 0.0049 Sv/year, but the positive trend is not statistically different from zero. During the overlapping period among all data sets, from 2004 to 2014, AX18-XBT data similarly show a non-significant decrease (positive trend) in M_{ov}.

In addition, we have estimated the mean MOC (Figure 3.2b) and MHT (Figure 3.2c) from the AX18-XBT time series, which are 19.6 $\pm$ 2.9 Sv and 0.59 $\pm$ 0.16 PW, respectively (Table 3.2), consistent with previous estimates of northward mass and heat transport across 34.5ºS in the South Atlantic. Both MOC and MHT have been strengthening throughout the full data set at a rate of 0.1713 $\pm$ 0.1589 Sv/year and 0.0034 $\pm$ 0.0090 PW/year, respectively (the increasing trend is only significant with 95% confidence for MOC). During the overlapping period of 2004-2014, MOC and MHT also show positive trends but are not significantly different from zero.

Table 3.2. Mean, trends, and 95% Confidence Intervals (CI) for M_{ov} (Sv), MOC (Sv), and MHT (PW) derived from AX18-XBT transects nominally across 34.5ºS in the South Atlantic for two periods: full record length (2002-2019) and overlapping period among all data sets analyzed (2004-2014).

Meridional transports		**2002-2019**	**2004-2014**
M_{ov}	Mean (Sv)	-0.15±0.09	-0.16±0.09
	Trends and 95% CI (Sv/year)	0.0033±0.0049	0.0053±0.0091
MOC	Mean (Sv)	19.6±2.9	19.3±2.7
	Trends and 95% CI (Sv/year)	0.1713±0.1589	0.1677±0.2789
MHT	Mean (PW)	0.59±0.16	0.59±0.16
	Trends and 95% CI (PW/year)	0.0034±0.0090	0.0015±0.0168

Note. Trends are given in units of Sv/year for M_{ov} and MOC, and in PW/year for MHT.

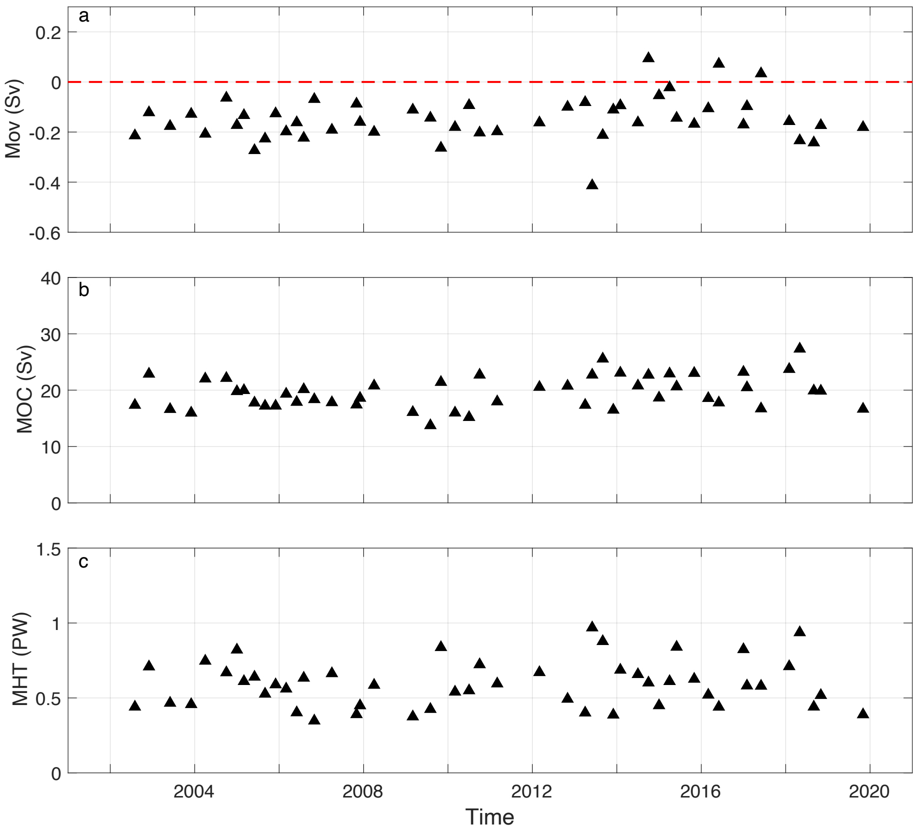

Figure 3.2. Time series of (a) M_{ov} (Sv), (b) MOC (Sv), and (c) MHT (PW) in the South Atlantic nominally across 34.5ºS from 49 AX18-XBT section estimates (black triangles) for the period 2002-2019.

3.3.2 Comparison with two Argo-derived data sets

We have similarly estimated the M_{ov} using two different Argo-derived products to complement the AX18-XBT observations (red and blue lines, respectively, in Figure 3.3a). In both Argo time series, M_{ov} is always negative. When averaged over the overlapping period (2004-2014), both Argo data sets have a negative M_{ov} mean, -0.18 $\pm$ 0.02 Sv from Argo Alt. and -0.14 $\pm$ 0.01 Sv from RG Argo, in good agreement with the AX18-XBT M_{ov} mean of -0.15 $\pm$ 0.09 Sv (Figure 3.3a and Table 3.3).

During the overlapping period of 2004-2014 among all observational and model data sets, the positive M_{ov} trends of the Argo Alt. and RG Argo time series indicate a non-significant weakening of the M_{ov}, similar to the AX18-XBT trend. However, M_{ov} trends are only significant for the full period of both Argo Alt. and RG Argo data sets. Over the full record length of Argo Alt. (1993-2022) and RG Argo (2004-2022), both data sets have weak but significant negative (increasing) M_{ov} trends.

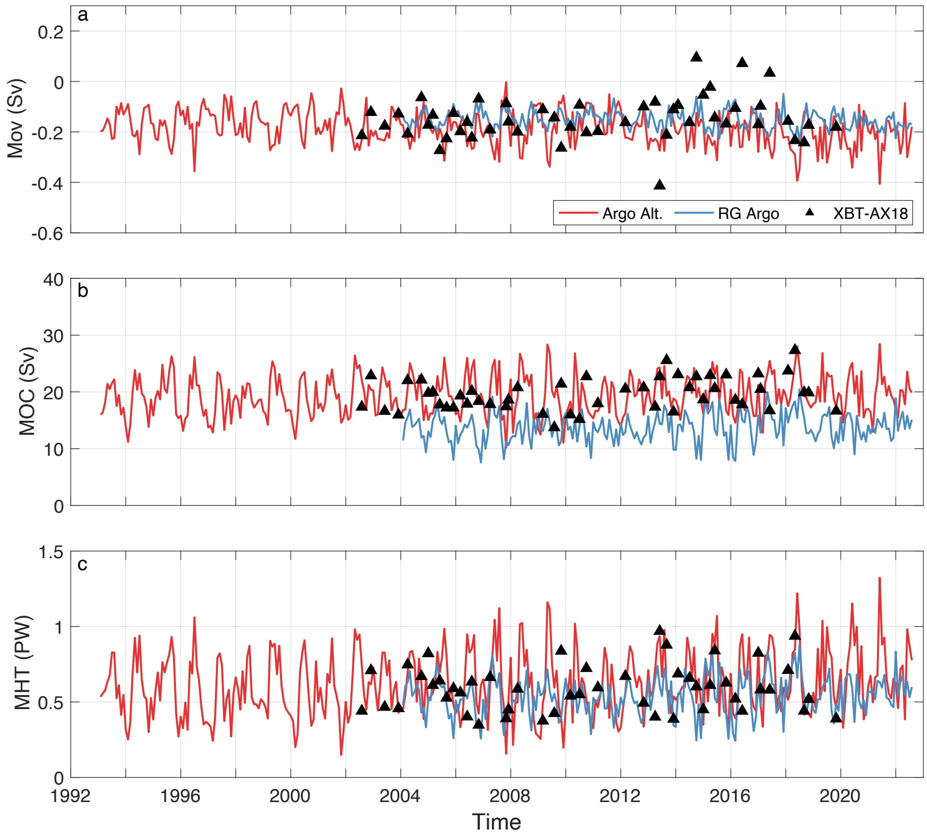

Figure 3.3. Time series of (a) M_{ov} (Sv), (b) MOC (Sv), and (c) MHT (PW) in the South Atlantic at 34.5ºS derived from observational data from AX18-XBT (black triangles), Argo Alt. (red solid line), and RG Argo (dark-blue solid line) estimates for the period 2002-2019, 1993-2022, and 2004-2022, respectively.

Table 3.3. Mean without considering seasonal variability, trends, and 95% Confidence Intervals (CI) of M_{ov} (Sv), MOC (Sv), and MHT (PW) from observational data from AX18-XBT, Argo Alt. and RG Argo nominally across 34.5ºS in the South Atlantic for two periods: full record length (AX18-XBT: 2002-2019, Argo Alt.: 1993-2022, and RG Argo: 2004-2022) and the overlapping period (2004-2014).

Meridional transports			AX18-XBT	Argo Alt.	RG Argo
M_{ov}	**Mean (Sv)**	Full record length	-0.15±0.09	-0.19±0.03	-0.15±0.01
		2004-2014	-0.16±0.09	-0.18±0.02	-0.14±0.01
	Trends and 95% CI (Sv/year)	Full record length	0.0033±0.0049	-0.0020±0.0008	-0.0011±0.0009
		2004-2014	0.0053±0.0091	0.0011±0.0035	0.0011±0.0018
MOC	**Mean (Sv)**	Full record length	19.6±2.9	19.3±0.9	13.8±0.8
		2004-2014	19.3±2.7	19.3±0.8	13.4±0.4
	Trends and 95% CI (Sv/year)	Full record length	0.1713±0.1589	0.0478±0.0421	0.0655±0.0617
		2004-2014	0.1677±0.2789	-0.0002±0.1965	-0.0262±0.1293
MHT	**Mean (PW)**	Full record length	0.59±0.16	0.62±0.05	0.54±0.04
		2004-2014	0.59±0.16	0.62±0.04	0.52±0.02
	Trends and 95% CI (PW/year)	Full record length	0.0034±0.0090	0.0041±0.0025	0.0034±0.0031
		2004-2014	0.0015±0.0168	-0.0012±0.0113	-0.0026±0.0063

Note. Trends are given in units of Sv/year for M_{ov} and MOC, and in PW/year for MHT.

The time series of MOC from Argo Alt. has a mean MOC of 19.3 $\pm$ 0.8 Sv, which is similar to the results obtained from AX18-XBT data (19.3 $\pm$ 2.7 Sv), while the RG Argo presents a significantly weaker MOC with a mean of 13.4 $\pm$ 0.4 Sv (Figure 3.3b and Table 3.3). The time series of MHT from Argo Alt. and RG Argo with a mean of 0.62 $\pm$ 0.04 PW and 0.52 $\pm$ 0.02 PW, respectively, agree with that obtained from AX18-XBT data (0.59 $\pm$ 0.16 PW) (Figure 3.3c and Table 3.3). The time series of the MOC and MHT (Figure 3.3b and c), as well as their trends, measured at 95% confidence intervals, from Argo Alt. and RG Argo data (Table 3.3), show that both meridional fluxes have been strengthening (0.0478-0.0655 Sv/year and 0.0034-0.0041 PW/year, respectively) throughout the full record of each data set. During the overlapping period, both Argo products suggest a small weakening of the MOC and MHT, which have the opposite sign from the trends estimated from XBT-derived data (Table 3.3). However, the trends for MOC and MHT are only significant for the full period of both Argo Alt. and RG Argo data sets.

3.3.3 Comparison with OGCMs and CGCMs data

Next, we have estimated the M_{ov} using different ocean and coupled numerical models: OFES, GLORYS, MOM6-JRA, MOM6-MERRA, and CMIP6 ensemble mean (hereafter CMIP6-mean), to further complement our AX18-XBT observations. The time series of M_{ov} from the OGCMs have predominantly negative values, with mean M_{ov} values of -0.11 $\pm$ 0.04 Sv for OFES and -0.09 $\pm$ 0.02 Sv for MOM6-JRA, which do not significantly differ from the AX18-XBT M_{ov} mean of -0.15 $\pm$ 0.09 Sv, except -0.03 $\pm$ 0.02 Sv for GLORYS and -0.03 $\pm$ 0.02 Sv for MOM6-MERRA2 which present lower negative M_{ov} (Figure 3.4a and Table 3.4). However, in contrast to negative M_{ov} values from observations and models mentioned above, the M_{ov} time series of the CMIP6-mean has a positive mean with a large standard deviation (0.06 $\pm$ 0.15 Sv; Figure 3.4a and Table 3.4). Consistent with the AX18-XBT data, the trends of the model time series, presented in Figure 3.4 and Table 3.4, all indicate a positive (weakening) M_{ov} trend during the overlapping period except for the CMIP6-mean. However, only the MOM-MERRA2 and CMIP6-mean have a significant trend during the overlapping period.

The time-mean MOC during the overlapping period of 17.6 $\pm$ 0.7 Sv from OFES, 19.9 $\pm$ 1.0 Sv for GLORYS, 15.9 $\pm$ 1.0 Sv for MOM6-MERRA2, and 20.4 $\pm$ 4.7 Sv for CMIP6-mean, do not significantly differ from the results obtained using AX18-XBT data (19.3 $\pm$ 2.7 Sv), except MOM6-JRA that presents a slightly weaker MOC of 15.4 $\pm$ 0.6 Sv (Figure 3.4b and Table 3.4). During the overlapping period, the time series of MOC (Figure 3.4b) and their trends, measured at 95% confidence intervals (Table 3.4), show a strengthening trend of MOC for OFES, MOM6-JRA, MOM6-MERRA2, and CMIP6-mean, which agrees with the trend obtained from AX18-XBT data. In contrast, GLORYS suggests a weakening trend in MOC. Among these results, the only significant trend in MOC is observed for MOM6-MERRA during the overlapping period.

Additionally, the time-mean MHT of 0.57 $\pm$ 0.06 PW for OFES, 0.45 $\pm$ 0.05 PW for GLORYS, 0.40 $\pm$ 0.04 PW for MOM6-JRA, and 0.59 $\pm$ 0.25 PW for CMIP6-mean, do not significantly differ from the results estimated using AX18-XBT data (0.59 $\pm$ 0.16 Sv), except MOM6-MERRA2 presenting a slightly weaker MHT of 0.35 $\pm$ 0.04 PW (Figure 3.4c and Table 3.4). However, during the overlapping period, when we examine the time series of MHT (Figure 3.4c) and their trends, measured at 95% confidence intervals, there is a discrepancy between numerical models and AX18-XBT data: the numerical models indicate a weakening trend instead of the strengthening trend shown by AX18-XBT data (Table 3.4). It's important to note that none of these trends are statistically significant.

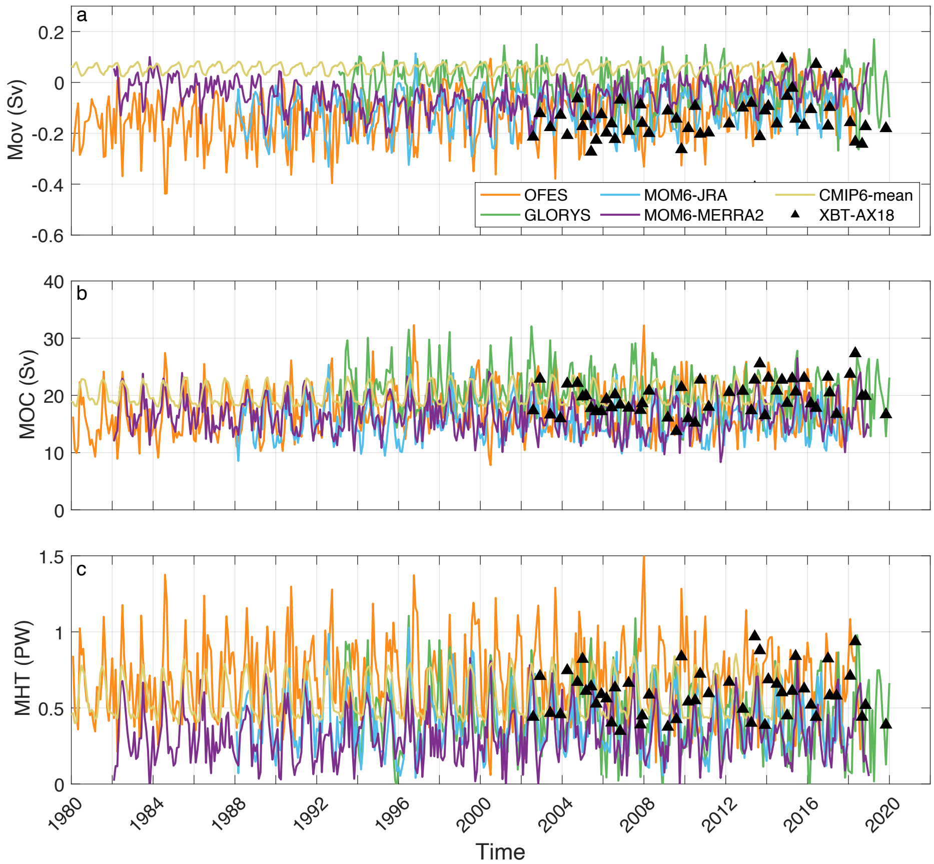

Figure 3.4. Time series of (a) M_{ov} (Sv), (b) MOC (Sv), and (c) MHT (PW) in the South Atlantic across 34.5ºS from observational AX18-XBT derived data (black triangles) and numerical modeling data from OFES (orange solid line), GLORYS (green solid line), MOM6-JRA (light-blue solid line), MOM6-MERRA2 (purple solid line), and CMIP6-mean (yellow solid line) monthly data for the period 1980-2020.

Table 3.4. Mean without considering seasonal variability, trends, and 95% Confidence Intervals (CI) for M_{ov} (Sv), MOC (Sv), and MHT (PW) from AX18-XBT derived data and numerical model data at nominally 34.5ºS in the South Atlantic for two periods: full record length (OFES: 1980-2017, GLORYS: 1993-2019, MOM6-JRA: 1988-2017, MOM6-MERRA2: 1982-2020, CMIP6-mean: 1850-2014) and the overlapping period (2004-2014).

Meridional transports			AX18-XBT	OFES	GLORYS	MOM6-JRA	MOM6-MERRA2	CMIP6-mean
M_{ov}	Mean (Sv)	Full record length	-0.15±0.09	-0.13±0.04	-0.02±0.03	-0.11±0.02	-0.05±0.03	0.05±0.14
		2004-2014	-0.16±0.09	-0.11±0.04	-0.03±0.02	-0.09±0.02	-0.03±0.02	0.06±0.15
	Trends and 95% CI (Sv/year)	Full record length	0.0033±0.0049	0.0028±0.0008	-0.0018±0.0011	0.0017±0.0008	0.0006±0.0005	0.0002±0.0000
		2004-2014	0.0053±0.0091	0.0048±0.0050	0.0007±0.0042	0.0014±0.0026	0.0034±0.0017	-0.0012±0.0011
MOC	Mean (Sv)	Full record length	19.6±2.9	17.4±1.1	20.3±1.1	15.8±0.9	16.4±0.9	19.9±4.7
		2004-2014	19.3±2.7	17.6±0.7	19.9±1.0	15.4±0.6	15.9±1.0	20.4±4.7

	Trends and 95% CI (Sv/year)	Full record length	0.1713±0.1589	0.0517±0.0328	-0.0888±0.0557	-0.0187±0.0397	-0.0107±0.0270	0.0067±0.0016
		2004-2014	0.1677±0.2789	0.0679±0.2226	-0.1742±0.2008	0.0203±0.1162	0.1471±0.1058	0.0024±0.1011
MHT	**Mean (PW)**	Full record length	0.59±0.16	0.58±0.06	0.45±0.05	0.41±0.04	0.33±0.04	0.55±0.25
		2004-2014	0.59±0.16	0.57±0.06	0.45±0.05	0.40±0.04	0.35±0.04	0.59±0.25
	Trends and 95% CI (PW/year)	Full record length	0.0034±0.0090	-0.0009±0.0010	-0.0024±0.0031	-0.0009±0.0023	0.0011±0.0016	0.0004±0.0001
		2004-2014	0.0015±0.0168	-0.0042±0.0045	-0.0077±0.0114	-0.0008±0.0070	-0.0022±0.0058	-0.0001±0.0076

Note. Trends are given in units of Sv/year for M_{ov} and MOC, and in PW/year for MHT.

3.3.4 M_{ov} in CGCMs data

To understand the disagreement between the CMIP6-mean M_{ov} and the other estimates, we examined the individual time-mean M_{ov} values from each of the 32 CMIP6 historical simulations for the periods 1850-2014 (Figure 3.5a) and 2004-2014 (Figure 3.5b). We have found that only 12 out of 32 CMIP6 models present a negative sign for M_{ov} in both periods (Figure 3.5a and b), with seven of them showing a M_{ov} mean not significantly different from the AX18-XBT M_{ov} mean for the same period (2004-2014) (Figure 3.5b).

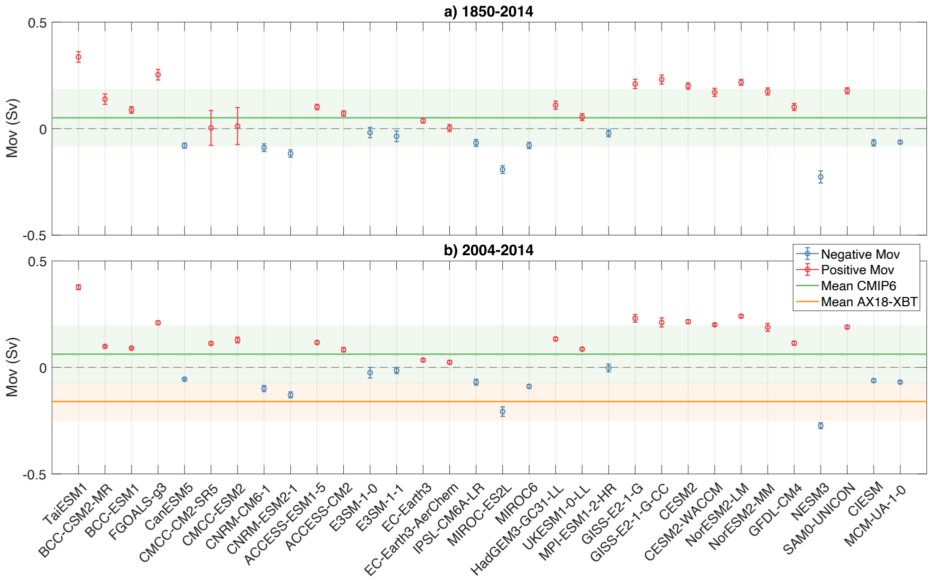

Figure 3.5. M_{ov} across 34.5ºS in the Atlantic Ocean, employing historical data from 32 CMIP6 models for the periods (a) 1850-2014 and (b) 2004-2014. Circles and error bars indicate the mean and the standard deviation of the models without considering seasonal variability, using blue and red error bars to indicate a positive or negative model mean of M_{ov}, respectively. The green solid line represents the multi-model CMIP6 M_{ov} mean with light green shading for standard deviation in both periods (a and b). The orange solid line indicates the AX18-XBT M_{ov} mean with light orange shading for standard deviation for the period 2004-2014 (b).

Next, to clarify the causes of the opposite sign of the M_{ov}, we have analyzed the different patterns in the vertical profiles of salinity, temperature, and meridional velocity across 34.5ºS from the 32 CMIP6 models (Figure 3.6). Our results show differences in salinity and velocity profiles, but only the salinity profiles exhibit a clear separation between models with positive and negative M_{ov}. Specifically, models with positive M_{ov} have clearly fresher upper and saltier deep waters compared to those with negative M_{ov} (Figure 3.6). This result is consistent with previous results from CMIP4 (Liu et al., 2014) and CMIP5 (Liu et al., 2017) models.

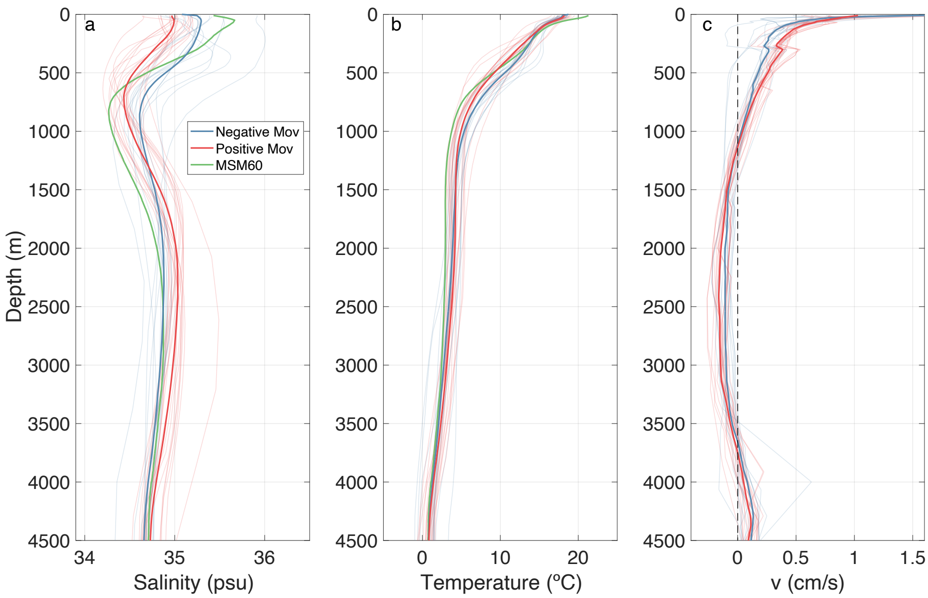

Figure 3.6. Time- and zonal-averages of vertical profiles of (a) salinity, (b) temperature, and (c) meridional velocity for the 32 CMIP6 models across 34.5ºS. Light blue and red colors indicate positive and negative model mean of M_{ov}, respectively, while solid blue/red lines represent the mean of the models with negative/positive M_{ov}. The green solid line represents the hydrographic profiles of (a) salinity and (b) temperature from MSM60 at 34.5ºS for reference.

When comparing the profiles of salinity with observations (Figure 3.6a), the observed data show saltier surface and fresher intermediate waters, more closely resembling the CMIP6 models with negative and positive M_{ov}, respectively. The salinity in the deep waters resembles the mean of the CMIP6 models with negative M_{ov}. Therefore, these findings suggest an alternate correspondence between observed and simulated salinity profiles in different water layers.

3.3.5 Covariability of the meridional fluxes

The results presented in Table 3.5 demonstrate that, from the full record length of all data sets used in this study, there is a consistent positive correlation in magnitude between the variability of MOC and M_{ov} and MHT and M_{ov}, as well as a positively correlated variability of MOC and MHT. Our analysis reveals different degrees of relationships between the South Atlantic meridional fluxes at 34.5ºS. Starting with the relationship between MOC and M_{ov}, the analysis of AX18-XBT data a weak linear relationship, with the MOC explaining only 3% of the M_{ov} variance with a linear regression slope of approximately -0.0050 $\pm$ 0.0043 Sv/Sv (positively correlated in magnitude). However, it is important to remember that there are only 49 AX18-XBT realizations. When using the Argo data sets, a stronger linear relationship is observed, with the MOC explaining 59-76% of the M_{ov} variance and linear regression slopes of about -0.0149 $\pm$ 0.0007 Sv/Sv (Argo Alt.) and -0.0123 $\pm$ 0.0005 Sv/Sv (RG Argo). Additionally, analyses using numerical models also show a moderately strong linear relationship between MOC and M_{ov}, explaining 30-74% of the variance, with regression slopes ranging from -0.0091 to -0.0195 Sv/Sv.

Table 3.5. Correlation between the South Atlantic Meridional fluxes at 34.5ºS from the full record length of observational and model-based data.

Data	**M_{ov}/MOC (Sv/Sv)**		**M_{ov}/MHT (Sv/PW)**		**MHT/MOC (PW/Sv)**	
	Slope	R^2	Slope	R^2	Slope	R^2
AX18-XBT	-0.0050 ± 0.0043	0.03	-0.2310 ± 0.0733	0.17	0.0407 ± 0.0053	0.56
Argo Alt.	-0.0149 ± 0.0007	0.59	-0.2750 ± 0.0087	0.74	0.0557 ± 0.0013	0.85
RG Argo	-0.0123 ± 0.0005	0.76	-0.4383 ± 0.0141	0.82	0.0484 ± 0.0009	0.93
OFES	-0.0174 ± 0.0002	0.52	-0.3527 ± 0.0111	0.69	0.0604 ± 0.0003	0.87
GLORYS	-0.0106 ± 0.0009	0.30	-0.3061 ± 0.0126	0.65	0.0483 ± 0.0015	0.76
MOM6-JRA	-0.0195 ± 0.0006	0.74	-0.3245 ± 0.0095	0.76	0.0560 ± 0.0009	0.92
MOM6-MERRA2	-0.0124 ± 0.0007	0.38	-0.2914 ± 0.0110	0.61	0.0525 ± 0.0011	0.83
CMIP6-mean	-0.0091 ± 0.0002	0.57	-0.1265 ± 0.0022	0.63	0.0738 ± 0.0004	0.94

Our analysis of AX18-XBT data shows a weak linear relationship between MHT and M_{ov}, with the MHT explaining only 17% of the M_{ov} variance and a linear regression slope of approximately -0.2310$\pm$0.0733 Sv/PW (positively correlated in magnitude). The linear relationship between MHT and M_{ov} is stronger in the Argo data sets, where the MHT explains 74-82% of the M_{ov} variance, with linear regression slopes of -0.2750$\pm$0.0087 Sv/PW (Argo Alt.) and -0.4383$\pm$0.0141 Sv/PW (RG Argo). Likewise, all of the numerical models exhibit a strong linear relationship between MHT and M_{ov}, explaining 61-76% of the variance, with linear regression slopes ranging from -0.1265 to -0.3527 Sv/PW.

As expected from previous studies, there is a moderately strong relationship between the MOC and MHT in the AX18-XBT data. The MOC explains 56% of the MHT variance, with a linear regression slope of about 0.0407 $\pm$ 0.0053 PW/Sv (positively correlated). The linear relationship between the MOC and MHT is even stronger in the Argo data sets, where the MOC explains 85-93% of the MHT variance, with linear regression slopes of 0.0557 $\pm$ 0.0013 PW/Sv (Argo Alt.) and 0.0484 $\pm$ 0.0009 PW/Sv (RG Argo). Similarly, all of the numerical models exhibit a strong linear relationship between MOC and MHT, explaining 76-94% of the variance, with linear regression slopes ranging from 0.0483 to 0.0738 PW/Sv.

In summary, our analysis reveals a modest linear (positively correlated in magnitude) relationship between MOC and M_{ov}, a stronger linear (positively correlated in magnitude) dependence between MHT and M_{ov}, and an even stronger linear relationship (positively correlated) between MOC and MHT derived from the data sets used. Most of the correlations exhibit moderately high R^2 values, indicating a linear relationship between these South Atlantic meridional fluxes at 34.5ºS (Table 3.5), suggesting that an increase in M_{ov} corresponds to an increase in MOC and MHT. The strengthened MOC increases the northward transport of warm surface waters, thereby increasing MHT (positively correlated). Conversely, the positively correlated M_{ov}/MOC relationship in magnitude takes into account that a weakening of MOC reduces the transport of salty surface waters from the South Atlantic to the North Atlantic. This reduction contributes to the accumulation of freshwater and lighter surface waters in the subpolar North Atlantic, hindering the sinking process and further contributing to AMOC weakening.

3.3.6 Seasonal variability of the meridional fluxes

Figure 3.7 illustrates the seasonal variability of M_{ov} (first column), MOC (second column), and MHT (third column) in the Atlantic Ocean at nominally 34.5ºS using observational and numerical model data. It is worth noticing the difficulty in inferring the seasonal variability of the South Atlantic meridional fluxes with the AX18-XBT data due to their limited sample size for some months (only February, March, May, October, and November have more than four samples), (Figure 3.7a-c). OFES does not show strong seasonal variability in any of the South Atlantic meridional fluxes (Figure 3.7j-l). The other data sets have similar seasonal cycles for M_{ov}, MOC, and MHT, with stronger negative M_{ov} values and stronger positive MOC and MHT values observed during late austral autumn and winter months, specifically from April to August.

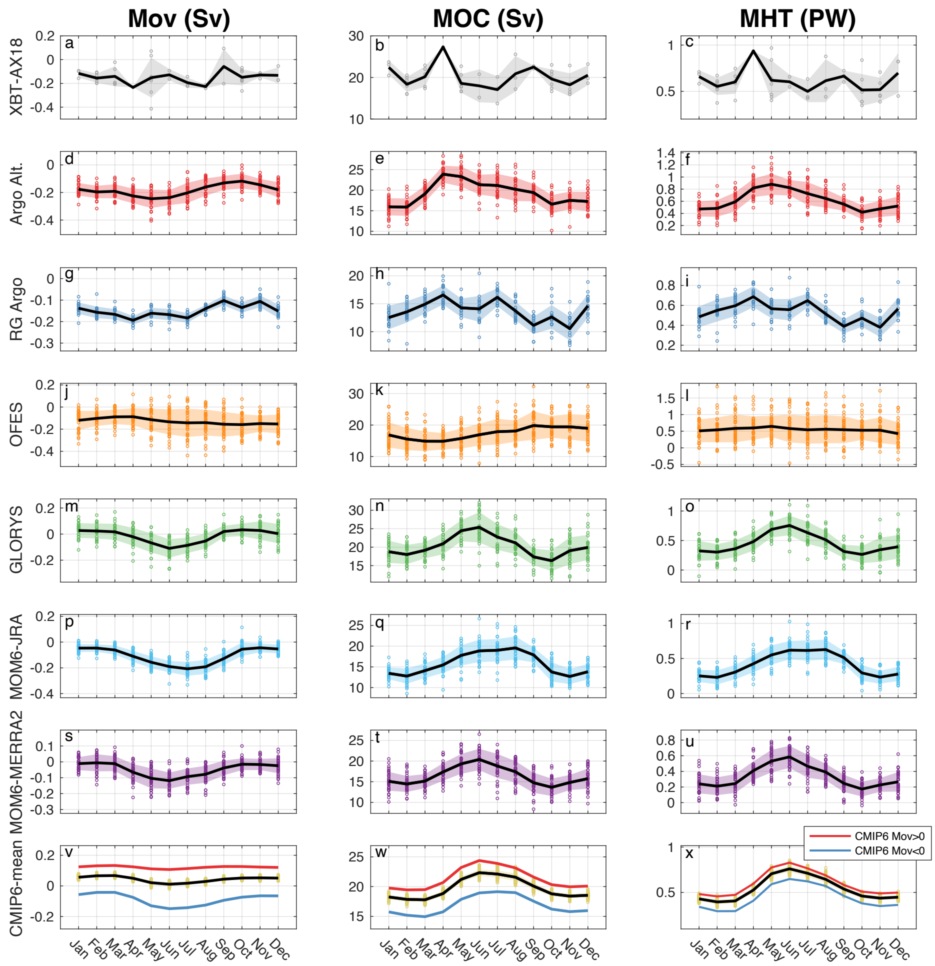

Figure 3.7. Seasonal variability of M_{ov} (Sv), MOC (Sv), and MHT (PW) derived from the full record length of observational and numerical model data across 34.5ºS in the Atlantic Ocean for the different data sets indicated on the y-axis. The circles correspond to the meridional flux values for each month in the period of the corresponding data set. The black solid line connects the mean meridional flux value for each month, averaged by the different years with the standard deviation of each month included in a light color. The data sets used are AX18-XBT (a–c), Argo Alt. (d–f), RG Argo (g–i), OFES (j–l), GLORYS (m–o), MOM6-JRA (p–r), MOM6-MERRA2 (s–u), and CMIP6-mean (v–x), we have also included the mean values of the CMIP6 models that estimate $M_{ov} > 0$ in red and $M_{ov} < 0$ in blue.

These findings support the previously described covariability between the South Atlantic meridional fluxes discussed in Section 3.3.4. Note that the CMIP6-mean M_{ov} values remain positive throughout most of the year. However, when we examine the average seasonal variability of the CMIP6 models with positive M_{ov} (20 CMIP6 models) versus those with negative M_{ov} mean (12 CMIP6 models), the results indicate that M_{ov} exhibits stronger seasonal variability for CMIP6 models with $M_{ov} < 0$. Additionally, on average the CMIP6 models with a positive M_{ov} mean have stronger MOC and MHT values during all months.

3.4 Discussion and Conclusions

In this study, we use high-density AX18-XBT data along with Argo float-derived data sets and numerical model data to conduct a multi-data set analysis of M_{ov}, as well as MOC and MHT in the South Atlantic Ocean at 34.5ºS. Through our updated AX18-XBT data analysis, an 18-year time series of the South Atlantic meridional fluxes is generated, which are then compared with data from Argo Alt., RG Argo, OFES, GLORYS, MOM6-JRA, MOM6-MERRA2, and 32 CMIP6 models. Our comparison is aimed at determining the consistency between the observational and modeling data in the South Atlantic region, as well as investigating the correlation and seasonal variability of the South Atlantic meridional fluxes.

The stability of the MOC is assessed in this study by estimating the meridional freshwater flux (M_{ov}) at 34.5ºS in the Atlantic Ocean. This flux is crucial in determining the basin-scale MOC salt feedback because it regulates the amount of freshwater entering the basin, thereby influencing the salt concentration and density of the water. The M_{ov} results obtained during the overlapping period from AX18-XBT sections, as well as from monthly data of Argo Alt., RG Argo, OFES, MOM6-JRA, and CMIP6-mean are not significantly different. However, GLORYS and MOM6-MERRA present lower M_{ov} negative values. The observations consistently show a negative M_{ov} with a mean value from AX18-XBT of -0.16 $\pm$ 0.09 Sv, as well as the other mean estimates of [-0.03 to -0.18] from Argo float-derived data and OGCMs. In contrast, only the CMIP6 ensemble has a positive M_{ov} with a mean value of 0.06 $\pm$ 0.15 Sv. The negative M_{ov} values observed at approximately 34.5ºS in the Atlantic Ocean indicate that the AMOC transports freshwater toward the south, which requires a net inflow of freshwater north of 34.5ºS to maintain the salinity associated with the overturning circulation. Therefore, our study suggests that the AMOC is currently in a bistable regime and could collapse if a large enough freshwater perturbation occurs (Rahmstorf, 1996). In addition to freshwater perturbation, Liu et al. (2017) showed that the bistable AMOC can collapse under double CO_2 warming. Our XBT-derived mean is consistent with prior studies that employed observational data to demonstrate the export of freshwater [-0.08 Sv to -0.34 Sv] from the Atlantic Ocean through its southern boundary by the overturning circulation Bryden et al. (2011), McDonagh & King (2005), Garzoli et al. (2013), Caínzos et al. (2022a), Weijer et al. (1999), and Huisman et al. (2010). In contrast, Caínzos et al. (2022a) estimated from observations an inconclusive M_{ov} result of 0.0 $\pm$ 0.02 Sv, hence indicating that the AMOC is not exporting enough freshwater from the Atlantic Ocean. As mentioned, the negative M_{ov} derived from AX18-XBT data differs from the CMIP6-mean results providing $M_{ov} > 0$. This $M_{ov} > 0$ CMIP6-mean result agrees with previous model-based estimates in the South Atlantic of [0.09-0.18 Sv] by Drijfhout et al. (2011) and Mecking et al. (2017), as well as from a range of 0.24 to -0.11 Sv at 33ºS estimated by de Vries & Weber

(2005). In addition, our study analyzed trends of M_{ov}, measured at 95% confidence intervals, and found a positive (decreasing) trend during the overlapping period in all models except the multi-model CMIP6-mean. It is important to note that the interannual variability is highly dependent on the data set and period used, mostly exhibiting non-significant trends during the overlapping period. Therefore, based on the trends measured at 95% confidence intervals from the data sets used in our study, we cannot definitively determine whether the M_{ov} has been decreasing or increasing its negative value over time.

We find that only 12 out of 32 CMIP6 models exhibited a negative M_{ov} mean value. It is well-known that there is a positive salinity bias in several current generations of CGCMs at nominally 34.5ºS in the South Atlantic Ocean, as found using data from CMIP3 models by Liu et al. (2014), CMIP4 models by Mecking et al. (2017), and CMIP5 models by Weijer et al. (2019) and Liu et al. (2017) in the same region. Our analysis of vertical salinity profiles has identified a clear differentiation between CMIP6 models presenting positive and negative M_{ov} values. Models with positive M_{ov} values have fresher upper and saltier deep waters than those with negative M_{ov} values, suggesting that the salinity structure may play a role in determining the sign of M_{ov}. We have attempted to understand the differences among these models by conducting calculations in three specific sections (a zonal section at 34.5ºS, and two meridional sections at Drake Passage and south of South Africa). These calculations included computing the freshwater flux through each section, the evaporation minus precipitation within the enclosed region, and the overall salinity transport and its divergence (not shown). Despite our efforts, we have not identified any specific patterns or behaviors in the respective fluxes that can explain the differences in M_{ov}'s sign.

We have estimated that the strength of MOC at nominally 34.5ºS, using AX18-XBT data during the overlapping period (2004-2014), is 19.3 $\pm$ 2.7 Sv. This value is consistent with our estimates of [15.9-20.4 Sv] using Argo Alt., OFES, GLORYS, MOM6-MERRA2, and CMIP6-mean data sets. Nevertheless, we have estimated a slightly weaker MOC of 15.4 $\pm$ 0.6 Sv from MOM6-JRA, and a significantly weaker MOC of 13.4 $\pm$ 0.4 Sv when using RG Argo data compared to the AX18-XBT result. Our estimate of the strength of MOC at nominally 34.5ºS using AX18-XBT data is also consistent with previous observational and model estimates of [14.7-20.7 Sv] by Manta et al. (2021), Kersalé et al. (2021), Meinen et al. (2018), Perez et al. (2011), Dong et al. (2011, 2015), Majumder et al. (2016), Garzoli et al. (2013), as well as Weijer et al. (2020). However, our AX18-XBT mean result shows a stronger MOC than the 14.8 $\pm$ 1.0 Sv estimated by Arumí-Planas et al. (2023).

The significantly weaker MOC estimated with RG Argo compared to AX18-XBT data could be explained by the absence of Argo data in the regions shallower than 2,000 m depth near the east and west coasts, as well as the uneven distribution of Argo data in space and time. Argo floats provide discrete profiles at specific locations and times, which can introduce sampling errors when interpolated. Additionally, Argo float data may have biases in the measurements of ocean properties, such as temperature and salinity, that can affect the estimation of transports (Roemmich & Gilson, 2009). However, this is not the case with the Argo Alt. product, which combines temperature and salinity profiles from Argo floats with monthly satellite altimetry SLA, reducing the underestimation of MOC.

Our estimate of MHT from the AX18-XBT transect data, which is 0.59 ± 0.16 PW, establishes that the South Atlantic Ocean transports heat northward. This result is consistent with mean MHT estimates of [0.40-0.62 PW] from Argo Alt., RG Argo, OFES, GLORYS, MOM6-JRA, and CMIP6-mean. However, MOM6-MERRA presents a lower MHT of 0.35 $\pm$ 0.04 PW compared to the AX18-XBT result. These findings align with previously published observational studies, presenting [0.49-0.55 PW] by Garzoli & Baringer (2007), Dong et al. (2009, 2015), Garzoli et al. (2013), and Kersalé et al. (2021), as well as previous studies using numerical model data of [0.38-0.42 PW] by Perez et al. (2011) and Dong et al. (2011). Therefore, our estimates of MOC and MHT are consistent with earlier estimates obtained by models and observations in the South Atlantic at 34.5ºS, demonstrating the robustness of those earlier estimates of MOC strength of $\approx$19 Sv and northward MHT of $\approx$0.60 PW. We have also analyzed time series trends measured at 95% confidence intervals and found that MOC and MHT have been strengthening using AX18-XBT data for both the full data set period and the overlapping period. While OFES, MOM6-JRA, MOM6-MERRA2, and CMIP6-mean show strengthening trends in MOC during the overlapping period, which agrees with the AX18-XBT data, Argo Alt., RG Argo and GLORYS suggest a weakening, consistent with RAPID array's findings at 26ºN (Frajka-Williams et al., 2019). However, Frajka-Williams et al. (2019) reported different trends across latitudes in the Atlantic Ocean from 2004 to 2017, noting strengthening and weakening trends in MOC at 16ºN and 26ºN, respectively. The study highlighted latitudinal dependence in AMOC variability and suggests that comparisons between results at 34.5ºS and 26ºN are challenging. It's essential to emphasize that, among these data sets, only MOM6-MERRA presents a significant trend in MOC during the overlapping period. For MHT, Argo data sets, OGCMs, and CGCMs indicate a non-significant weakening trend during the overlapping period instead of the strengthening MHT obtained using AX18-XBT data.

Based on our estimates, we have examined the correlation between M_{ov}/MOC, M_{ov}/MHT, and MHT/MOC across 34.5ºS in the South Atlantic Ocean. We found a linear relationship between the variability of these South Atlantic meridional fluxes, estimating a negative linear regression slope between M_{ov}/MOC and M_{ov}/MHT (positively correlated in magnitude), and a positive slope between MHT/MOC (positively correlated). Our analysis reveals different degrees of relationships between MOC and M_{ov}: AX18-XBT data shows a weak linear relationship, explaining only 3% of the M_{ov} variance with a linear regression slope of approximately -0.0050 $\pm$ 0.0043 Sv/Sv; Argo data sets explain 59-76% of the variance, with linear regression slopes from -0.0149 to -0.0123 Sv/Sv; and numerical models explain 30-74% of the variance, with slopes ranging from -0.0091 to -0.0195 Sv/Sv. Similarly, we found a linear relationship between MHT and M_{ov} with AX18-XBT data explaining only 17% of the M_{ov} variance with a linear regression slope of -0.2310 $\pm$ 0.0733 Sv/PW; Argo data sets explain 74-82% with linear regression slopes from -0.2750 to -0.4383 Sv/PW; and numerical models explain 61-76% of the variance, with linear regression slopes ranging from -0.1265 to -0.3527 Sv/PW. Finally, the relationship between MOC and MHT derived from the AX18-XBT data explain 56% of the MHT variance, with a slope of about 0.0407 $\pm$ 0.0053 PW/Sv; Argo data sets explain 85-93% of the variance, with slopes of 0.0484-0.0557 PW/Sv; and numerical models explain 76-94% of the variance, with slopes ranging from 0.0483 to 0.0738 PW/Sv. This finding is consistent with the previous results of the correlated variability between MOC and MHT with a slope of

≈0.05 PW/Sv from observations and models at nominally 34.5ºS in the South Atlantic Ocean (Dong et al., 2009, 2011; Perez et al., 2011). Therefore, the linear regressions suggest that a higher M_{ov} corresponds to a higher MOC and MHT.

The positive relationship between MOC and MHT can be explained by the fact that a strengthening of MOC, which carries warm surface waters northward, results in an increase of MHT due to the associated increased transport of warm surface waters. However, the positive correlation in magnitude between MOC and M_{ov} is more complex. This relationship can be explained by the fact that as the AMOC weakens, the transport of salty surface waters from the South Atlantic to the North Atlantic decreases. Within the subpolar North Atlantic, these waters undergo cooling, densification, and subsequent sinking to deeper layers before flowing southward. Consequently, the weakened AMOC contributes to the accumulation of less saline surface waters in the subpolar North Atlantic. This reduced transport in the upper layers by the AMOC may exert an influence on the density of surface waters, hindering the sinking process in the North Atlantic and thereby exacerbating the overall weakening of the AMOC.

The lower R^2 values obtained from the AX18-XBT data may be attributed to the small sample size of the data set, as well as to the inherent limitations of the XBT data. XBTs do not directly measure salinity or velocity, which can introduce errors and limitations in capturing the complete picture of ocean circulation. Due to changes in the orientation of the shipping routes, the AX18-XBT lines are not always across fixed latitudes, which could also influence the relationships of M_{ov}/MHT with AMOC. The higher R^2 values obtained from the numerical models can be explained by the fact that these models are based on physical equations and incorporate various data sets and parameterizations, allowing them to capture complex interactions and processes that might not be fully captured by the limited observations from AX18-XBT data. This results in a stronger linear relationship between M_{ov}/MOC, M_{ov}/MHT and MHT/MOC when using numerical models.

The time series of the South Atlantic meridional fluxes exhibit significant interannual variability from all data sets used in our study. Across almost all of the observational and numerical model data sets, the seasonal cycle in M_{ov}, MOC, and MHT, vary such that there are minima in M_{ov} (largest negative values relative to the mean) and maxima in MOC and MHT (largest positive values relative to the mean) from late austral autumn to winter, specifically from April to August, which agrees with the seasonal variability previously reported by Dong et al. (2009). Nevertheless, we cannot infer the seasonal cycle from the AX18-XBT data due to limited sampling, as the transect is only sampled every 3 months, and the data for some months are limited. Specifically, we only have more than four samples available for February, March, May, October, and November. Additionally, sampling aliasing in space and time may influence the XBT data, as the mean latitude of each AX18 transect varies between 30ºS and 35ºS (Figure 3.1, Dong et al., 2014).

In conclusion, this study improves our understanding of the variability of freshwater transport by the Atlantic Meridional Overturning Circulation and its impact on the global climate system. The M_{ov} findings from observational data, ocean models, and some coupled climate models considered here suggest a bistable regime of the meridional overturning circulation according to a simple conceptual model and a global circulation model (Rahmstorf, 1996). Additionally, this study highlights the different salinity structures for CMIP6 models with positive M_{ov} mean, indicating that the salinity biases may be responsible for the opposite sign of M_{ov}. Specifically, models with positive M_{ov} values show fresher upper and deeper saltier waters compared to those estimating negative M_{ov} values. Therefore, we emphasize the need for refining CMIP6 model representations, specifically the salinity bias, to enhance the reliability of AMOC projections in CMIP6 models, especially given the significant implications for IPCC risk analyses. Finally, our results demonstrate that seasonal variability of the data sets provides a coherent picture of the concomitant variability and correlation of the South Atlantic meridional fluxes at 34.5ºS: M_{ov} is positively correlated in magnitude to MOC and MHT, and MOC is positively correlated to MHT, presenting higher negative M_{ov} values and higher positive MOC/MHT transports from April to August.

Chapter 4

Variability in the meridional overturning circulation at 32ºS in the Pacific Ocean diagnosed by inverse box models

Chapter published at:

Arumí-Planas, C., Hernández-Guerra, A., Caínzos, V., Vélez-Belchí, P., Farneti, R., Mazloff, M. R., Mecking, S., Rosso, I., Schulze Chretien, L. M., Speer, K. G. & Talley, L. D (2022). Variability in the meridional overturning circulation at 32ºS in the Pacific Ocean diagnosed by inverse box models. *Progress in Oceanography, 203, 102780.* https://doi.org/10.1016/j.pocean.2022.102780

4.1 Introduction

The World Ocean Circulation Experiment (WOCE) was a global oceanographic research program carried out in the 1990s, which assessed every ocean basin with high-quality hydrographic data, from transoceanic zonal and meridional sections of closely spaced stations. The results from this study allowed estimation of the oceanic transports of mass, heat, freshwater and other properties from the sea surface to the seafloor of every ocean (Chapman, 1998; Ganachaud, 2003; Ganachaud & Wunsch, 2000; Macdonald & Wunsch, 1996). As summarized by Gordon (1986) and Schmitz (1995), the general features of the ocean's global overturning predate WOCE. However, the newly-developed approach of inverse modeling along with the newly collected data, allowed an improved, internally consistent, quantification of global transports (Roemmich & Wunsch, 1985; Wunsch, 1996). From these data, a clear picture of the Meridional Overturning Circulation (MOC) emerged, which is a variable-in-time three dimensional system joining all the ocean basins (Gordon, 1986; Lumpkin & Speer, 2007; Talley, 2003). Therefore, the next step consists of estimating how the property transports and patterns of circulation change over time. In order to accomplish this purpose, repeated hydrographic sections in key latitudes and longitudes have been carried out in the framework of the Global Ocean Ship-Based Hydrographic Investigation Program (GO-SHIP) (www.go-ship.org). Sampling of different ocean properties (including temperature, salinity, nutrients and oxygen) are collected by high accuracy measurements from the surface to the bottom of the ocean with an approximate decadal base, with a spatial resolution according to the internal Rossby radius, and sections that extend from coast to coast or enclose regions. In addition, an inverse method is used to estimate the ocean circulation and property transports from closed hydrographic sections of every ocean (Casanova-Masjoan et al., 2018; Hernández-Guerra et al., 2005, 2010, 2014, 2017, 2019; Hernández-Guerra & Talley, 2016; Pérez-Hernández et al., 2013).

This study is centered at 32ºS in the South Pacific Ocean, where the boundary currents in the thermocline layers of the subtropical gyre are the East Australian Current (EAC) in the western boundary, and a set of eastern boundary flows alternating in the north/south direction: the equatorward Peru-Chile Current and the poleward Peru-Chile Undercurrent. The EAC is the intense western boundary current flowing along the east Australian shelf break and slope as part of the anticyclonic circulation of the south Pacific gyre (Hamon & Tranter, 1971; Tomczak & Godfrey, 1994). The presence of New Zealand, near 34ºS, distorts the circulation in the southern limb (Godfrey, 1989), causing the EAC to separate from the Australian coast and to flow eastward, with its southern boundary forming a strongly eddying feature: the Tasman Front (Mulhearn, 1987). The Peru-Chile Current is the wide eastern boundary current, flowing northward along the upper waters off the west coast of South America. The Peru-Chile Undercurrent is a subsurface current flowing poleward over the slope along the Peruvian and Chilean coasts (Strub et al., 1998). The Indonesian Throughflow (ITF) is the main gateway of upper layer waters from the Pacific Ocean transported westward into the surface waters of the Indian Ocean (Hernández-Guerra & Talley, 2016).

The main goal of this work is to extend a previous study of the Pacific Ocean at 32ºS carried out by Hernández-Guerra & Talley (2016), which was focused on the 2003 and 2009 sections, as well as to estimate the changes of the ocean circulation across different decades, by analyzing and comparing hydrographic data collected in 1992 and in 2017, together with those in 2003 and 2009. Furthermore, an attempt to infer the dynamical forcing causing the change in ocean circulation is carried out. To accomplish these goals, Section 4.2 presents the hydrographic and numerical model data used in this study. Section 4.3 exhibits the vertical sections of the different ocean properties to describe the main water masses present at 32ºS. Next, Section 4.4 describes the geostrophic transport relative to the reference level, followed by the characteristics of the inverse model. The final mass and silicate transports obtained after applying the inverse model are described in Section 4.5, including the estimate of the meridional overturning circulation and its change in time. Section 4.6 describes the horizontal circulation focusing on the upper, deep, and abyssal layers with a specific study of the EAC and the Peru-Chile Current and Undercurrent. Section 4.7 shows a comparison between the hydrographic data and output of numerical model data with the aim of studying if the circulation changes are reproduced by these models. Section 4.8 presents the Sea Surface Height Anomaly (SSHA) and Rossby wave dynamics as responsible of the circulation variability at 30ºS in the South Pacific Ocean. Section 4.9 shows the temperature and freshwater transports for the four hydrographic realizations, and finally, a discussion with the conclusive remarks is provided in Section 4.10.

4.2 Hydrographic and Numerical Model Data

Hydrographic data collected in 1992 (02/05-13/07) and 2017 (03/07-30/09) over the entire water column at stations along section P06 at nominally 32ºS in the South Pacific Ocean area added to the surveys done in 2003 (03/08-16/10) and 2009 (21/11-10/02) (Figure 4.1). Previous studies carried out by Ganachaud (2003) and Hernández-Guerra & Talley (2016) have already analyzed the data compiled in 1992, and 2003 and 2009, respectively. In this study, we have again processed and analyzed the 1992 data. All these data were collected as part of the WOCE and GO-SHIP (Talley et al., 2016), and are publicly available through the CLIVAR and Carbon Hydrographic Data Office (CCHDO, http://cchdo.ucsd.edu) (Table 4.1).

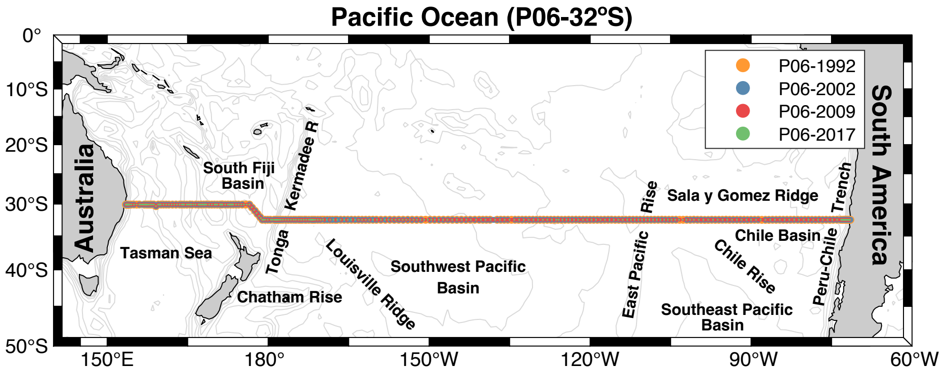

Figure 4.1. Station positions for P06 cruises carried out at nominally 32ºS in the Pacific Ocean in 1992, 2003, 2009, and 2017.

Additionally, SADCP data for 2017, collected using a 38 kHz narrowband RDI system were used for geostrophic velocity referencing, complemented by some LADCP station profiles. A system formed by an upward-looking (300 kHz) and a downward-looking (150 kHz) LADCP was used to provide a velocity profile from the surface to the bottom of the ocean at each station. The LADCP data were processed using the LDEO Matlab package, using the bottom-track (BT) and ship-drift (GSP) constraints and blending the SADCP data with LADCP data (https://currents.soest.hawaii.edu/go-ship/ladcp_rst_2015-

2018/2017_P06_ancillary-data.html#ancillary-data-2017-p06). Figure 4.3 shows the velocity profiles of LADCP and SADCP, which sometimes don't match. This profile of SADCP is computed as the average velocity from one station to the next station, while the SADCP used to compute the LADCP velocities are the SADCP in each hydrographic station. As geostrophy integrates the velocity between stations, LADCP velocities on each station fail to resolve the horizontal sampling due to the fact that they are located in each station and not in the middle as geostrophic velocity is calculated. However, the continuous underway SADCP data set can be used to average between stations, so it matches the integration in geostrophy (E. Firing, personal communication). For this reason, SADCP data are expected to be a more useful tool to estimate the velocity at the reference level.

We complement our hydrographic data with simulations from a set of ocean models, as follows.

The Geophysical Fluid Dynamics Laboratory (GFDL) OM4 ocean/sea ice model is used (Adcroft et al., 2019). The ocean component of OM4 uses version 6 of the Modular Ocean Model (MOM, hereafter) and has a nominal 0.25° horizontal spacing with no mesoscale eddy parameterization and 50 vertical levels. The dynamical core of MOM is based on the hydrostatic primitive equations formulated in their generalized vertical coordinate form. MOM was forced with the JRA55-do atmospheric reanalysis product (Tsujino et al., 2020) over the years 1958-2018 and monthly averages were stored for the entire length of the simulation.

Table 4.1. Hydrographic cruise information. All CTD data are available online from the CLIVAR and Carbon Hydrographic Data Office (CCHDO, http://cchdo.ucsd.edu/). In 2017, LADCP and SADCP data for P06-West and P06-East are available online from the CLIVAR archive https://usgoship.ucsd.edu/cruise-data-submit-download/.

Cruise	Dates	No. stations	CCHDO Expocode	Ship	Chief scientist
P06-East	1992-05-02 to 1992-05-26	69	316N138_3	KNORR	H. L. Bryden (Woods Hole Oceanographic Institution, Woods Hole, MA 02543, USA)
P06-Center	1992-05-30 to 1992-07-07	114	316N138_4	KNORR	M. McCartney (Woods Hole Oceanographic Institution, Woods Hole, MA 02543, USA)
P06-West	1992-07-13 to 1992-07-30	78	316N138_5	KNORR	J. Toole (Woods Hole Oceanographic Institution, Woods Hole, MA 02543, USA)
P06-West	2017-07-03 to 2017-08-17	143	320620170703	Nathaniel B. Palmer	S. Mecking (Applied Physics Laboratory, University of Washington, USA)
P06-East	2017-08-20 to 2017-09-30	107	320620170820	Nathaniel B. Palmer	K. Speer (Department of Oceanography, The Florida State University, USA)

ECCOv4r3 (Estimating the Circulation and Climate of the Ocean Version 4 Release 3; ECCO, hereafter) is a data-assimilating model produced by the Jet Propulsion Laboratory. ECCOv4r3 includes monthly data of the state of ocean's evolution over time for the period 1992-2015 with a nominal 1º horizontal resolution configuration of the MIT general circulation model over the entire globe (Forget et al., 2015; Fukumori et al., 2017).

The Southern Ocean State Estimate (SOSE) is a sea ice-ocean data-assimilating model developed at the Scripps Institution of Oceanography which provides a monthly gridded dataset at 1/6º horizontal resolution for the period 2005-2010. While this model does not come with explicit uncertainty estimates, the major biases are well documented and include too-shallow pycnocline in the subpolar gyres and too broad of a range in mixed-layer depth (Mazloff & National Center for Atmospheric Research Staff (Eds.). 2016).

The CMEMS (Copernicus Marine Environment Monitoring Service) ocean model GLORYS12V1 (Global Ocean Physics Reanalysis; GLORYS, hereafter) is a global ocean reanalysis at eddy-resolving resolution describing ocean circulation, including forcing by satellite altimetry measurements of sea level from the period 1993-2019. It is based on the current real-time global forecasting CMEMS system. The model hydrodynamics are based on NEMO (Nucleus for European Modelling of the Ocean). In situ observations are assimilated from CORA4 database, and atmospheric forcing from ERA-Interim data. Furthermore, altimeter data (sea level anomaly), satellite sea surface temperature, sea ice concentration, and in situ temperature and salinity vertical profiles are jointly assimilated. The monthly gridded datasets are displayed on a standard regular grid at 1/12° (~ 8 km) and on 50 standard levels (Drévillon et al., 2018).

In summary, three of the models used (ECCO, SOSE and GLORYS) are data-assimilating models spanning from coarse to eddy-permitting horizontal resolution (1º, 1/6º and 1/12º), and the fourth one (MOM) is a free-running model with a relatively high horizontal resolution (1/4º). Also, the models have been run over different periods of time with at least two model outputs available for each P06 occupation. Monthly data over the entire water column along 30ºS in the South Pacific Ocean for June 1992 (MOM and ECCO), September 2003 (MOM, ECCO, and GLORYS), January 2010 (MOM, ECCO, SOSE, and GLORYS), and August 2017 (MOM and GLORYS) are compared with the mass transports from hydrographic data after the inverse model is applied. The latitude chosen for the models is 30ºS in order to match the western part of the P06 section. With this choice, the EAC is better represented and there are no major changes between the circulation in the ocean interior between 30ºS and 32ºS.

4.3 Vertical Sections and Water Masses

Transpacific vertical sections of potential temperature, salinity, neutral density γ^n (Jackett & McDougall, 1997), oxygen and silicate at the P06 nominal latitude of 32ºS are used to identify the existing water masses in the South Pacific Ocean (Figure 4.2), following Talley et al. (2011). Figure 4.2 shows the labels of the water masses.

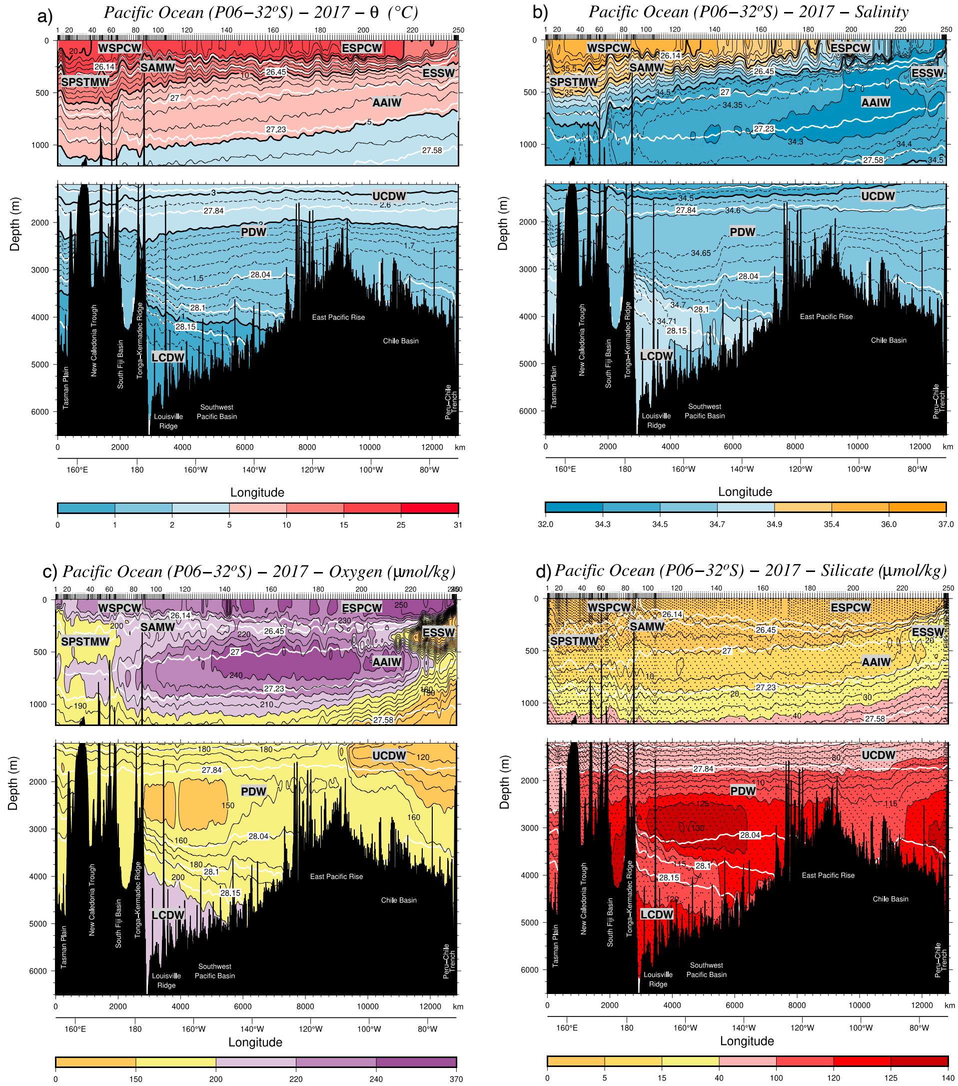

Figure 4.2. Vertical sections of (a) θ (ºC), (b) salinity, (c) oxygen (μmol/kg), and (d) silicate (μmol/kg) at 32ºS in the Pacific Ocean for data collected in 2017. The water masses identified are: Eastern South Pacific Central Water (ESPCW), Western South Pacific Central Water (WSPCW), South Pacific Subtropical Mode Water (SPSTMW), Equatorial Subsurface Water (ESSW), Subantarctic Mode Water (SAMW), Antarctic Intermediate Water (AAIW), Upper Circumpolar Deep Water (UCDW), Pacific Deep Water (PDW), and Lower Circumpolar Deep Water (LCDW). Tick-marks on the top axis indicate the location of stations. The isoneutrals labeled (white lines) are the γ^n layers used to estimate the geostrophic transport.

In the upper layer, between the surface and γ^n = 26.45 kg/m^3 (above ~200 m depth) the South Pacific Central Water (SPCW) is found with relatively high potential temperature (>15ºC, Figure 4.2a), relatively high salinity (>34.5, Figure 4.2b) and high dissolved oxygen and low silicate values (>220 µmol/kg and <2 µmol/kg, Figure 4.2c and d respectively). This water mass is characterized by subtropical thermocline waters formed by subduction (Talley et al., 2011). The SPCW can be divided into two different water masses: Western South Pacific Central Water (WSPCW) and Eastern South Pacific Central Water (ESPCW). The WSPCW (S > 35.5 and dissolved oxygen ~230 µmol/kg) is separated from the eastern boundary by the fresher ESPCW (34.5 < S < 35 and dissolved oxygen ~230-250 µmol/kg) (Emery, 2001; Emery & Meincke, 1986; Sprintall & Tomczak, 1993).

In the western boundary, the South Pacific Subtropical Mode Water (SPSTMW) is found below the WSPCW to roughly γ^n = 27.00 kg/m^3, which corresponds to ~300-600 m depth. SPSTMW is formed by the subduction of thick winter mixed layer and characterized in the vertical by low levels of dissolved oxygen (< 200 µmol/kg, Figure 4.2c), salinities of ~35-35.5 (Figure 4.2b), and potential temperatures of about 10-19ºC (Figure 4.2a).

The Equatorial Subsurface Water (ESSW), found in eastern coastal regions between 26.45 kg/m^3 <γ^n < 27.00 kg/m^3 (~300-500 m depth), is formed near the equator by vertical mixing of waters. The ESSW is carried eastward by the Equatorial Undercurrent and the Southern Subsurface Countercurrent, and then the Peru-Chile Undercurrents transport ESSW southward to approximately 48ºS (Montes et al., 2010; Neshyba, 1979; Stramma et al., 2010; Tsuchiya & Talley, 1998; Wyrtki, 1967). ESSW is characterized by potential temperatures of about 6-10ºC (Figure 4.2a), relatively low salinities (>34.3, Figure 4.2b), silicate concentrations of >10 μmol/kg (Figure 4.2d), and extremely low oxygen values (<150 μmol/kg, Figure 4.2c) (Brink & Robinson, 2005; Silva et al., 2009).

The Subantarctic Mode Water (SAMW) is found between 26.45 kg/m^3 < γ^n < 27.00 kg/m^3, which corresponds to ~300-500 m depth. SAMW is formed by subduction of thick winter mixed layer from Subantarctic Front and is characterized in the vertical by potential temperatures of about 10-15ºC (Figure 4.2a), relatively high salinities (~35-35.5, Figure 4.2b), oxygen values of about 200 μmol/kg (Figure 4.2c), and low silicate concentrations (< 5 μmol/kg, Figure 4.2d).

Below this layer, in the intermediate waters (between 27.00 kg/m^3 < γ^n < 27.58 kg/m^3, which corresponds to ~500-1500 m depth, the Antarctic Intermediate Water (AAIW) is located. The AAIW is formed by advection of fresh Subantarctic Surface Waters (SASW). The AAIW is a relatively cold water mass with potential temperatures of about 4-8ºC (Figure 4.2a), and it is characterized in the vertical by the minimum salinity values (<34.4, Figure 4.2b), high dissolved oxygen concentration (>200 μmol/kg, Figure 4.2c), and a silicate concentration of ~5-50 μmol/kg (Figure 4.2d) (Talley et al., 2011; Tsuchiya, 1991; Tsuchiya & Talley, 1996).

In the deep layer, with a neutral density range of 27.58 kg/m^3 < γ^n < 28.10 kg/m^3, extending in the range ~1500-4000 m depth, is found the core of the Pacific Deep Water (PDW), which is formed by mixing and aging of deep waters that flow into the Southern Ocean. Because of its formation mechanism and source, the waters in the PDW are the oldest of the global ocean. The PDW is characterized in the vertical by low levels of oxygen (<200 µmol/kg, with a minimum of 150 µmol/kg in the ocean interior, Figure 4.2c), low potential temperatures (1-3ºC, Figure 4.2a), salinity values of about 34.5-34.7 (Figure 4.2b), and the maximum silicate concentration among the different water masses (about 70-130 µmol/kg, Figure 4.2d) (Knauss, 1962; Talley et al., 2011; Wijffels et al., 2001).

In the South Pacific, the Upper Circumpolar Deep Water (UCDW) is located in shallower layers 27.58 $< \gamma^n <$ 28.04 kg/m^3 than the core of the PDW. The UCDW is formed by the mixing of deep waters in the Southern Ocean, and is characterized in the vertical by low levels of oxygen (<160 µmol/kg, Figure 4.2c), low potential temperatures (~1.4-4 ºC, Figure 4.2a), a silicate concentration of about 40-125 µmol/kg (Figure 4.2d), and salinity values of ~34.4-34.69 (Figure 4.2b) (Callahan, 1972; Talley et al., 2011).

The densest water mass in the Pacific, γ^n > 28.1 kg/m^3 from approximately 4000 m depth to the seafloor, is called the Lower Circumpolar Deep Water (LCDW). The analogous layer in the Atlantic is commonly called Antarctic Bottom Water (AABW). As stated in Talley et al. (2011), this water mass comes from the Southern Ocean formed by a mixture of the deep waters of all three Oceans: North Atlantic Deep Water (NADW), PDW and Indian Deep Water (IDW). LCDW is identified in the Pacific Ocean by low potential temperatures (<1ºC, Figure 4.2a) and high salinity (>34.7, Figure 4.2b). Moreover, if compared with PDW, the higher oxygen concentration (~200 µmol/kg, Figure 4.2c) and lower silicate concentration (~120 µmol/kg, Figure 4.2c) of the LCDW, indicate that it is significantly younger than the PDW (Kawano et al., 2006; Talley et al., 2011).

In addition, the tilted isotherms and isoneutrals in the transpacific vertical sections allow to identify the effect of the East Australian Current (EAC) in the western basin, and the Peru-Chile Current (PCC) in the eastern basin and the Deep Western Boundary Current (DWBC) on the eastern flank of the Tonga-Kermadec Trench (Figure 4.2).

4.4 Relative Geostrophic Transport and Inverse Model

Geostrophic velocity and transport are calculated using temperature-salinity profiles collected at each station pairs along section P06 in 1992, previously computed by Ganachaud (2003), and in 2017 (Figure 4.1). The distance between stations takes into account the internal Rossby radius, with smaller spacing across boundary currents and across strong topographic slopes, both in the interior and close to the coasts. At each station, the temperature and salinity every two decibars were collected for the full water column depth using a SeaBird 911+ Conductivity-Temperature-Depth (CTD), as well as water samples for salinity, oxygen, silicate, and other chemical tracers.

The thermal wind equation is used to compute the relative geostrophic velocity profile at each station pair, with a reference layer of no motion chosen at the neutral density γ^n = 28.1 kg/m^3 that separates the deep and the abyssal waters (Figure 4.2). This layer, also known as ZVS "Zero Velocity Surface", is the same used in previous studies carried out using hydrographic data at 30ºS in the Pacific Ocean (Ganachaud, 2003; Hernández-Guerra & Talley, 2016; Hernández-Guerra et al., 2019). If the deepest common level of the stations pairs is shallower than the reference layer, the bottom is used as the initial reference level of no motion. Below the deepest common depth of each station pair, velocities are considered to be constant. In addition, the velocities at the reference level are estimated from Lowered Acoustic Doppler Current Profiler (LADCP) and Shipboard Acoustic Doppler Current Profiler (SADCP) data from the 2017 occupation (Comas-Rodríguez et al., 2010; Joyce et al., 2001; Wijffels et al., 1998). Finally, the velocities at the reference level are adjusted from an inverse box model for 1992 and 2017, in which only the mass and silicate transports were used. For the inverse model, the same constraints as in Hernández-Guerra & Talley (2016) have been used to be able to compare both results.

Figure 4.3 shows a comparison between the initial geostrophic velocity (dashed black lines), the SADCP velocity averaged between stations (red line), LADCP velocity (blue line) calculated as the mean of the LADCP velocities in each hydrographic station, and the geostrophic velocity adjusted to the SADCP or LADCP velocity (black solid line), with four different adjustments. Firstly, either if both LADCP and SADCP (Figure 4.3a) or just the SADCP data agree (Figure 4.3b) with the profile of the geostrophic velocity, the initial geostrophic velocity is adjusted to the SADCP data. Secondly, if only the LADCP data agrees with the pattern of the geostrophic velocity, the initial geostrophic velocity is adjusted to LADCP data (Figure 4.3c). If neither the structure of the LADCP nor SADCP data agree with the profile of geostrophic velocity, the initial geostrophic velocity is not adjusted (Figure 4.3d).

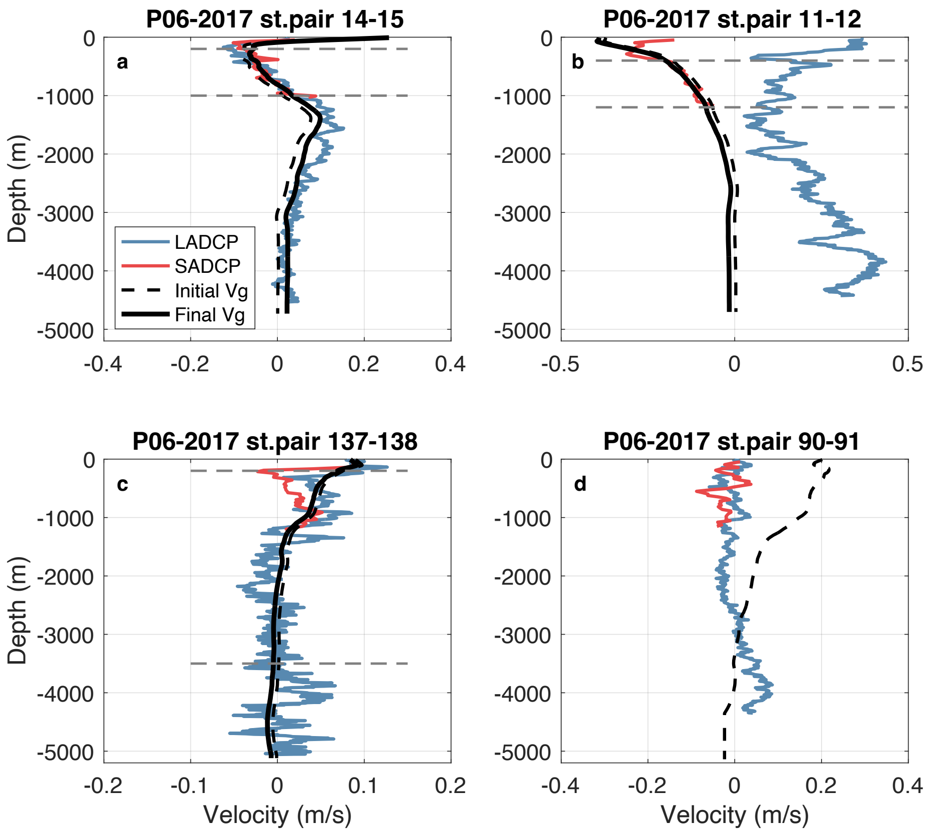

Figure 4.3. Comparison between the initial geostrophic velocity profile (dashed black lines), the LADCP (blue line) and SADCP (red line) velocity normal to the station pairs, and the geostrophic velocity adjusted with LADCP or SADCP data (black solid line). The subplots correspond to different adjustment examples: (a) both, SADCP and LADCP, data agree with the geostrophic velocities, (b) only SADCP data agree, (c) only LADCP data agree, and (d) none agree.

Following Hernández-Guerra & Talley (2016), Hernández-Guerra et al. (2019) and Talley (2008), mass and property transports are computed for the different isoneutral layers that divide the water column (Figure 4.2). The surface geostrophic transport includes the net Ekman transport into the first layer in both 1992 and 2017. The Ekman transport is computed using the NCEP (National Centers for Environmental Prediction) wind-stress (Kalnay et al., 1996) corresponding to the time of the cruise following Hernández-Guerra & Talley (2016). The resulting surface winds for the cruise periods give an Ekman transport of 0.31 $\pm$ 0.16 Sv and 0.33 $\pm$ 0.16 Sv for 1992 and 2017, respectively (1 Sv = 10^6 m^3/s $\approx 10^9$ kg/s). The inverse model adjusts these initial Ekman transports to 0.31 $\pm$ 0.16 Sv and 0.29 $\pm$ 0.15 Sv for 1992 and 2017, respectively.

The initial zonally-integrated mass and silicate transports per layer through 32ºS in the Pacific Ocean are shown in Figure 4.4. The initial mass and silicate transport include the estimation of the velocity at the reference layer from ADCP data. The total mass transport presents a northward initial imbalance of 7.1 Sv for 1992 and of 26.3 Sv for 2017 (Table 4.2). The circulation schema presents an equatorward mass transport for the upper and bottom layers, and a southward mass transport at deep layers. The initial silicate transport structure is similar to the mass transport and presents a northward initial imbalance of -689.6 kmol/s and of 801.4 kmol/s for 1992 and 2017 (Table 4.2), respectively.

In order to reduce this large imbalance, an inverse model has been applied to estimate an adjustment to the velocity at the reference layer, subject to chosen constraints and uncertainties (Wunsch, 1978, 1996). The subsequent equation for mass transport must be solved:

$$\iint \rho b dxdz = -\iint \rho V_r dxdz + E_k$$

where ρ is the density, b is the unknown reference velocity, V_r is the relative geostrophic velocity obtained from the thermal wind equation with the estimated referenced velocities from ADCP data, E_k is the Ekman transport normal to the section, and x and z designate the along-section and vertical coordinates, respectively. See the Appendix A to know how to introduce the ITF and Bering Strait transport constraints. For silicate transport, the above equation has to be multiplied for the silicate concentration.

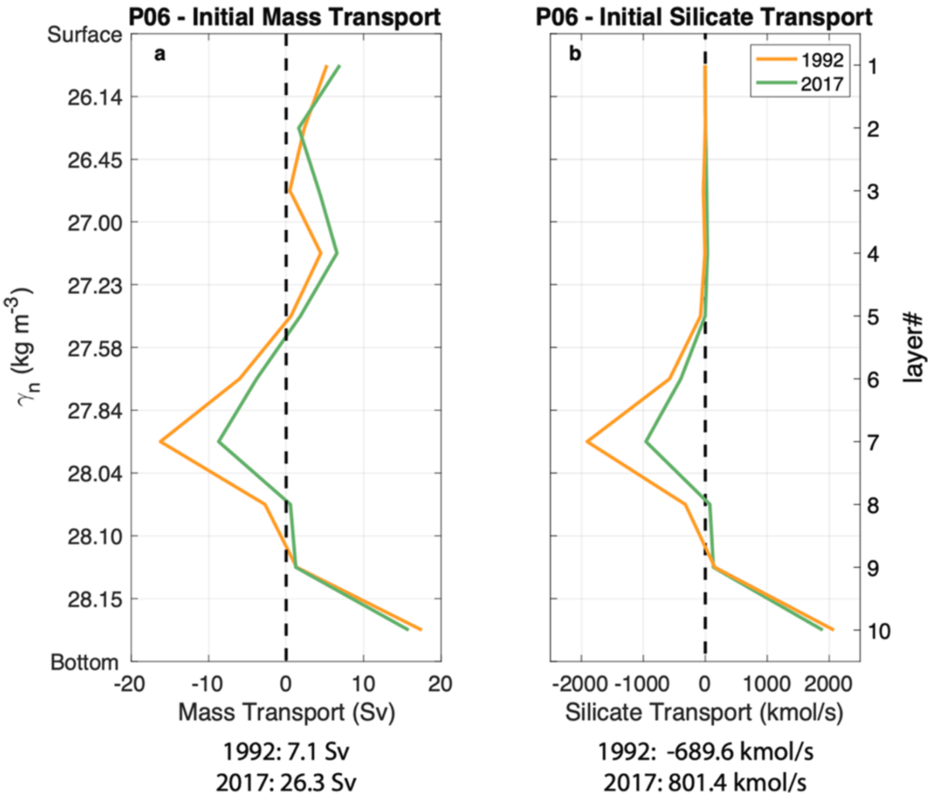

Figure 4.4. Initial zonally-integrated meridional mass (Sv) (a) and silicate transport (kmol/s) (b) per layer across 32ºS in the Pacific Ocean for data collected in 1992 and in 2017.

This procedure provides one single equation for each vertically integrated mass and silica constraint with 228 and 248 unknowns (the number of station pairs) for 1992 and 2017, respectively. The silicate transport constraint applied in this study differs from the no net meridional silica transport previously applied in the inverse model by Hernández-Guerra & Talley (2016), Robbins & Toole (1997), and Wijffels et al. (2001). This study uses a more recent silicate transport constraint estimated by Talley & Sprintall (2005). In addition to total mass and silica constraints, several regional constraints were introduced for different longitude and depth ranges (Table 4.2). Previous studies of earlier occupations of these sections in the Pacific (Hernández-Guerra & Talley, 2016; Wijffels et al., 2001) included the same mass transport constraints in specific longitude ranges and depths from independent data. Thus, equatorward mass transport for the narrow Deep Western Boundary Current (DWBC) just east of the Tonga-Kermadec Ridge (TKR) is constrained (Whitworth et al., 1999).

The solution of the inverse model follows the same approach developed in Joyce et al. (2001) and subsequently carried out by Casanova-Masjoan et al. (2018) and Casanova-Masjoan et al. (2020), with some specific differences. The closed box for the inverse model is composed of the transpacific 32ºS section plus the ITF and Bering Strait transport. The full matrix equation and its derivation are provided in the Appendix A. Following Wunsch (1996), the inverse problem is solved through the Gauss-Markov method, which requires *a priori* variance for each equation and solution chosen to be the same as in Hernández-Guerra & Talley (2016). The *a priori* velocity variance for the solution is set to $(2\ cm/s)^2$, except in regions with strong shear that increases to $(4\ cm/s)^2$, corresponding to the EAC and the DWBC. The *a priori* variance expressed as standard deviation of each equation is shown in Table 4.2. The Gauss-Markov method solves an undetermined system of equations by choosing the one that minimizes its variance, providing the velocities at the reference layer together with their uncertainties. From here, we have estimated mass transports and uncertainties.

Table 4.2. Regional transport constraints and inverse model results for the Pacific Ocean (P06) at 32ºS in 1992 and 2017. Positive transports are northward, and negative are southward. Initial and final transports relative to the ZVS at γ^n = 28.1 kg/m^3 are listed.

Pacific Ocean - P06	Property	Longitude	Layers	Constraint	1992 Initial	1992 Final	2017 Initial	2017 Final
Total mass[1]	ITF and Bering Strait transport (Sv)	All	1:10	15 ± 5	7.1	15.2 ± 10.3	26.3	15.3 ± 10.4
Silicate conservation[2]	Total Silicate (kmol/s)	All	1:10	120 ± 20	-689.6	120.4 ± 1166	801.4	0.1 ± 256
Deep transport[3]	Tasman Sea (Sv)	150-161ºE	9:10	0.5 ± 0.5	0.2	0.75 ± 1.0	0.1	1.2 ± 0.5
Deep transport[3]	Tasman Sea (Sv)	161-173ºE	7:10	0 ± 0.5	0.4	0.0 ± 0.5	1.2	0.0 ± 0.5
Deep transport[3]	Tasman Sea (Sv)	173-181ºE	7:10	0 ± 0.5	-1.0	-0.0 ± 0.6	1.5	0.0 ± 0.5
Deep transport[3]	Eastern Basin (Sv)	110-70ºW	8:10	0.75 ± 0.75	-1.0	0.7 ± 0.7	-0.8	0.7 ± 0.7
DWBC constraint[4]	Tonga-Kermadec Ridge (Sv)	180-168ºW	8:10	15 ± 4	10.8	14.8 ± 4.7	13.5	13.5 ± 3.1

Boundary current result	East Australian Current (Sv)	Coast to 154.3ºE (1992) 156.6ºE (2017)	1:8	NA	NA	-35.1 ± 2.0	NA	-39.2 ± 1.6
Boundary current result	East Australian Current Recirculation (Sv)	154.3º to 156.7ºE (1992) 156.6º to 158.5ºE (2017)	1:8	NA	NA	17.2 ± 1.9	NA	12.3 ± 2.5
Boundary current result	Peru-Chile Current (Sv)	85ºW to coast	1:3	NA	NA	4.4 ± 1.0	NA	4.4 ± 0.8
Boundary current result	Peru-Chile Undercurrent (Sv)	75ºW to coast	4:5	NA	NA	–	NA	-1.5 ± 0.8
Boundary current result	Deep Eastern Boundary Current	76.3ºW to coast (1992) 86.0ºW to coast (2017)	6:7	NA	NA	-6.9 ± 4.9	NA	-8.5 ± 6.8

[a]ITF transport from Gordon et al. (2010) and Sprintall et al. (2009). [b]Silicate conservation from Talley & Sprintall (2005). [c]Deep transport constraints from Wijffels et al. (2001). [d] DWBC constraint from Whitworth et al. (1999).

The velocities at the reference level estimated from SADCP and LADCP data and from the inverse model for 2017 are presented in Figure 4.5. The adjusted velocities from ADCP data (Figure 4.5a) are higher than the velocities from the inverse model (Figure 4.5b), which are not significantly different from zero (i.e., -0.02 ± 0.08 cm/s) at all stations as in previous inverse models (Hernández-Guerra et al., 2019; Hernández-Guerra & Talley, 2016).

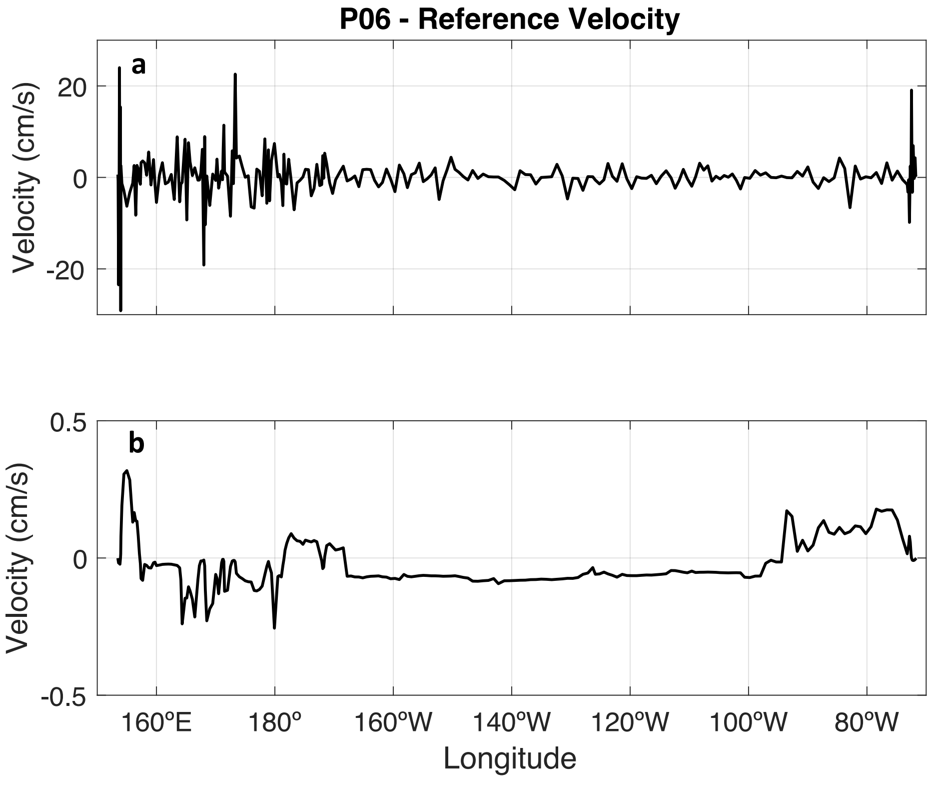

Figure 4.5. Geostrophic velocity (cm/s) adjusted to the SADCP or LADCP data (a) and reference velocities from the inverse model (b) at each station pair for 2017 P06 section at nominally 32ºS in the Pacific Ocean.

4.4 Final Adjusted Transport

4.5.1. Meridional transport per layer

Figure 4.6 shows the final mass and silicate transports per neutral density layer after the inverse model, where both mass and silicate transports from Hernández-Guerra & Talley (2016) for 2003 and 2009 are included, is applied. For both 1992 and 2017, the net initial mass (7.1 and 26.3 Sv, respectively) and silicate transports imbalances (-689.6 kmol/s and 801.4 kmol/s, respectively) are adjusted to the constraints (15.2 $\pm$ 10.3 Sv and 15.3 $\pm$ 10.4 Sv, and 120.4 $\pm$ 1166 kmol/s and 0.1$\pm$ 256 kmol/s, in 1992 and 2017, respectively) as seen from the total transports in Table 4.2. Thus, the final transports satisfy the constraints within the uncertainty. The total mass transport for 1992 is comparable with the mass transport 16.1 $\pm$ 5.1 Sv estimated from the inverse model developed by Ganachaud (2003). Results show the same pattern as previous analyses of the mass transport per layer at this latitude for 2003 and 2009 (Hernández-Guerra & Talley, 2016), with a roughly similar transport pattern in 1992, 2003, 2009 and 2017: northward mass transport in the upper (Layers 1-5) and abyssal layers (Layers 9-10), and southward mass transport in the deep layers (Layers 6-8). In 2017, layer 8 has a slight northward mass transport probably due to warming of the abyssal layers (Purkey et al., 2019), but it has been included in the deep layers according to its density following Hernández-Guerra & Talley (2016).

Inverse model results show that abyssal equatorward flow in the transoceanic section at 32ºS is bottom intensified (Figure 4.6), with a northward flow of 20.5 $\pm$ 6.7 Sv and 16.1 $\pm$ 7.8 Sv for 1992 and 2017, respectively. This bottom Pacific mass transport is consistent with previous estimates. For the 32ºS WOCE section, Wijffels et al. (2001) estimated a similar net northward inflow of 18 $\pm$ 2 Sv. Weaker net equatorward mass transports were estimated by Wunsch et al. (1983) (12 Sv in the lowest layers) using the 1968 Scorpio sections. Using Reid (1997)'s absolute geostrophic velocity for the Scorpio sections. Talley et al. (2003) estimated a deep inflow of 10 Sv, and Katsumata & Fukasawa (2011) obtained a Pacific deep inflow of 10 Sv below γ^n = 28.0 kg/m^3, which was larger than their 8 Sv result for the 1992 WOCE occupation. A more moderate inflow of 7 $\pm$ 2 Sv at 32ºS in 1992 was estimated with a global inverse model by Ganachaud & Wunsch (2000). More recently, with a global inverse model, Lumpkin & Speer (2007) presented a stronger inflow of 14.9 $\pm$ 3.4 Sv. Most recently, Hernández-Guerra & Talley (2016) estimated a net equatorward deep inflow of 15.5 $\pm$ 6.9 Sv for 2003 and 10.8 $\pm$ 6.5 Sv for the 2009 GO-SHIP section, which are not significantly different from our results for 1992 and 2017.

The deep and bottom layers of the adjusted silicate transport (Figure 4.6b) resemble the profile of mass transport (Figure 4.6a). There is a northward silicate transport in the deepest layers (Layers 8-10), as well as a poleward silicate transport in the deep layers (Layers 6-7) that extends up to layer 5. Low silicate transports in the uppermost layers (Layers 1–4) result from very low silicate values in the first 1000 m of the water column (Figure 4.2d and 4.6b). Once again, silicate transports resemble the profile of 2003 and 2009 results computed by Hernández-Guerra & Talley (2016), with a roughly similar silicate transport pattern in years 1992, 2003, 2009 and 2017.

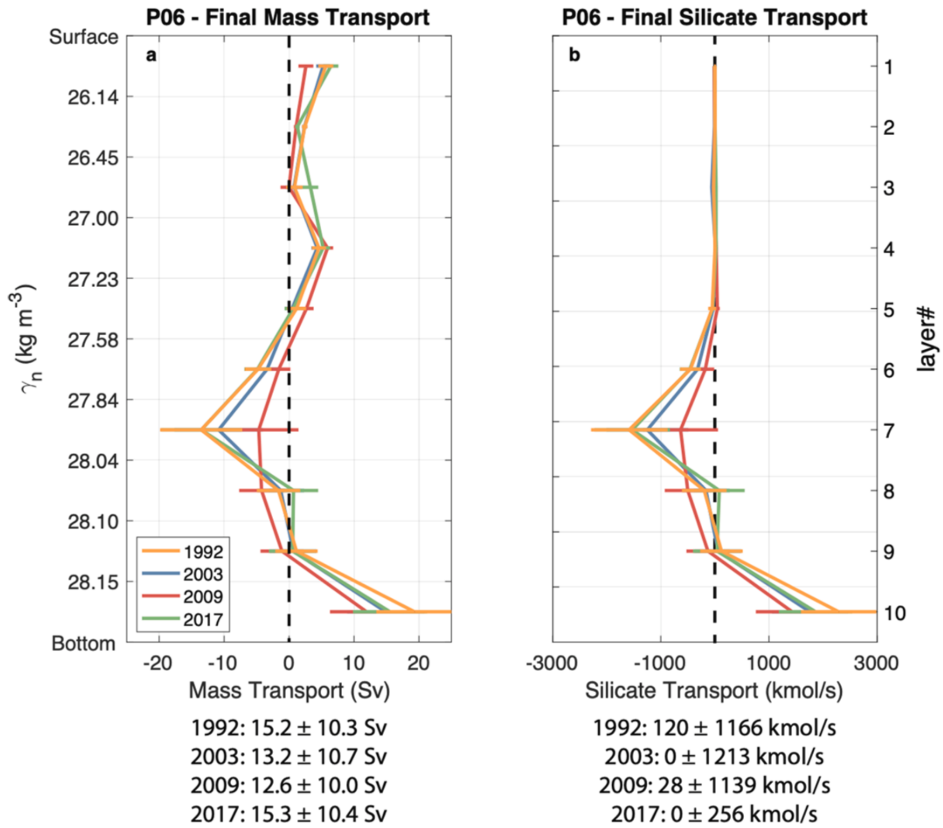

Figure 4.6. Final zonal-integrated meridional mass transport (Sv) (a) and silicate transport (kmol/s) (b) per layer, with error bars, across 32ºS in the Pacific Ocean for data collected in 1992, 2003, 2009 and 2017.

4.5.2. Meridional Overturning Transport

The meridional overturning transport across 32ºS for the Pacific Ocean is computed by vertically integrating the mass transport from the bottom to the surface of the ocean (Figure 4.7). The resulting overturning streamfunction for 2003 and 2009, computed by Hernández-Guerra & Talley (2016) and reproduced in Figure 4.7, presents a nearly zero net flow in layer 3. Such characteristic may be caused by the balance between net northward flow for the ITF and net southward flow in the thermocline associated with the shallow overturn of the subtropical gyre (Talley, 2003,

2008) that can be also observed in our results for 1992, but not in 2017. The intensity of the overturning, called Pacific Meridional Overturning Circulation (PMOC), is generally described as the maximum in the overturning streamfunction, comprising equatorward flow within the South Pacific Ocean and returning poleward flow as PDW (1500-4000 m). The PMOC in 1992 and in 2017 shows the same pattern as in 2003 and in 2009. However, as shown in Table 4.3, the PMOC presents a minimum in 2009 (-11.6 ± 8.0 Sv), although not significantly different from the PMOC in 1992 (-19.9 ± 7.4 Sv), 2003 (-15.5 ± 7.9 Sv) and 2017 (-18.4 ± 6.5 Sv).

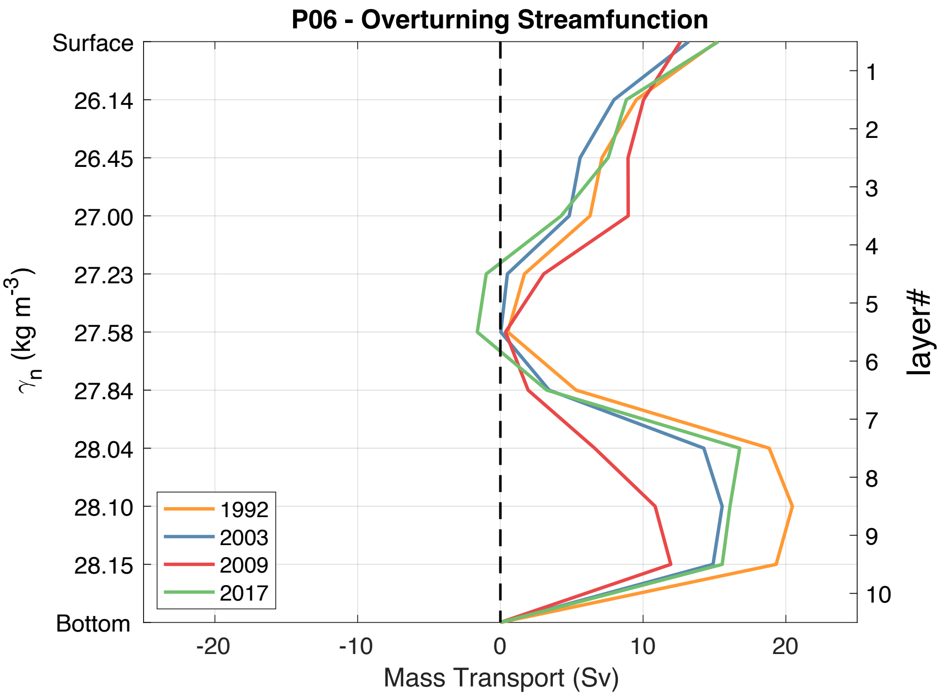

Figure 4.7. Overturning mass transport stream function across 32ºS in the Pacific Ocean for 1992, 2003, 2009 and 2017. This function is computed as the zonally- and vertically-integrated mass transports in isoneutral layers (along the entire section from the seafloor to the sea surface).

Table 4.3. Intensity of the deep Pacific Meridional Overturning Circulation (PMOC) results for the Pacific Ocean (P06) at 32ºS in 1992, 2003, 2009 and in 2017. Negative (southward) deep transports are summed to estimate the PMOC.

Year	**PMOC (Sv)**
1992	-19.9 $\pm$ 7.4
2003	-15.5 $\pm$ 7.9
2009	-11.6 $\pm$ 8.0
2017	-18.4 $\pm$ 6.5

4.6 Horizontal distribution of final adjusted transport

Figure 4.8 shows the eastward zonally accumulated mass transport in isoneutral layers for 1992 and 2017, and for 2003 and 2009 computed by Hernández-Guerra & Talley (2016). The accumulated transport is obtained by integrating the mass transport in each layer eastward from zero at the western boundary, and then summing together northward and southward layer transports as in Figure 4.6. The Pacific Ocean is then divided into a three-layer system: northward mass transport in the uppermost layers (1-5, Figure 4.8a), southward in the deep layers (6-8, Figure 4.8b), and northward in the abyssal layers (9-10, Figure 4.8c).

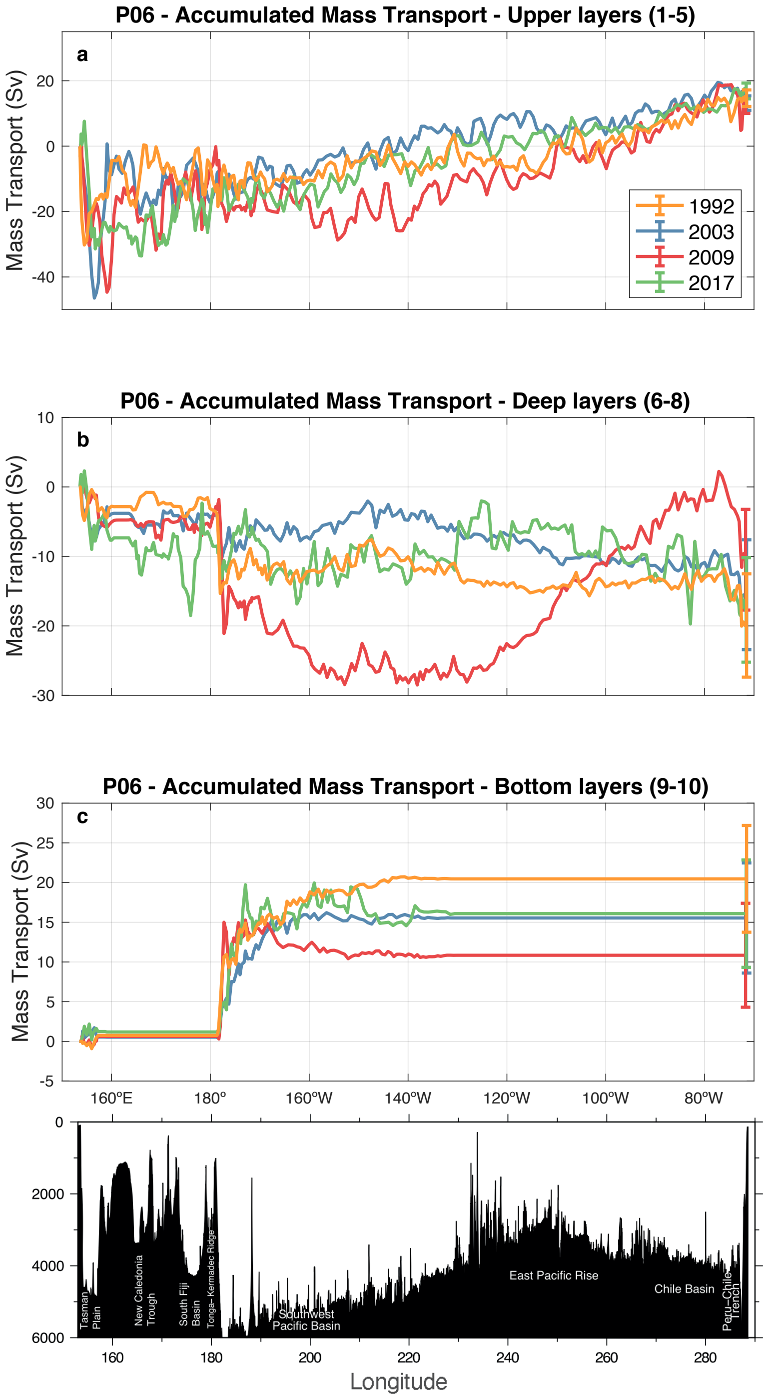

Figure 4.8. Eastward accumulated mass transport (Sv) at 32ºS in the Pacific Ocean for (a) upper, (b) deep, and (c) bottom layers for 1992, 2003, 2009 and 2017. Bottom plot shows the bathymetry for reference.

4.6.1. Upper Ocean Circulation

The accumulated upper ocean mass transport (Figure 4.8a), consisting of thermocline and intermediate waters (surface to γ^n =27.58 kg/m^3, about 1500 m depth), presents an intense western boundary current flowing poleward, an equatorward recirculation east and close to the western boundary, and a net equatorward Sverdrup mass transport across the ocean interior with a wide and slow Peru-Chile Current in the eastern boundary, representing the usual subtropical gyre feature. Eddies are the responsible for the alternating mass transports present along the whole subtropical gyre and are intensified in the westernmost part of the circulation, corresponding to the Tasman Sea as noted in both Hernández-Guerra & Talley (2016) and Wijffels et al. (2001).

4.6.1.1 Interior Gyre Circulation

The Pacific Ocean interior circulation for 1992, 2003 and 2017 differs noticeably from that of 2009 (Figure 4.8a). These marked differences are also found in deep and bottom accumulated mass transports (Figure 4.8b and c). West of the TKR, located at approximately 175ºW encompassing the Tasman Sea and South Fiji Basin, the horizontal mass transports for the three years are similar, with net poleward mass transport dominated by the southward EAC and its equatorward recirculation, and a major eddy field. The ocean circulation of the full water column across the mid-Pacific, between the TKR and the East Pacific Rise (EPR) at 110ºW, is significantly different in 2009 compared with the ocean circulation in 1992, 2003 and 2017.

In the upper layers, the 2003 mass transport is a “classic gyre” with a northward mass transport from the TKR to the EPR, whereas in 2009 the structure of the mass transport is a "bowed gyre", reaching maximum southward values at around 140ºW, then rebounding with compensating equatorward mass transport (Hernández-Guerra & Talley, 2016). The pattern of the circulation in 2017 has changed from the "bowed" circulation in 2009, and resembles again the "classic gyre" of 1992 and 2003. The mass transports for the four years seem to coalesce at the EPR, with a net equatorward mass transports of 14.7 ± 2.5 Sv in 1992, 13.2 ± 2.2 Sv in 2003, 12.3 ± 2.3 Sv in 2009 and 16.9 ± 2.4 Sv in 2017. Therefore, the net northward mass transports obtained in 1992 and in 2017 are comparable with the estimated mass transports previously computed by Ganachaud (2003) for 1992 (16.1 ± 5.1 Sv), and for 2003 and 2009 computed by Hernández-Guerra & Talley (2016). The "bowed gyre", subject to significant interannual variability (M. C. McCarthy et al., 2000), was previously observed by Wyrtki (1975) with a classic surface dynamic model, and by McCarthy et al. (2000). Using the original WOCE P06 section in 1992, Wijffels et al. (2001) identified a double gyre. In contrast, Reid (1997)'s surface circulation showed a circulation similar to the "regular gyre" years as in our results.

4.6.1.2 Western Boundary Current: East Australian Current (EAC)

The EAC is an intense western boundary current that flows southward offshore along the east Australian continental boundary. Recent studies at approximately 32ºS indicate that most of the EAC poleward mass transport is confined between the continental shelf to ~155ºE, a width of approximately 123 km, with a relative intense net northward return flow to the east of the boundary current (Chiswell et al., 1997; Hernández-Guerra & Talley, 2016; Ridgway & Godfrey, 1997; Talley et al., 2011). From the hydrographic sections analyzed in this study, the EAC has a width from approximately 79 km in 1992 to 517 km in 2009, which covers the approximately 123 km estimated by Sloyan et al. (2016) from 18-month mean along-slope velocity. As seen in Figure 4.9, the EAC includes both upper and deep layers (Layers 1-8) and presents a net poleward mass transport of -35.1 ± 2.0 Sv in 1992 and of -39.2 ± 1.6 Sv in 2017 (Table 4.4 and Figure 4.9). The maximum southward mass transport is found at 156.6ºE in 2017, which is close to the 2003 estimate by Hernández-Guerra & Talley (2016), and the minimum position is found at 154.5ºE in 1992. The offshore equatorward recirculation of the EAC, extending approximately 2º eastward from the EAC, is summed over both upper and deep layers (Layers 1-8), and this recirculation presents a mass transport weaker than the EAC in 1992 (17.2 ± 1.9 Sv from 154.3º to 156.7ºE), and in 2017 (12.3 ± 2.5 Sv, between 156.6º and 158.5ºE).

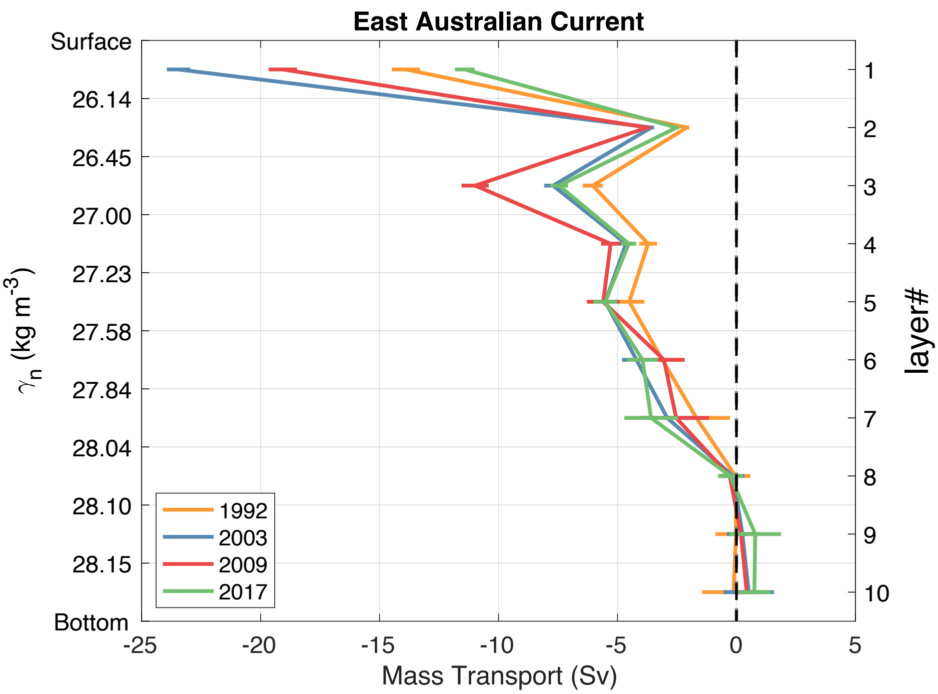

Figure 4.9. Mass transport (Sv) per layer corresponding to the East Australian Current at 32ºS in the Pacific Ocean for 1992, 2003, 2009 and 2017.

Table 4.4. Mass transports inverse model results and uncertainty (Sv) for the East Australian Current, East Australian Current recirculation, Peru-Chile Current, Peru-Chile Undercurrent and Deep Eastern Boundary Current for the Pacific Ocean (P06) at 32ºS in 1992, 2003, 2009 and 2017. Positive transports are northward and negative transports are southward.

Mass Transport (Sv)	Longitude	Layers	Final 1992	Final 2003	Final 2009	Final 2017
East Australian Current	Coast to 154.3ºE (1992)	1:8	-35.1 ± 2.0	-54.3 ± 2.6	-50.5 ± 2.0	-39.2 ± 1.6
	Coast to 156.3ºE (2003)					
	Coast to 158.9ºE (2009)					
	Coast to 156.6ºE (2017)					
East Australian Current Recirculation	154.3º to 156.7ºE (1992)	1:8	17.2 ± 1.9	52.1 ± 4.2	30.4 ± 1.6	12.3 ± 2.5
	156.3º to 158.9ºE (2003)					
	158.9º to 160.8ºE (2009)					
	156.6º to 158.5ºE (2017)					
Peru-Chile Current	85ºW to coast	1:3	4.4 ± 1.0	3.3 ± 0.9[a]	2.3 ± 0.8[a]	4.4 ± 0.8

Peru-Chile Undercurrent	75ºW to coast	4:5	–	-2.8 ± 1.2[a]	-3.8 ± 1.2[a]	-1.5 ± 0.8
Deep Eastern Boundary Current	76.3ºW to coast (1992)	6:7	-6.9 ± 4.9	-5.3 ± 5.5	-9.3 ± 5.0	-8.5 ± 6.8
	78.6ºW to coast (2003)					
	78.8ºW to coast (2009)					
	86.0ºW to coast (2017)					

[a] Final mass transports computed by Hernández-Guerra & Talley (2016).

EAC mass transports for 1992 and 2017, according to the results shown in this study, are comparable to the previous estimates for the 1992 WOCE P06 section: -40 ± 8 Sv reported by Macdonald et al. (2009), and -36 ± 10 Sv reported by Ganachaud & Wunsch (2003). However, Wijffels et al. (2001) reported a much weaker EAC mass transport for the early 1990s of -22.1 ± 4.6 Sv, with a rms variability of 32 Sv estimated from altimetry, based on their 1991–1994 current meter study accompanied by ten EAC hydrographic sections from the coast of Australia to 154.4ºE (Mata et al., 2000). Most recently, Hernández-Guerra & Talley (2016) estimated a stronger EAC mass transport of -51.1 ± 2.0 Sv and -49.9 ± 2.1 Sv for 2003 and 2009, respectively, based on the mass transports for the whole water column. Since Figure 4.9 suggests that the EAC mass transport is present only in layers 1-8, the resulting mass transports of this current are recalculated for these layers obtaining a poleward mass transport of -54.3 ± 2.6 Sv and of -50.5 ± 2.0 Sv in 2003 and 2009, respectively. These results are not significantly different from those estimated by Hernández-Guerra & Talley (2016) and are listed in Table 4.4. EAC recirculation presents a relatively intense net northward mass transport adjacent to the EAC, flowing over both upper and deep waters in the South Pacific Ocean (Figure 4.8 and Table 4.4). The offshore equatorward recirculation of the EAC presents a mass transport weaker than the EAC in 2009 (30.4 ± 1.6 Sv, between 158.9º and 160.8ºE) as in 1992 and 2017 (Table 4.4). However, in 2003 the equatorward EAC recirculation, from 156.3º to 158.9ºE, has a similar mass transport (52.1 ± 4.2 Sv) to the poleward EAC transport (Table 4.4). These results are consistent with time series of a full-depth current meter and property mooring array at 27ºS analyzed by Sloyan et al. (2016): their results showed a weaker EAC recirculation in most occasions, but also a stronger than or of similar magnitude to that of the southward EAC transport in different periods.

Under a changing climate, the EAC has been found to be strengthening over the last decades (Johnson et al., 2011; Wu et al., 2012). However, our results show that the EAC increased in mass transport from 1992 (-35.1 $\pm$ 2.0 Sv) to 2003 (-54.3 $\pm$ 2.6 Sv), and then decreased slightly in mass transport in 2009 (-50.5 $\pm$ 2.0 Sv) and 2017 (-39.2 $\pm$ 1.6 Sv), with a very vigorous eddy field across the topographically-complex Tasman Sea, between the Australian coast and the Tonga-Kermadec Ridge (Table 4.4). This fact could be explained by seasonal variability, as the EAC presents a stronger poleward flow in summer (Oke et al., 2019; Ridgway, 2007), with a seasonal amplitude up to 6.2 Sv (Archer et al., 2017; Kerry & Roughan, 2020; Ribbat et al., 2020; Ridgway & Godfrey, 1997). This behavior is observed in our results: the EAC presents stronger transport in 2009, which section was in November (summer), than in July (winter) in 1992 and 2017, except in 2003 that presents a similar value possibly due to interannual variability.

4.6.1.3 Eastern Boundary Current: Peru-Chile Current (PCC) and Peru-Chile Undercurrent (PCUC)

The PCC is the eastern boundary current in the Pacific Ocean. As any other eastern boundary current, like the Canary Current in the North Atlantic Subtropical Gyre (Casanova-Masjoan et al., 2020; Hernández-Guerra et al., 2017; Vélez-Belchí et al., 2017), it is difficult to identify in the accumulated mass transport due to the fact that the current is weak (~3-4 Sv estimated by Shaffer et al. (2004)) and the variability induced by the eddy field is relatively strong.

The equatorward PCC is evident in the upward slope of the isotherms and isoneutrals in the upper layers (>700 m) off the west coast of South America (Figure 4.2) (Strub et al., 1998; Talley et al., 2011; Tsimplis et al., 1998). The Peru-Chile Undercurrent (PCUC) is found below the PCC (Wooster & Reid, 1963), and extends over the continental shelf and slope, where the isotherms and isoneutral slope downward (Shaffer et al., 1999). Following Hernández-Guerra & Talley (2016), the PCC is estimated from the surface to γ^n = 27.0 kg/m^3 (Layers 1-3) and from 85ºW to the coast of Chile, while the PCUC in the Layers 4-5 and from 75ºW to the Chilean coast (Table 4.4). Thus, the flow of PCC is estimated to be 4.4 $\pm$ 1.0 Sv in 1992, 3.3 $\pm$ 0.9 Sv in 2003, 2.3 $\pm$ 0.8 Sv in 2009, and 4.4 $\pm$ 0.8 Sv in 2017, which are all not significantly different, except for 2009. The PCUC does not appear in 1992, and the mass transport is estimated to be -2.8 $\pm$ 1.2 Sv in 2003, -3.8 $\pm$ 1.2 Sv in 2009, and of -1.5 $\pm$ 0.8 Sv in 2017, which again shows that the estimations for 2003 and 2017 are not significantly different, but that a more intense PCUC is found in 2009. These results are consistent with the moderate average estimated mass transport of the PCUC at 30ºS of 1-1.3 Sv previously reported by Huyer et al. (1987), Shaffer et al. (2004), and Shaffer et al. (1999). According to the Sverdrup relation (Sverdrup, 1947), a negative nearshore wind stress curl (WSC) drives a poleward mass transport. According to Vergara et al. (2016), the poleward decrease of WSC in 2009 could be related to the poleward increase in the PCUC intensity of that year. Interestingly, Chaigneau et al. (2013) estimated a strong PCUC intensification in winter 2010 using SADCP data, similar to the intensification estimated in our results for the P06 cruise in 2009 that took place in the eastern boundary in winter 2010.

4.6.2. Deep Ocean Circulation

Figure 4.8b shows the accumulated mass transport for the PDW layers (layers 6-8). The net poleward mass transport of PDW through 32ºS in 1992 (-19.9 ± 7.4 Sv), 2003 (-15.5 ± 7.9 Sv), 2009 (-10.5 ± 7.3 Sv), and in 2017 (-17.7 ± 7.5 Sv) are not significantly different. The overall zonal structure for 1992 and 2017 is remarkably different from 2009, but similar to 2003. There are two deep western boundaries, one at ~155ºE and the other one at ~175ºW. The mass transport at ~155ºE, which corresponds to the deepest part of the EAC as shown in Mata et al. (2000), does not present any significant difference in 1992 (-3.3 ± 2.5 Sv), 2003 (-5.3 ± 3.7 Sv), 2009 (-5.4 ± 1.9 Sv) and 2017 (-6.4 ± 2.0 Sv). In contrast, noticeable differences are shown in the mass transport at approximately 175ºW, with a southward mass transport of -10.7 ± 2.6 Sv in 1992, -5.3 ± 3.7 Sv in 2003, the strongest southward mass transport in 2009 (-17.9 ± 4.0 Sv), and -4.0 ± 6.0 Sv in 2017. In 1992, 2003 and 2017 -the "classic gyre" years- net poleward mass transport was mostly accomplished by gradual accumulation of mass transport across the width of the section. In 2009, the ''bowed gyre" year, the large southward mass transport in the Southwest Pacific Basin, obtained between the deep western boundary found at 175ºE and west of 140ºW, is compensated by northward flow across eastern Pacific to about 78ºW (of about 25 Sv), and then a southward flow in the eastern boundary, with a net mass transport similar to the other years (Hernández-Guerra & Talley, 2016).

Furthermore, a narrow deep eastern boundary current in the Chilean basin, previously described by Schulze Chretien & Speer (2019) and Shaffer et al. (2004), is centered above the Peru-Chile Trench at about 2500-3400 m depth (Layers 6-7) and from ~85ºW to the Chilean coast.

This current presents a poleward mass transport of -6.9 ± 4.9 Sv in 1992, -5.3 ± 5.5 Sv in 2003, -9.3 ± 5.0 Sv in 2009, and -8.5 ± 6.8 Sv in 2017 (Table 4.4). The southward mass transports of this boundary current are consistent with the approximately -5 Sv in all four occupations previously estimated using WOCE P06 data by Shaffer et al. (2004) for 1992, and by Schulze Chretien & Speer (2019) for the 2003, 2009, and 2017.

4.6.3. Abyssal Ocean Circulation

Figure 4.8c presents the accumulated mass transport for the LCDW layers. The mass transport for layers 9 and 10, as shown in Figure 4.6a, describes a northward flow into the Pacific close to the TKR to 140ºW (Figure 4.8c). The net abyssal northward mass transport in 1992 (20.5 ± 6.7 Sv), 2003 (15.5 ± 6.9 Sv), 2009 (10.8 ± 6.5 Sv), and in 2017 (16.1 ± 6.8 Sv) are not significantly different. In 1992, 2003 and 2017, the equatorward mass transport was broadly distributed over the deepest part of the Southwest Pacific Basin. However, most of the northward mass transport in 2009 is in the narrow DWBC, which resembles Reid (1997)'s abyssal circulation maps based on a 1968 hydrographic section.

4.7. Numerical Ocean Models

Ocean models give a description of the state of the ocean's evolution over time. From these models, data covering the period of each hydrographic section have been used (Figures 4.10 and 4.11), with the aim of identifying whether the observed changes in circulation are reproduced by these models and to try to find out whether the 2009 "bowed gyre" circulation has occurred in other periods.

The model outputs (ECCO, SOSE, GLORYS, and MOM) show roughly similar patterns as the hydrographic data in the upper layers for 1992, 2003, 2009 and 2017 (Figures 4.10a, 4.10d, 4.11a, and 4.11d) although, as previously mentioned, with a weaker EAC and a similar pattern circulation in in the ocean interior for the upper layers. In the deep layers (Figure 4.10b, 4.10e, 4.11b, and 4.11e), none of the models is able to represent the strong poleward mass transport east of TKR, possibly due to their relatively coarse horizontal resolution. In fact, only the eddy-resolving GLORYS reanalysis shows a distinct poleward transport intensification in 2009. In contrast, models show a roughly similar pattern in circulation as hydrographic data in the ocean interior except in 2009. In abyssal layers, models noticeably differ from the hydrographic data in 1992, 2003, and 2017 (Figures 4.10c, 4.10f, and 4.11f), with very weak LCDW equatorward transports. Interestingly, all models simulate transports close to the hydrographic data, both in terms of zonal structures and accumulated transports, in the bottom layers of 2009 (Figure 4.11c). Finally, none of the ocean models reproduces the "bowed" circulation of the hydrographic data present in 2009.

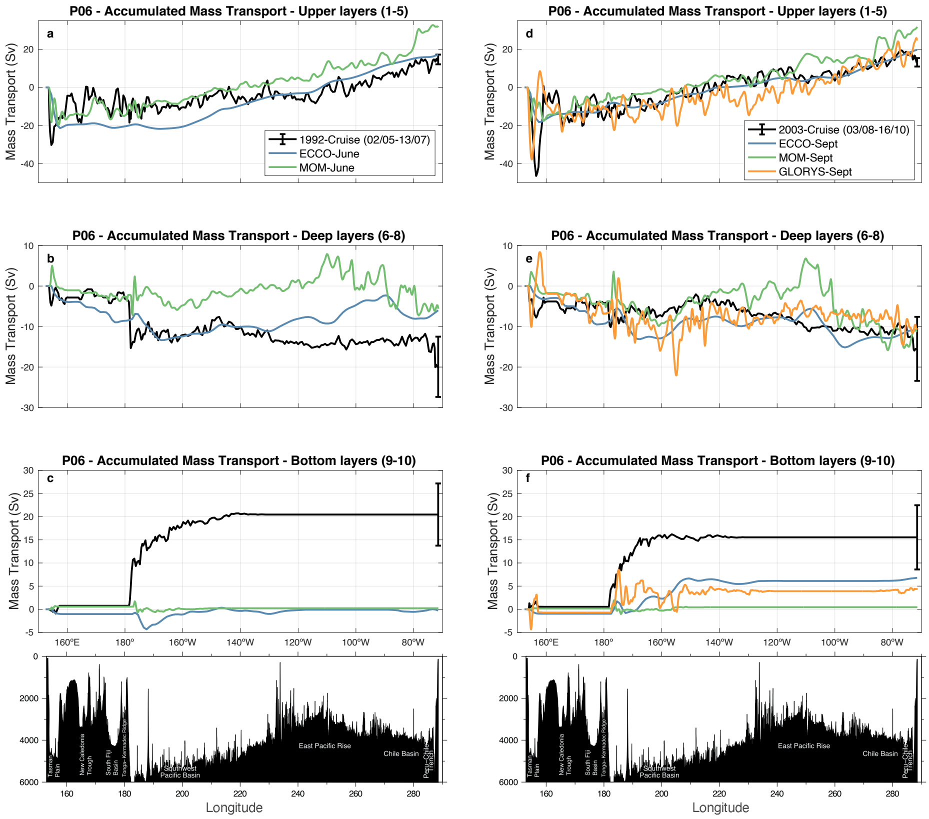

Figure 4.10. Eastward accumulated mass transport (Sv) at 32ºS in the Pacific Ocean for (a, d) upper, (b, e) deep, and (c, f) bottom layers for 1992 and 2003, respectively, estimated from hydrographic data and from the ocean models ECCO, GLORYS, and MOM.

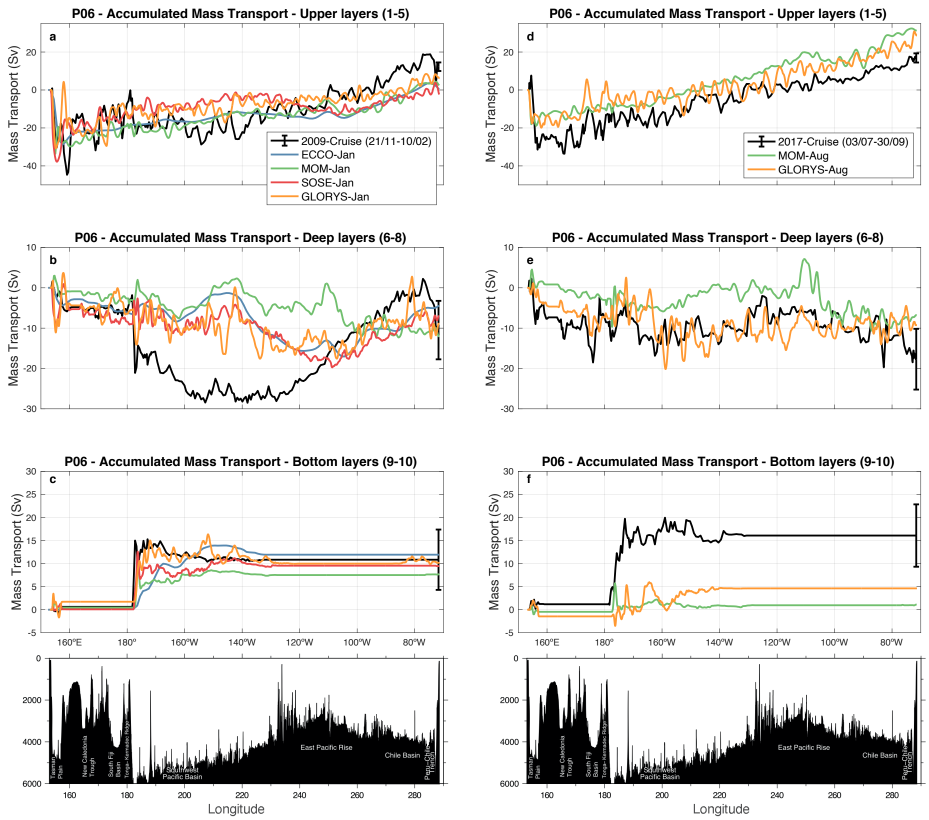

Figure 4.11. Eastward accumulated mass transport (Sv) at 32ºS in the Pacific Ocean for (a, d) upper, (b, e) deep, and (c, f) bottom layers for 2009 and 2017, respectively, estimated from hydrographic data and from the ocean models ECCO, SOSE, GLORYS, and MOM.

4.8. Rossby wave dynamics as responsible for circulation variability

Large-scale Sea Surface Height Anomalies (SSHA) at 30ºS in the South Pacific Ocean are investigated using satellite altimetry data from the AVISO product for the past 27 years (http://las.aviso.oceanobs.com), which are instrumental in clarifying the dynamics underlying mesoscale eddies and Rossby waves. Figure 4.12 presents two Hovmöller diagrams of the SSHA along 30ºS from January 1993 to December 2019. Figure

4.12a and 4.12b are obtained after removing the trend and the steric component following Chelton & Schlax (1996). In Figure 4.12b, a low-pass filter is also applied to the SSHA observations to retain scales longer than 110 days and larger than 7º of longitude.

This diagram shows a large-scale, westward propagating disturbances of 10-15 cm amplitude as also noted in Hernández-Guerra & Talley (2016). These disturbances are initiated in the eastern Pacific, at ~100ºW, similar to the previously described ~100º-120ºW region by Hill et al. (2010) and Li et al. (2020). This region is close to the EPR where topographic steering over the ridge topography produces an intensification of the baroclinic Rossby waves signals produced by a WSC perturbation in the central South Pacific. These waves are intensified as they propagate westward, taking approximately 5-7 years to cross the 8500 km to NZ, which corresponds to a speed of 3 cm/s. This is approximately the speed of long baroclinic Rossby waves at this latitude. The corresponding westward intensification was previously reported by Moore & Wilkin (1998) using results from the Los Alamos National Laboratory global ocean model, which properly represents planetary long waves. In addition, using different Pacific current meter arrays, they described a persistent train of crests and troughs west of 175ºW, approximately along the TKR, where most of the long-wave energy is lost into an eastward topographic wave. As indicated in Hernández-Guerra & Talley (2016), the 2003 P06 section was occupied when an anomalously lower SSHA was centered over the EPR and a high SSHA over the southwest South Pacific Basin. A downwelling Rossby wave was present in the central Pacific between 160ºW and 150ºW when the 2009 P06 occurred. Finally, the 2017 P06 occurred during a period with alternate high and low SSHA over the Southwest Pacific Basin.

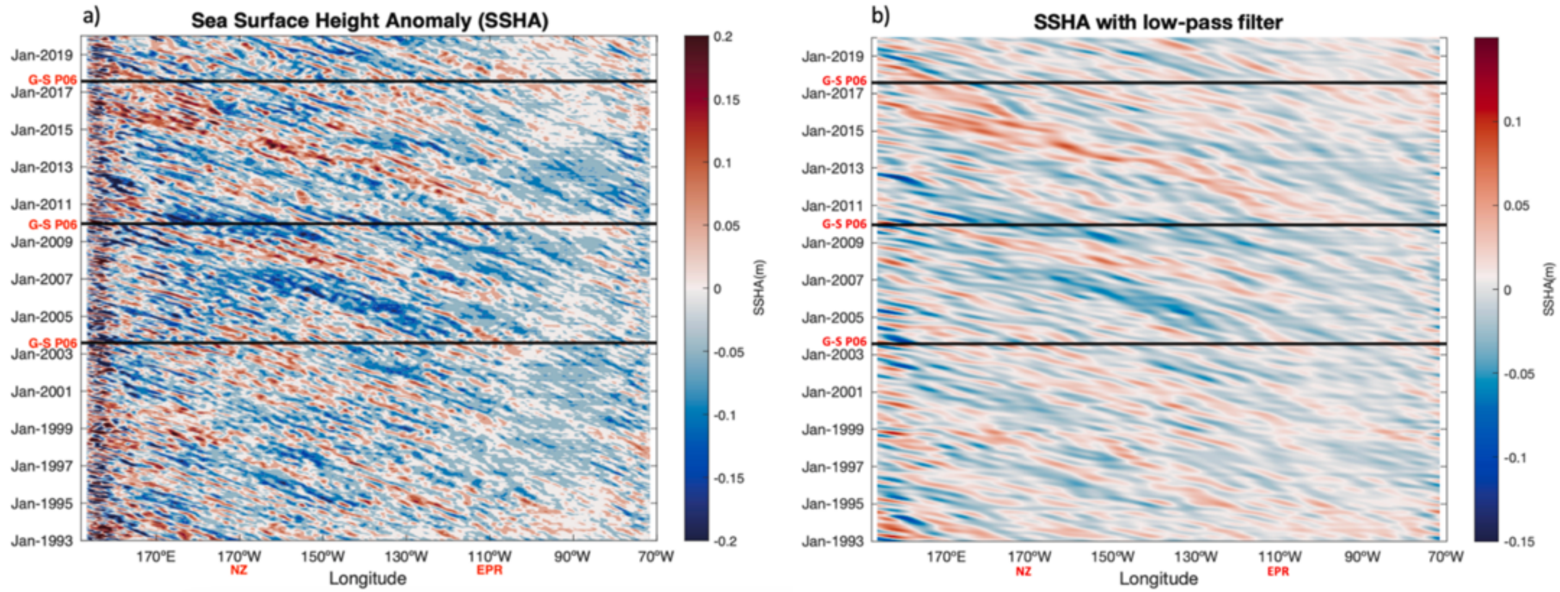

Figure 4.12. Sea Surface Height Anomaly (m) along 30ºS in the Pacific Ocean for the altimetry complete time series from January 1993 to December 2019. The trend and the steric component are removed to (a) and (b); and a low-pass filter is applied to retain scales longer than 110 days and larger than 7º of longitude to (b). The GO-SHIP (G-S) P06 cruise periods in 2003, 2009, and 2017 are indicated. The longitudes of New Zealand (NZ) and East Pacific Rise (EPR) are also shown. Merged AVISO product (http://las.aviso.oceanobs.com).

4.8.1. Linear Rossby wave model

To study the causes of the observed spatially varying SSHA signals in 2009, as visualized in Figure 4.12, a linear Rossby wave model is adopted following Fu & Qiu (2002) and Vélez-Belchí et al. (2017). The model includes the WSC variability, and the responses forced by SSHA changes along 28-32ºS. The long-wave equation for the sea surface height, h, is

$$\frac{\partial h}{\partial t} - \frac{\beta g' H_e}{f^2}\frac{\partial h}{\partial x} = -\frac{g' H_e^2 \nabla \times \tau}{\rho_0 g f H_1^2} \quad (1)$$

where t is time, x is the longitudinal coordinate (positive eastward), H_e is the equivalent depth of the model ($H_e = H_1 H_2/(H_1 + H_2)$), H_1 and H_2 are the upper- and lower-layer thicknesses respectively, ρ_0 is the mean density of sea water, $g' = \left(\frac{\delta\rho}{\rho_0}\right) g$ is the reduced gravity ($\delta\rho$ is the density difference between the two layers), f is the Coriolis parameter, and β is its meridional gradient. Integrating Eq. (1) along the Rossby wave characteristics in the $x - t$ plane we obtain the following solution:

$$h(x,t) = h\left(x_e, t - \frac{x - x_e}{c}\right) - \frac{f H_e}{\rho_0 g \beta H_1^2} \int_{x_e}^{x} \nabla \times \tau \left(x', t - \frac{x - x'}{c}\right) \quad (2)$$

where $c = -\frac{\beta g' H_e}{f^2}$ is the phase speed of long baroclinic Rossby waves, x_e is the longitudinal location of the eastern boundary. The first and second term in the RHS of Eq. (2) represent the influence of the free Rossby waves propagating from the eastern boundary and the effects of wind forcing, respectively.

Eqs. (1) and (2) can be solved from zero initial conditions in a forward time-stepping mode using the WSC anomaly across 30ºS obtained from the reanalysis wind products of NCEP that were used in the inverse modeling. Following Fu and Qiu (2002), we set g'= 0.03 m/s^2, $H_1 = 440$ m and $H_1 + H_2 = 5000$ m, leading to $H_e = 400$ m.

Figure 4.13a presents the results of SSH difference between the eastern boundary and the western boundary (from 175ºE to 68ºW) for the upper layers due to baroclinic waves. As shown in Figure 4.8, the net equatorward mass transports of the four hydrographic sections are not significantly different in the upper layers. Thus, as the linear wave model has used the same upper layers, the differences in SSH shown in Figure 4.13a are expected to match during the four sections. This is true for 2003 (23.4 $\pm$ 0.1 cm), 2009 (23.7 $\pm$ 0.3 cm) and 2017 (24.7 $\pm$ 0.3 cm), but it is not the case for 1992 (22.5 $\pm$ 0.2 cm), which is characterized by a relatively weak SSH difference, possibly suggesting that wind stress data during this year were not appropriate.

The difference in SSH between 140ºW and 68ºW, presented in Figure 4.13b, corresponds to the slope of the sea surface at each time. A large positive slope of the sea surface indicates a strong mass transport flowing north and, therefore, a weaker net southward mass transport. Conversely, if the positive slope is weakened, the flow due to Rossby waves would still be directed northwards but with less intensity, thus resulting in a weaker northward mass transport and a larger net southward mass transport. Figure 4.13b shows a weaker slope in 2009 (14.7 ± 0.1 cm) than in 2003 (16.6 ± 0.1 cm) and 2017 (16.5 ± 0.2 cm). Consequently, the poleward mass transport between 140ºW and 68ºW in 2009 had to be the highest, as corroborated in Figure 4.8. Again, the results for 1992

(14.6 ± 0.2 cm) suggest that the wind data during this year were not appropriate, as they disagree with the hydrographic data circulation pattern. It is worth mentioning that this model suggests another "bowed gyre" event in the period of 2000-2002 (<14 cm), that can presumably be observed in the low SSHA during this period in Figure 4.12.

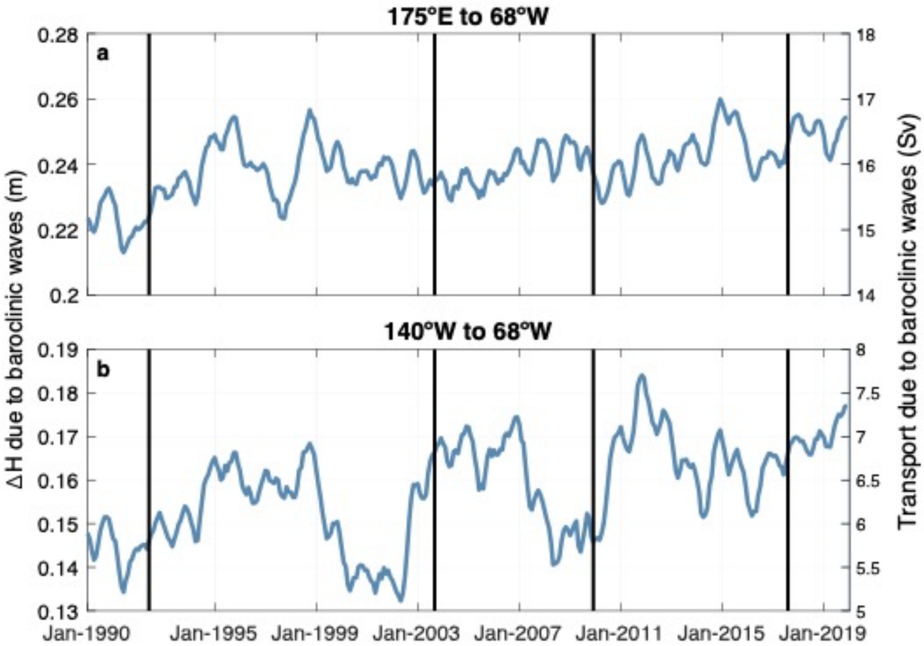

Figure 4.13. Sea surface height difference (m) at 28-32ºS and its corresponding transport (Sv) in the Pacific Ocean from the Rossby wave model, obtained using the NCEP wind stress curl from (a) 175ºE to 68ºW and from (b) 140ºW to 68ºW. Black vertical lines mark the times of the cruises.

Figure 4.14 presents four Hovmöller diagrams of the SSHA along 30ºS obtained using output of numerical modelling data. In the output of ECCO and SOSE (Figures 4.14a and 4.14b), the Rossby wave originated at 110ºW is not present in 2005, however, we can see the low SSHA found at ~175ºW in 2009 but not its propagation. Figure 4.14d shows the SSHA using the MOM output, where the Rossby wave originated at 110ºW in

2005 with negative SSHA cannot be observed, as well as the low SSHA found at ~175ºW in 2009.

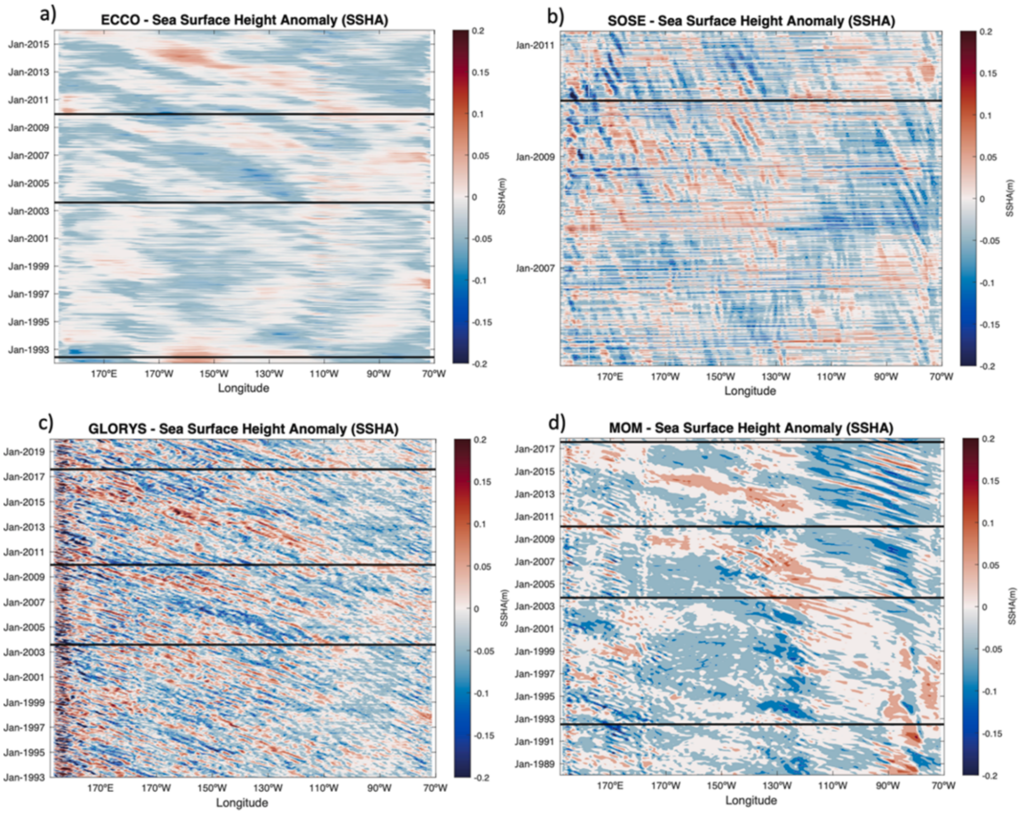

Figure 4.14. Sea Surface Height Anomaly (m) along 30ºS in the Pacific Ocean for the altimetry time series of (a) ECCO, (b) SOSE, (c) GLORYS, and (d) MOM.

In contrast, Figure 4.14c shows that the Hovmöller diagram obtained with the output of the GLORYS model is very similar to the *in situ* data (Figure 4.12). To find out why the GLORYS model shows the Rossby wave signal in the Hovmöller diagram but not the "bowed gyre" circulation in the accumulated mass transport in 2009, Figure 4.15 presents transpacific vertical sections of potential temperature (a) and salinity (b) differences between GLORYS and hydrographic data in 2009, which indicate that the vertical stratification of potential temperature and salinity data at the thermocline layer of both data set are different. The panel (a) shows warm bias and (b) shows high-salinity bias of the GLORYS model. In terms of geostrophic transport, the dynamic height has a high-bias from temperature and a low-bias from salinity. Indeed, at a potential temperature of 10ºC, salinity of 34.8 psu, and pressure of 300 dbar, the thermal expansion is about $1.7 \cdot 10^{-4}$ and the haline contraction is about $7.5 \cdot 10^{-4}$. Moreover, Figure 4.10 shows the warm bias is roughly 1ºC and high-salinity bias is about 0.2 psu. While salinity bias is 1/5 in magnitude of the potential temperature bias, haline contraction is about 4 times larger and thus thermal and haline effects are compensating. This compensation is much weaker west of 140ºW where high-salinity bias is suppressed. There, the warm bias gives a density anomaly of $1.7 \cdot 10^{-4}$ * 1(ºC) * 1025 (kg/m^3) = 0.17 kg/m^3 density anomaly over a 400 m tall water column, which translates into $400 \cdot 10^4$ (depth [Pa]) * (1/(1025-0.17) – 1/1025 [kg/m^3]) / 9.8 (gravity [m/s^2]) = 6.6 cm dynamic height anomaly. Therefore, GLORYS model simulates the low SSH anomaly in 2009, but this low dynamic height anomaly is compensated by the high dynamic height anomaly in the upper 400 m caused by warm anomaly in the GLORYS and its failure to reproduce the internal pressure field correctly. Consequently, GLORYS model does not reproduce the “bowed” circulation.

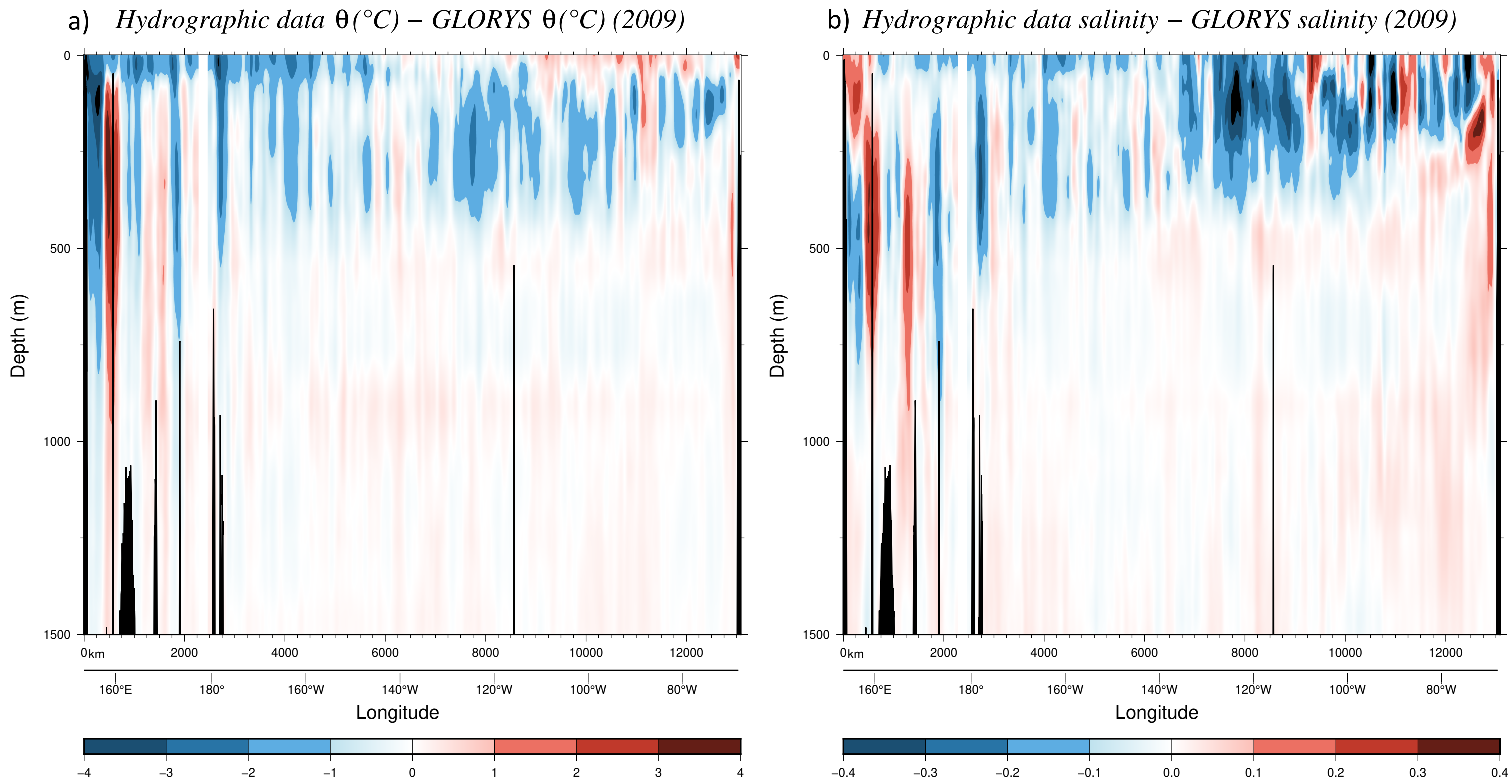

Figure 4.15. Vertical sections for the GLORYS data and hydrographic data differences of (a) potential temperature (ºC) and (b) salinity along section P06 in the Pacific Ocean.

4.8. Temperature and Freshwater Transports

Table 4.5 shows a comparison between the temperature transport (in PW) and freshwater flux (in FSv, Sverdrup for freshwater transport without mass balance) for the section P06 in 1992 and in 2017 resulting from this work and those estimated by Hernández-Guerra & Talley (2016) for 2003 and 2009.

Meridional temperature transports from the inverse model in 1992 (0.42 $\pm$ 0.12 PW), 2003 (0.38 $\pm$ 0.12 PW), 2009 (0.16 $\pm$ 0.12 PW), and 2017 (0.42 $\pm$ 0.12 PW) indicate that the results are all not significantly different except for the temperature transport estimated in 2009 (Table 4.5).

The freshwater flux is estimated following Joyce et al. (2001):

$$\bar{F} = \sum_{i} \sum_{j} T_{ij} S'_{ij} / S_0$$

where T_{ij} is the absolute mass transport, S'_{ij} is the anomaly of salinity (Salinity-S_0), both in layer i at station pair j, and S_0 is the global ocean mean salinity set to 34.9 as in Hernández-Guerra & Talley (2016) and Talley (2008). Positive freshwater values are induced by higher evaporation than precipitation (freshwater flux from the ocean to the atmosphere). The freshwater results in 1992 (0.25 $\pm$ 0.02 FSv), 2003 (0.25 $\pm$ 0.02 FSv), 2009 (0.50 $\pm$ 0.03 FSv) and 2017 (0.34 $\pm$ 0.08 FSv) are all similar, but significantly different from the freshwater transport estimated in 2009 (Table 4.5). Overall, the freshwater results show an increase in net evaporation-precipitation from 2003 to 2009, that is nearly recovered in 2017.

Table 4.5. Temperature transport (PW) and net freshwater transport (FSv), which is equivalent to the net evaporation minus precipitation (positive is net evaporation), for the Pacific Ocean north of 32ºS.

Year	Temperature Transport (PW)	Freshwater Flux (FSv)
1992	0.42 ± 0.12	0.26 ± 0.08
2003[a]	0.38 ± 0.12	0.25 ± 0.02
2009[a]	0.16 ± 0.12	0.50 ± 0.03
2017	0.42 ± 0.12	0.34 ± 0.08

[a] Heat transports and freshwater fluxes computed by Hernández-Guerra & Talley (2016).

Our temperature and freshwater transport results for 1992 are similar to the ones estimated by Wijffels et al. (2001) using WOCE data during the same year (0.75 ± 0.56 PW and 0.1 ± 0.1 FSv, respectively), as well as to the heat and freshwater transport (0.44 ± 0.25 PW and 0.06 FSv, respectively) estimated by Tsimplis et al. (1998).

4.9. Discussion and Conclusions

The Deep Pacific MOC shows similar patterns in 1992, 2003, 2009 and 2017. The intensity of the overturning in 2009 (-11.6 ± 8.0 Sv) is weaker but not significantly different than in 1992 (-19.9 ± 7.4 Sv), 2003 (-15.5 ± 7.9 Sv), and 2017 (-18.4 ± 2.4 Sv). At the same time, the "classic gyre" circulation pattern presented in years 1992, 2003, and 2017, characterized by a more zonal and regular shape, differs noticeably from the "bowed gyre" shape found in 2009. These noticeable differences in the circulation pattern are displayed in the three-layer sets of the accumulated mass transport at approximately 175ºE, where a downwelling due to a

Rossby wave as seen in SSHA, causes a strong poleward mass transport from the surface towards the bottom of the ocean. This southward mass transport in the Southwest Pacific Basin is then compensated at ~140ºW by an equatorward flow across eastern Pacific in both the upper and deep layers, yet it is not found in the bottom layers. Moreover, after studying these changes in the circulation pattern using four different ocean models (ECCO, MOM, SOSE, and GLORYS), we find that the "bowed gyre" shift presented in 2009 is not represented in any numerical modelling output. Thus, it cannot be inferred from the output of these models if the "bowed gyre" circulation pattern has been repeated in any other occasion in the South Pacific Ocean at 30ºS through the different decades.

Furthermore, satellite altimetry suggests that changes in sea surface height anomaly in 1992 are associated with large-scale disturbances of 10-15 cm amplitude. These disturbances propagate slowly westward at roughly the speed of long baroclinic Rossby waves of ~3 cm/s, although the associated shifts in the circulation appear to be quasi-barotropic, extending to the bottom of the ocean. The disturbances seem to be generated in the eastern Pacific, between the East Pacific Rise and South America. Additionally, several apparent discontinuities along the westward propagating pathways obscure the propagating patterns of many Rossby waves. These discontinuities can be explained by the influence of the superimposed local factors also acting along the propagation track, including the effects of bathymetry and of atmosphere and ocean states, in addition to the remote forcing by the winds that first generated Rossby waves (Li et al., 2020; Maharaj et al., 2005; Perkins & Holbrook, 2001; Vivier et al., 1999). A downwelling Rossby wave caused an anomalously lower SSHA centered over the East Pacific Rise in 2003, and then propagated to the west arriving at the central Pacific between 160ºW and

140ºW when the cruise P06 in 2009 occurred. A baroclinic Rossby wave model provided a dynamical framework for a better understanding of the observed large-scale sea surface height signals. The variability of these signals in the South Pacific Ocean depends on the regional wind-stress curl forcing accumulated over the years prior to any specific time. The results from this model provide an explanation for the stronger poleward mass transport in the accumulated mass transport at aproximately 175ºE in 2009. As a result, changes due to the quasi-barotropic shift of the horizontal structure of the Pacific circulation within the different neutral density layers and years are independent from changes in the Deep Pacific MOC, extending into the deepest layers and including the Deep Western Boundary Current, which is part of the overturning circulation. As also noted in Hernández-Guerra & Talley (2016), this result suggests that the horizontal and overturning circulations are not coupled, and are affected by processes with independent time scales.

Finally, the "bowed gyre" circulation changes the temperature transport, as well as the freshwater transport across 32ºS in the Pacific Ocean in 2009, as the estimated temperature and freshwater transports for this year are significantly different from the "classic gyre" years (0.42 $\pm$ 0.12 PW and 0.25 $\pm$ 0.02 FSv in 1992; 0.38 $\pm$ 0.12 PW and 0.25 $\pm$ 0.02 FSv in 2003; 0.16 $\pm$ 0.12 PW and 0.50 $\pm$ 0.03 FSv in 2009; 0.42 $\pm$ 0.12 PW and 0.34 $\pm$ 0.08 FSv in 2017). This is consistent with previous studies of Behrens et al. (2021), Bowen et al. (2017), Gnanaseelan & Vaid (2010), Polito et al. (2000), and Polito & Liu (2003), that also reported Rossby waves, forced by wind-stress curl changes across the South Pacific Ocean, to be responsible for the change in the local heat and freshwater content of the water column.

In conclusion, the contribution of the downwelling Rossby waves not only provides a plausible explanation for the stronger poleward flow in the accumulated mass transport at approximately 175ºE, which gave rise to the "bowed gyre" circulation pattern in 2009, but also for the modification in the local amount of heat and freshwater content of the water column north of 32ºS in the Pacific Ocean in 2009, as the comprehensive analysis performed herein suggests.

Chapter 5

Conclusions

This thesis has comprehensively understood the South Atlantic circulation above the Mid-Atlantic Ridge (MAR) in terms of mass, heat, and freshwater transports by employing an inverse method to hydrographic data and velocity measurements. Furthermore, through a thorough analysis of multiple data sets, this thesis describes the freshwater transport by the Atlantic Meridional Overturning Circulation (AMOC) at 34.5ºS, referred to as M_{ov}, which serves as a key indicator of the AMOC stability. This thesis highlights differences in the sign of M_{ov} between observational data and numerical model estimates. Additionally, an inverse method applied to hydrographic data in the South Pacific Ocean has allowed us to describe two circulation patterns over different decades, identifying a "bowed gyre" in 2009 and a "classic gyre" in 1992, 2003, and 2017. Utilizing a linear Rossby wave model, which includes the wind stress curl variability and responses forced by sea surface height anomaly changes along the South Pacific region, this research sheds light on the contribution of a downwelling Rossby wave in explaining the differences in mass, heat, and freshwater transports during the year characterized by the "bowed gyre". Thus, this thesis enhances our understanding of the complex dynamics of ocean circulation in the South Atlantic and Pacific Oceans, providing valuable insights into their respective roles in global climate processes.

Conclusions arising from Chapter 2:

Firstly, our inverse box model has provided a detailed view of the South Atlantic circulation by estimating the different ocean current transports at each layer set through 24ºS and 34.5ºS, as well as above the MAR at 10ºW between these two latitudes using hydrographic data. The main results from this chapter are:

1. The transports in the upper layers are consistent with the course of the subtropical South Atlantic anticyclonic gyre and the northwest route of the Benguela Current.
2. The deep waters show the southward flow of the Deep Western Boundary Current and Deep Eastern Boundary Current, together with an eastward interbasin flow at the northern stations (close to 24ºS) of the 10ºW section, and different recirculation routes linking both basins.
3. The abyssal layers exhibit northward mass transports through the Argentina and Cape basins, before the latest returns southward in the ocean interior.
4. There is a northward heat transport across the subtropical South Atlantic Ocean.
5. In this study region, evaporation dominates over precipitation.

Conclusions arising from Chapter 3:

Secondly, the multi-data set used to estimate the freshwater transport by the AMOC, referred to as M_{ov}, improves our understanding of the variability of the M_{ov} and its impact on the global climate system. The main results are as follows:

6. Observational data, ocean models, and some coupled climate models considered here suggest a bistable regime of the meridional overturning circulation according to a simple conceptual model and a global circulation model (Rahmstorf, 1996).
7. The different salinity structures for CMIP6 models with positive M_{ov} indicate that the salinity biases may be responsible for the

opposite sign of M_{ov}. Specifically, models with positive M_{ov} values show fresher upper and deeper saltier waters compared to those with negative M_{ov} values. Therefore, we emphasize the need to refine CMIP6 model representations, specifically the salinity bias, to enhance the reliability of AMOC projections in CMIP6 models, especially given the significant implications for IPCC risk analyses.

8. The seasonal variability of the data sets provides a coherent picture of the concomitant variability and correlation of the South Atlantic meridional fluxes at 34.5ºS: M_{ov} is positively correlated in magnitude to MOC and MHT, and MOC is positively correlated to MHT, presenting higher negative M_{ov} values and higher positive MOC/MHT transports from April to August.

Conclusions arising from Chapter 4:

Finally, our second inverse box model applied at 32ºS in the Pacific Ocean revealed two different horizontal circulation patterns by analyzing hydrographic data from 1992, 2003, 2009, and 2017. The main findings are as follows:

9. The "classic gyre" circulation pattern, characterized by a more zonal and regular shape, differs noticeably from the "bowed gyre" shape found in 2009.

10. The Deep Pacific MOC shows similar patterns across all years analyzed, with the intensity of the overturning in 2009 "bowed gyre" (-11.6 ± 8.0 Sv) being weaker but not significantly different from the other "classic gyre" years: 1992 (-19.9 ± 7.4 Sv), 2003 (-15.5 ± 7.9 Sv), and 2017 (-18.4 ± 2.4 Sv).

11. Despite noticeable differences in circulation patterns displayed in the three-layer sets of the accumulated mass transport in 2009, where downwelling causes a strong poleward mass transport from the surface to the ocean bottom at about 175ºE and then is compensated by an equatorward flow across the eastern Pacific at approximately 140ºW, the net accumulated mass transport remained consistent across neutral density layer sets and years.

12. None of the numerical ocean models (ECCO, MOM, SOSE, and GLORYS) captured the “bowed gyre” shift observed in 2009. Consequently, these models leave uncertainty regarding whether the “bowed gyre” circulation pattern has been repeated at 30ºS in the Pacific Ocean on any other occasion.

13. Changes in SSHA in 1992 are associated with large-scale disturbances of 10-15 cm amplitude, propagating westward at about 3 cm/s, similar to long baroclinic Rossby waves. These disturbances originate in the eastern Pacific and exhibit discontinuities along their westward propagating pathways. This behavior is influenced by local factors like bathymetry, atmosphere conditions, and ocean states, and the initial wind forcing that generates the Rossby waves.

14. A downwelling Rossby wave caused a lower SSHA near the East Pacific Rise in 2003, which then propagated westward arriving at the central Pacific in 2009. The baroclinic Rossby wave model results explain the quasi-barotropic shift of stronger poleward mass transport in the accumulated mass transport at approximately 175ºE in 2009.

15. In 2009, the "bowed gyre" circulation significantly modifies the temperature and freshwater transports across 32ºS in the Pacific Ocean, yielding notable different estimations compared to the "classic gyre" years. This is consistent with previous studies indicating that Rossby waves forced by wind-stress curl changes influence the local heat and freshwater content of the water column in the South Pacific Ocean.

16. The contribution of a downwelling Rossby wave not only provides a plausible explanation for the stronger poleward flow in the accumulated mass transport at about 175ºE, which gives rise to the "bowed gyre" circulation pattern in 2009, but also for the modification in the local amount of heat and freshwater content of the water column north of 32ºS in the Pacific Ocean in 2009.

Appendixes

Appendix A. Inverse Box Models

The absolute geostrophic velocity (v_a) for a given station pair, as a function of depth (z), is the summation of the relative velocity (v) and the velocity (b) at the reference level:

$$v_a(z) = v(z) + b$$

The inverse model finds the optimal solution for b at each station pair. Firstly, the mass conservation is applied to the entire water column:

$$\iint \rho v_a dS = 0$$

$$\iint \rho(v + b)dS = 0 \qquad \text{(A.1a, b, c)}$$

$$\sum_{j=1}^{N} \sum_{q=1}^{Q} \rho_{jq}\left(v_{jq} + b_j\right)a_{jq} = 0$$

where the area integral dS is over the entire section area, a_{jq} is the area for each station pair j and isoneutral layer q. In (A.1) and the next equations, the term $\rho_{jq}v_{jq}$ is first summed over each 2 dbar interval within layer q. When mass transport is constrained to a particular non-zero value, M, (A.1c) becomes:

$$\sum_{j=1}^{N} \sum_{q=1}^{Q} \rho_{jq}\left(v_{jq} + b_j\right)a_{jq} = M \qquad \text{(A.1)}$$

where M is the mass transport constraint including the Bering Imbalance, and the limits for layers and station pairs are related to the constraint (Table 2.1 for Chapter 2, and Table 4.2 for Chapter 4). The total mass conservation is not exact because of the noise from eddies, internal waves, aliasing, measurements errors, etc.:

$$\sum_{j=1}^{N}\sum_{q=1}^{Q}\rho_{jq}b_j a_{jq} + n_{Total} = -\sum_{j=1}^{N}\sum_{q=1}^{Q}\rho_{jq}v_{jq}a_{jq} + M_{Total} \qquad \text{(A.2)}$$

where n_{Total} is the noise.

The following equations are obtained considering mass conservation in each layer q:

$$\sum_{j=1}^{N}\rho_{jq}b_j a_{jq} + n_q = -\sum_{j=1}^{N}\rho_{jq}v_{jq}a_{jq} + M_q \qquad q = 1,2,\dots,Q \qquad \text{(A.3)}$$

where M_q is the layer transport constraint and n_q is the layer noise. Next, this equation is written as:

$$\sum_{j=1}^{N} e_{jq}b_j + n_q = -y_q \qquad q = 1,2,\dots,Q \qquad \text{(A.4)}$$

where:

$$e_{jq} = \rho_{jq}a_{jq}$$

$$y_q = \sum_{j=1}^{N}\rho_{jq}v_{jq}a_{jq} - M_q \qquad \text{(A.5)}$$

The matrix equation is rewritten as:

Ab + n = -Y (A.6)

where **b** is a N x 1 vector of the unknowns (reference velocities and adjustment of the Ekman transport), **A** is a (Q + 1) x N matrix, **n** is a (Q + 1) x 1 vector, and **Y** is a (Q + 1) x 1 vector of values calculated from the CTD data and the externally imposed mass transports. (Q is for the equations for each layer and the +1 is the equation for conservation of the whole water column.)

The Ekman transport is included in the first layer, leading to the following system:

$$\begin{pmatrix} e_{11} & \cdots & e_{1n} & 1 \\ e_{21} & & e_{2n} & 0 \\ \vdots & \ddots & \vdots & \vdots \\ e_{q,1} & & e_{q,n} & 0 \\ e_{q+1,1} & \cdots & e_{q+1,n} & 1 \end{pmatrix} \begin{pmatrix} b_1 \\ \vdots \\ b_n \\ \Delta T_{Ek} \end{pmatrix} = \begin{pmatrix} y_1 + T_{Ek} \\ y_2 \\ \vdots \\ y_q \\ y_{q+1} + T_{Ek} \end{pmatrix}$$

To solve this matrix, the Gauss-Markov estimator is applied (Wunsch, 1996), as in Hernández-Guerra and Talley (2016).

For the inverse model in Chapter 2, 15 different constraints are applied corresponding to the mass conservation in each of the three enclosed regions, as well as 12 additional mass transport constraints based on previous studies of boundary currents and deep currents (listed in Table 2.1). For the inverse model in Chapter 4, 7 different constraints were applied corresponding to the mass and silica conservation for the Pacific Ocean, plus 5 additional mass transport constraints (to boundary currents and deep currents) as detailed in Table 4.2.

Appendix B. Data Availability Statement

Data Availability for Chapter 2:

The wind data were collected from NCEP Reanalysis Derived data can be found at http://www.eslr.noaa.gov/psd/. Hydrographic data were collected from the Carbon Hydrographic Data Office (CCHDO) website in the frame of International WOCE and GO-SHIP projects (https://cchdo.ucsd.edu/). The hydrographic data at 34.5°S were collected during the expedition of the German Research Vessel Maria S. Merian (MSM60) conducted in the summer of 2017 (Karstensen, 2020) can be found at https://doi.org/10.1594/PANGAEA.915898. The hydrographic data at 24°S were collected as part of the Ocean Regulation of Climate by Heat and Carbon Sequestration and Transports (ORCHESTRA) program funded by the UK Natural Environment Research Council (NERC, Grant NE/N018095/1). ECCO data are available for download at https://ecco.jpl.nasa.gov/. GLORYS data are available for download at https://resources.marine.copernicus.eu/. The satellite altimetry data were collected from the Aviso database (http://las.aviso.oceanobs.com).

Data Availability for Chapter 3:

Additional information on AX18-XBT data for each transect line can be found at http://www.aoml.noaa.gov/phod/hdenxbt/ax_home.php. Other data sets used in this study are publicly available for download from different websites. These include satellite altimetry data collected from the Aviso database at http://las.aviso.oceanobs.com, Argo Climatology data available at https://sio-argo.ucsd.edu/RG_Climatology.html which were complemented using YoMaHa data accessible at http://apdrc.soest.hawaii.edu/projects/yomaha/, GLORYS data from https://resources.marine.copernicus.eu/, MOM6-JRA data available at https://www.gfdl.noaa.gov/mom-ocean-model/, MOM6-MERRA2 output by Harrison (2022) is archived with an associated https://doi.org/10.5281/zenodo.6342240, and the 32 CMIP6 models' data can be found at https://esgf-node.llnl.gov/search/cmip6 (Bader et al., 2019b, 2019a; Bentsen et al., 2019; Boucher et al., 2018; Cao & Wang, 2019; Danabasoglu, 2019b, 2019a; Dix et al., 2019; (EC-Earth), 2019, 2020; Guo et al., 2018; Hajima et al., 2019; Huang, 2019; Jungclaus et al., 2019; Lee & Liang, 2020; Li, 2019; Lovato et al., 2021; Lovato & Peano, 2020; (NASA/GISS), 2018, 2019; Park & Shin, 2019; Ridley et al., 2019; Seferian, 2018; Seland et al., 2019; Stouffer, 2019; Swart et al., 2019; Tang et al., 2019; Tatebe & Watanabe, 2018; Voldoire, 2018; Wu et al., 2018; Zhang et al., 2018; Ziehn et al., 2019)).

Data Availability for Chapter 4:

The wind data were collected from NCEP Reanalysis Derived data (http://www.eslr.noaa.gov/psd/). Hydrographic data were collected from the CCHDO website in the frame of International WOCE and GO-SHIP projects (https://cchdo.ucsd.edu/), as well as ADCP data (https://currents.soest.hawaii.edu/go-ship/ladcp_rst_2015-2018/2017_P06_ancillary-data.html#ancillary-data-2017-p06). ECCO data are available for download at https://ecco.jpl.nasa.gov/. MOM data are available at https://www.gfdl.noaa.gov/mom-ocean-model/. SOSE data are available at http://sose.ucsd.edu. GLORYS data are available for download at https://resources.marine.copernicus.eu/. The SSHA data were collected from the Aviso database (http://las.aviso.oceanobs.com).

Appendix C. Institutional Acknowledgments

This thesis was completed as part of Cristina Arumí Planas' work at IOCAG, in the doctoral program in Oceanography and Global Change, as well as at the Unidad Océano y Clima from Universidad de Las Palmas de Gran Canaria, an R&D&I CSIC-associate unit. This thesis was supported by the SAGA (RTI2018-100844-B-C31, RTI2018-100844-B-C32 and RTI2018-100844-B-C33) and SACO (PID2022-139403NB-C21 and PID2022-139403NB-C22) projects funded by the Ministerio de Ciencia, Innovación y Universidades of the Spanish Government, and Feder.

Cristina Arumí Planas acknowledges the Agencia Canaria de Investigación, Innovación y Sociedad de la Información (ACIISI) and the Fondo Social Europeo Plus (FSE+) Programa Operativo Integrado de Canarias 2021-2027, Eje 3 Tema Prioritario 74 (85%) grant program of "Apoyo al personal investigador en formación" TESIS2021010028. The research stay at Atlantic Oceanographic and Meteorological Laboratory (AOML-NOAA) and the University of Miami in Miami (Florida, United States) was supported by the ACIISI and FSE+ grant for "Estancias Breves en España y en el Extranjero 2022" EST2022010028. The research stay at Scripps Institution of Oceanography (SIO) and the University of California San Diego (UCSD) in San Diego (California, United States) was supported by the ACIISI and FSE+ grant for "Estancias Breves en España y en el Extranjero 2023" EST2023010008. Finally, the research stay at University of Hamburg in Hamburg (Germany) was supported by the ACIISI and FSE+ grant for "Estancias Breves en España y en el Extranjero 2024" EST2024010002.

Finally, Cristina Arumí-Planas gratefully acknowledge the major efforts of the WOCE/GO-SHIP program's chief scientists and teams who collected the hydrographic transects data: B. King, M. Emelianov, J. Karstensen, H. L. Bryden, M. McCartney, J. Toole M. Fukasawa, S. Watanabe, Y. Yoshikawa, A. Macdonald, R. Curry, S. Mecking, and K. Speer.

Appendix D. Resumen en Castellano

D.1 Objetivos

En un contexto de cambio climático, la Circulación Meridional de Retorno (MOC, por sus siglas en inglés, *Meridional Overturning Circulation)* se espera que cambie significativamente, con el riesgo de interrumpir la distribución global de propiedades oceánicas que mantienen los ecosistemas marinos, el ciclo del carbono y otras propiedades (Lee et al., 2023; van Westen et al., 2024). Por esta razón, la estimación de la variabilidad de la MOC es crucial y puede llevarse a cabo a partir de múltiples fuentes. Esta investigación, utilizando observaciones *in situ* y datos de modelos numéricos, se centra en la variabilidad de la circulación a gran escala con el objetivo de entender la dinámica de la circulación oceánica en los océanos Atlántico Sur y Pacífico Sur en términos de transportes de masa, calor y agua dulce, los cuales juegan un papel crucial en los procesos climáticos globales.

Específicamente, el primer enfoque de esta tesis es describir la circulación oceánica por encima de la Dorsal Mesoatlántica (MAR, por sus siglas en inglés, *Mid-Atlantic Ridge*), utilizando un modelo inverso de cajas para analizar datos de secciones hidrográficas junto con medidas de velocidad. Nuestra motivación es determinar el transporte de masa de la corriente de Brasil que fluye hacia el sur y de la corriente de Benguela que fluye hacia el noroeste, ambas en las capas superficiales e intermedias, pero también estimar la ruta de retorno de las aguas frías en capas profundas. Además, esta tesis tiene como objetivo estimar la intensidad de la Circulación Meridional de Retorno Atlántica (AMOC, por sus siglas en inglés, *Atlantic Meridional Overturning Circulation)* incluyendo los transportes característicos de calor y agua dulce en la cuenca subtropical del Atlántico Sur.

En otro capítulo de esta tesis se describe el transporte de agua dulce debido a la AMOC en el Océano Atlántico, específicamente en 34.5ºS, conocido como M_{ov}, que se considera una herramienta importante para determinar la estabilidad de la AMOC. Para ello se analizan múltiples series de datos: batiTermógrafo eXpendible (XBT), boyas Argo, Modelos Oceánicos de Circulación General (OGCM) y Modelos Acoplados de Circulación General (CGCM). Por lo tanto, el segundo objetivo de esta tesis está dedicado a describir la estabilidad de la AMOC a través de la estimación del M_{ov} usando observaciones para proporcionar un análisis actualizado del estudio realizado por Garzoli et al. (2013). Además, se comparan estos resultados con múltiples series de datos de observaciones y modelos, con el objetivo de destacar y explicar las diferencias entre ellos. Concretamente se analiza el sesgo de salinidad en los modelos acoplados. Estos modelos numéricos acoplados se utilizan para estimar las proyecciones de la AMOC y, así, informar a los grupos de análisis de riesgo del Grupo Intergubernamental de Expertos sobre el Cambio Climático (IPCC, por sus siglas en inglés, *Intergovernmental Panel on Climate Change).*

Esta tesis, además, pretende describir la circulación horizontal y meridional del Océano Pacífico Sur, empleando un modelo inverso de caja usando datos hidrográficos y de velocidad en 1992 y 2017 para complementar el estudio previamente publicado por Hernández-Guerra y Talley (2016) para las secciones realizadas en 2003 y 2009. También se emplea un modelo lineal de ondas de Rossby que incorpora la variabilidad del estrés del viento y las respuestas oceánicas forzadas por los cambios en las anomalías de altura de la superficie del mar (SSHA, por sus siglas en inglés, *Sea Surface Height Anomalies*) a lo largo de la región del Pacífico Sur. En este capítulo, intentamos describir los dos patrones de circulación en esta región utilizando datos hidrográficos de cuatro años diferentes (1992, 2003, 2009 y 2017), así como estimar la intensidad de la la Circulación Meridional de Retorno del Pacífico (PMOC, por sus siglas en inglés, *Pacific Meridional Overturning Circulation)* en esta cuenca, sus transportes asociados de calor y agua dulce, y el forzamiento dinámico que causa el cambio en la circulación oceánica.

En resumen, esta tesis pretende no sólo hacer contribuciones significativas en el campo de la oceanografía física mediante la descripción de la dinámica de los océanos Atlántico Sur y Pacífico Sur utilizando tanto observaciones como resultados de modelos numéricos, sino también proporcionar ideas prácticas para predecir la variabilidad climática y mejorar los informes del IPCC.

D.2 Esquema de la tesis

Esta tesis presenta los resultados de tres estudios realizados en el hemisferio sur, centrados en los procesos dinámicos dentro de las regiones de los océanos Atlántico Sur y Pacífico Sur. Los estudios incluyen un análisis de la circulación del Océano Atlántico Sur utilizando un modelo inverso de caja, un análisis del transporte de agua dulce por la AMOC empleando múltiples conjuntos de datos, y un segundo modelo inverso de caja que utiliza tres décadas de datos in situ combinados con datos de vientos y altimetría para analizar la circulación del Océano Pacífico Sur. Esta tesis está organizada en tres capítulos principales, cada uno de los cuales incluye una introducción, una sección detallada sobre los datos y la metodología utilizada, una presentación de los resultados, una discusión en profundidad y las conclusiones. La tesis finaliza con un capítulo de conclusiones generales, que resume los principales resultados de esta investigación.

El capítulo 2 utiliza un modelo inverso de cajas para examinar la circulación esquemática del Océano Atlántico Sur entre 34,5ºS, 24ºS y por encima de la Dorsal Mesoatlántica. Publicado en el *Journal of Geophysical Research: Oceans* (Arumí-Planas et al., 2023), este estudio describe la circulación horizontal y meridional del océano Atlántico Sur utilizando datos de secciones hidrográficas, así como analiza los transportes de masa, calor y agua dulce en la región.

El capítulo 3 se centra en examinar el transporte de agua dulce debido a la AMOC en 34,5ºS basándose en observaciones XBT. Estos resultados se comparan con conjuntos de datos de boyas Argo, OGCMs y CGCMs. Además, este capítulo cuantifica los transportes meridionales de masa y calor, la correlación entre ellos y su variabilidad interanual y estacional. Este capítulo también se encuentra publicado en el *Journal of Geophysical Research: Oceans* (Arumí-Planas et al., 2024).

El capítulo 4 estudia la circulación del Pacífico Sur utilizando un modelo inverso de caja y se encuentra publicado en *Progress in Oceanography* (Arumí-Planas et al. 2022). En este capítulo se identifican dos patrones de circulación diferentes basados en datos hidrográficos recogidos a en cuatro años diferentes y se analizan los transportes de masa, calor y agua dulce. Además, se utilizan datos del estrés del viento y anomalías de altura de la superficie del mar para explicar las diferencias observadas en los patrones de circulación utilizando un modelo lineal de ondas de Rossby.

Por último, el capítulo 5 ofrece un resumen general y destaca las principales conclusiones de la tesis doctoral.

D.3 Conclusiones generales

En resumen, esta tesis ha logrado una comprensión exhaustiva de la circulación en el Atlántico Sur sobre la MAR en términos de transporte de masa, calor y agua dulce mediante el empleo de un modelo inverso de caja utilizando datos de secciones hidrográficas. Además, a través de un análisis intensivo de múltiples conjuntos de datos, esta tesis describe el transporte de agua dulce por la AMOC a 34,5ºS, denominado M_{ov}, que es un indicador de la estabilidad de la AMOC. Esta tesis señala las diferencias en el signo del M_{ov} entre los datos observacionales y las estimaciones de los modelos numéricos. Además, un modelo inverso de caja aplicado a los datos hidrográficos del Océano Pacífico Sur nos ha permitido describir dos patrones de circulación horizontal a lo largo de cuatro años, identificando un "giro arqueado" en 2009 y un "giro clásico" en 1992, 2003 y 2017. Un modelo lineal de ondas de Rossby, que incluye la variabilidad del estrés del viendo y las respuestas forzadas por los cambios en la anomalía de la altura de la superficie del mar a lo largo de la región del Pacífico Sur, demuestra que es la contribución de una onda de Rossby la que explica las diferencias en los transportes de masa, calor y agua dulce durante el año caracterizado por el "giro arqueado". Así pues, esta tesis mejora nuestra comprensión de la compleja circulación oceánica en el Atlántico Sur y Pacífico Sur.

Conclusiones originadas en el capítulo 2:

En primer lugar, nuestro modelo inverso de caja ha proporcionado una visión detallada de la circulación en el Atlántico Sur mediante la estimación de los diferentes transportes de corrientes oceánicas en cada conjunto de capas a través de 24ºS y 34.5ºS, así como sobre el MAR en 10ºW. Los principales resultados de este estudio son:

1. Los transportes en las capas superiores son consistentes con el curso del giro anticiclónico del Atlántico Sur subtropical y la ruta noroeste de la Corriente de Benguela.
2. Las aguas profundas muestran el flujo hacia el sur de la Corriente Profunda de Contorno Occidental (DWBC, por sus siglas en inglés, *Deep Western Boundary Current*) y la Corriente profunda de Contorno Oriental (DEBC, por sus siglas en inglés, *Deep Eastern Boundary Current*), junto con un flujo entre cuentas hacia el este en las estaciones situadas más al norte (cerca de 24ºS) de la sección 10ºW, y diferentes rutas de recirculación que enlazan ambas cuencas.
3. Las capas abisales presentan transportes de masa hacia el norte a través de las cuencas de Argentina y del Cabo, antes de que la última regrese hacia el sur en el interior del océano.
4. Existe un transporte de calor hacia el norte a través del Océano Atlántico Sur subtropical.
5. En esta región de estudio, la evaporación domina sobre la precipitación.

Conclusiones originadas en el capítulo 3:

En segundo lugar, los múltiples conjuntos de datos utilizados para estimar el transporte de agua dulce debido a la AMOC, denominado M_{ov}, mejora nuestra comprensión de la variabilidad del M_{ov} y de su impacto en el sistema climático global. Los principales resultados de este trabajo son los siguientes:

6. Los datos observacionales, de modelos oceánicos y de algunos modelos climáticos acoplados considerados en esta tesis sugieren un régimen biestable de la circulación meridional de retorno según un modelo conceptual simple y un modelo de circulación global (Rahmstorf, 1996).

7. Las diferentes estructuras del perfil de salinidad para los modelos CMIP6 (modelos climáticos acoplados) con una media de M_{ov} positiva indican que el sesgo de salinidad puede ser el responsable del signo opuesto del M_{ov}. Concretamente, los modelos acoplados con valores de M_{ov} positivos muestran aguas superficiales más dulces y aguas profundas más saladas en comparación con los modelos acoplados con valores de M_{ov} negativos. Por lo tanto, enfatizamos la necesidad de refinar las representaciones de los modelos CMIP6, específicamente el sesgo de salinidad, para mejorar la fiabilidad de las proyecciones de AMOC en los modelos CMIP6, especialmente dadas las importantes implicaciones para los análisis de riesgo del IPCC.

8. La variabilidad estacional de los conjuntos de datos proporciona una estimación coherente de la variabilidad y correlación de los flujos meridionales del Atlántico Sur en 34.5ºS: el M_{ov} está

positivamente correlacionado en magnitud con la MOC y el Transporte Meridional de Calor (MHT, por sus siglas en inglés, *Meridional Heat Transport*), mientras que la MOC está positivamente correlacionada con el MHT, presentando valores más negativos de M_{ov} y transportes más positivos de MOC/MHT de abril a agosto.

Conclusiones originadas en el capítulo 4:

Por último, nuestro segundo modelo inverso de caja ha revelado dos patrones diferentes de circulación horizontal mediante el análisis de datos hidrográficos de 1992, 2003, 2009 y 2017 en 32ºS en el Océano Pacífico. Las principales conclusiones son las siguientes:

9. El patrón de circulación del "giro clásico", caracterizado por una forma más zonal y regular, difiere notablemente de la forma del "giro arqueado" encontrada en 2009.

10. La MOC del Pacífico muestra patrones similares en todos los años analizados, siendo la intensidad de la MOC del "giro arqueado" en 2009 (-11,6 $\pm$ 8,0 Sv) más débil pero no significativamente diferente a la intensidad de los años correspondientes al "giro clásico": 1992 (-19,9 $\pm$ 7,4 Sv), 2003 (-15,5 $\pm$ 7,9 Sv) y 2017 (-18,4 $\pm$ 2,4 Sv).

11. A pesar de las notables diferencias en los patrones de circulación mostrados en los tres grupos de capas del transporte de masa acumulado, en los que el hundimiento causa un fuerte transporte de masa hacia el sur desde la superficie hasta el fondo del océano en 175ºE, el cual es compensado por un flujo hacia el norte a través del Pacífico oriental en 140ºW, el transporte acumulado de masa

neto se mantiene constante en todos los grupos de capas de densidad neutra y a lo largo de los diferentes años.

12. Ninguno de los modelos numéricos oceánicos (ECCO, MOM, SOSE y GLORYS) capta el hundimiento del “giro arqueado” observado en 2009. En consecuencia, no podemos saber si el patrón de circulación del “giro arqueado” en 30ºS en el Océano Pacífico se ha repetido en alguna otra ocasión.

13. Los cambios en la SSHA en 1992 están asociados a perturbaciones a gran escala de 10-15 cm de amplitud, que se propagan hacia el oeste a unos 3 cm/s, similares a las velocidades de propagación de las ondas baroclínicas de Rossby. Estas perturbaciones se originan en el Pacífico oriental y presentan discontinuidades a lo largo de sus trayectorias de propagación hacia el oeste. En este comportamiento influyen factores como la batimetría, las condiciones atmosféricas y los estados oceánicos, así como el forzamiento inicial del viento que genera las ondas de Rossby.

14. Una onda de Rossby de hundimiento causó una SSHA más baja cerca de la Dorsal del Pacífico Oriental en 2003, que luego se propagó hacia el oeste llegando al Pacífico central en 2009. Los resultados del modelo baroclínico de ondas de Rossby explican el hundimiento casi barotrópico del transporte horizontal de masa acumulado (más intenso hacia el sur) aproximadamente en 175ºE en 2009.

15. En 2009, la circulación del “giro arqueado” modifica significativamente los transportes de temperatura y de agua dulce a través de 32ºS en el Océano Pacífico, dando lugar a estimaciones

notablemente diferentes en comparación con los años del “giro clásico”. Esto está de acuerdo con estudios anteriores que indican que las ondas de Rossby forzadas por cambios en el estrés del viento influyen en el contenido local de calor y agua dulce de la columna de agua en el Océano Pacífico Sur.

16. La contribución de las ondas de Rossby de hundimiento no sólo proporciona una explicación plausible para el flujo más intenso hacia el sur en el transporte acumulado de masa en torno a 175ºE, que da lugar al patrón de circulación del “giro arqueado” en 2009, sino también para la modificación en la cantidad local de calor y contenido de agua dulce de la columna de agua al norte de 32ºS en el Océano Pacífico en 2009.

References

Adcroft, A., Anderson, W., Balaji, V., Blanton, C., Bushuk, M., Dufour, C. O., Dunne, J. P., Griffies, S. M., Hallberg, R., Harrison, M. J., Held, I. M., Jansen, M. F., John, J. G., Krasting, J. P., Langenhorst, A. R., Legg, S., Liang, Z., McHugh, C., Radhakrishnan, A., … Zhang, R. (2019). The GFDL Global Ocean and Sea Ice Model OM4.0: Model Description and Simulation Features. *Journal of Advances in Modeling Earth Systems*, *11*(10), 3167–3211. https://doi.org/10.1029/2019MS001726

Ansorge, I. J., Baringer, M. O., Campos, E. J. D., Dong, S., Fine, R. A., Garzoli, S. L., Goni, G., Meinen, C. S., Perez, R. C., Piola, A. R., Roberts, M. J., Speich, S., Sprintall, J., Terre, T., & Van den Berg, M. A. (2014). Basin-Wide Oceanographic Array Bridges the South Atlantic. *Eos, Transactions American Geophysical Union*, *95*(6), 53–54. https://doi.org/10.1002/2014EO060001

Archer, M. R., Roughan, M., Keating, S. R., & Schaeffer, A. (2017). On the Variability of the East Australian Current: Jet Structure, Meandering, and Influence on Shelf Circulation. *Journal of Geophysical Research: Oceans*, *122*(11), 8464–8481. https://doi.org/10.1002/2017JC013097

Arhan, M., Mercier, H., & Park, Y.-H. (2003). On the deep water circulation of the eastern South Atlantic Ocean. *Deep Sea Research Part I: Oceanographic Research Papers*, *50*(7), 889–916. https://doi.org/10.1016/S0967-0637(03)00072-4

Arumí-Planas, C., Dong, S., Perez, R., Harrison, M. J., Farneti, R., & Hernández-Guerra, A. (2024). A Multi-Data Set Analysis of the Freshwater Transport by the Atlantic Meridional Overturning Circulation at Nominally 34.5°S. *Journal of Geophysical Research: Oceans*, *129*(6). https://doi.org/10.1029/2023JC020558

Arumí-Planas, C., Hernández-Guerra, A., Caínzos, V., Vélez-Belchí, P., Farneti, R., Mazloff, M. R., Mecking, S., Rosso, I., Schulze Chretien, L. M., Speer, K. G., & Talley, L. D. (2022). Variability in the meridional overturning circulation at 32°S in the Pacific Ocean diagnosed by inverse box models. *Progress in Oceanography*, *203*. https://doi.org/10.1016/j.pocean.2022.102780

Arumí-Planas, C., Pérez-Hernández, M. D., Pelegrí, J. L., Vélez-Belchí, P., Emelianov, M., Caínzos, V., Cana, L., Firing, Y. L., García-Weil, L., Santana-Toscano, D., & Hernández-Guerra, A. (2023). The South Atlantic Circulation Between 34.5°S, 24°S and Above the Mid-Atlantic Ridge From an Inverse Box Model. *Journal of Geophysical Research: Oceans*, *128*(5), 1–21. https://doi.org/10.1029/2022JC019614

Bader, D. C., Leung, R., Taylor, M., & McCoy, R. B. (2019a). *E3SM-Project E3SM1.0 model output prepared for CMIP6 CMIP historical [Dataset]*. Version 20221114. Earth System Grid Federation.

Bader, D. C., Leung, R., Taylor, M., & McCoy, R. B. (2019b). *E3SM-Project E3SM1.1 model output prepared for CMIP6 CMIP historical [Dataset]*. Version 20221114. Earth System Grid Federation.

Baker, J. A., Bell, M. J., Jackson, L. C., Renshaw, R., Vallis, G. K., Watson, A. J., Wood, R. A., & Baker, J. (2023). *Overturning Pathways Control AMOC Weakening in CMIP6 Models*. https://doi.org/10.22541/essoar.167751597.72764615/v1

Baringer, M. O., & Garzoli, S. L. (2007). Meridional heat transport determined with expendable bathythermographs-Part I: Error estimates from model and hydrographic data. *Deep-Sea Research Part I: Oceanographic Research Papers*, *54*(8), 1390–1401. https://doi.org/10.1016/j.dsr.2007.03.011

Behrens, E., Hogg, A. M., England, M. H., & Bostock, H. (2021). Seasonal and Interannual Variability of the Subtropical Front in the New Zealand Region. *Journal of Geophysical Research: Oceans*, *126*(2). https://doi.org/10.1029/2020JC016412

Bentsen, M., Oliviè, D. J. L., Seland, Ø., Toniazzo, T., Gjermundsen, A., Graff, L. S., Debernard, J. B., Gupta, A. K., He, Y., Kirkevåg, A., Schwinger, J., Tjiputra, J., Aas, K. S., Bethke, I., Fan, Y., Griesfeller, J., Grini, A., Guo, C., Ilicak, M., … Schulz, M. (2019). *NCC NorESM2-MM model output prepared for CMIP6 CMIP historical [Dataset]*. Version 20221116. Earth System Grid Federation. https://doi.org/https://doi.org/10.22033/ESGF/CMIP6.8040

Biastoch, A., Schwarzkopf, F. U., Getzlaff, K., Rühs, S., Martin, T., Scheinert, M., Schulzki, T., Handmann, P., Hummels, R., & Böning, C. W. (2021). Regional imprints of changes in the Atlantic Meridional Overturning Circulation in the eddy-rich ocean model

VIKING20X. *Ocean Science*, *17*(5), 1177–1211. https://doi.org/10.5194/os-17-1177-2021

Boucher, O., Denvil, S., Levavasseur, G., Cozic, A., Caubel, A., Foujols, M.-A., Meurdesoif, Y., Cadule, P., Devilliers, M., Ghattas, J., Lebas, N., Lurton, T., Mellul, L., Musat, I., Mignot, J., & Cheruy, F. (2018). *IPSL IPSL-CM6A-LR model output prepared for CMIP6 CMIP historical [Dataset]*. Version 20221107. Earth System Grid Federation. https://doi.org/10.22033/ESGF/CMIP6.5195

Bowen, M., Markham, J., Sutton, P., Zhang, X., Wu, Q., Shears, N. T., & Fernandez, D. (2017). Interannual Variability of Sea Surface Temperature in the Southwest Pacific and the Role of Ocean Dynamics. *Journal of Climate*, *30*(18), 7481–7492. https://doi.org/10.1175/JCLI-D-16-0852.1

Brink, K. H., & Robinson, A. R. (Eds.). (2005). *The Global Coastal Ocean-Regional Studies and Syntheses* (Vol. 11). Harvard University Press.

Broecker, W. (1991). The Great Ocean Conveyor. *Oceanography*, *4*(2), 79–89. https://doi.org/10.5670/oceanog.1991.07

Bryden, H. L., & Imawaki, S. (2001). Chapter 6.1 Ocean heat transport. In G. Siedler, J. Church, & J. Gould (Eds.), *Ocean Circulation & Climate: Observing and modelling the global ocean* (pp. 455–474). Academic Press. https://doi.org/10.1016/S0074-6142(01)80134-0

Bryden, H. L., King, B. A., & McCarthy, G. D. (2011). South Atlantic overturning circulation at 24°S. *Journal of Marine Research*, *69*(1), 38–55. https://doi.org/10.1357/002224011798147633

Buckley, M. W., & Marshall, J. (2016). Observations, inferences, and mechanisms of the Atlantic Meridional Overturning Circulation: A review. *Reviews of Geophysics*, *54*(1), 5–63. https://doi.org/10.1002/2015RG000493

Caínzos, V., Hernández-Guerra, A., McCarthy, G. D., McDonagh, E. L., Cubas Armas, M., & Pérez-Hernández, M. D. (2022). Thirty Years of GOSHIP and WOCE Data: Atlantic Overturning of Mass, Heat, and Freshwater Transport. *Geophysical Research Letters*, *49*(4), 1–12. https://doi.org/10.1029/2021GL096527

Caínzos, V., Pérez-Hernández, M. D., Santana-Toscano, D., Arumí-Planas, C., & Hernández-Guerra, A. (2023). Consistent picture of the horizontal circulation of the Atlantic Ocean over 3 decades. *Ocean Science*, *19*(4), 1009–1045. https://doi.org/10.5194/os-19-1009-2023

Caínzos, V., Velo, A., Pérez, F. F., & Hernández-Guerra, A. (2022). Anthropogenic Carbon Transport Variability in the Atlantic Ocean Over Three Decades. *Global Biogeochemical Cycles*, *36*(11). https://doi.org/10.1029/2022GB007475

Callahan, J. E. (1972). The structure and circulation of deep water in the Antarctic. *Deep Sea Research and Oceanographic Abstracts*, *19*(8), 563–575. https://doi.org/10.1016/0011-7471(72)90040-X

Cao, J., & Wang, B. (2019). *NUIST NESMv3 model output prepared for CMIP6 CMIP historical [Dataset]*. Version 20221116. Earth System Grid Federation. https://doi.org/10.22033/ESGF/CMIP6.8769

Casanova-Masjoan, M., Joyce, T. M., Pérez-Hernández, M. D., Vélez-Belchí, P., & Hernández-Guerra, A. (2018). Changes across 66°W, the Caribbean Sea and the Western boundaries of the North Atlantic Subtropical Gyre. *Progress in Oceanography*, *168*, 296–309. https://doi.org/10.1016/j.pocean.2018.09.013

Casanova-Masjoan, M., Pelegrí, J. L., Sangrà, P., Martínez, A., Grisolía-Santos, D., Pérez-Hernández, M. D., & Hernández-Guerra, A. (2017). Characteristics and evolution of an Agulhas ring. *Journal of Geophysical Research: Oceans*, *122*(9), 7049–7065. https://doi.org/10.1002/2017JC012969

Casanova-Masjoan, M., Pérez-Hernández, M. D., Vélez-Belchí, P., Cana, L., & Hernández-Guerra, A. (2020). Variability of the Canary Current Diagnosed by Inverse Box Models. *Journal of Geophysical Research: Oceans*, *125*(8). https://doi.org/10.1029/2020JC016199

Chaigneau, A., Dominguez, N., Eldin, G., Vasquez, L., Flores, R., Grados, C., & Echevin, V. (2013). Near-coastal circulation in the Northern Humboldt Current System from shipboard ADCP data. *Journal of Geophysical Research: Oceans*, *118*(10), 5251–5266. https://doi.org/10.1002/jgrc.20328

Chapman, P. (1998). The World Ocean Circulation Experiment (WOCE). *Marine Technology Society Journal*, *32*(3), 23.

Chelton, D. B., & Schlax, M. G. (1996). Global Observations of Oceanic Rossby Waves. *Science*, *272*(5259), 234–238. https://doi.org/10.1126/science.272.5259.234

Chidichimo, M. P., Perez, R. C., Speich, S., Kersalé, M., Sprintall, J., Dong, S., Lamont, T., Sato, O. T., Chereskin, T. K., Hummels, R., & Schmid, C. (2023). Energetic overturning flows, dynamic interocean exchanges, and ocean warming observed in the South Atlantic. In *Communications Earth and Environment* (Vol. 4, Issue 1). Nature Publishing Group. https://doi.org/10.1038/s43247-022-00644-x

Chidichimo, M. P., Piola, A. R., Meinen, C. S., Perez, R. C., Campos, E. J. D., Dong, S., Lumpkin, R., & Garzoli, S. L. (2021). Brazil Current Volume Transport Variability During 2009–2015 From a Long-Term Moored Array at 34.5°S. *Journal of Geophysical Research: Oceans*, *126*(5). https://doi.org/10.1029/2020JC017146

Chiswell, S. M., Toole, J., & Church, J. (1997). Transports across the Tasman Sea from WOCE repeat sections: The East Australian Current 1990–94. *New Zealand Journal of Marine and Freshwater Research*, *31*(4), 469–475. https://doi.org/10.1080/00288330.1997.9516780

Cimatoribus, A. A., Drijfhout, S. S., den Toom, M., & Dijkstra, H. A. (2012). Sensitivity of the Atlantic meridional overturning circulation to South Atlantic freshwater anomalies. *Climate Dynamics*, *39*(9–10), 2291–2306. https://doi.org/10.1007/s00382-012-1292-5

Coachman, L. K., & Aagaard, K. (1988). Transports through Bering Strait: Annual and interannual variability. *Journal of Geophysical Research: Oceans*, *93*(C12), 15535. https://doi.org/10.1029/JC093iC12p15535

Coles, V. J., McCartney, M. S., Olson, D. B., & Smethie, W. M. (1996). Changes in Antarctic Bottom Water properties in the western South Atlantic in the late 1980s. *Journal of Geophysical Research C: Oceans*, *101*(C4), 8957–8970. https://doi.org/10.1029/95JC03721

Comas-Rodríguez, I., Hernández-Guerra, A., & McDonagh, E. L. (2010). Referencing geostrophic velocities using ADCP data Referencing geostrophic velocities using ADCP data. *Scientia Marina*, *74*(2), 331–338. https://doi.org/10.3989/scimar.2010.74n2331

Danabasoglu, G. (2019a). *NCAR CESM2 model output prepared for CMIP6 CMIP historical [Dataset]*. Version 20221103. Earth System Grid Federation.

Danabasoglu, G. (2019b). *NCAR CESM2-WACCM model output prepared for CMIP6 CMIP historical [Dataset]*. Version 20221109. Earth System Grid Federation. https://doi.org/10.22033/ESGF/CMIP6.10071

de Carvalho Ferreira, M. L., & Kerr, R. (2017). Source water distribution and quantification of North Atlantic Deep Water and Antarctic Bottom Water in the Atlantic Ocean. *Progress in Oceanography*, *153*, 66–83. https://doi.org/10.1016/j.pocean.2017.04.003

de Vries, P., & Weber, S. L. (2005). *The Atlantic freshwater budget as a diagnostic for the existence of a stable shut down of the meridional overturning circulation*. *32*, 1–4. https://doi.org/10.1029/2004GL021450

Dijkstra, H. A. (2007). Characterization of the multiple equilibria regime in a global ocean model. *Tellus, Series A: Dynamic Meteorology and Oceanography*, *59*(5), 695–705. https://doi.org/10.1111/j.1600-0870.2007.00267.x

Dix, M., Bi, D., Dobrohotoff, P., Fiedler, R., Harman, I., Law, R., Mackallah, C., Marsland, S., O'Farrell, S., Rashid, H., Srbinovsky, J., Sullivan, A., Trenham, C., Vohralik, P., Watterson, I., Williams, G., Woodhouse, M., Bodman, R., Dias, F. B., … Yang, R. (2019). *CSIRO-ARCCSS ACCESS-CM2 model output prepared for CMIP6 CMIP historical [Dataset]*. Version 20221106. Earth System Grid Federation. https://doi.org/10.22033/ESGF/CMIP6.4271

Dong, S., Baringer, M. O., Goni, G. J., Meinen, C. S., & Garzoli, S. L. (2014). Seasonal variations in the South Atlantic Meridional Overturning Circulation from observations and numerical models. *Geophysical Research Letters*, *41*(13), 4611–4618. https://doi.org/10.1002/2014GL060428

Dong, S., Garzoli, S., & Baringer, M. (2011). The role of interocean exchanges on decadal variations of the meridional heat transport in the South Atlantic. *Journal of Physical Oceanography*, *41*(8), 1498–1511. https://doi.org/10.1175/2011JPO4549.1

Dong, S., Garzoli, S., Baringer, M., Meinen, C., & Goni, G. (2009). Interannual variations in the Atlantic meridional overturning circulation and its relationship with the net northward heat transport in the South Atlantic. *Geophysical Research Letters*, *36*(20), L20606. https://doi.org/10.1029/2009GL039356

Dong, S., Goni, G., & Bringas, F. (2015). Temporal variability of the South Atlantic Meridional Overturning Circulation between 20°S and 35°S. *Geophysical Research Letters*, *42*(18), 7655–7662. https://doi.org/10.1002/2015GL065603

Dong, S., Goni, G., Domingues, R., Bringas, F., Goes, M., Christophersen, J., & Baringer, M. (2021). Synergy of In Situ and Satellite Ocean Observations in Determining Meridional Heat Transport in the Atlantic Ocean. *Journal of Geophysical Research: Oceans*, *126*(4). https://doi.org/10.1029/2020JC017073

Drévillon, M., Bahurel, P., Bazin, D., Benkiran, M., Beuvier, J., Crosnier, L., Drillet, Y., Durand, E., Fabardines, M., Garcia Hermosa, I., Giordan, C., Gutknecht, E., Hernandez, F., Chune, S., Le Traon, P.-Y., Lellouche, J.-M., Levier, B., Melet, A., Obaton, D., … Thomas-Courcoux, C. (2018). Learning about Copernicus Marine Environment Monitoring Service "CMEMS": A Practical Introduction to the Use of the European Operational Oceanography Service. In *New Frontiers in Operational Oceanography*. GODAE OceanView. https://doi.org/10.17125/gov2018.ch25

Drijfhout, S. S., Weber, S. L., & van der Swaluw, E. (2011). The stability of the MOC as diagnosed from model projections for pre-industrial, present and future climates. *Climate Dynamics*, *37*(7–8), 1575–1586. https://doi.org/10.1007/s00382-010-0930-z

ECCO Consortium, Fukumori, I., Wang, O., Fenty, I., Forget, G., Heimbach, P., & Ponte, R. M. (2020). *ECCO central estimate (version 4 release 4)*. https://ecco.jpl.nasa.gov/drive/files/Version4/Release4/interp_monthly

ECCO Consortium, Fukumori, I., Wang, O., Fenty, I., Forget, G., Heimbach, P., & Ponte, R. M. (2021). Synopsis of the ECCO central production global ocean and sea-ice state estimate (version 4 release 4). *Zenodo*. https://doi.org/https://doi.org/10.5281/zenodo.4533349

(EC-Earth), E.-E. C. (2019). *EC-Earth-Consortium EC-Earth3 model output prepared for CMIP6 CMIP historical [Dataset]*. Version 20221115. Earth System Grid Federation. https://doi.org/10.22033/ESGF/CMIP6.4700

(EC-Earth), E.-E. C. (2020). *EC-Earth-Consortium EC-Earth3-AerChem model output prepared for CMIP6 CMIP historical [Dataset]*. Version 20221115. Earth System Grid Federation. https://doi.org/10.22033/ESGF/CMIP6.4701

Emery, W. J. (2001). Water Types And Water Masses. In *Encyclopedia of Ocean Sciences* (Vol. 6, pp. 3179–3187). Elsevier. https://doi.org/10.1006/rwos.2001.0108

Emery, W. J., & Meincke, J. (1986). Global water masses-summary and review. *Oceanologica Acta*, *9*(4), 383–391.

Evans, G. R., McDonagh, E. L., King, B. A., Bryden, H. L., Bakker, D. C. E., Brown, P. J., Schuster, U., Speer, K. G., & van Heuven, S. M. A. C. (2017). South Atlantic interbasin exchanges of mass, heat, salt and anthropogenic carbon. *Progress in Oceanography*, *151*, 62–82. https://doi.org/10.1016/j.pocean.2016.11.005

Finucane, G., & Hautala, S. (2022). Transport of Antarctic Bottom Water entering the Brazil Basin in a Planetary Geostrophic Inverse Model. *Geophysical Research Letters*, 1–9. https://doi.org/10.1029/2022gl100121

Forget, G., Campin, J. M., Heimbach, P., Hill, C. N., Ponte, R. M., & Wunsch, C. (2015). ECCO version 4: An integrated framework for non-linear inverse modeling and global ocean state estimation. *Geoscientific Model Development*, *8*(10), 3071–3104. https://doi.org/10.5194/gmd-8-3071-2015

Frajka-Williams, E., Ansorge, I. J., Baehr, J., Bryden, H. L., Chidichimo, M. P., Cunningham, S. A., Danabasoglu, G., Dong, S., Donohue, K. A., Elipot, S., Heimbach, P., Holliday, N. P., Hummels, R., Jackson, L. C., Karstensen, J., Lankhorst, M., Le Bras, I. A., Susan Lozier, M., McDonagh, E. L., … Wilson, C. (2019). Atlantic meridional overturning circulation: Observed transport and variability. *Frontiers in Marine Science*, *6*(JUN), 1–18. https://doi.org/10.3389/fmars.2019.00260

Fu, L.-L. (1981). The General Circulation and Meridional Heat Transport of the Subtropical South Atlantic Determined by Inverse Methods. *Journal of Physical Oceanography*, *11*(9), 1171–1193. https://doi.org/10.1175/1520-0485(1981)011<1171:TGCAMH>2.0.CO;2

Fu, L.-L., & Qiu, B. (2002). Low-frequency variability of the North Pacific Ocean: The roles of boundary- and wind-driven baroclinic Rossby waves. *Journal of Geophysical Research: Oceans*, *107*(C12), 3220. https://doi.org/10.1029/2001JC001131

Fukumori, I., Wang, O., Fenty, I., Forget, G., Heimbach, P., & Ponte, R. M. (2017). *ECCO Version 4 Release 3*. *2*(2015), 10. https://doi.org/1721.1/110380

Fukumori, I., Wang, O., Fenty, I., Forget, G., Heimbach, P., & Ponte, R. M. (2020). *ECCO version 4 release 4*.

Ganachaud, A. (2003). Large-scale mass transports, water mass formation, and diffusivities estimated from World Ocean Circulation Experiment (WOCE) hydrographic data. *Journal of Geophysical Research*, *108*(C7), 3213. https://doi.org/10.1029/2002JC001565

Ganachaud, A., & Wunsch, C. (2000). Improved estimates of global ocean circulation, heat transport and mixing from hydrographic data. *Nature*, *408*(6811), 453–457. https://doi.org/10.1038/35044048

Garcia, H., Weathers, K., Paver, C., Smolyar, I., Boyer, T., Locarnini, M., Zweng, M., Mishonov, A., Baranova, O., Seidov, D., & Reagan, J. (2019). *World Ocean Atlas 2018. Vol. 4: Dissolved Inorganic Nutrients (phosphate, nitrate and nitrate+nitrite, silicate)*. A. Mishonov Technical Editor. https://archimer.ifremer.fr/doc/00651/76336/

Garzoli, S. L., & Baringer, M. O. (2007). Meridional heat transport determined with expandable bathythermographs-Part II: South Atlantic transport. *Deep-Sea Research Part I: Oceanographic Research Papers*, *54*(8), 1402–1420. https://doi.org/10.1016/j.dsr.2007.04.013

Garzoli, S. L., Baringer, M. O., Dong, S., Perez, R. C., & Yao, Q. (2013). South Atlantic meridional fluxes. *Deep Sea Research Part I:*

Oceanographic Research Papers, *71*, 21–32. https://doi.org/10.1016/j.dsr.2012.09.003

Garzoli, S. L., Dong, S., Fine, R., Meinen, C. S., Perez, R. C., Schmid, C., van Sebille, E., & Yao, Q. (2015). The fate of the Deep Western Boundary Current in the South Atlantic. *Deep Sea Research Part I: Oceanographic Research Papers*, *103*, 125–136. https://doi.org/10.1016/j.dsr.2015.05.008

Garzoli, S. L., & Gordon, A. L. (1996). Origins and variability of the Benguela Current. *Journal of Geophysical Research: Oceans*, *101*(C1), 897–906. http://dx.doi.org/10.1029/95JC03221

Garzoli, S. L., & Matano, R. (2011). The South Atlantic and the Atlantic Meridional Overturning Circulation. *Deep Sea Research Part II: Topical Studies in Oceanography*, *58*(17–18), 1837–1847. https://doi.org/10.1016/j.dsr2.2010.10.063

Gent, P. R. (2018). A commentary on the Atlantic meridional overturning circulation stability in climate models. *Ocean Modelling*, *122*(December 2017), 57–66. https://doi.org/10.1016/j.ocemod.2017.12.006

Gnanaseelan, C., & Vaid, B. H. (2010). Interannual variability in the Biannual Rossby waves in the tropical Indian Ocean and its relation to Indian Ocean Dipole and El Nino forcing. *Ocean Dynamics*, *60*(1), 27–40. https://doi.org/10.1007/s10236-009-0236-z

Godfrey, J. S. (1989). A Sverdrup model of the depth-integrated flow for the world ocean allowing for island circulations. *Geophysical & Astrophysical Fluid Dynamics*, *45*(1–2), 89–112. https://doi.org/10.1080/03091928908208894

Goes, M., Christophersen, J., Dong, S., Goni, G., & Baringer, M. O. (2018). An Updated Estimate of Salinity for the Atlantic Ocean Sector Using Temperature–Salinity Relationships. *Journal of Atmospheric and Oceanic Technology*, *35*(9), 1771–1784. https://doi.org/10.1175/JTECH-D-18-0029.1

Gordon, A. L. (1981). South Atlantic thermocline ventilation. *Deep Sea Research Part A. Oceanographic Research Papers*, *28*(11), 1239–1264. https://doi.org/10.1016/0198-0149(81)90033-9

Gordon, A. L. (1985). Indian-Atlantic transfer of thermocline water at the Agulhas retroflection. *Science*, *227*(4690), 1030–1033. https://doi.org/10.1126/science.227.4690.10

Gordon, A. L. (1986). Interocean exchange of thermocline water. *Journal of Geophysical Research*, *91*(C4), 5037. https://doi.org/10.1029/JC091iC04p05037

Gordon, A. L. (1989). Brazil-Malvinas Confluence–1984. *Deep Sea Research Part A. Oceanographic Research Papers*, *36*(3), 359–384. https://doi.org/10.1016/0198-0149(89)90042-3

Gordon, A. L., Sprintall, J., Van Aken, H. M., Susanto, D., Wijffels, S., Molcard, R., Ffield, A., Pranowo, W., & Wirasantosa, S. (2010). The Indonesian throughflow during 2004–2006 as observed by the INSTANT program. *Dynamics of Atmospheres and Oceans*, *50*(2), 115–128. https://doi.org/10.1016/j.dynatmoce.2009.12.002

Gordon, A. L., Weiss, R. F., Smethie, W. M., & Warner, M. J. (1992). Thermocline and intermediate water communication between the south Atlantic and Indian oceans. *Journal of Geophysical Research*, *97*(C5), 7223. https://doi.org/10.1029/92jc00485

Guo, H., John, J. G., Blanton, C., McHugh, C., Nikonov, S., Radhakrishnan, A., Rand, K., Zadeh, N. T., Balaji, V., Durachta, J., Dupuis, C., Menzel, R., Robinson, T., Underwood, S., Vahlenkamp, H., Bushuk, M., Dunne, K. A., Dussin, R., Gauthier, P. P. G., … Zhang, R. (2018). *NOAA-GFDL GFDL-CM4 model output historical [Dataset]*. Version 2022 Earth System Grid Federation. https://doi.org/10.22033/ESGF/CMIP6.8594

Guo, Y., Li, Y., & Wang, F. (2023). Destinations and pathways of the Indonesian Throughflow water in the Indian Ocean. *Journal of Climate*, 1–39. https://doi.org/10.1175/jcli-d-22-0631.1

Hajima, T., Abe, M., Arakawa, O., Suzuki, T., Komuro, Y., Ogura, T., Ogochi, K., Watanabe, M., Yamamoto, A., Tatebe, H., Noguchi, M. A., Ohgaito, R., Ito, A., Yamazaki, D., Ito, A., Takata, K., Watanabe, S., Kawamiya, M., & Tachiiri, K. (2019). *MIROC MIROC-ES2L model output prepared for CMIP6 CMIP historical [Dataset]*. Version 20221107. Earth System Grid Federation. https://doi.org/10.22033/ESGF/CMIP6.5602

Hamon, B. V., & Tranter, D. J. (1971). East Australian Current. *Australian Natural History*, *17*(4), 129–133. https://doi.org/http://hdl.handle.net/102.100.100/317290?index=1

Harrison, M. (2022). *MJHarrison-GFDL/Harrison_JAMES_2021: v1.0.0 (v1.0.0) [Dataset]*. *Zenodo*. https://doi.org/https://doi.org/10.5281/zenodo.6342240

Harrison, M., Adcroft, A., Hallberg, R., & Sergienko, O. (2022). Improved Surface Mass Balance Closure in Ocean Hindcast Simulations. *Journal of Advances in Modeling Earth Systems*, *14*(7). https://doi.org/10.1029/2021MS002888

Hernández-Guerra, A., Espino-Falcón, E., Vélez-Belchí, P., Dolores Pérez-Hernández, M., Martínez-Marrero, A., & Cana, L. (2017). Recirculation of the Canary Current in fall 2014. *Journal of Marine Systems*, *174*, 25–39. https://doi.org/10.1016/j.jmarsys.2017.04.002

Hernández-Guerra, A., Fraile-Nuez, E., López-Laatzen, F., Martínez, A., Parrilla, G., & Vélez-Belchí, P. (2005). Canary Current and North Equatorial Current from an inverse box model. *Journal of Geophysical Research: Oceans*, *110*(12), 1–16. https://doi.org/10.1029/2005JC003032

Hernández-Guerra, A., Joyce, T. M., Fraile-Nuez, E., & Vélez-Belchí, P. (2010). Using Argo data to investigate the Meridional Overturning Circulation in the North Atlantic. *Deep Sea Research Part I: Oceanographic Research Papers*, *57*(1), 29–36. https://doi.org/10.1016/j.dsr.2009.10.003

Hernández-Guerra, A., Machín, F., Antoranz, A., Cisneros-Aguirre, J., Gordo, C., Marrero-Díaz, A., Martínez, A., Ratsimandresy, A. W., Rodríguez-Santana, A., Sangrá, P., López-Laazen, F., Parrilla, G., & Pelegrí, J. L. (2002). Temporal variability of mass transport in the Canary Current. *Deep Sea Research Part II: Topical Studies in Oceanography*, *49*(17), 3415–3426. https://doi.org/10.1016/S0967-0645(02)00092-9

Hernández-Guerra, A., Pelegrí, J. L., Fraile-Nuez, E., Benítez-Barrios, V. M., Emelianov, M., Pérez-Hernández, M. D., & Vélez-Belchí, P. (2014). Meridional Overturning Transports at 7.5N and 24.5N in the Atlantic Ocean during 1992-93 and 2010-11. *Progress in*

Oceanography, *128*, 98–114. https://doi.org/10.1016/j.pocean.2014.08.016.

Hernández-Guerra, A., & Talley, L. D. (2016). Meridional overturning transports at 30°S in the Indian and Pacific Oceans in 2002–2003 and 2009. *Progress in Oceanography*, *146*, 89–120. https://doi.org/10.1016/j.pocean.2016.06.005

Hernández-Guerra, A., Talley, L. D., Pelegrí, J. L., Vélez-Belchí, P., Baringer, M. O., Macdonald, A. M., & McDonagh, E. L. (2019). The upper, deep, abyssal and overturning circulation in the Atlantic Ocean at 30°S in 2003 and 2011. *Progress in Oceanography*, *176*, 102136. https://doi.org/10.1016/j.pocean.2019.102136

Heywood, K. J., & King, B. A. (2002). Water masses and baroclinic transports in the South Atlantic and Southern oceans. *Journal of Marine Research*, *60*(5), 639–676.

Hill, K. L., Rintoul, S. R., Oke, P. R., & Ridgway, K. (2010). Rapid response of the East Australian Current to remote wind forcing: The role of barotropic-baroclinic interactions. *Journal of Marine Research*, *68*(3), 413–431. https://doi.org/10.1357/002224010794657218

Hogg, N., Biscaye, P., Gardner, W., & Sclunitz, W. J. (1982). On the transport and modification of Antarctic Bottom Water in the Vema Channel. *Journal of Marine Research*, *40*(23), 231–263.

Huang, W. (2019). *THU CIESM model output prepared for CMIP6 CMIP historical [Dataset]*. Version 20221116. Earth System Grid Federation. https://doi.org/10.22033/ESGF/CMIP6.8843

Huisman, S. E., Toom, M. Den, Dijkstra, H. A., & Drijfhout, S. (2010). An indicator of the multiple equilibria regime of the Atlantic meridional overturning circulation. *Journal of Physical Oceanography*, *40*(3), 551–567. https://doi.org/10.1175/2009JPO4215.1

Huyer, A., Smith, R. L., & Paluszkiewicz, T. (1987). Coastal upwelling off Peru during normal and El Niño times, 1981–1984. *Journal of Geophysical Research*, *92*(C13), 14297. https://doi.org/10.1029/JC092iC13p14297

Jackett, D. R., & McDougall, T. J. (1997). A neutral density variable for the world's oceans. *Journal of Physical Oceanography*, *27*(2), 237–263. https://doi.org/10.1175/1520-0485(1997)027<0237:ANDVFT>2.0.CO;2

Jackson, L. C., Kahana, R., Graham, T., Ringer, M. A., Woollings, T., Mecking, J. V., & Wood, R. A. (2015). Global and European climate impacts of a slowdown of the AMOC in a high resolution GCM. *Climate Dynamics*, *45*(11–12), 3299–3316. https://doi.org/10.1007/s00382-015-2540-2

Johnson, C. R., Banks, S. C., Barrett, N. S., Cazassus, F., Dunstan, P. K., Edgar, G. J., Frusher, S. D., Gardner, C., Haddon, M., Helidoniotis, F., Hill, K. L., Holbrook, N. J., Hosie, G. W., Last, P. R., Ling, S. D., Melbourne-Thomas, J., Miller, K., Pecl, G. T., Richardson, A. J., … Taw, N. (2011). Climate change cascades: Shifts in oceanography, species' ranges and subtidal marine community dynamics in eastern Tasmania. *Journal of Experimental Marine Biology and Ecology*, *400*(1–2), 17–32. https://doi.org/10.1016/j.jembe.2011.02.032

Johnson, G. C., Mecking, S., Sloyan, B. M., & Wijffels, S. E. (2007). Recent Bottom Water Warming in the Pacific Ocean*. *Journal of Climate*, *20*(21), 5365–5375. https://doi.org/10.1175/2007JCLI1879.1

Johnson, G. C., & Toole, J. M. (1993). Flow of deep and bottom waters in the Pacific at 10°N. *Deep Sea Research Part I: Oceanographic Research Papers*, *40*(2), 371–394. https://doi.org/10.1016/0967-0637(93)90009-R

Johnson, H. L., Cessi, P., Marshall, D. P., Schloesser, F., & Spall, M. A. (2019). Recent Contributions of Theory to Our Understanding of the Atlantic Meridional Overturning Circulation. *Journal of Geophysical Research: Oceans*, *124*(8), 5376–5399. https://doi.org/10.1029/2019JC015330

Joyce, T. M., Hernández-Guerra, A., & Smethie, W. M. (2001). Zonal circulation in the NW Atlantic and Caribbean from a meridional World Ocean Circulation Experiment hydrographic section at 66 W. *Journal of Geophysical Research: Oceans*, *106*(C10), 22095–22113.

Jungclaus, J., Bittner, M., Wieners, K.-H., Wachsmann, F., Schupfner, M., Legutke, S., Giorgetta, M., Reick, C., Gayler, V., Haak, H., de Vrese, P., Raddatz, T., Esch, M., Mauritsen, T., von Storch, J.-S., Behrens, J., Brovkin, V., Claussen, M., Crueger, T., … Roeckner, E. (2019). *MPI-M MPI-ESM1.2-HR model output prepared for CMIP6 CMIP historical [Dataset]*. Version 20221114. Earth System Grid Federation. https://doi.org/10.22033/ESGF/CMIP6.6594

Kalnay, E., Kanamitsu, M., Kistler, R., Collins, W., Deaven, D., Gandin, L., Iredell, M., Saha, S., White, G., Woollen, J., Zhu, Y., Leetmaa, A., Reynolds, R., Chelliah, M., Ebisuzaki, W., Higgins, W., Janowiak, J., Mo, K. C., Ropelewski, C., … Joseph, D. (1996). The NCEP/NCAR 40-Year Reanalysis Project. *Bulletin of the American Meteorological Society*, *77*(3), 437–471. https://doi.org/10.1175/1520-0477(1996)077<0437:TNYRP>2.0.CO;2

Karsten, R. H., & Marshall, J. (2002). Constructing the Residual Circulation of the ACC from Observations. *Journal of Physical Oceanography*, *32*(12), 3315–3327. https://doi.org/10.1175/1520-0485(2002)032<3315:CTRCOT>2.0.CO;2

Katsumata, K., & Fukasawa, M. (2011). Changes in meridional fluxes and water properties in the Southern Hemisphere subtropical oceans between 1992/1995 and 2003/2004. *Progress in Oceanography*, *89*(1–4), 61–91. https://doi.org/10.1016/j.pocean.2010.12.008

Kawabe, M., & Fujio, S. (2010). Pacific ocean circulation based on observation. *Journal of Oceanography*, *66*(3), 389–403. https://doi.org/10.1007/s10872-010-0034-8

Kawabe, M., Fujio, S., Yanagimoto, D., & Tanaka, K. (2009). Water masses and currents of deep circulation southwest of the Shatsky Rise in the western North Pacific. *Deep Sea Research Part I: Oceanographic Research Papers*, *56*(10), 1675–1687. https://doi.org/10.1016/j.dsr.2009.06.003

Kawabe, M., Yanagimoto, D., & Kitagawa, S. (2006). Variations of deep western boundary currents in the Melanesian Basin in the western North Pacific. *Deep Sea Research Part I: Oceanographic Research Papers*, *53*(6), 942–959. https://doi.org/10.1016/j.dsr.2006.03.003

Kawano, T., Fukasawa, M., Kouketsu, S., Uchida, H., Doi, T., Kaneko, I., Aoyama, M., & Schneider, W. (2006). Bottom water warming along the pathway of lower circumpolar deep water in the Pacific Ocean. *Geophysical Research Letters*, *33*(23), L23613. https://doi.org/10.1029/2006GL027933

Keller, K., Tan, K., Morel, F. M., & Bradford, D. F. (2000). Preserving the ocean circulation: Implications for climate policy. *Climatic Change*, *47*(1), 17–43.

Kelly, K. A., Thompson, L., & Lyman, J. (2014). The Coherence and Impact of Meridional Heat Transport Anomalies in the Atlantic Ocean Inferred from Observations. *Journal of Climate*, *27*(4), 1469–1487. https://doi.org/10.1175/JCLI-D-12-00131.1

Kerry, C., & Roughan, M. (2020). Downstream Evolution of the East Australian Current System: Mean Flow, Seasonal, and Intra-annual Variability. *Journal of Geophysical Research: Oceans*, *125*(5). https://doi.org/10.1029/2019JC015227

Kersalé, M., Meinen, C. S., Perez, R. C., Piola, A. R., Speich, S., Campos, E. J. D., Garzoli, S. L., Ansorge, I., Volkov, D. L., Le Hénaff, M., Dong, S., Lamont, T., Sato, O. T., & van den Berg, M. (2021). Multi-Year Estimates of Daily Heat Transport by the Atlantic Meridional Overturning Circulation at 34.5°S. *Journal of Geophysical Research: Oceans*, *126*(5), 1–23. https://doi.org/10.1029/2020JC016947

Kersalé, M., Perez, R. C., Speich, S., Meinen, C. S., Lamont, T., Le Hénaff, M., van den Berg, M. A., Majumder, S., Ansorge, I. J., Dong, S., Schmid, C., Terre, T., & Garzoli, S. L. (2019). Shallow and Deep Eastern Boundary Currents in the South Atlantic at 34.5°S: Mean Structure and Variability. *Journal of Geophysical Research: Oceans*, *124*, 1–26. https://doi.org/10.1029/2018JC014554.

Knauss, J. A. (1962). On some aspects of the deep circulation of the Pacific. *Journal of Geophysical Research*, *67*(10), 3943–3954. https://doi.org/10.1029/JZ067i010p03943

Laxenaire, R., Speich, S., Blanke, B., Chaigneau, A., Pegliasco, C., & Stegner, A. (2018). Anticyclonic Eddies Connecting the Western Boundaries of Indian and Atlantic Oceans. *Journal of Geophysical*

Research: Oceans, *123*(11), 7651–7677. https://doi.org/10.1029/2018JC014270

Lebedev, K., Yoshinari, H., Maximenko, N. A., & Hacker, P. W. (2007). YoMaHa'07: Velocity data assessed from trajectories of Argo floats at parking level and at the sea surface. *IPRC Technical Note No.*, *4*(2), 16.

Lee, S.-K., Lumpkin, R., Gomez, F., Yeager, S., Lopez, H., Takglis, F., Dong, S., Aguiar, W., Kim, D., & Baringer, M. (2023). Human-induced changes in the global meridional overturning circulation are emerging from the Southern Ocean. *Communications Earth & Environment*, *4*(1), 69. https://doi.org/10.1038/s43247-023-00727-3

Lee, W.-L., & Liang, H.-C. (2020). *AS-RCEC TaiESM1.0 model output prepared for CMIP6 CMIP historical [Dataset]*. Version 20221116. Earth System Grid Federation. https://doi.org/10.22033/ESGF/CMIP6.9755

Li, G., Cheng, L., Zhu, J., Trenberth, K. E., Mann, M. E., & Abraham, J. P. (2020). Increasing ocean stratification over the past half-century. *Nature Climate Change*, *10*(12), 1116–1123. https://doi.org/10.1038/s41558-020-00918-2

Li, L. (2019). *CAS FGOALS-g3 model output prepared for CMIP6 CMIP historical [Dataset]*. Version 20221115. Earth System Grid Federation. https://doi.org/10.22033/ESGF/CMIP6.3356

Li, Z., Holbrook, N. J., Zhang, X., Oliver, E. C. J., & Cougnon, E. A. (2020). Remote Forcing of Tasman Sea Marine Heatwaves. *Journal of Climate*, *33*(12), 5337–5354. https://doi.org/10.1175/JCLI-D-19-0641.1

Little, C. M., Hu, A., Hughes, C. W., McCarthy, G. D., Piecuch, C. G., Ponte, R. M., & Thomas, M. D. (2019). The Relationship Between U.S. East Coast Sea Level and the Atlantic Meridional Overturning Circulation: A Review. *Journal of Geophysical Research: Oceans*, *124*(9), 6435–6458. https://doi.org/10.1029/2019JC015152

Liu, W., Fedorov, A. V, Xie, S.-P., & Hu, S. (2020). Climate impacts of a weakened Atlantic Meridional Overturning Circulation in a warming climate. *Science Advances*, *6, eaaz4876*.

Liu, W., & Liu, Z. (2013). A diagnostic indicator of the stability of the atlantic meridional overturning circulation in CCSM3. *Journal of Climate*, *26*(6), 1926–1938. https://doi.org/10.1175/JCLI-D-11-00681.1

Liu, W., & Liu, Z. (2014). A note on the stability indicator of the Atlantic meridional overturning circulation. *Journal of Climate*, *27*(2), 969–975. https://doi.org/10.1175/JCLI-D-13-00181.1

Liu, W., Liu, Z., & Brady, E. C. (2014). Why is the AMOC monostable in coupled general circulation models? *Journal of Climate*, *27*(6), 2427–2443. https://doi.org/10.1175/JCLI-D-13-00264.1

Liu, W., Liu, Z., & Hu, A. (2013). The stability of an evolving Atlantic meridional overturning circulation. *Geophysical Research Letters*, *40*(8), 1562–1568. https://doi.org/10.1002/grl.50365

Liu, W., Xie, S. P., Liu, Z., & Zhu, J. (2017). Overlooked possibility of a collapsed atlantic meridional overturning circulation in warming climate. *Science Advances*, *3*(1), 1–8. https://doi.org/10.1126/sciadv.1601666

Locarnini, M., Mishonov, A., Baranova, O., Boyer, T., Zweng, M., Garcia, H., Reagan, J., Seidov, D., Weathers, K., Paver, C., & Smolyar, I. (2018). *World Ocean Atlas 2018, Volume 1: Temperature*. A. Mishonov Technical Editor. https://archimer.ifremer.fr/doc/00651/76338/

Lovato, T., & Peano, D. (2020). *CMCC CMCC-CM2-SR5 model output prepared for CMIP6 CMIP historical [Dataset]*. Version 20221106. Earth System Grid Federation. https://doi.org/10.22033/ESGF/CMIP6.3825

Lovato, T., Peano, D., & Butenschön, M. (2021). *CMCC CMCC-ESM2 model output prepared for CMIP6 CMIP [Dataset]*. Version 20221116. Earth System Grid Federation. https://doi.org/10.22033/ESGF/CMIP6.13164

Lumpkin, R., & Speer, K. (2007). Global Ocean Meridional Overturning. *Journal of Physical Oceanography*, *37*(10), 2550–2562. https://doi.org/10.1175/JPO3130.1

Lynch-Stieglitz, J. (2017). The Atlantic Meridional Overturning Circulation and Abrupt Climate Change. *Annual Review of Marine Science*, *9*(1), 83–104. https://doi.org/10.1146/annurev-marine-010816-060415

Macdonald, A. M., Mecking, S., Robbins, P. E., Toole, J. M., Johnson, G. C., Talley, L., Cook, M., & Wijffels, S. E. (2009). The WOCE-era 3-D Pacific Ocean circulation and heat budget. *Progress in Oceanography*, *82*(4), 281–325. https://doi.org/10.1016/j.pocean.2009.08.002

Macdonald, A. M., & Wunsch, C. (1996). An estimate of global ocean circulation and heat fluxes. *Nature*, *382*(6590), 436–439. https://doi.org/10.1038/382436a0

Maharaj, A. M., Cipollini, P., & Holbrook, N. J. (2005). Observed variability of the South Pacific westward sea level anomaly signal in the presence of bottom topography. *Geophysical Research Letters*, *32*(4). https://doi.org/10.1029/2004GL020966

Majumder, S., & Schmid, C. (2018). A study of the variability in the Benguela Current volume transport. *Ocean Science*, *14*(2), 273–283. https://doi.org/10.5194/os-14-273-2018

Majumder, S., Schmid, C., & Halliwell, G. (2016a). An observations and model-based analysis of meridional transports in the South Atlantic. *Journal of Geophysical Research: Oceans*, *121*(8), 5622–5638. https://doi.org/10.1002/2016JC011693

Majumder, S., Schmid, C., & Halliwell, G. (2016b). An observations and model-based analysis of meridional transports in the South Atlantic. *Journal of Geophysical Research: Oceans*, *121*(8), 5622–5638.

Manabe, S., & Stouffer, R. J. (1988). Two Stable Equilibria of a Coupled Ocean-Atmosphere Model. *Journal of Climate*, *1*(9), 841–866. https://doi.org/10.1175/1520-0442(1988)001<0841:TSEOAC>2.0.CO;2

Manta, G., Speich, S., Karstensen, J., Hummels, R., Kersalé, M., Laxenaire, R., Piola, A., Chidichimo, M. P., Sato, O. T., Cotrim da Cunha, L., Ansorge, I., Lamont, T., van den Berg, M. A., Schuster, U., Tanhua, T., Kerr, R., Guerrero, R., Campos, E., & Meinen, C. S. (2021). The South Atlantic Meridional Overturning Circulation and

Mesoscale Eddies in the First GO-SHIP Section at 34.5°S. *Journal of Geophysical Research: Oceans*, *126*(2), 1–25. https://doi.org/10.1029/2020JC016962

Mantyla, A. W., & Reid, J. L. (1983). Abyssal characteristics of the World Ocean waters. *Deep Sea Research Part A. Oceanographic Research Papers*, *30*(8), 805–833.

Marshall, J., & Radko, T. (2003). Residual-Mean Solutions for the Antarctic Circumpolar Current and Its Associated Overturning Circulation. *Journal of Physical Oceanography*, *33*(11), 2341–2354. https://doi.org/10.1175/1520-0485(2003)033<2341:RSFTAC>2.0.CO;2

Marshall, J., & Speer, K. (2012). Closure of the meridional overturning circulation through Southern Ocean upwelling. In *Nature Geoscience* (Vol. 5, Issue 3, pp. 171–180). https://doi.org/10.1038/ngeo1391

Masumoto, Y., Sasaki, H., Kagimoto, T., Komori, N., Ishida, A., Sasai, Y., Miyama, T., Motoi, T., Mitsudera, H., Takahashi, K., Sakuma, H., & Yamagata, T. (2004). A Fifty-Year Eddy-Resolving Simulation of the World Ocean: Preliminary Outcomes of OFES (OGCM for the Earth Simulator). *Journal of the Earth Simulator*, *1*, 35–36. https://doi.org/10.1109/oceans.2004.1406350

Mata, M. M., Tomczak, M., Wijffels, S., & Church, J. A. (2000). East Australian Current volume transports at 30°S: Estimates from the World Ocean Circulation Experiment hydrographic sections PR11/P6 and the PCM3 current meter array. *Journal of Geophysical Research: Oceans*, *105*(C12), 28509–28526. https://doi.org/10.1029/1999JC000121

Matano, R. P., Palma, E. D., & Piola, A. R. (2010). The influence of the Brazil and Malvinas Currents on the Southwestern Atlantic Shelf circulation. *Ocean Science*, *6*(4), 983–995. https://doi.org/10.5194/os-6-983-2010

Matos, F. D. A. O., Pereira, J., & Dengler, M. (2020). Salinity Biases and the Variability of the Atlantic Meridional Overturning Circulation in GFDL-CM3. *Ocean Science Journal*, *55*(4), 505–520. https://doi.org/10.1007/s12601-020-0040-8

Mazloff, M., & (Eds.)., N. C. for A. R. S. (n.d.). *The Climate Data Guide: Southern Ocean State Estimate (SOSE)*. Last Modified 09 Nov 2016. https://climatedataguide.ucar.edu/climate-data/southern-ocean-state-estimate-sose.

McCarthy, G. D., Brown, P. J., Flagg, C. N., Goni, G., Houpert, L., Hughes, C. W., Hummels, R., Inall, M., Jochumsen, K., Larsen, K. M. H., Lherminier, P., Meinen, C. S., Moat, B. I., Rayner, D., Rhein, M., Roessler, A., Schmid, C., & Smeed, D. A. (2020). Sustainable Observations of the AMOC: Methodology and Technology. *Reviews of Geophysics*, *58*(1). https://doi.org/10.1029/2019RG000654

McCarthy, M. C., Talley, L. D., & Roemmich, D. (2000). Seasonal to interannual variability from expendable bathythermograph and TOPEX/Poseidon altimeter data in the South Pacific subtropical gyre. *Journal of Geophysical Research: Oceans*, *105*(C8), 19535–19550. https://doi.org/10.1029/2000JC900056

McDonagh, E. L., Bryden, H. L., King, B. A., & Sanders, R. J. (2008). The circulation of the Indian Ocean at 32°S. *Progress in Oceanography*, *79*(1), 20–36. https://doi.org/10.1016/j.pocean.2008.07.001

McDonagh, E. L., & King, B. A. (2005). Oceanic Fluxes in the South Atlantic. *Journal of Physical Oceanography*, *35*(1), 109–122. https://doi.org/10.1175/JPO-2666.1

McDonagh, E. L., King, B. A., Bryden, H. L., Courtois, P., Szuts, Z., Baringer, M., Cunningham, S. A., Atkinson, C., & McCarthy, G. (2015). Continuous estimate of Atlantic oceanic freshwater flux at 26.5°N. *Journal of Climate*, *28*(22), 8888–8906. https://doi.org/10.1175/JCLI-D-14-00519.1

Mecking, J. V., Drijfhout, S. S., Jackson, L. C., & Andrews, M. B. (2017). The effect of model bias on Atlantic freshwater transport and implications for AMOC bi-stability. *Tellus, Series A: Dynamic Meteorology and Oceanography*, *69*(1), 1–15. https://doi.org/10.1080/16000870.2017.1299910

Mecking, J. V., Drijfhout, S. S., Jackson, L. C., & Graham, T. (2016). Stable AMOC off state in an eddy-permitting coupled climate model. *Climate Dynamics*, *47*(7–8), 2455–2470. https://doi.org/10.1007/s00382-016-2975-0

Meinen, C. S., & Garzoli, S. L. (2014). Attribution of deep western boundary current variability at 26.5ºN. *Deep Sea Research Part I: Oceanographic Research Papers*, *90*, 81–90. https://doi.org/http://dx.doi.org/10.1016/ j. dsr.2014.04.016.

Meinen, C. S., Garzoli, S. L., Perez, R. C., Campos, E., Piola, A. R., Chidichimo, M. P., Dong, S., & Sato, O. T. (2017). Characteristics and causes of Deep Western Boundary Current transport variability at 34.5° S during 2009-2014. *Ocean Science*, *13*(1), 175–194. https://doi.org/10.5194/os-13-175-2017

Meinen, C. S., Speich, S., Perez, R. C., Dong, S., Piola, A. R., Garzoli, S. L., Baringer, M. O., Gladyshev, S., & Campos, E. J. D. (2013). Temporal variability of the meridional overturning circulation at 34.5°S: Results from two pilot boundary arrays in the South Atlantic. *Journal of Geophysical Research: Oceans*, *118*(12), 6461–6478. https://doi.org/10.1002/2013JC009228

Meinen, C. S., Speich, S., Piola, A. R., Ansorge, I., Campos, E., Kersalé, M., Terre, T., Chidichimo, M. P., Lamont, T., Sato, O. T., Perez, R. C., Valla, D., Berg, M., Le Hénaff, M., Dong, S., & Garzoli, S. L. (2018). Meridional Overturning Circulation Transport Variability at 34.5°S During 2009–2017: Baroclinic and Barotropic Flows and the Dueling Influence of the Boundaries. *Geophysical Research Letters*, *45*(9), 4180–4188. https://doi.org/10.1029/2018GL077408

Mercier, H., Arhan, M., & Lutjeharms, J. R. E. (2003). Upper-layer circulation in the eastern Equatorial and South Atlantic Ocean in January-March 1995. *Deep-Sea Research Part I: Oceanographic Research Papers*, *50*(7), 863–887. https://doi.org/10.1016/S0967-0637(03)00071-2

Moffa-Sánchez, P., & Hall, I. R. (2017). North Atlantic variability and its links to European climate over the last 3000 years. *Nature Communications*, *8*(1), 1726. https://doi.org/10.1038/s41467-017-01884-8

Montes, I., Colas, F., Capet, X., & Schneider, W. (2010). On the pathways of the equatorial subsurface currents in the eastern equatorial Pacific and their contributions to the Peru-Chile Undercurrent. *Journal of Geophysical Research*, *115*(C9), C09003. https://doi.org/10.1029/2009JC005710

Moore, M. I., & Wilkin, J. L. (1998). Variability in the South Pacific Deep Western Boundary Current from current meter observations and a high-resolution global model. *Journal of Geophysical Research: Oceans*, *103*(C3), 5439–5457. https://doi.org/10.1029/97jc03207

Mulhearn, P. J. (1987). The Tasman Front: A study using satellite infrared imagery. *Journal of Physical Oceanography*, *17*(8), 1148–1155.

Müller, T. J., Ikeda, Y., Zangenberg, N., & Nonato, L. V. (1998). Direct measurements of western boundary currents off Brazil between 20°S and 28°S. *Journal of Geophysical Research: Oceans*, *103*(C3), 5429–5437. https://doi.org/10.1029/97JC03529

Munk, W., & Wunsch, C. (1998). Abyssal recipes II: energetics of tidal and wind mixing. *Deep Sea Research Part I: Oceanographic Research Papers*, *45*(12), 1977–2010. https://doi.org/10.1016/S0967-0637(98)00070-3

(NASA/GISS), N. G. I. for S. S. (2018). *NASA-GISS GISS-E2.1G model output prepared for CMIP6 CMIP historical [Dataset]*. Version 20221109. Earth System Grid Federation. https://doi.org/10.22033/ESGF/CMIP6.7127

(NASA/GISS), N. G. I. for S. S. (2019). *NASA-GISS GISS-E2-1-G-CC model output prepared for CMIP6 CMIP historical [Dataset]*. Version 20221114. Earth System Grid Federation.

Neshyba, S. (1979). On the southernmost extension of the Peru-Chile undercurrent. *Deep Sea Research Part A. Oceanographic Research Papers*, *26*(12), 1387–1393. https://doi.org/10.1016/0198-0149(79)90006-2

Oke, P. R., Roughan, M., Cetina-Heredia, P., Pilo, G. S., Ridgway, K. R., Rykova, T., Archer, M. R., Coleman, R. C., Kerry, C. G., Rocha, C., Schaeffer, A., & Vitarelli, E. (2019). Revisiting the circulation of the East Australian Current: Its path, separation, and eddy field. *Progress in Oceanography*, *176*, 102139. https://doi.org/10.1016/j.pocean.2019.102139

Palma, E. D., & Matano, R. P. (2017). South Atlantic circulation and variability from a data assimilating model. In *Marine pollution and climate change* (pp. 39–65). CRC Press.

Palter, J. B. (2015). The role of the Gulf Stream in European climate. *Annual Review of Marine Science*, *7*(1), 113–137. https://doi.org/10.1146/annurev-marine-010814-015656

Park, S., & Shin, J. (2019). *SNU SAM0-UNICON model output prepared for CMIP6 CMIP historical [Dataset]*. Version 20221115. Earth System Grid Federation. https://doi.org/10.22033/ESGF/CMIP6.7789

Perez, R. C., Garzoli, S. L., Meinen, C. S., & Matano, R. P. (2011). Geostrophic velocity measurement techniques for the meridional overturning: Circulation and meridional heat transport in the South Atlantic. *Journal of Atmospheric and Oceanic Technology*, *28*(11), 1504–1521. https://doi.org/10.1175/JTECH-D-11-00058.1

Pérez-Hernández, M. D., Hernández-Guerra, A., Fraile-Nuez, E., Comas-Rodríguez, I., Benítez-Barrios, V. M., Domínguez-Yanes, J. F., Vélez-Belchí, P., & De Armas, D. (2013). The source of the Canary current in fall 2009. *Journal of Geophysical Research: Oceans*, *118*(6), 2874–2891. https://doi.org/10.1002/jgrc.20227

Perkins, M. L., & Holbrook, N. J. (2001). Can Pacific Ocean Thermocline Depth Anomalies Be Simulated by a Simple Linear Vorticity Model? *Journal of Physical Oceanography*, *31*(7), 1786–1806. https://doi.org/10.1175/1520-0485(2001)031<1786:CPOTDA>2.0.CO;2

Peterson, R. G., & Stramma, L. (1991). Upper-level circulation in the South Atlantic Ocean. *Progress in Oceanography*, *26*(1), 1–73. https://doi.org/10.1016/0079-6611(91)90006-8

Peterson, R. G., & Whitworth, T. (1989). The subantarctic and polar fronts in relation to deep water masses through the southwestern Atlantic. *Journal of Geophysical Research*, *94*(C8), 10817. https://doi.org/10.1029/JC094iC08p10817

Pita, I., Goes, M., Volkov, D. L., Dong, S., Goni, G., & Cirano, M. (2024). An ARGO and XBT Observing System for the Atlantic Meridional Overturning Circulation and Meridional Heat Transport (AXMOC) at 22.5°S. *Journal of Geophysical Research: Oceans*, *129*(1). https://doi.org/10.1029/2023jc020010

Polito, P. S., & Liu, W. T. (2003). Global characterization of Rossby waves at several spectral bands. *Journal of Geophysical Research*, *108*(C1), 3018. https://doi.org/10.1029/2000JC000607

Polito, P. S., Sato, O. T., & Liu, W. T. (2000). Characterization and validation of the heat storage variability from TOPEX/Poseidon at four oceanographic sites. *Journal of Geophysical Research: Oceans*, *105*(C7), 16911–16921. https://doi.org/10.1029/1999JC000048

Poole, R., & Tomczak, M. (1999). Optimum multiparameter analysis of the water mass structure in the Atlantic Ocean thermocline. *Deep Sea Research Part I: Oceanographic Research Papers*, *46*(11), 1895–1921. https://doi.org/10.1016/S0967-0637(99)00025-4

Pujol, M. I., Faugère, Y., Taburet, G., Dupuy, S., Pelloquin, C., Ablain, M., & Picot, N. (2016). DUACS DT2014: The new multi-mission altimeter data set reprocessed over 20 years. *Ocean Science*, *12*(5), 1067–1090. https://doi.org/10.5194/os-12-1067-2016

Purkey, S. G., Johnson, G. C., Talley, L. D., Sloyan, B. M., Wijffels, S. E., Smethie, W., Mecking, S., & Katsumata, K. (2019). Unabated Bottom Water Warming and Freshening in the South Pacific Ocean. *Journal of Geophysical Research: Oceans*, *124*(3), 1778–1794. https://doi.org/10.1029/2018JC014775

Rahmstorf, S. (1996). On the freshwater forcing and transport of the Atlantic thermohaline circulation. *Climate Dynamics*, *12*(12), 799–811. https://doi.org/10.1007/s003820050144

Reid, J. L. (1989). On the total geostrophic circulation of the South Atlantic Ocean: Flow patterns, tracers, and transports. *Progress in Oceanography*, *23*(3), 149–244. https://doi.org/10.1016/0079-6611(89)90001-3

Reid, J. L. (1997). On the total geostrophic circulation of the pacific ocean: flow patterns, tracers, and transports. *Progress in Oceanography*, *39*(4), 263–352. https://doi.org/10.1016/S0079-6611(97)00012-8

Reid, J. L., Nowlin, W. D., & Patzert, W. C. (1977). On the Characteristics and Circulation of the Southwestern Atlantic Ocean. *Journal of Physical Oceanography*, *7*(1), 62–91. https://doi.org/10.1175/1520-0485(1977)007<0062:OTCACO>2.0.CO;2

Ribbat, N., Roughan, M., Powell, B., Rao, S., & Kerry, C. G. (2020). Transport variability over the Hawkesbury Shelf (31.5–34.5°S) driven by the East Australian Current. *PLOS ONE*, *15*(11), e0241622. https://doi.org/10.1371/journal.pone.0241622

Richardson, P. L., & Garzoli, S. L. (2003). Characteristics of intermediate water flow in the Benguela current as measured with RAFOS floats. *Deep-Sea Research Part II: Topical Studies in Oceanography*, *50*(1), 87–118. https://doi.org/10.1016/S0967-0645(02)00380-6

Ridgway, K. R. (2007). Long-term trend and decadal variability of the southward penetration of the East Australian Current. *Geophysical Research Letters*, *34*(13). https://doi.org/10.1029/2007GL030393

Ridgway, K. R., & Godfrey, J. S. (1997). Seasonal cycle of the East Australian Current. *Journal of Geophysical Research: Oceans*, *102*(C10), 22921–22936. https://doi.org/10.1029/97JC00227

Ridley, J., Menary, M., Kuhlbrodt, T., Andrews, M., & Andrews, T. (2019). *MOHC HadGEM3-GC31-LL model output prepared for CMIP6 CMIP historical [Dataset]*. Version 20221108. Earth System Grid Federation. https://doi.org/10.22033/ESGF/CMIP6.6109

Rienecker, M. M., Suarez, M. J., Gelaro, R., Todling, R., Bacmeister, J., Liu, E., Bosilovich, M. G., Schubert, S. D., Takacs, L., Kim, G.-K., Bloom, S., Chen, J., Collins, D., Conaty, A., da Silva, A., Gu, W., Joiner, J., Koster, R. D., Lucchesi, R., … Woollen, J. (2011). MERRA: NASA's Modern-Era Retrospective Analysis for Research and Applications. *Journal of Climate*, *24*(14), 3624–3648. https://doi.org/10.1175/JCLI-D-11-00015.1

Rintoul, S. R. (1991). South Atlantic interbasin exchange. *Journal of Geophysical Research: Oceans*, *96*(C2), 2675–2692.

Robbins, P. E., & Toole, J. M. (1997). The dissolved silica budget as a constraint on the meridional overturning circulation of the Indian Ocean. *Deep Sea Research Part I: Oceanographic Research Papers*, *44*(5), 879–906. https://doi.org/10.1016/S0967-0637(96)00126-4

Rodrigues, R. R., Rothstein, L. M., & Wimbush, M. (2007). Seasonal Variability of the South Equatorial Current Bifurcation in the Atlantic Ocean: A Numerical Study. *Journal of Physical Oceanography*, *37*(1), 16–30. https://doi.org/10.1175/JPO2983.1

Roemmich, D., & Gilson, J. (2009). The 2004-2008 mean and annual cycle of temperature, salinity, and steric height in the global ocean from the Argo Program. *Progress in Oceanography*, *82*(2), 81–100. https://doi.org/10.1016/j.pocean.2009.03.004

Roemmich, D., & Owens, B. (2000). The Argo Project: Global Ocean Observations for Understanding and Prediction of Climate Variability. *Oceanography*, *13*(2), 45–50. https://doi.org/10.5670/oceanog.2000.33

Roemmich, D., & Wunsch, C. (1985). Two transatlantic sections: meridional circulation and heat flux in the subtropical North Atlantic Ocean. *Deep Sea Research Part A. Oceanographic Research Papers*, *32*(6), 619–664. https://doi.org/10.1016/0198-0149(85)90070-6

Santana-Toscano, D., Pérez-Hernández, M. D., Macdonald, A. M., Arumí-Planas, C., Caínzos, V., & Hernández-Guerra, A. (2023). Zonal circulation in the North Atlantic ocean at 52°W from WOCE-WHP and CLIVAR sections: 1997, 2003 and 2012. *Progress in Oceanography*, *216*. https://doi.org/10.1016/j.pocean.2023.103069

Sasaki, H., Nonaka, M., Masumoto, Y., Sasai, Y., Uehara, H., & Sakuma, H. (2008). An Eddy-Resolving Hindcast Simulation of the Quasiglobal Ocean from 1950 to 2003 on the Earth Simulator. In *High Resolution Numerical Modelling of the Atmosphere and Ocean* (pp. 157–185). Springer New York. https://doi.org/10.1007/978-0-387-49791-4_10

Saunders, P. M., & King, B. A. (1995). Oceanic Fluxes on the WOCE A11 Section. *Journal of Physical Oceanography*, *25*(9), 1942–1958. https://doi.org/10.1175/1520-0485(1995)025<1942:OFOTWA>2.0.CO;2

Schmid, C., & Majumder, S. (2018). Transport variability of the Brazil Current from observations and a data assimilation model. *Ocean Science*, *14*(3), 417–436. https://doi.org/10.5194/os-14-417-2018

Schmitz, W. J. (1995). On the interbasin-scale thermohaline circulation. *Reviews of Geophysics*, *33*(2), 151. https://doi.org/10.1029/95RG00879

Schulze Chretien, L. M., & Speer, K. (2019). A Deep Eastern Boundary Current in the Chile Basin. *Journal of Geophysical Research: Oceans*, *124*(1), 27–40. https://doi.org/10.1029/2018JC014400

Seferian, R. (2018). *CNRM-CERFACS CNRM-ESM2-1 model output prepared for CMIP6 CMIP historical [Dataset]*. Version 20221106. Earth System Grid Federation. https://doi.org/10.22033/ESGF/CMIP6.4068

Seland, Ø., Bentsen, M., Olivié, D. J. L., Toniazzo, T., Gjermundsen, A., Graff, L. S., Debernard, J. B., Gupta, A. K., He, Y., Kirkevåg, A., Schwinger, J., Tjiputra, J., Aas, K. S., Bethke, I., Fan, Y., Griesfeller, J., Grini, A., Guo, C., Ilicak, M., … Schulz, M. (2019). *NCC NorESM2-LM model output prepared for CMIP6 CMIP historical [Dataset]*. Version 20221116. Earth System Grid Federation. https://doi.org/10.22033/ESGF/CMIP6.8036

Shaffer, G., Hormazabal, S., Pizarro, O., & Ramos, M. (2004). Circulation and variability in the Chile Basin. *Deep Sea Research Part I: Oceanographic Research Papers*, *51*(10), 1367–1386. https://doi.org/10.1016/j.dsr.2004.05.006

Shaffer, G., Hormazabal, S., Pizarro, O., & Salinas, S. (1999). Seasonal and interannual variability of currents and temperature off central Chile. *Journal of Geophysical Research: Oceans*, *104*(C12), 29951–29961.

Shannon, L. V., & Hunter, D. (1988). Notes on Antarctic intermediate water around southern Africa. *South African Journal of Marine Science*, *6*(1), 107–117. https://doi.org/10.2989/025776188784480735

Silva, N., Rojas, N., & Fedele, A. (2009). Water masses in the Humboldt Current System: Properties, distribution, and the nitrate deficit as a chemical water mass tracer for Equatorial Subsurface Water off Chile. *Deep Sea Research Part II: Topical Studies in Oceanography*, *56*(16), 1004–1020. https://doi.org/10.1016/j.dsr2.2008.12.013

Sitz, L. E., Farneti, R., & Griffies, S. M. (2015). Simulated South Atlantic transports and their variability during 1958–2007. *Ocean Modelling*, *91*, 70–90. https://doi.org/10.1016/j.ocemod.2015.05.001

Skliris, N., Marsh, R., Mecking, J. V., & Zika, J. D. (2020). Changing water cycle and freshwater transports in the Atlantic Ocean in observations and CMIP5 models. *Climate Dynamics*, *54*(11–12), 4971–4989. https://doi.org/10.1007/s00382-020-05261-y

Sloyan, B. M., Ridgway, K. R., & Cowley, R. (2016). The East Australian Current and Property Transport at 27°S from 2012 to 2013. *Journal of Physical Oceanography*, *46*(3), 993–1008. https://doi.org/10.1175/JPO-D-15-0052.1

Sloyan, B. M., & Rintoul, S. R. (2001). The Southern Ocean Limb of the Global Deep Overturning Circulation*. *Journal of Physical Oceanography*, *31*(1), 143–173. https://doi.org/10.1175/1520-0485(2001)031<0143:TSOLOT>2.0.CO;2

Smethie, W. M., & Fine, R. A. (2001). Rates of North Atlantic Deep Water formation calculated from chlorofluorocarbon inventories. *Deep Sea Research Part I: Oceanographic Research Papers*, *48*(1), 189–215. https://doi.org/10.1016/S0967-0637(00)00048-0

Speer, K. G., Siedler, G., & Talley, L. (1995). The Namib Col Current. *Deep Sea Research Part I: Oceanographic Research Papers*, *42*(11–12), 1933–1950. https://doi.org/10.1016/0967-0637(95)00088-7

Speich, S., Blanke, B., & Madec, G. (2001). Warm and cold water routes of an O.G.C.M. thermohaline conveyor belt. *Geophysical Research Letters*, *28*(2), 311–314. https://doi.org/10.1029/2000GL011748

Sprintall, J., & Tomczak, M. (1993). On the formation of Central Water and thermocline ventilation in the southern hemisphere. *Deep-Sea Research Part I: Oceanographic Research Papers*, *40*(4), 827–848.

Sprintall, J., Wijffels, S. E., Molcard, R., & Jaya, I. (2009). Direct estimates of the Indonesian Throughflow entering the Indian Ocean: 2004–2006. *Journal of Geophysical Research*, *114*(C07001). https://doi.org/10.1029/2008JC005257

Stommel, H. (1961). Thermohaline Convection with Two Stable Regimes of Flow. *Tellus*, *13*(2), 224–230. https://doi.org/10.1111/j.2153-3490.1961.tb00079.x

Stouffer, R. (2019). *UA MCM-UA-1-0 model output prepared for CMIP6 CMIP historical [Dataset]*. Version 20221116. Earth System Grid Federation. https://doi.org/10.22033/ESGF/CMIP6.8888

Stramma, L. (1989). The Brazil current transport south of 23°S. *Deep Sea Research Part A. Oceanographic Research Papers*, *36*(4), 639–646. https://doi.org/10.1016/0198-0149(89)90012-5

Stramma, L. (1991). Geostrophic transport of the South Equatorial Current in the Atlantic. *Journal of Marine Research*, *49*(2), 281–294. https://doi.org/10.1357/002224091784995864

Stramma, L., & England, M. (1999). On the water masses and mean circulation of the South Atlantic Ocean. *Journal of Geophysical Research: Oceans*, *104*(C9), 20863–20883. https://doi.org/10.1029/1999JC900139

Stramma, L., Johnson, G. C., Firing, E., & Schmidtko, S. (2010). Eastern Pacific oxygen minimum zones: Supply paths and multidecadal changes. *Journal of Geophysical Research*, *115*(C9), C09011. https://doi.org/10.1029/2009JC005976

Strub, P. T., Mesias, J. M., Montecino, V., Ruttlant, J., & Salinas, S. (1998). Coastal ocean circulation off western south America. *The Sea*, *11*, 273–314.

Suga, T., & Talley, L. D. (1995). Antarctic Intermediate Water circulation in the tropical and subtropical South Atlantic. *Journal of Geophysical Research*, *100*(C7), 13441. https://doi.org/10.1029/95JC00858

Sun, C., Thresher, A., Keeley, R., Hall, N., Hamilton, M., Chinn, P., Tran, A., Goni, G., PETIT de la VILLEON, L., Carval, T., Cowen, L., Manzella, G., Gopalakrishna, V., Guerrero, R., Reseghetti, F., Kanno, Y., Klein, B., Rickards, L., Baldoni A., … Nagaya, Y. (2010). The Data Management System for the Global Temperature and Salinity Profile Programme. In J. Hall, D. E. Harrison, & D. Strammer (Eds.), *Proceedings of OceanObs'09: Sustained Ocean Observations and Information for Society* (pp. 931–938). European Space Agency. https://doi.org/10.5270/OceanObs09.cwp.86

Sverdrup, H. U. (1947). Wind-Driven Currents in a Baroclinic Ocean; with Application to the Equatorial Currents of the Eastern Pacific.

Proceedings of the National Academy of Sciences, *33*(11), 318–326. https://doi.org/10.1073/pnas.33.11.318

Swart, N. C., Cole, J. N. S., Kharin, V. V, Lazare, M., Scinocca, J. F., Gillett, N. P., Anstey, J., Arora, V., Christian, J. R., Jiao, Y., Lee, W. G., Majaess, F., Saenko, O. A., Seiler, C., Seinen, C., Shao, A., Solheim, L., von Salzen, K., Yang, D., … Sigmond, M. (2019). *CCCma CanESM5 model output prepared for CMIP6 CMIP historical [Dataset]*. Version 20221106. Earth System Grid Federation. https://doi.org/10.22033/ESGF/CMIP6.3610

Talley, L. D. (1996). Antarctic Intermediate Water in the South Atlantic. In *The South Atlantic* (pp. 219–238). Springer Berlin Heidelberg. https://doi.org/10.1007/978-3-642-80353-6_11

Talley, L. D. (2003). Shallow, Intermediate, and Deep Overturning Components of the Global Heat Budget. *Journal of Physical Oceanography*, *33*(3), 530–560. https://doi.org/10.1175/1520-0485(2003)033<0530:SIADOC>2.0.CO;2

Talley, L. D. (2008). Freshwater transport estimates and the global overturning circulation: Shallow, deep and throughflow components. *Progress in Oceanography*, *78*(4), 257–303. https://doi.org/10.1016/j.pocean.2008.05.001

Talley, L. D. (2013). Closure of the Global Overturning Circulation Through the Indian, Pacific, and Southern Oceans: Schematics and Transports. *Oceanography*, *26*(1), 80–97. https://doi.org/10.5670/oceanog.2013.07

Talley, L. D., Feely, R. A., Sloyan, B. M., Wanninkhof, R., Baringer, M. O., Bullister, J. L., Carlson, C. A., Doney, S. C., Fine, R. A., Firing, E., Gruber, N., Hansell, D. A., Ishii, M., Johnson, G. C., Katsumata, K., Key, R. M., Kramp, M., Langdon, C., Macdonald, A. M., … Zhang, J.-Z. (2016). Changes in Ocean Heat, Carbon Content, and Ventilation: A Review of the First Decade of GO-SHIP Global Repeat Hydrography. *Annual Review of Marine Science*, *8*(1), 185–215. https://doi.org/10.1146/annurev-marine-052915-100829

Talley, L. D., & McCartney, M. S. (1982). Distribution and Circulation of Labrador Sea Water. *Journal of Physical Oceanography*, *12*(11), 1189–1205. https://doi.org/10.1175/1520-0485(1982)012<1189:DACOLS>2.0.CO;2

Talley, L. D., Pickard, G. L., Emery, W. J., & Swift, J. H. (2011). *Descriptive Physical Oceanography: An Introduction* (Sixth). Elsevier Ltd.

Talley, L. D., & Sprintall, J. (2005). Deep expression of the Indonesian Throughflow: Indonesian Intermediate Water in the South Equatorial Current. *Journal of Geophysical Research*, *110*(C10009). https://doi.org/10.1029/2004JC002826

Tang, Y., Rumbold, S., Ellis, R., Kelley, D., Mulcahy, J., Sellar, A., Walton, J., & Jones, C. (2019). *MOHC UKESM1.0-LL model output prepared for CMIP6 CMIP historical [Dataset]*. Version 20221110. Earth System Grid Federation. https://doi.org/10.22033/ESGF/CMIP6.6113

Tatebe, H., & Watanabe, M. (2018). *MIROC MIROC6 model output prepared for CMIP6 CMIP historical [Dataset]*. Version 20221107. Earth System Grid Federation. https://doi.org/10.22033/ESGF/CMIP6.5603

Tomczak, M., & Godfrey, J. S. (1994). *Regional oceanography: an introduction*.

Toole, J. M., Curry, R. G., Joyce, T. M., McCartney, M., & Peña-Molino, B. (2011). Transport of the North Atlantic Deep Western Boundary Current about 39°N, 70°W: 2004–2008. *Deep Sea Research Part II: Topical Studies in Oceanography*, *58*(17–18), 1768–1780. https://doi.org/10.1016/j.dsr2.2010.10.058

Tsimplis, M. N., Bacon, S., & Bryden, H. L. (1998). The circulation of the subtropical South Pacific derived from hydrographic data. *Journal of Geophysical Research: Oceans*, *103*(C10), 21443–21468. https://doi.org/10.1029/98JC01881

Tsuchiya, M. (1991). Flow path of the Antarctic Intermediate Water in the western equatorial South Pacific Ocean. *Deep Sea Research Part A. Oceanographic Research Papers*, *38*, S273–S279. https://doi.org/10.1016/S0198-0149(12)80013-6

Tsuchiya, M., & Talley, L. D. (1996). Water-property distributions along an eastern Pacific hydrographic section at 135W. *Journal of Marine Research*, *54*(3), 541–564. https://doi.org/10.1357/0022240963213583

Tsuchiya, M., & Talley, L. D. (1998). A Pacific hydrographic section at 88° W: Water-property distribution. *Journal of Geophysical Research*, *103*(C6), 12899–12918.

Tsujino, H., Urakawa, L. S., Griffies, S. M., Danabasoglu, G., Adcroft, A. J., Amaral, A. E., Arsouze, T., Bentsen, M., Bernardello, R., Böning, C. W., Bozec, A., Chassignet, E. P., Danilov, S., Dussin, R., Exarchou, E., Fogli, P. G., Fox-Kemper, B., Guo, C., Ilicak, M., … Yu, Z. (2020). Evaluation of global ocean–sea-ice model simulations based on the experimental protocols of the Ocean Model Intercomparison Project phase 2 (OMIP-2). *Geoscientific Model Development*, *13*(8), 3643–3708. https://doi.org/10.5194/gmd-13-3643-2020

van Sebille, E., England, M. H., & Froyland, G. (2012). Origin, dynamics, and evolution of ocean garbage patches from observed surface drifters. *Environmental Research Letters*, *7*(4), 044040. https://doi.org/https://doi.org/10.1088/1748-9326/7/4/044040

van Westen, R. M., Kliphuis, M., & Dijkstra, H. A. (2024). Physics-based early warning signal shows that AMOC is on tipping course. *Science Advances*, *10*(6). https://doi.org/10.1126/sciadv.adk1189

Vanicek, M., & Siedler, G. (2002). Zonal fluxes in the deep water layers of the western South Atlantic Ocean. *Journal of Physical Oceanography*, *32*(8), 2205–2235. https://doi.org/10.1175/1520-0485(2002)032<2205:ZFITDW>2.0.CO;2

Vélez-Belchí, P., Pérez-Hernández, M. D., Casanova-Masjoan, M., Cana, L., & Hernández-Guerra, A. (2017). On the seasonal variability of the Canary Current and the Atlantic Meridional Overturning Circulation. *Journal of Geophysical Research: Oceans*, *122*(6), 4518–4538. https://doi.org/10.1002/2017JC012774

Vellinga, M., & Wood, R. A. (2002). Global climatic impacts of a collapse of the Atlantic thermohaline circulation. *Climatic Change*, *54*(3), 251–267.

Vergara, O. A., Echevín, V., Sepúlveda, H. H., Colas, F., & Quiñones, R. A. (2016). Modelling the seasonal dynamics of the Peru-Chile Undercurrent off Central Chile (30–40°S). *Continental Shelf Research*, *123*, 61–79. https://doi.org/10.1016/j.csr.2016.04.001

Vivier, F., Kelly, K. A., & Thompson, L. (1999). Contributions of wind forcing, waves, and surface heating to sea surface height observations in the Pacific Ocean. *Journal of Geophysical Research: Oceans*, *104*(C9), 20767–20788. https://doi.org/10.1029/1999JC900096

Voldoire, A. (2018). *CMIP6 simulations of the CNRM-CERFACS based on CNRM-CM6-1 model for CMIP experiment historical [Dataset]*. Version 20221106. Earth System Grid Federation. https://doi.org/10.22033/ESGF/CMIP6.4066

Wang, O., Fukumori, I., & Fenty, I. (2020). *ECCO version 4 release 4 user guide*.

Warren, B. A., & Speer, K. G. (1991). Deep circulation in the eastern South Atlantic Ocean. *Deep Sea Research Part A. Oceanographic Research Papers*, *38*, S281–S322. https://doi.org/10.1016/S0198-0149(12)80014-8

Weber, S. L., & Drijfhout, S. S. (2007). Stability of the Atlantic Meridional Overturning Circulation in the last glacial maximum climate. *Geophysical Research Letters*, *34*(22), 1–5. https://doi.org/10.1029/2007GL031437

Weijer, W., Cheng, W., Drijfhout, S. S., Fedorov, A. V., Hu, A., Jackson, L. C., Liu, W., McDonagh, E. L., Mecking, J. V., & Zhang, J. (2019). Stability of the Atlantic Meridional Overturning Circulation: A Review and Synthesis. *Journal of Geophysical Research: Oceans*, *124*(8), 5336–5375. https://doi.org/10.1029/2019JC015083

Weijer, W., Cheng, W., Garuba, O. A., Hu, A., & Nadiga, B. T. (2020). CMIP6 Models Predict Significant 21st Century Decline of the Atlantic Meridional Overturning Circulation. *Geophysical Research Letters*, *47*(12). https://doi.org/10.1029/2019GL086075

Weijer, W., & Dijkstra, H. A. (2003). Multiple oscillatory modes of the global ocean circulation. *Journal of Physical Oceanography*, *33*(11), 2197–2213. https://doi.org/10.1175/1520-0485(2003)033<2197:MOMOTG>2.0.CO;2

Weijer, W. jer, De Ruijter, W. P. M., Dijkstra, H. A., & Van Leeuwen, P. J. (1999). Impact of interbasin exchange on the Atlantic overturning circulation. *Journal of Physical Oceanography*, *29*(9), 2266–2284. https://doi.org/10.1175/1520-0485(1999)029<2266:IOIEOT>2.0.CO;2

Whitworth III, T., Warren, B. A., Nowlin, Jr, W. D., Rutz, S. B., Pillsbury, R. D., & Moore, M. I. (1999). On the deep western-boundary current in the Southwest Pacific Basin. *Progress in Oceanography*, *43*(1), 1–54. https://doi.org/10.1016/S0079-6611(99)00005-1

Wijffels, S. E., Hall, M. M., Joyce, T., Torres, D. J., Hacker, P., & Firing, E. (1998). Multiple deep gyres of the western North Pacific: A WOCE section along 149°E. *Journal of Geophysical Research: Oceans*, *103*(C6), 12985–13009. https://doi.org/10.1029/98JC01016

Wijffels, S. E., Toole, J. M., & Davis, R. (2001). Revisiting the South Pacific subtropical circulation: A synthesis of World Ocean Circulation Experiment observations along 32°S. *Journal of Geophysical Research: Oceans*, *106*(C9), 19481–19513. https://doi.org/10.1029/1999JC000118

Wooster, W. S., & Reid, J. L. (1963). Eastern boundary currents. *The Sea, Ideas and Observations on Progress in the Study of the Seas*, *2 MN Hill*, 253–280.

Wu, L., Cai, W., Zhang, L., Nakamura, H., Timmermann, A., Joyce, T., McPhaden, M. J., Alexander, M., Qiu, B., Visbeck, M., Chang, P., & Giese, B. (2012). Enhanced warming over the global subtropical western boundary currents. *Nature Climate Change*, *2*(3), 161–166. https://doi.org/10.1038/nclimate1353

Wu, T., Chu, M., Dong, M., Fang, Y., Jie, W., Li, J., Li, W., Liu, Q., Shi, X., Xin, X., Yan, J., Zhang, F., Zhang, J., Zhang, L., & Zhang, Y. (2018). *BCC BCC-CSM2MR model output prepared for CMIP6 CMIP historical [Dataset]*. Version 20221109. Earth System Grid Federation. https://doi.org/10.22033/ESGF/CMIP6.2948

Wunsch, C. (1978). The North Atlantic general circulation west of 50°W determined by inverse methods. *Reviews of Geophysics*, *16*(4), 583–620. https://doi.org/10.1029/RG016i004p00583

Wunsch, C. (1996). *The Ocean Circulation Inverse Problem*. Cambridge University Press. https://doi.org/10.1017/CBO9780511629570

Wunsch, C., & Heimbach, P. (2009). The Global Zonally Integrated Ocean Circulation, 1992–2006: Seasonal and Decadal Variability. *Journal of Physical Oceanography*, *39*(2), 351–368. https://doi.org/10.1175/2008JPO4012.1

Wunsch, C., Hu, D., & Grant, B. (1983). Mass, Heat, Salt and Nutrient Fluxes in the South Pacific Ocean. *Journal of Physical Oceanography*, *13*(5), 725–753. https://doi.org/10.1175/1520-0485(1983)013<0725:MHSANF>2.0.CO;2

Wyrtki, K. (1967). Circulation and Water Masses in the Eastern Equatorial Pacific Ocean. *Int. J. Oceanol. & Limnol*, *1*(2), 117–147.

Wyrtki, K. (1975). Fluctuations of the Dynamic Topography in the Pacific Ocean. *Journal of Physical Oceanography*, *5*(3), 450–459. https://doi.org/10.1175/1520-0485(1975)005<0450:FOTDTI>2.0.CO;2

Yan, X., Zhang, R., & Knutson, T. R. (2017). The role of Atlantic overturning circulation in the recent decline of Atlantic major hurricane frequency. *Nature Communications*, *8*(1), 1695. https://doi.org/10.1038/s41467-017-01377-8

Yin, J., & Stouffer, R. J. (2007). Comparison of the Stability of the Atlantic Thermohaline Circulation in Two Coupled Atmosphere–Ocean General Circulation Models. *Journal of Climate*, *20*(17), 4293–4315. https://doi.org/10.1175/JCLI4256.1

Zemba, J. C. (1991). *The Structure and Transport of the Brazil Current between* 27^{o} *and* 36^{o} *South.* Massachusetts Institute of Technology and Woods Hole Oceanographic Institution.

Zenk, W., Siedler, G., Lenz, B., & Hogg, N. G. (1999). Antarctic Bottom Water Flow through the Hunter Channel. *Journal of Physical Oceanography*, *29*(11), 2785–2801. https://doi.org/10.1175/1520-0485(1999)029<2785:ABWFTT>2.0.CO;2

Zhang, J., Wu, T., Shi, X., Zhang, F., Li, J., Chu, M., Liu, Q., Yan, J., Ma, Q., & Wei, M. (2018). *BCC BCC-ESM1 model output prepared for*

CMIP6 CMIP historical [Dataset]. Version 20221116. Earth System Grid Federation. https://doi.org/10.22033/ESGF/CMIP6.2949

Zhang, R., Sutton, R., Danabasoglu, G., Kwon, Y., Marsh, R., Yeager, S. G., Amrhein, D. E., & Little, C. M. (2019). A Review of the Role of the Atlantic Meridional Overturning Circulation in Atlantic Multidecadal Variability and Associated Climate Impacts. *Reviews of Geophysics*, *57*(2), 316–375. https://doi.org/10.1029/2019RG000644

Zhu, J., Liu, Z., Zhang, J., & Liu, W. (2015). AMOC response to global warming: dependence on the background climate and response timescale. *Climate Dynamics*, *44*(11–12), 3449–3468. https://doi.org/10.1007/s00382-014-2165-x

Ziehn, T., Chamberlain, M., Lenton, A., Law, R., Bodman, R., Dix, M., Wang, Y., Dobrohotoff, P., Srbinovsky, J., Stevens, L., Vohralik, P., Mackallah, C., Sullivan, A., O'Farrell, S., & Druken, K. (2019). *CSIRO ACCESS-ESM1.5 model output prepared for CMIP6 CMIP historical [Dataset]*. Version 20221106. Earth System Grid Federation. https://doi.org/10.22033/ESGF/CMIP6.4272

Zweng, M., Reagan, J., Seidov, D., Boyer, T., Locarnini, M., Garcia, H., Mishonov, A., Baranova, O., Weathers, K., Paver, C., & Smolyar, I. (2019). *World Ocean Atlas 2018, Volume 2: Salinity*. A. Mishonov Technical Editor. https://archimer.ifremer.fr/doc/00651/76339/